UNIVERSIDADE FEDERAL DO CEARÁ

CENTRO DE CIÊNCIAS

DEPARTAMENTO DE FÍSICA

PROGRAMA DE PÓS-GRADUAÇÃO EM FÍSICA

DOUTORADO EM FÍSICA

WELLISSON PIRES LIMA

STRAINED LIEB-KAGOME LATTICES: EVOLUTION OF THE ELECTRONIC SPECTRUM AND TOPOLOGICAL PHASE TRANSITIONS

FORTALEZA

2024

WELLISSON PIRES LIMA

STRAINED LIEB-KAGOME LATTICES: EVOLUTION OF THE ELECTRONIC SPECTRUM AND TOPOLOGICAL PHASE TRANSITIONS

Tese apresentada ao Programa de Pós-Graduação em Física do Centro de Ciências da Universidade Federal do Ceará, como requisito parcial à obtenção do título de doutor em Física. Área de Concentração: Física da Matéria Condensada.

Orientador: Prof. Dr. João Milton Pereira Júnior.
Coorientador: Prof. Dr. Diego Rabelo da Costa.

FORTALEZA

2024

Dados Internacionais de Catalogação na Publicação
Universidade Federal do Ceará
Sistema de Bibliotecas
Gerada automaticamente pelo módulo Catalog, mediante os dados fornecidos pelo(a) autor(a)

L711s Lima, Wellisson Pires.
Strained Lieb-Kagome lattices : Evolution of the electronic spectrum and topological phase transitions / Wellisson Pires Lima. – 2024.
233 f. : il. color.

Tese (doutorado) – Universidade Federal do Ceará, Centro de Ciências, Programa de Pós-Graduação em Física , Fortaleza, 2024.
Orientação: Prof. Dr. João Milton Pereira Júnior.
Coorientação: Prof. Dr. Diego Rabelo da Costa.

1. topological phase transition. 2. Lieb-Kagome lattice. 3. strain. 4. electronic spectrum. I. Título.
CDD 530

WELLISSON PIRES LIMA

STRAINED LIEB-KAGOME LATTICES: EVOLUTION OF THE ELECTRONIC SPECTRUM AND TOPOLOGICAL PHASE TRANSITIONS

Tese apresentada ao Programa de Pós-Graduação em Física do Centro de Ciências da Universidade Federal do Ceará, como requisito parcial à obtenção do título de doutor em Física. Área de Concentração: Física da Matéria Condensada.

Aprovada em: 28/06/2024

BANCA EXAMINADORA

Prof. Dr. João Milton Pereira Júnior (Orientador)
Universidade Federal do Ceará (UFC)

Prof. Dr. Diego Rabelo da Costa (Coorientador)
Universidade Federal do Ceará (UFC)

Prof. Dr. Márcio de Melo Freire
Universidade Federal do Ceará (UFC)

Profa. Dra. Silvia Helena Roberto de Sena
Universidade da Integração Internacional da Lusofonia Afro-Brasileira (Unilab)

Prof. Dr. Natanael de Carvalho Costa
Universidade Federal do Rio de Janeiro (UFRJ)

To my beloved wife, my dear father, my exceptional mother, my devoted siblings, and my local church, whose support and love are the pillars of my life in God the Father, in Christ Jesus, through the power of the Holy Spirit.

ACKNOWLEDGEMENTS

I extend my deepest gratitude to the Fundação Cearense de Apoio ao Desenvolvimento Científico e Tecnológico (FUNCAP) for their financial support through the doctoral scholarship granted in the first year. This study was financed in part by the Coordenação de Aperfeiçoamento de Pessoal de Nível Superior - Brasil (CAPES) - Finance Code 001, and by the Conselho Nacional de Desenvolvimento Científico e Tecnológico (CNPq).

My sincere thanks go to Prof. Dr. João Milton Pereira Júnior for his patient and insightful guidance, and to Prof. Dr. Diego Rabelo da Costa for his excellent co-guidance, which greatly enriched my experience in the postgraduate program in Physics.

I am grateful to the members of the examining board, Dr. Márcio de Melo Freire, Dr. Silvia Helena Roberto de Sena, and Dr. Natanael de Carvalho Costa, for their time, valuable contributions, and insightful suggestions.

Finally, I appreciate all my colleagues from the Condensed Matter Theory Group (GTMC) for their reflections, critiques, and suggestions that have been pivotal in shaping my research.

"Whatsoever thy hand findeth to do, do it with thy might; for there is no work, nor device, nor knowledge, nor wisdom, in the grave, whither thou goest." (Ecclesiastes 9:10)

ABSTRACT

We systematically investigate the effects of simple shear and uniaxial strains, applied along various crystallographic directions, as well as biaxial and pure shear strains, on the electronic spectra of Lieb and Kagome lattices using a tight-binding model. This model employs a general Hamiltonian that characterizes both lattice types through a single control parameter, θ. Our findings indicate that such deformations do not open an energy gap in their electronic spectra but can lead to (i) convergence of energy cones, (ii) anisotropy in energy levels, and (iii) deformation of the flat band. Consequently, the triply degenerate Dirac point in the Lieb lattice transforms into two doubly degenerate Dirac points. Our analysis of hypothetical strain scenarios, in which the hopping parameters are unchanged, shows that effects such as the flat band deformation and the splitting of the triply degenerate Dirac point result solely from strain-induced changes in hopping parameters. Additionally, we identify cases where non-zero strain-induced pseudovector potentials arise in Lieb and Kagome lattices. Moreover, when considering intrinsic spin-orbit coupling, these lattices exhibit two-dimensional topological insulator behavior with a $\mathbb{Z}_2$ topological classification. Our comprehensive study reveals that such deformations can induce topological phase transitions by altering the structural lattice angle, strain amplitude, and the magnitude of the intrinsic spin-orbit coupling. These transitions are evidenced by the evolution of Berry curvature and shifts in the Chern number when the gap closes. By analyzing hypothetical strain scenarios where the hopping and intrinsic spin-orbit coupling parameters remain intentionally unchanged, we demonstrate that the strain-induced phase transitions stem from simultaneous modifications in the hopping and intrinsic spin-orbit coupling parameters. Further analysis extends to finite-size effects on the topological properties of these lattices, evaluating the energy spectrum for nanoribbons with straight, bearded, and asymmetric edges. The results confirm strain-driven topological phase transitions, supported by the bulk-edge correspondence. Additionally, the evolution of edge states under strain suggests the generation of opposite spin currents.

Keywords: topological phase transition; Lieb-Kagome lattice; strain; electronic spectrum.

RESUMO

Investigamos sistematicamente os efeitos de deformações por cisalhamento simples e deformações uniaxiais, aplicadas ao longo de várias direções cristalográficas, bem como deformações biaxiais e cisalhamento puro, nos espectros eletrônicos das redes de Lieb e Kagome usando um modelo *tight-binding*. Este modelo emprega um Hamiltoniano geral que caracteriza ambos os tipos de rede através de um único parâmetro de controle, θ. Nossas descobertas indicam que tais deformações não abrem um gap de energia nos seus espectros eletrônicos, mas podem levar a (i) convergência dos cones de energia, (ii) anisotropia nos níveis de energia e (iii) deformação da banda plana. Consequentemente, o ponto de Dirac triplamente degenerado na rede de Lieb se transforma em dois pontos de Dirac duplamente degenerados. Nossa análise de cenários hipotéticos de deformação, nos quais os parâmetros de *hopping* são inalterados, mostra que efeitos como a deformação da banda plana e a divisão do ponto de Dirac triplamente degenerado resultam exclusivamente de mudanças nos parâmetros de *hopping* induzidas pela deformação. Adicionalmente, identificamos casos onde potenciais pseudovetoriais induzidos por deformação surgem nas redes de Lieb e Kagome. Além disso, ao considerar o acoplamento spin-órbita intrínseco, essas redes exibem comportamento de isolante topológico bidimensional com uma classificação topológica $\mathbb{Z}_2$. Nosso estudo abrangente revela que tais deformações podem induzir transições de fase topológicas ao alterar o ângulo estrutural da rede, a amplitude da deformação e a magnitude do acoplamento spin-órbita intrínseco. Essas transições são evidenciadas pela evolução da curvatura de Berry e mudanças no número de Chern quando o gap se fecha. Ao analisar cenários hipotéticos de deformação onde os parâmetros de *hopping* e acoplamento spin-órbita intrínseco permanecem intencionalmente inalterados, demonstramos que as transições de fase induzidas pela deformação originam-se de modificações simultâneas nos parâmetros de *hopping* e acoplamento spin-órbita intrínseco. Análises adicionais se estendem aos efeitos de tamanho finito nas propriedades topológicas dessas redes, avaliando o espectro de energia para nanofitas com bordas retas, barbadas e assimétricas. Os resultados confirmam transições de fase topológicas decorrentes da aplicação de deformações, sustentadas pela correspondência *bulk-edge*. Além disso, a evolução dos estados de borda sob deformação sugere a geração de correntes de spin opostas.

Palavras-chave: transição de fase topológica; rede de Lieb-Kagome; tensão; espectro eletrônico.

LIST OF FIGURES

Figure 46 – (a) Lieb-Kagome lattice. $\mathbf{a_{01}}$ and $\mathbf{a_{02}}$ are the primitive vectors of the unstrained lattice, and the shaded unit cell contains three non-equivalent sites: A (blue empty circle), B (yellow filled circle), and C (green circle with a dot inside). The distance between NN sites is a_0, and the non-zero hopping parameters are represented by t_{AB}, t'_{AB}, t_{BC}, t'_{BC}, t_{AC}, and t'_{AC}. The intrinsic spin-orbit (ISO) phase is positive ($+i\lambda_{\langle ij\rangle}$) for spin-up electrons moving along the blue ($\lambda_{\langle ij\rangle}$) or red ($\lambda_{\langle\langle ij\rangle\rangle}$) dotted line counterclockwise, since $|\mathbf{e_{ij}}| = +1$. Otherwise, the ISO coupling phase is negative ($-i\lambda_{ij}$) where $|\mathbf{e_{ij}}| = -1$. (b-g) Comparison of the unit cell of the Lieb-Kagome lattice: (i) unstrained (black solid lines), $\varepsilon = 0$, and (ii) strained (red dashed lines), $\varepsilon > 0$, subjected to: (b) UX, (c) UY, (d) BI, (e) SX, (f) SY, and (g) PS strains. 114

Figure 47 – (a) Transition lattice - D_{2h} with $\theta = 105^\circ$, (b) Lieb lattice - D_{4h} ($\theta = 90^\circ$), and (c) Kagome lattice - D_{6h} ($\theta = 120^\circ$). The primitive vectors are $\mathbf{a_1}$ and $\mathbf{a_2}$, and the unit cells contain three non-equivalent sites A (blue empty circle), B (yellow filled circle), and C (green circle with a dot inside). Neighboring sites are denoted by $\mathbf{R^{\pm}_{BA}} = \pm\mathbf{a_2}/2$ (solid black vectors), $\mathbf{R'^{\pm}_{BA}} = \pm(\mathbf{a_2}/2 - \mathbf{a_1})$ (green dot-dashed vectors), $\mathbf{R^{\pm}_{BC}} = \pm\mathbf{a_1}/2$ (solid black vectors), $\mathbf{R'^{\pm}_{BC}} = \pm(\mathbf{a_1}/2 - \mathbf{a_2})$ (blue dotted vectors), $\mathbf{R^{\pm}_{AC}} = \pm(\mathbf{a_1} - \mathbf{a_2})/2$ (dashed orange vectors), and $\mathbf{R'^{\pm}_{AC}} = \pm(\mathbf{a_1} + \mathbf{a_2})/2$ (red short dashed vectors). (b-c) The ISO phase is positive ($+i\lambda_{\langle ij\rangle}$) for spin-up electrons moving counterclockwise along the blue solid ($+i\lambda_{\langle ij\rangle}$), red dashed ($+i\lambda_{\langle\langle ij\rangle\rangle}$), or green dot-dashed ($+i\lambda_{\langle\langle\langle ij\rangle\rangle\rangle}$) lines, where $|\mathbf{e_{ij}}| = +1$. Conversely, the ISO coupling phase is negative ($-i\lambda_{ij}$) where $|\mathbf{e_{ij}}| = -1$. In Lieb and transition lattices, the term ($+i\lambda_{\langle ij\rangle}$) remains in the Lieb-Kagome lattice Hamiltonian as complex hoppings connecting NN sites for completeness, aimed at observing their effects on the energy evolution when transitioning from Kagome to Lieb, through stages of evolution. The terms ($+i\lambda_{\langle\langle\langle ij\rangle\rangle\rangle}$) are effectively null in Lieb lattice, due to Eq. (3.6), but are retained in the Lieb-Kagome model as they become ($+i\lambda_{\langle\langle ij\rangle\rangle}$) in Kagome lattice. 119

LIST OF TABLES

LIST OF ABBREVIATIONS AND ACRONYMS

2D	two-dimensional
AHC	anomalous Hall conductivity
BI	biaxial
BI_h	hypothetical biaxial
BP	Black Phosphorus
BZ	first Brillouin zone
CLS	compact localized state
COF	covalent-organic framework
DOS	density of states
hBN	hexagonal boron nitride
ISO	intrinsic spin-orbit
MOF	metal-organic framework
MoS_2	Molybdenum Disulfide
NN	nearest-neighbor
NNN	next-nearest-neighbor
PS	pure shear
PS_h	hypothetical pure shear
QAH	anomalous quantum Hall
QH	quantum Hall
QSH	quantum spin Hall
QSHI	quantum spin Hall insulator
QVH	quantum valley Hall
RSO	Rashba spin-orbit
SR	symmetry representation
SX	simple shear along the x direction
SX_h	hypothetical simple shear along the x direction
SY	simple shear along the y direction
SY_h	hypothetical simple shear along the y direction
TB	tight-binding
TI	topological insulator

TKNN	Thouless–Kohmoto–Nightingale–Nijs
TMDC	Transition Metal Dichalcogenide
TPT	topological phase transition
TR	time-reversal
TRIM	time-reversal invariant momenta
UX	uniaxial along the x direction
UX_h	hypothetical uniaxial along the x direction
UY	uniaxial along the y direction
UY_h	hypothetical uniaxial along the y direction

CONTENTS

1 INTRODUCTION

1.1 Lieb-Kagome lattices

In this section, we present the motivation for studying Lieb-Kagome lattices, highlighting that they are two-dimensional (2D) structures that exhibit flat bands in their energy spectrum, are interconvertible by applying strain along the diagonal direction, and exhibit robust edge states against backscattering.

1.1.1 From graphene to Lieb and Kagome lattices

Electronic devices from the industry have become increasingly prevalent in people's lives, generating a need and expectation for more sophisticated and modern equipment. However, it is believed that the semiconductor industry is reaching the limit of performance improvements for current technologies dominated by silicon. Thus, there is a continuous search for new non-traditional materials whose properties can be controlled by an electric field (NOVOSELOV *et al.*, 2004). This has driven research in the area of Condensed Matter Physics, which constitutes the basis for the advancement of modern electronics (SIMON, 2013).

In this context, in 2004, a research group led by physicists Andre Geim and Konstantin Novoselov managed to isolate a single layer of graphite, called graphene (NOVOSELOV *et al.*, 2004), 2D crystal composed of carbon atoms arranged in a flat hexagonal lattice only one atom thick (Fig. 1). Since its synthesis, this material has attracted the attention of the scientific community. Firstly, because it was believed to be experimentally unfeasible to obtain 2D crystals (MERMIN, 1968). Secondly, because graphene has exhibited many unusual, peculiar, and interesting properties that could potentially generate new electronic devices (CASTRO NETO *et al.*, 2009). For example, it exhibits semiconductor behavior with a zero bandgap, with valence and conduction bands meeting at the vertices of the first Brillouin zone (BZ), the so-called K and K' points (Fig. 1), resulting in a null density of states (CASTRO NETO *et al.*, 2009). Its dispersion relation at low energies is a linear function of momentum. Therefore, in this region, electrons behave like massless fermionic particles, obeying the Dirac equation (CASTRO NETO *et al.*, 2009; KIM *et al.*, 2012).

The synthesis of graphene sparked interest in the search for other 2D crystals, leading to the synthesis of materials such as hexagonal boron nitride (hBN) (ALEM *et al.*, 2009; DEAN *et al.*, 2010; XUE *et al.*, 2011), Transition Metal Dichalcogenides (TMDC) (MAK *et al.*, 2010;

Figure 1 – (a) Representation of the crystal structure of graphene. (b) Representation of graphene's π bands, obtained by the tight-binding (TB) method.

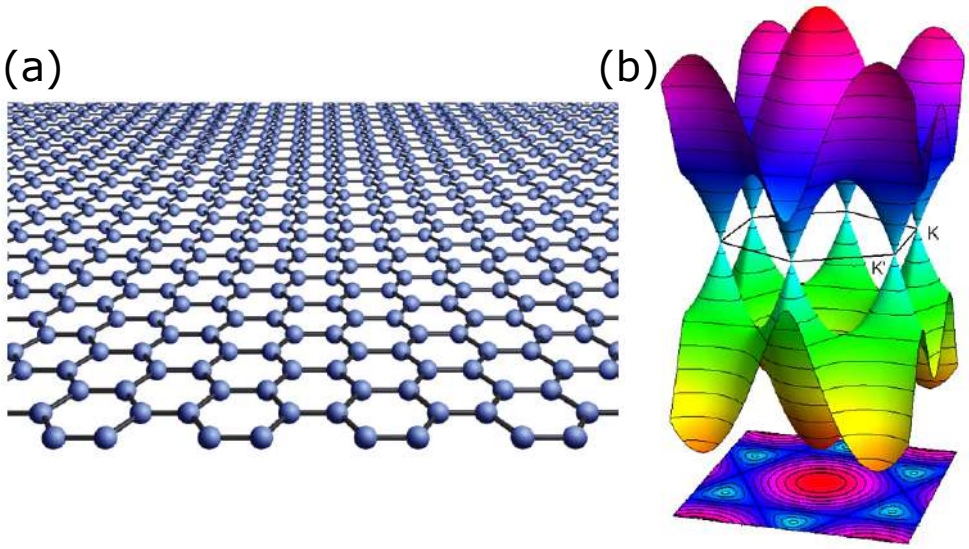

Source: Adapted from Novoselov (2011, p. 837) and Pereira *et al.* (2010, p. 2).

Figure 2 – From left to right: crystal structure (upper panel) and energy bands (lower panel) of monolayers of hBN, TMDC MoS_2, BP, and graphene.

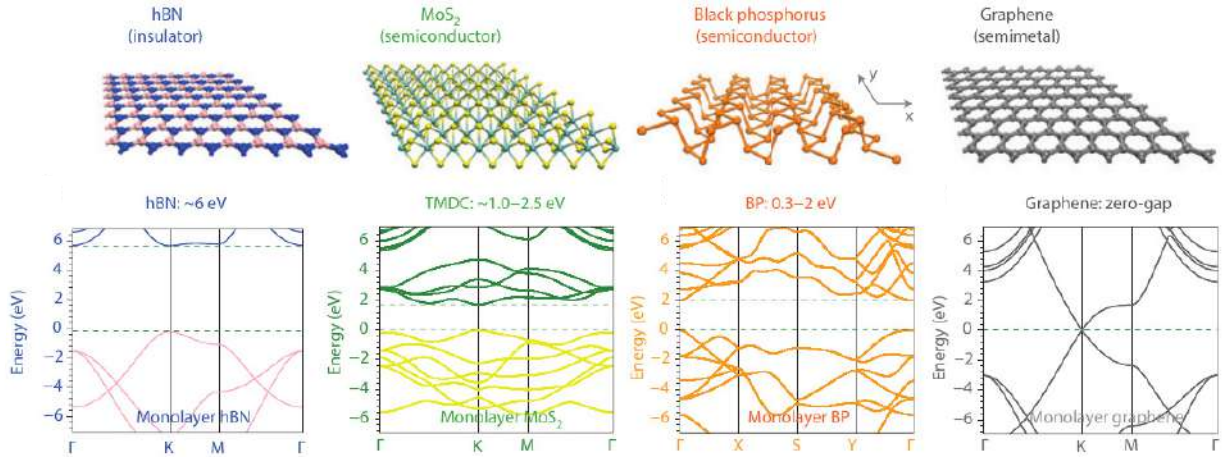

Source: Adapted from Xia *et al.* (2014, p. 900).

RADISAVLJEVIC *et al.*, 2011; WANG *et al.*, 2012), silicene (LALMI *et al.*, 2010; TAO *et al.*, 2015), germanene (DÁVILA *et al.*, 2014), and Black Phosphorus (BP) (LI *et al.*, 2014a; LIU *et al.*, 2014). Some of these are depicted in Fig. 2, through which we see that 2D materials exhibit a variety of energy gap values. Thus, we can classify them as: (i) insulators, like hBN, (ii) semiconductors, such as MoS_2 and BP, and (iii) semimetals, which is the case with graphene. In general, the expectations placed on 2D materials stem from their electronic properties, which essentially depend on the characteristic geometry they exhibit.

Geometry is the fundamental factor for the shape of the electronic band structure, such that specific geometries give rise to energy spectra that can lead to potentially useful electronic properties (SLOT *et al.*, 2017). Hence, in addition to 2D materials obtained by

Figure 3 – Representation of the (a) crystal structure and (b) electronic spectrum of the Lieb lattice, obtained by the TB method for nearest-neighbor (NN) sites.

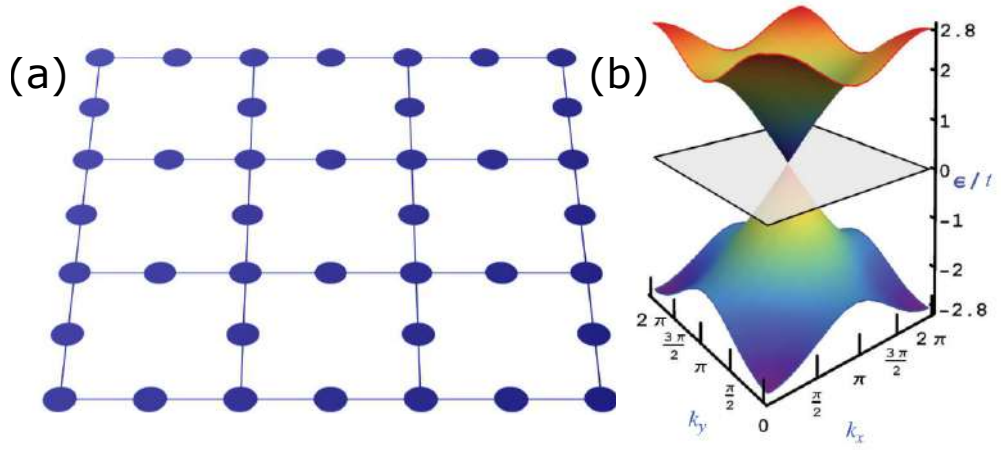

Source: Adapted from Bercioux (2017, p. 628) and Nita *et al.* (2013, p. 2).

micromechanical exfoliation of three-dimensional crystals, theoretical predictions have triggered the exploration of alternative 2D geometries that, when theoretically exhibiting peculiar electronic properties, promptly motivate the experimental scientific community to their fabrication. These structures can be photonic lattices (BANDRES *et al.*, 2014; GUZMÁN-SILVA *et al.*, 2014; MUKHERJEE *et al.*, 2015a; MUKHERJEE *et al.*, 2015b; DIEBEL *et al.*, 2016; XIA *et al.*, 2016; ZONG *et al.*, 2016; SCHULZ *et al.*, 2017; ZHONG *et al.*, 2018; LANG *et al.*, 2023),[1] artificial electronic lattices,[2] formed by covalent-organic framework (COF) (JIANG *et al.*, 2019d; LIMA *et al.*, 2019b; JIANG *et al.*, 2019a; JIN *et al.*, 2017), metal-organic framework (MOF) (LIMA *et al.*, 2019b), or metal-inorganic framework (WU *et al.*, 2024).

This is the case for the Lieb lattice, *i.e.*, a 2D edge-centered square lattice [Fig. 3 (a)] (LIEB, 1989), and the Kagome lattice [Fig. 4 (a)] (KANÔ; NAYA, 1953; MIELKE, 1992; MEKATA, 2003), formed by equilateral triangles sharing vertices, creating a structure of intercalated hexagons and triangles.

Though quite rare, by Figs. 3 (b) and 4 (b-c), we observe that the energy bands displayed by Lieb and Kagome lattices are exotic, as they do not obey the common dispersion relation $E(\vec{k}) \propto |\vec{k}|^2$. We observe the rare coexistence of two types of unconventional energy bands: linear bands ($E(\vec{k}) \propto |\vec{k}|^1$) and flat bands ($E(\vec{k}) \propto |\vec{k}|^0$) (JIANG *et al.*, 2019c), *i.e.*, in these 2D systems where both Dirac and flat bands coexist. However, the arrangement of the Dirac

[1] The periodic waveguides play the role of states with different potentials, where photons in a photonic lattice behave similar to electrons in a crystal (THOULESS *et al.*, 1982).

[2] Electronic lattices are constituted by atoms or molecules organized into a periodic arrangement, thereby establishing a periodic potential landscape for electrons (SLOT *et al.*, 2019; SLOT *et al.*, 2017; LI *et al.*, 2018; GARDENIER *et al.*, 2020).

Figure 4 – (a) Representation of the real Kagome lattice and the structure of the energy bands calculated by the TB model with one orbital per site in the approximation of NN considering (b) positive and (c) negative hopping parameters. It is noticeable that the choice of the sign of the hopping parameter determines the position of the flat band, which is located at the lower or upper region of the electronic spectrum for positive or negative hopping parameters, respectively.

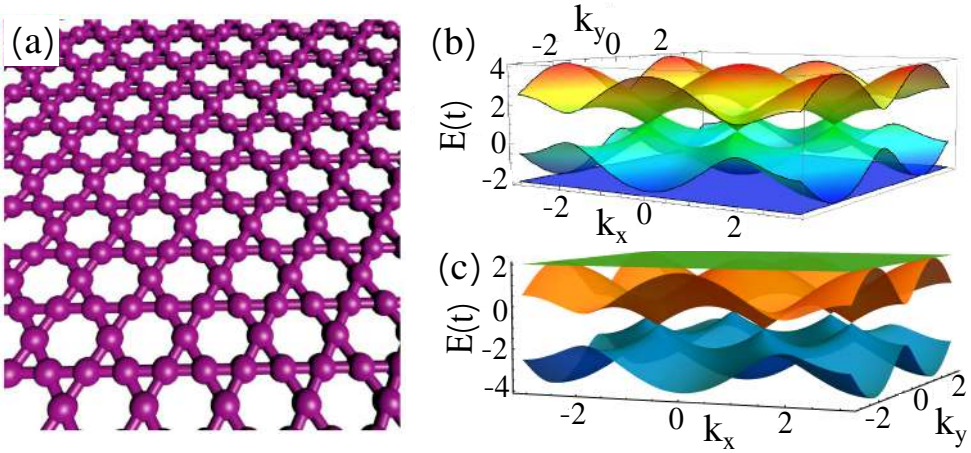

Source: Adapted from Ramires e Lado (2018, p. 84), Jiang *et al.* (2019b, p. 215), and Jiang *et al.* (2019c, p. 399).

bands and the flat band are quite different. In the Lieb lattice, the flat band is located in the middle of the Dirac bands, while in the Kagome lattice, the flat band is located either at the top or the bottom of the Dirac bands (JIANG *et al.*, 2019c).

Flat bands are notable for their completely null kinetic energy, high density of states, and impeded transport due to zero group velocity (GUO; FRANZ, 2009; TANG *et al.*, 2011; DEPENBROCK *et al.*, 2012; LI *et al.*, 2016; LU *et al.*, 2017). In the Kagome lattice, the flat band arises from the destructive interference of the phases of the Bloch functions from the face sites, which cancel out at the vertex sites (KIMURA *et al.*, 2002; PETRESCU *et al.*, 2012; LI *et al.*, 2018; YAZYEV, 2019)[3]. Similarly, in the Lieb lattice, it is found that its flat band is linked to the lattice topology that allows bound states with finite wave function amplitudes at the face sites, and null amplitudes at the vertex sites (GOLDMAN *et al.*, 2011b).

The Lieb lattice is found in nature in the Cu-O_2 planes of cuprate superconductors[4] (LIEB, 1989; NITA *et al.*, 2013), but it has not yet been isolated in a 2D structure. On the other hand, it is possible to synthesize photonic Lieb lattices using waveguides and to create Lieb lattices of cold atoms (SHEN *et al.*, 2010; GOLDMAN *et al.*, 2011b; GUZMÁN-SILVA *et al.*, 2014; MUKHERJEE *et al.*, 2015a; MUKHERJEE *et al.*, 2015b; TAIE *et al.*, 2015; XIA *et al.*, 2016; DIEBEL *et al.*, 2016). In 2017, Slot *et al.* (2017) synthesized the electronic Lieb lattice by assembling a molecular lattice on a substrate with surface states, thereby forcing the electrons to

[3] For a dynamic representation of electron behavior in the Kagome lattice, see the video of the UOWNOW (2019).

[4] The term cuprates derives from the Latin word for copper, *cuprum*. The word is commonly used to refer to oxide materials.

Figure 5 – Lieb lattice by (a) Femtosecond laser-writing technique. (b) Microscope image at the output facet of a Lieb lattice for white-light propagation. (c) Electronic Lieb lattice with CO molecules in Cu(111). Organic Lieb lattice (d) sp^2C-COF, (e) CuO_2 planar, (f) CuO_2 separated by Ba/Ca insulating sheets, (g) sp^2N-COF.

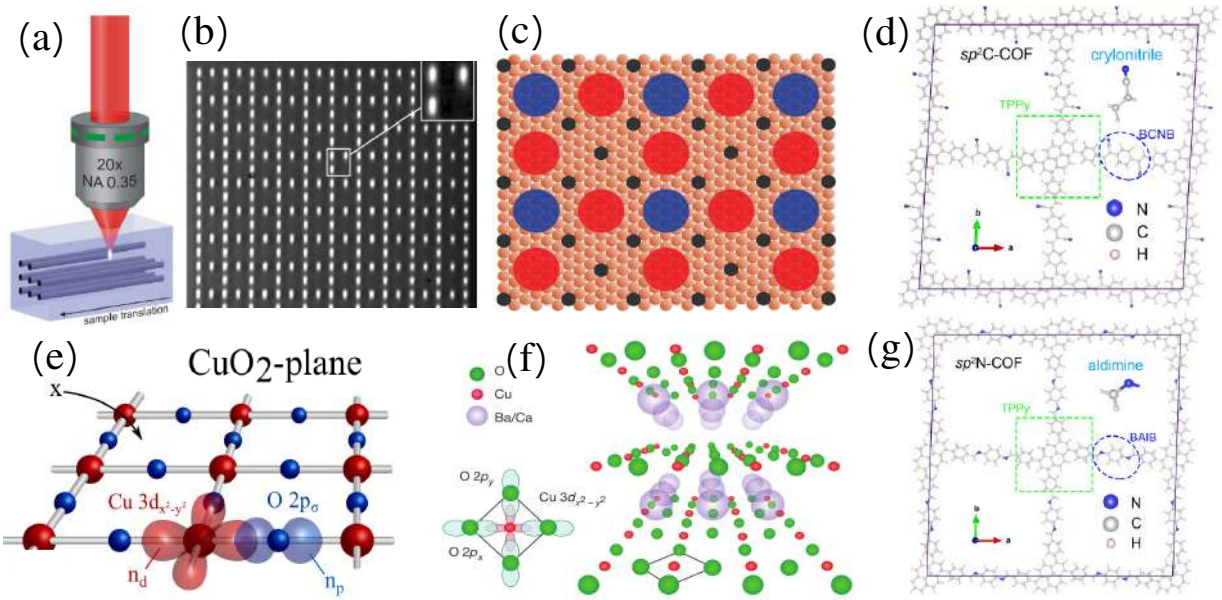

Source: Adapted from (a,b) Vicencio *et al.* (2015, p. 3), (c) Slot *et al.* (2017, p. 2), (d) Cui *et al.* (2020, p. 5), (e) Reichardt *et al.* (2018, p. 2), (f) Keimer *et al.* (2015, p. 180) and (g) Cui *et al.* (2020, p. 5).

remain in the desired geometry (SLOT *et al.*, 2017). They utilized electrons from the surface state of Cu(111), confined by an array of carbon monoxide molecules, with a scanning tunneling microscope (SLOT *et al.*, 2017). Therefore, the absence of 2D Lieb structures isolated in organic materials would not hinder experimental exploration of this lattice (SLOT *et al.*, 2017). However, the scarcity of organic Lieb lattices has been resolved. According to Jiang *et al.* (2019a), COF, specifically sp_2C-COF and sp_2N-COF, synthesized in recent experiments (JIN *et al.*, 2017), are the first two material realizations of organic-ligand-based Lieb lattices (see Fig. 5).[5]

The Kagome lattice, in turn, can also be realized photonically (SCHULZ *et al.*, 2017) or electronically (LI *et al.*, 2018). For example, Li *et al.* (2018) synthesized a Kagome structure in twisted silicene multilaminae, such that the electrons remain localized in the Kagome lattice by destructive quantum interference of the phases of the Bloch functions, guaranteeing zero kinetic energy that gives rise to a peak in density of states corresponding to the flat band (LI *et al.*, 2018). Furthermore, the Kagome lattice can be synthesized with organic bonds with different atoms and molecules, such as: $Cs_2TiCu_3F_{12}$ and $Rb_2TiCu_{\ 3}F_{12}$ (DOWNIE *et al.*, 2015), the ferromagnetic

[5] Crystal lattices are arrays of mathematical points, where each site in the lattice can represent an atom, ion, or molecule (ASCROFT; MERMIM, 1976; SAITO *et al.*, 1998; KITTEL, 2005). To classify a structure as a crystal lattice, it is sometimes necessary to identify arrangements of atoms periodically distributed in space that can be represented by points in the real lattice. This is the case with the experimentally fabricated arrays of the Lieb and Kagome lattices.

Figure 6 – Kagome lattice (a) geometric, (b,c) electronics with silicene blades in Ag(111), (d) photonics, (e) $Cs_2TiCu_3F_{12}$, (f) $BaCu_3V_2O_8(OH)_2$, (g) Co_3 Sn_2S_2, (h) $Rb_2SnCu_3F_{12}$ and $Cs_2ZrCu_3F_{12}$, (i) $Cs_2NaMn_3F_{12}$, (j) $Cs_2Cu_3SnF_{12}$, (k) $Rb_2Cu_3SnF_{12}$.

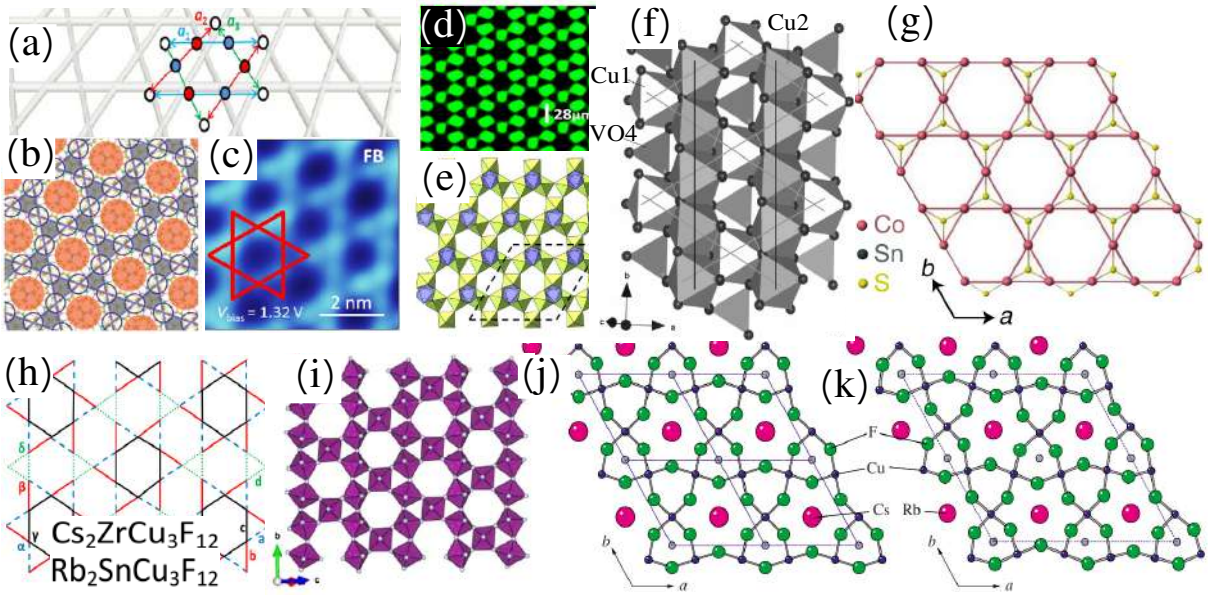

Source: Adapted from (a) Li *et al.* (2018, p. 2), (b,c) Li *et al.* (2018, p. 3), (d) Zong *et al.* (2016, p. 5), (e) Downie *et al.* (2015, p. 231), (f) Zhang *et al.* (2010, p. 2), (g) Yazyev (2019, p. 1), (h) [p. 2]Downie2014, (i) Cui *et al.* (2017, p. 2), (j,k) Ono *et al.* (2009, p. 3).

materials Fe_3Sn_2 (YE *et al.*, 2018) and $Co_3Sn_2S_2$ (LIU *et al.*, 2018), antiferromagnetic Mn_3Sn and Mn_3Ge (NAKATSUJI *et al.*, 2015), among others shown in Fig. 6.

1.1.2 The interconvertibility: Lieb-Kagome lattices

As shown in Fig. 7 (a), the Lieb (LIEB, 1989) and Kagome (MIELKE, 1992) lattices have in common the fact that they both have three non-equivalent sites (GUO; FRANZ, 2009; DEPENBROCK *et al.*, 2012; LI *et al.*, 2016; LU *et al.*, 2017; YIN *et al.*, 2019). Curiously, Jiang *et al.* (2019c) noted that these lattices are interconvertible by diagonal strain, which allows them to be described by a generic tight-binding (TB) Hamiltonian constructed for a Lieb-Kagome lattice defined by a morphological parameter $90° \leq \theta \leq 120°$, setting the Hamiltonian to Lieb and Kagome configurations for $\theta = 90°$ and $\theta = 120°$, respectively, as well as transition lattices defined by $90° < \theta < 120°$.[6]

Notably, when θ changes from $\pi/2$ to $2\pi/3$, the BZ gradually changes from a square to a hexagonal parallelogram to a regular hexagon, as shown in Fig. 7 (b). The plotted band structures for the three lattices along the high-symmetry k paths in Fig. 7 (c) show the well-known

[6] Alternatively, Lang *et al.* (2023) used the interconvertibility between the Lieb and Kagome lattices to study transition lattices, defining an angle $\theta' = \theta - 90°$. However, in this thesis, we will use θ defined by Jiang *et al.* (2019c).

Figure 7 – The Lieb-Kagome lattice: (a) Structures of the Lieb lattice, transition lattice with $\theta = 105°$, and Kagome lattice. (b) The corresponding BZ for the three lattices with high-symmetry K paths are highlighted by red dashed lines. (c) The band structure along high-symmetry paths for the three lattices with (blue dashed lines) and without intrinsic spin-orbit (ISO) coupling (red solid lines). Blue (red) arrows indicate compressive (tensile) strain along the diagonal direction.

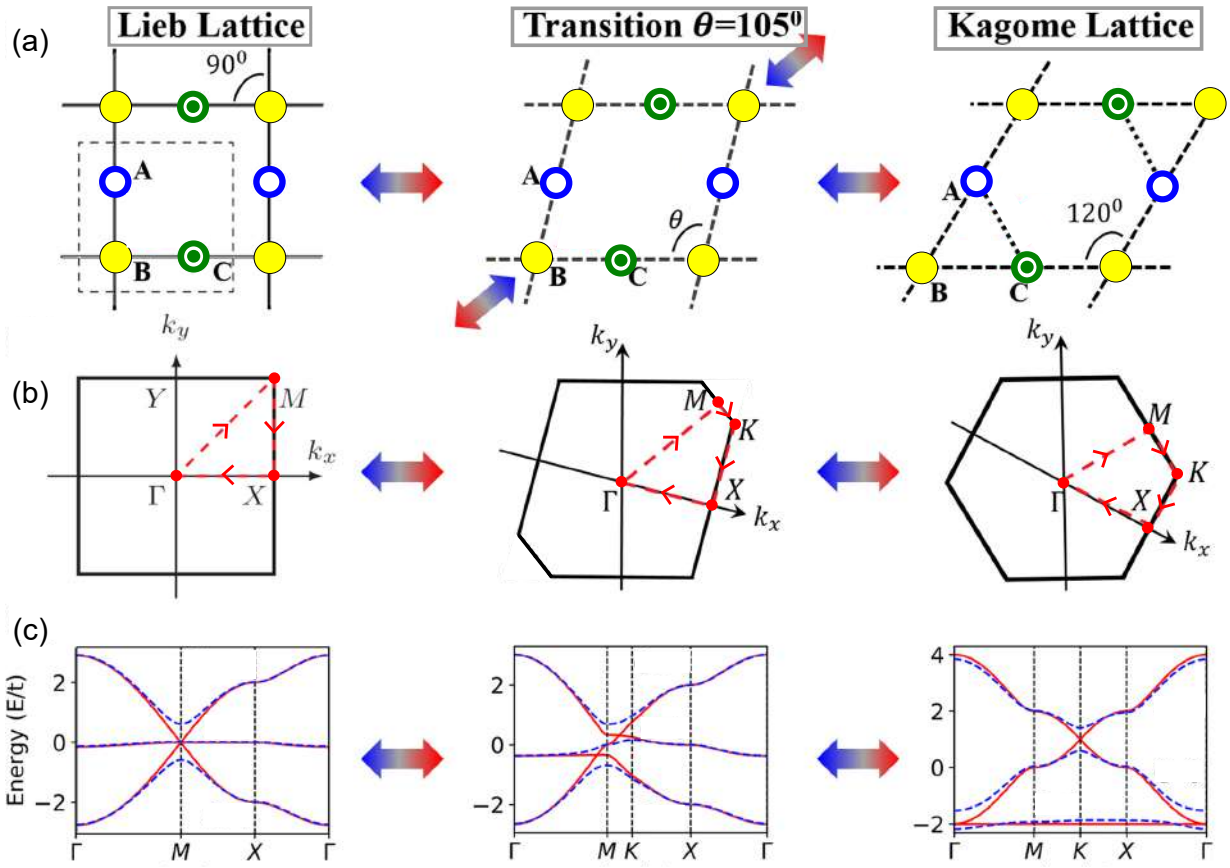

Source: Adapted from Jiang *et al.* (2019c, p. 2).

features of Lieb and Kagome bands, characterized by the coexistence of Dirac bands and a flat band.[7] The flat band is located in the middle of the Dirac bands in the Lieb lattice, while it is at the bottom in the Kagome lattice. Observing the band structure of the transition state [middle panel of Fig. 7(c)], one sees that the flat band has disappeared because the distortion has broken the required symmetry for the flat band (JIANG *et al.*, 2019c).

The interconvertibility between the Lieb and Kagome lattices has been used as an important theoretical resource in some recent works, allowing for both the systematic study of Lieb and Kagome lattices individually, as well as the evolution stages via transition lattices (JIANG *et al.*, 2019c; JIANG *et al.*, 2019a; LIM *et al.*, 2020; CUI *et al.*, 2020; LIMA *et al.*, 2023; LANG *et al.*, 2023). [8]

[7] In fact, the Dirac cone only exists in the absence of ISO coupling. The gap opens due to the ISO coupling, which will be explained in more detail in Ch. 3.

[8] The interconvertibility will be described in detail in Ch. 2.

Figure 8 – Transition lattice (a) Schematic diagram of waveguide systems of the Lieb lattice, transition lattice with $\theta = 105°$, and Kagome lattice. (b) On the left, diffraction patterns after propagating 40 mm through the transition lattices with $\theta = 115°$ shown on the right, which consist of the back facet of a SiO_2 sample with laser-written waveguides, forming two photonic lattices. The inset is a close-up of some waveguides, showing their elliptical cross sections.

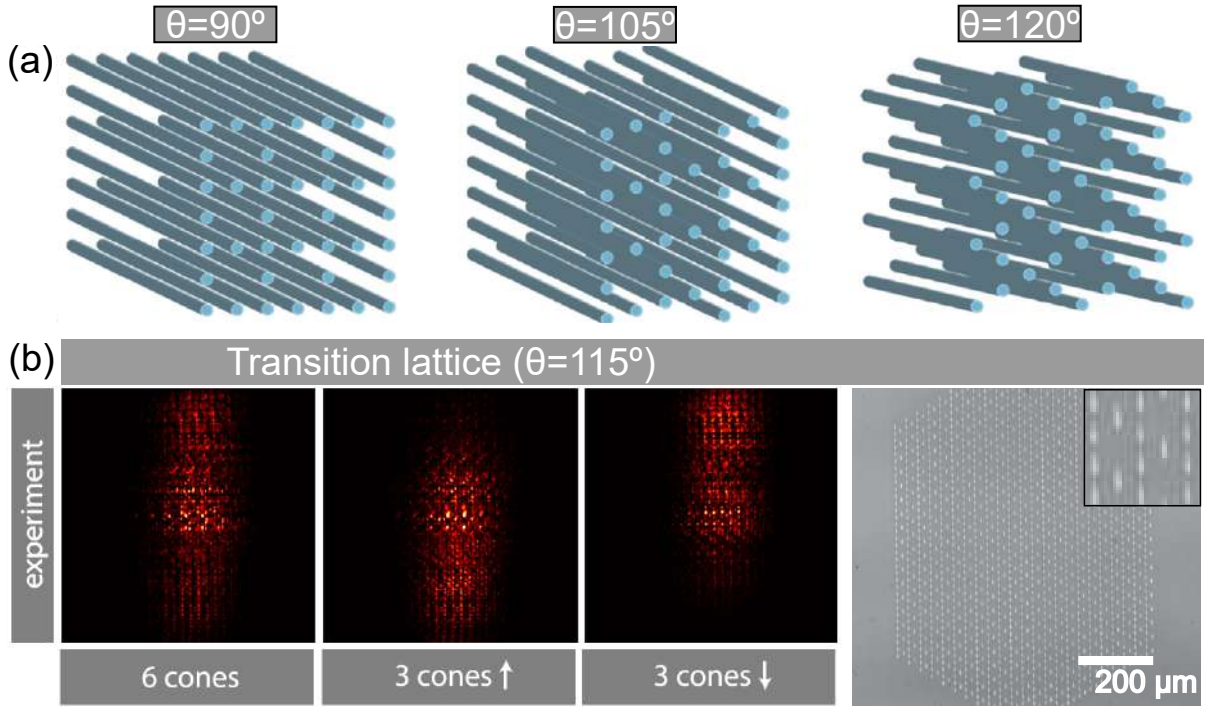

Source: Adapted from (a) Jiang *et al.* (2019c, p. 7), (b) Lang *et al.* (2023, p. 7).

Aiming to experimentally investigate the topological band evolution between the Lieb and Kagome lattices, including the transition lattices, Jiang *et al.* (2019c) proposed the construction of Lieb-Kagome photonic lattices [Fig. 8 (a)], which encompass the transition stages during the interconvertibility process. In these lattices, the periodic waveguides act as states with different potentials, and photons behave similarly to electrons in a crystal. Subsequently, Lang *et al.* (2023) successfully performed experiments with photonic lattices laser-written in fused silica (SiO_2) [Fig. 8 (b)], observing diffraction patterns characteristic of tilting Dirac cones in the transition lattice ($\theta = 115°$). These studies advance the experimental proposal of Lieb-Kagome lattices and provide a basis for further research into these interesting systems.

1.1.3 Robust edge states versus backscattering

The inclusion of ISO coupling[9] in Lieb, Kagome, and transition lattices opens two gaps in the energy spectrum, separating the three energy bands, as depicted in Fig. 7 (c). Upon calculating the energy spectrum corresponding to nanoribbons of these three lattices, the presence of edge states that link the bulk bands in the region of the gap opened by ISO coupling is observed [see Fig. 9 (a)] (JIANG *et al.*, 2019c). The red and blue colors of the edge states in Fig. 9 (a) represent the contributions from two sides of the ribbon, respectively, as confirmed by the edge state eigenfunction plot shown in Fig. 9 (b).[10]

In general, the energy gap opening driven by ISO coupling with edge states crossing the gap configures the Lieb, transition, and Kagome lattices as topological insulators (TI), as explained in the next section. Edge states arising from the application of an external magnetic field are linked to trivial topology, due to the breaking of time-reversal (TR) symmetry in this case. On the other hand, edge states caused solely by the inclusion of ISO coupling indicate non-trivial topology, as they preserve TR symmetry.[11]

Bandres *et al.* (2014) presented TB calculations of the Lieb photonic TI, highlighting the topological protection of its edge states. They assumed typical experimental parameters of the waveguides made in fused silica by femtosecond-direct-laser writing (RECHTSMAN *et al.*, 2013). They launched an edge state in a face of a square Lieb helical lattice with two types of terminations and two defects at the edges. The propagation of the edge state is shown in Fig. 9 (c). From it, they observed all the topological properties of the edge states: one-way propagation, no backscattering at corners, propagation around edge defects, different group velocities for different types of terminations, and coupling to the flat band.

Figure 9 (d) shows the topography of the Kagome lattice on a silicene surface Li *et al.* (2018). The edge state appears along all island edges with a regular shape in the Kagome lattice region [Fig. 9 (e)].

---

[9] Euristically, the ISO coupling has a relativistic origin and is associated with the interaction between the magnetic dipole moment of the electron's spin and the internal magnetic field of the atom itself (a consequence of the electron's orbital angular momentum). In the phenomenological description of graphene, ISO coupling originates from the spin-dependent NNN hopping, as proposed by Kane e Mele (2005b), who, following Haldane (HALDANE, 1988), introduced a term in the TB model that connects second neighbors with a spin-dependent amplitude, as we will discuss in detail in Ch. 3 (KONSCHUH *et al.*, 2010; ARAÚJO, 2018; VANDERBILT, 2018).

[10] Only spin-up states crossing the gap are presented in Fig. 9. When considering both the spin-up and spin-down components, these topological edge states will form a 1D Dirac cone within the gap. Edge states with opposite spin channels are observed crossing the two energy gaps, as shown in Ch. 4.

[11] The term TR symmetry is associated with the reversal of momentum (SAKURAI, 1994).

Figure 9 – Edge states. (a-b) Band structures of 15-unit nanoribbons (lines) for Lieb ($\theta = 90°$), transition ($\theta = 105°$), and Kagome ($\theta = 120°$) lattices. The upper and lower panels located below each energy spectrum show the wave function of the two edge states identified by the red and blue stars, respectively. Only spin-up states crossing the gap are presented. The red and blue colors of the edge states represent the contributions from the two sides of the ribbon, respectively. (c) TB calculation of the propagation of an edge state amplitude in a Lieb photonic . All lattice planes are in the rotating helical reference frame. (d) Large-area image of the Kagome lattice surrounded by silicene (R3 area) (50 nm $\times$ 50 nm). The boundary between them is marked by the black solid line. The red solid line shows the height profile along the white dashed line. The step height is the thickness of one layer of silicene. (e) DOS mapping simultaneously obtained at 1.45 V, which is the corresponding edge state energy. The position of the edge state is highlighted by the white arrow.

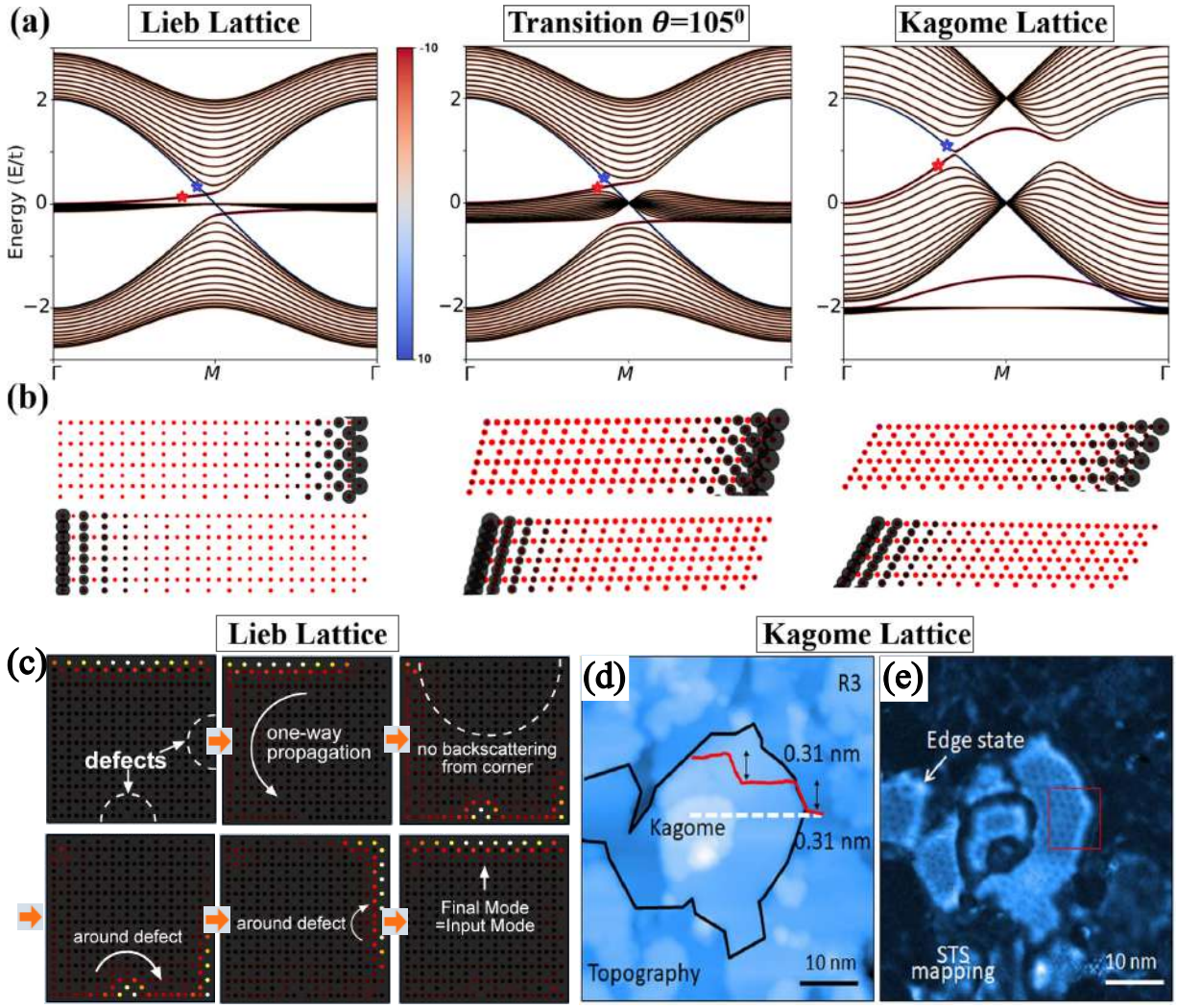

Source: (a,b) Jiang *et al.* (2019c, p. 4), (c) Bandres *et al.* (2014, p. 2), (d,e) Li *et al.* (2018, p. 5).

1.2 Topological insulators

In this section, we conceptualize TI, topological phase transition (TPT), and topological invariants in the context of the Haldane and Kane-Mele models with $\mathbb{Z}$ and $\mathbb{Z}_2$ classifications. We discuss the connection of these models with quantum anomalous Hall (QAH) and quantum spin Hall (QSH) physics in terms of the emergence of chiral and helical edge states, respectively. This is significant because the Lieb-Kagome lattices behave as 2D TI with a $\mathbb{Z}_2$ classification when ISO coupling is included in the TB model, which results in helical edge states.

1.2.1 Topological Insulators versus Ordinary Insulators

TI are materials that behave as ordinary insulators in the bulk, in that they exhibit an excitation gap, whereas the edge has robust conducting states, according to the bulk-boundary correspondence, which links the topological structure of the bulk crystal to the presence of gapless boundary modes (KANE, 2008; HASAN; KANE, 2010; MOORE, 2010; DROST *et al.*, 2017; WANG *et al.*, 2024). The topological properties of the bulk (the interior) of a material dictate the existence and characteristics of states on its boundaries (edges or surfaces) (GRAF; PORTA, 2013). In 2D TI, these boundaries are edges, and the topological phases are characterized by the presence of gapless edge states, protected against backscattering (WEEKS; FRANZ, 2010; BANDRES *et al.*, 2014).

TI are distinct from ordinary insulators due to their unique electronic properties. In a common insulator, electrons are bound to atoms in closed shells [Fig. 10 (a)], making the material electrically inert as it requires finite energy to dislodge an electron. This behavior is described by the band theory of solids, which uses the translational symmetry of the crystal to classify electronic states in terms of their crystal momentum k within a periodic BZ. The energy bands formed by the eigenvalues $E_m(k)$ of the Bloch Hamiltonian $H(k)$ create an energy gap that separates the occupied valence band states from the empty conduction band states [Fig. 10 (b)]. In contrast, the quantum Hall (QH) state provides a fascinating counterexample. When electrons confined to two dimensions are placed in a strong magnetic field, their circular orbits [Fig. 10 (d)] quantize into Landau levels with energy $\varepsilon_m = \hbar\omega_c(m+1/2)$ [Fig. 10 (e)]. If N Landau levels are filled, an energy gap similar to that of an insulator separates the occupied and empty states. However, unlike a conventional insulator, an electric field causes the cyclotron orbits to drift, resulting in a Hall current characterized by the quantized Hall conductivity $\sigma_{xy} = Ne^2/h$.

Figure 10 – States of matter. (a)–(c) The insulating state. (a) An atomic insulator. (b) A simple model insulating band structure. (d)–(f) The QH state. (d) The cyclotron motion of electrons. (e) The Landau levels, which may be viewed as a band structure. (c) and (f) Two surfaces which differ in their genus, g. (c) $g = 0$ for the sphere and (f) $g = 1$ for the donut. The Chern number that distinguishes the two states is a topological invariant similar to the genus.

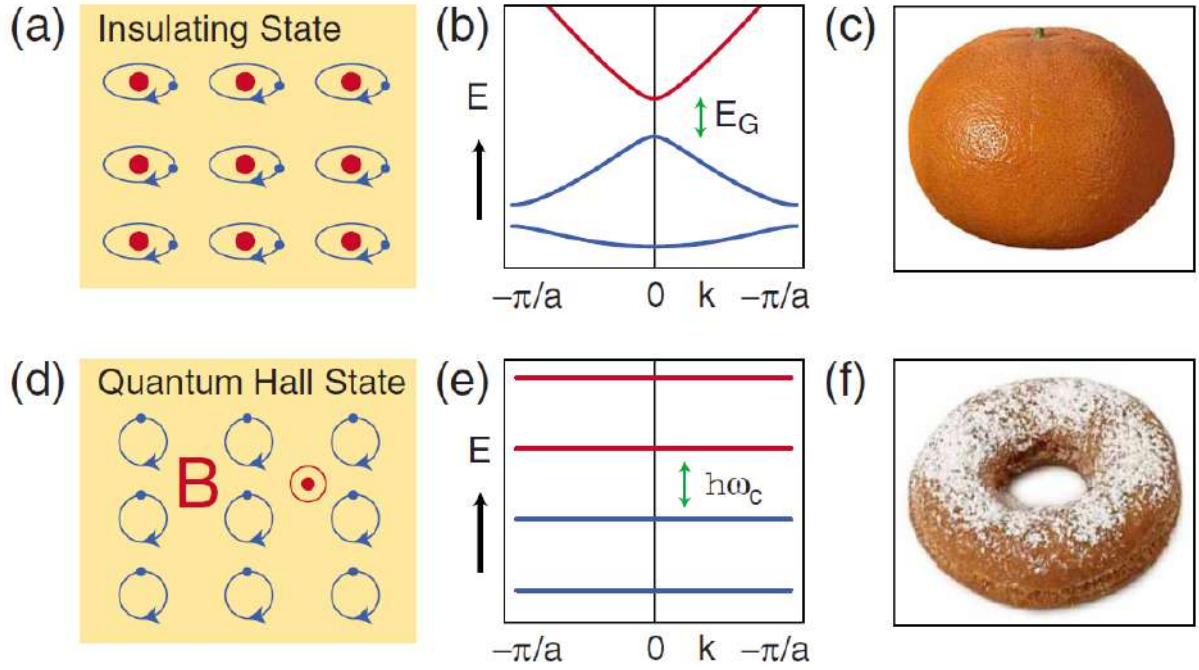

Source: Hasan e Kane (2010, p. 4)

This quantization is a manifestation of the topological nature of σ_{xy}, making the QH state a topologically distinct phase of matter. Landau levels, viewed as a band structure, disperse with k in the presence of a periodic potential, leading to a band structure that, while similar in appearance to that of an ordinary insulator, underlies fundamentally different physics due to its topological properties (HASAN; KANE, 2010).

1.2.2 Topological Phases

Topological phases of condensed matter have attracted immense attention since the 1980s when they were proposed to explain the properties of the QH effect in 2D electronic systems under a strong external magnetic field (THOULESS *et al.*, 1982). The state responsible for the QH effect does not break any symmetries, but it defines a topological phase in the sense that certain fundamental properties, such as the quantized value of the Hall conductance and the number of gapless boundary modes, are insensitive to smooth changes in material parameters and cannot change unless the system passes through a quantum phase transition (REN *et al.*, 2016; WEN, 2017).

In recent years, the investigation of topological phases of matter has been established as an important subfield in condensed matter physics (BERNEVIG, 2013; BANSIL *et al.*, 2016). The fundamental impact of this research topic stems from the fact that in TI, there is no symmetry that distinguishes the topological from the trivial state, and no order parameter that becomes nonzero on the topological side, leading to a paradigm shift in the understanding of the classification of phases of matter (VANDERBILT, 2018). Two insulators are said to belong to the same topological class if and only if their Hamiltonians can be continuously connected in such a way that the gap never closes at any point along the connecting path (BERNEVIG, 2013; BANSIL *et al.*, 2016; VANDERBILT, 2018). An insulating crystal is classified as "trivial" if it can be adiabatically connected without gap closure to an atomic limit[12], and is "topological" otherwise (HASAN; KANE, 2010; QI; ZHANG, 2011). In general, the topological phases are classified according to the topological invariants, which are determined based on their bulk properties (BERNEVIG, 2013).

1.2.3 Topological Invariant

The QH effect is characterized by a vanishing longitudinal conductance and a nonzero quantized Hall conductance in a six-terminal Hall-bar measurement (KLITZING *et al.*, 1980). This phenomenon arises from the insulating bulk contributing to zero longitudinal conductance, while the quantized Hall conductance originates from the Berry curvature of filled magnetic Bloch bands, as first reported by Thouless *et al.* (1982). The integration of Berry curvature over the filled bands in the magnetic BZ gives rise to an integer known as the Thouless–Kohmoto–Nightingale–Nijs (TKNN) number, later recognized as the first Chern class of a principal fiber bundle on a torus (NAKAHARA, 2018). This TKNN number, also known as the Chern number, is a topological invariant, meaning it remains unchanged as long as the bulk band gap remains open, indicating the topological nature of the QH effect.

The Chern invariant, while rooted in the mathematical theory of fiber bundles (NAKAHARA, 2018), can be understood physically through the Berry phase associated with the Bloch wave functions.[13] Conceptually, the Berry phase acquired around a closed loop in momentum space leads to the concept of Berry flux, which is integral to defining the Chern number. The Chern number, summed over all occupied bands, remains invariant even if there

[12] Crystal of well-separated atoms with discrete sets of occupied and unoccupied atomic orbitals.

[13] A mathematical synthesis of the definitions of the Berry phase and Chern number can be found in Appendix A. A detailed discussion is given by Bernevig (2013) and Vanderbilt (2018).

are degeneracies between occupied bands, as long as the gap between occupied and empty bands remains finite. This invariance underlies the robust quantization of the Hall conductivity observed in experiments.

A helpful analogy for understanding the Chern number involves classifying two-dimensional surfaces by their genus, which counts the number of holes. For example, a sphere has a genus of zero [Fig. 10 (c)], while a donut has a genus of one [Fig. 10 (f)]. A theorem by Gauss and Bonnet states that the integral of the Gaussian curvature over a closed surface is a quantized topological invariant related to the genus (NAKAHARA, 2018). Similarly, the Chern number is an integral of a related curvature over the BZ.

In general, non-magnetic insulators with broken TR symmetry obey the $\mathbb{Z}$ topological classification, whose invariants are Chern numbers, C (HALDANE, 1988; FRUCHART; CARPENTIER, 2013). In this case, 2D TI exhibit a non-zero net integer number of up-crossings or down-crossings of edge surface states for each side of the ribbon constructed from such TI material, resulting in chiral edge states at the boundary of the sample (HASAN; KANE, 2010; MOORE, 2010). On the other hand, non-magnetic insulators with preserved TR symmetry are characterized by a $\mathbb{Z}_2$ topological invariant, ν, such that (i) a 2D TI is characterized by ν-odd and (ii) a trivial (or ordinary) insulator is identified by ν-even (KANE; MELE, 2005b; KANE; MELE, 2005a; FU; KANE, 2007; QI *et al.*, 2008). This means that along half of the BZ, the 2D TI displays an odd number of edge surface states for each side of the ribbon, whereas trivial insulators display an even number, possibly zero (VANDERBILT, 2018). Therefore, the spin-up and spin-down states move in opposite directions along the edge of the system, generating spin-filtered edge states in the gap region of the bulk energy spectrum.

In the absence of spin-mixing perturbations, ν is related to the spin Chern number C^s by the simple relation $\nu = C^s \mod 2$, where $C^s = (C^{\uparrow} - C^{\downarrow})/2$ and C^{σ}, $\sigma = \{\uparrow, \downarrow\}$, represents the Chern number associated with the individual spins (FUKUI *et al.*, 2005; SHENG *et al.*, 2006; FUKUI; HATSUGAI, 2007).

In n-band insulators, the C determining the count of crossing edge states is just the total Chern number $C = \sum_n^{\text{occ}} C_n$; more generally, it is given in terms of the BZ integral of the band-traced Berry curvature (VANDERBILT, 2018). Analogously, the spin Chern number is $C^s = \sum_n^{\text{occ}} C_n^s$ (BEUGELING *et al.*, 2012).

Figure 11 – (a) Haldane model in real space. Lattice vectors $\mathbf{a}_1$ and $\mathbf{a}_2$ define a shaded parallelogram unit cell encompassing orbitals 1 (represented by filled circles) and 2 (indicated with open circles). Real transitions t_1 occur between NN, while imaginary transitions it_2 link NNN sites as denoted by the arrows (or $-it_2$ in the reverse direction). (b) The parallelogram-shaped BZ, outlined by reciprocal lattice vectors $\mathbf{b}_1$ and $\mathbf{b}_2$, features prominently labeled high-symmetry points.

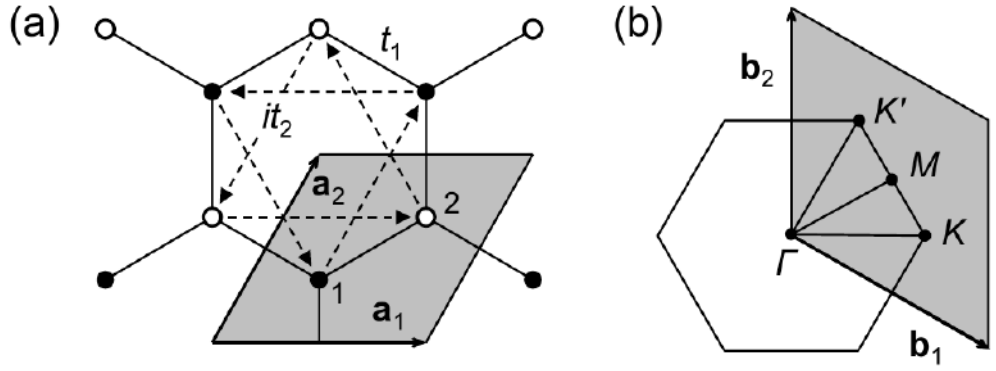

Source: Vanderbilt (2018, p. 215).

1.2.4 Haldane model and Kane-Mele model

Historically, the topological classification $\mathbb{Z}$ comes from the Haldane model (HALDANE, 1988), which in 1988 introduced imaginary hoppings it_2 connecting next-nearest-neighbor (NNN) sites of graphene, as illustrated in Fig. 11 (VANDERBILT, 2018). This term breaks TR symmetry. Significantly, a reversal between the character of the valence-band maximum and the conduction-band minimum is visible at $\boldsymbol{K'}$ [see Fig. 12(a,b)]. It turns out that such a "band inversion" is typical of many kinds of topological transition (VANDERBILT, 2018). The Fig. 12 (c) shows a surface state emerging out of the conduction band on the top edge of the ribbon, and another coming from the valence band on the bottom edge, but neither crosses the gap, manifesting a behavior trivial. On the other hand, we see in Fig. 12 (d) that there is an up-crossing of one surface state on the top edge of the ribbon and a down-crossing one on the bottom edge, signaling a topological behavior. The plot of Fig. 12 (e) shows that there are positive and negative concentrations of Berry curvature near $\boldsymbol{K}$ and $\boldsymbol{K'}$ which will cancel when integrated over the BZ, *i.e.* when we integrate the Berry curvature over the 2D BZ, we obtain the Chern number equals zero, as expected for this case (VANDERBILT, 2018). On the other hand, the Berry curvature becomes entirely positive [Fig. 12(f)] when calculated for the cases after the closing and reopening of the energy gap, *i.e.*, after the TPT.

The $\mathbb{Z}_2$ topological invariant was proposed in 2005 by the Kane-Mele model (KANE; MELE, 2005a; KANE; MELE, 2005b), which constructed a simple model system in which spin-up and spin-down electrons are described by a pair of complex-conjugated Haldane models

Figure 12 – Haldane model in a configuration of (a,c,e) trivial topology before closing the gap at point $\boldsymbol{K'}$, and (b,d,f) after closing and opening the energy gap, now being a TI of $\mathbb{Z}$ classification with Chern number $C = 1$. For these configurations we present the: (a,b) band structures, (c-d) edge states on a ribbon, since that the surface states on the top and bottom edges of the ribbon are indicated by full and reduced intensity respectively, and (e,f) contour plots of Berry curvature, in with the full and dashed lines denote positive and negative contour levels respectively.

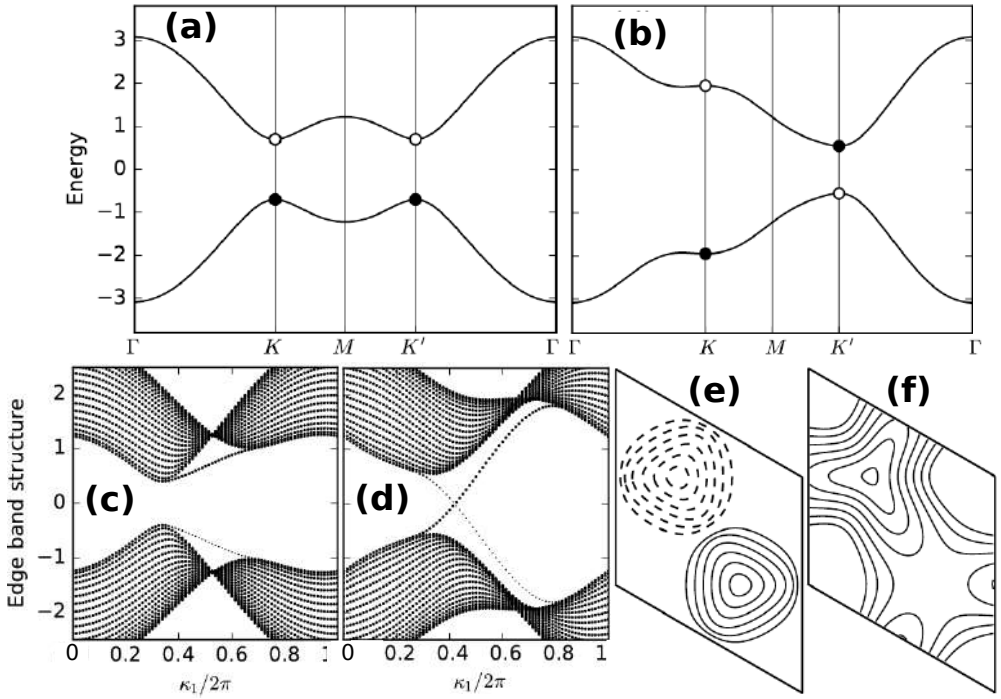

Source: Adapted from Vanderbilt (2018, p. 217, 218 and 220).

with some spin-mixing terms included. This restores the TR symmetry that had been broken in the Haldane model. Fig. 11 still describes the model, but there are now two basis states, spin-up and spin-down, on each site (VANDERBILT, 2018).

The band structure resulting from this model is illustrated in Fig. 13 (a,b). The left-right mirror symmetry and the enforcement of Kramers degeneracies[14] at the time-reversal invariant momenta (TRIM) $\boldsymbol{\Gamma}$ and $\boldsymbol{M}$ are evident in the plots. At a critical configuration of model, there is a simultaneous gap closure both the $\boldsymbol{K}$ and $\boldsymbol{K'}$ points, which we expect is accompanied by a change topology from $\mathbb{Z}_2$-even to $\mathbb{Z}_2$-odd. To confirm that this is the case, the ribbon edge band structure is plotted in Fig. 13 (c,d). A traversal of edge states across the gap in (d) but not (b), confirming the identification of topologically trivial and nontrivial states respectively. Equivalently, the number of crossings in the half BZ with any horizontal line drawn inside the energy gap would be even or odd in Panel (c) or (d) respectively (VANDERBILT, 2018).

[14] This theorem states: Any state of a system whose total angular momentum is half-integer (*i.e.*, a system composed of an odd number of particles with half-integer spin) and that exhibits TR symmetry, must be degenerate (SAKURAI, 1994; BALLENTINE, 2014).

Figure 13 – Kane-Mele model in a configuration of (a,c) trivial topology before closing the gap at points $\boldsymbol{K}$ and $\boldsymbol{K'}$, and (b,d) after closing and opening the energy gap, now being a TI of $\mathbb{Z}_2$ classification with $C^s = 1$. For these configurations we present the: (a,b) band structures, and (c,d) edge states on a ribbon, since that the surface states on the top and bottom edges of the ribbon are indicated by full and reduced intensity respectively.

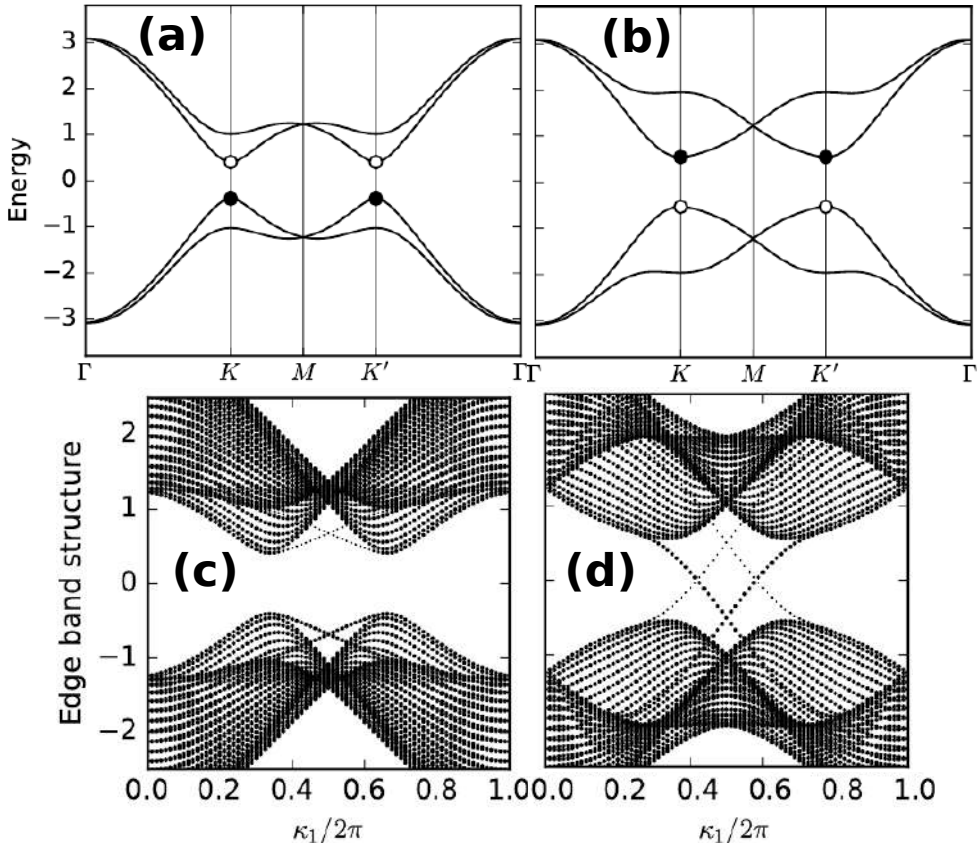

Source: Adapted from Vanderbilt (2018, p. 247 and 248).

1.2.5 Chiral and helical edge states

Edge states of a TI can be used to explore fundamental science emerging at the interface of low dimensionality and topology (HUANG *et al.*, 2024). Chiral and helical edge states arising from a non-trivial bulk topology are expected to be protected against backscattering and support a wealth of interesting topological, mesoscopic and interacting phenomena in low dimensions (SARMA; PINCZUK, 2008; QI; ZHANG, 2011). Chiral edge states of the QH and QAH effects are robust over long distances (CHANG *et al.*, 2013; DENG *et al.*, 2020; SERLIN *et al.*, 2020; LI *et al.*, 2021), harbor the physics of a chiral Luttinger liquid (CHANG, 2003), and are instrumental to the understanding of fractional and non-Abelian braiding statistics (NAYAK *et al.*, 2008; NAKAMURA *et al.*, 2020). Helical edge states of the QSH and quantum valley Hall (QVH) effects occur at zero external and internal magnetic field, which is generally more compatible with device applications (KÖNIG *et al.*, 2007; MARTIN *et al.*, 2008; LI *et al.*, 2010;

QIAO *et al.*, 2011; ZARENIA *et al.*, 2011; ZHANG *et al.*, 2013; QIAN *et al.*, 2014; DU *et al.*, 2015; JU *et al.*, 2015; LI *et al.*, 2015; LI *et al.*, 2016; FEI *et al.*, 2017; LEE *et al.*, 2017; LI *et al.*, 2018; WU *et al.*, 2018; MANIA *et al.*, 2019; CHEN *et al.*, 2020). Previously, QVH internal edge states, known as the kink states, were realized in Bernal bilayer graphene using lithographically patterned gates, and operations of a valley valve and electron beam splitter were demonstrated (LI *et al.*, 2016; LI *et al.*, 2018). The tunable beam splitter is analogous to the action of a quantum point contact, which is a powerful element used in a wide range of fundamental research and quantum devices (HOUTEN; BEENAKKER, 1996). The absence of precise resistance quantization, which implies backscattering is still present, is a critical impediment to the pursuit of some of the most exciting prospects of helical 1D systems, such as topological superconductors (KILLI *et al.*, 2010; HART *et al.*, 2014; LI *et al.*, 2015; WIEDER *et al.*, 2015; BOCQUILLON *et al.*, 2017; ZHANG; LIU, 2017; MAHONEY *et al.*, 2017; RHODES *et al.*, 2019; LODGE *et al.*, 2021), helical Luttinger liquid physics (KILLI *et al.*, 2010; LI *et al.*, 2015; WIEDER *et al.*, 2015; MAHONEY *et al.*, 2017; ZHANG; LIU, 2017; RHODES *et al.*, 2019) and the development of edge-based quantum transport devices (HOUTEN; BEENAKKER, 1996; QIAO *et al.*, 2011; QIAN *et al.*, 2014; MAHONEY *et al.*, 2017; LODGE *et al.*, 2021).

As a rule, TR symmetry-invariant TI exhibit QSH physics, while TI with broken TR symmetry present QAH physics. It is worth mentioning that in the QSH effect [Fig. 14 (a)], the strong ISO coupling leads to the formation of helical edge states, in which the spin orientation of the edge state depends on the direction of travel. That is, the helical edge states exist at the boundaries of two-dimensional topological insulators, with the spin of an electron locked to its direction of motion, so that electrons with opposite spins move in opposite directions along the edge. This spin-momentum locking provides robustness against backscattering from non-magnetic impurities, making helical edge states a hallmark of $\mathbb{Z}_2$ topological insulators. In this effect, the edge states exist regardless of an external bias.

In the QAH effect [Fig. 14 (b)], on the other hand, the edge states all carry the same spin direction, *i.e.*, they are chiral. This means they are unidirectional electronic states where electrons move in a single direction along the edge, regardless of their spin. These edge states exist regardless of an external bias or magnetic field.

In both cases, the topological invariants ν and C are closely related to QSH and QAH physics, respectively. The Chern number is directly related to the anomalous Hall conductivity (AHC) by $\sigma_{\mathrm{AHC}} = (\sum_n^{\mathrm{occ}} C_n)e^2/h = Ce^2/h$. Analogously, the spin Hall conductivity equals

Figure 14 – Schematic representation of: (a) QSH effect, (b) QAH effect, where M is the spontaneous magnetization inherent to this effect.

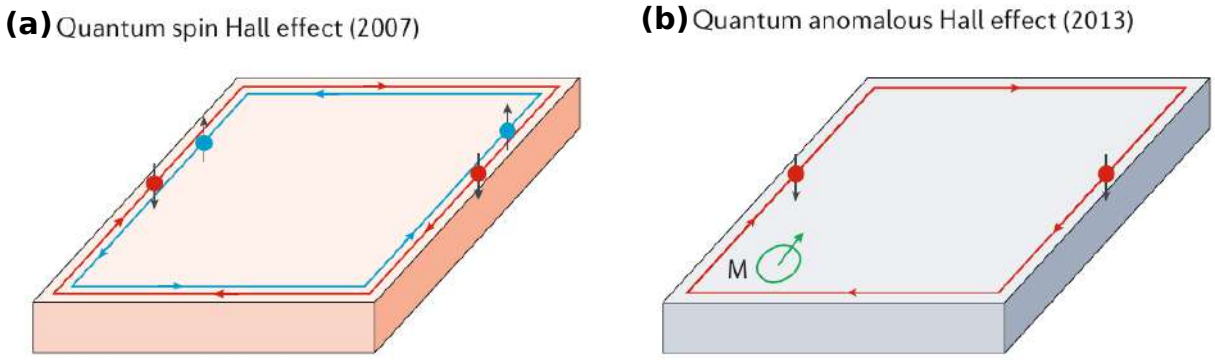

Source: Adapted from Klitzing *et al.* (2020, p. 399).

$\sigma_{SH} = (\sum_n^{occ} C_n^s e)/(4\pi) = C^s e/(4\pi)$.

Exceptions to this rule occur when one introduces Rashba spin-orbit (RSO) coupling and an exchange field, such that one can have an QSH-like phase in a system where the TR symmetry is broken (YANG *et al.*, 2011) or obtain an QAH-like phase in a system with invariant TR symmetry (QIAO *et al.*, 2010).

1.2.6 Topological phase transitions

The self-organization of a large number of nuclides and electrons leads to the emergence of various phases of matter. Each phase represents a specific organizational pattern that can be spatially replicated infinitely and has properties that change continuously in response to external fields, distinguishing it from other phases. Consequently, certain system properties are altered as the material undergoes a phase transition. A general characteristic of a phase transition is that it either involves a discontinuity in an order parameter, according to Landau's paradigm of phase transitions (MA, 1976; GOLDENFELD, 1992), or a change in a topological invariant in the case of TPT (CHRISTIAN, 2002; SACHDEV, 2011; FRADKIN, 2013; LI *et al.*, 2021).

The exploration of TPT began in the 1970s when phenomena such as the QH effect (KLITZING *et al.*, 1980) and 2D superfluid phase transitions (NELSON; KOSTERLITZ, 1977) were elucidated using the principles of topology (THOULESS *et al.*, 1982; HALDANE, 1983; KOSTERLITZ; THOULESS, 2018). These foundational studies significantly impacted electron band theory (BANSIL *et al.*, 2016). Topological states typically remain unaffected by gradual changes in material parameters, except when TPT occurs. Numerous TI with distinct band inversion mechanisms have been both theoretically proposed and experimentally confirmed, in

both periodic (ZHOU *et al.*, 2014; REIS *et al.*, 2017) and aperiodic systems (MITCHELL *et al.*, 2018; AGARWALA; SHENOY, 2017; HUANG; LIU, 2018a; HUANG; LIU, 2018b; HUANG; LIU, 2019).

Unlike conventional phase transitions described by Landau's theory of spontaneous symmetry breaking, which follow universal critical scaling laws, TPTs are marked by abrupt changes in topological invariants in response to continuous variations in system parameters. This change in the topological invariants due to TPT is characterized by the closing of the gap, which usually reopens after the transition (MURAKAMI, 2007; MURAKAMI *et al.*, 2007; HASAN; KANE, 2010). This can be understood through an analogy with geometric shapes. Consider a sphere and a donut: a sphere has a genus of $G = 0$ because it has no holes, while a donut has a genus of $G = 1$ due to its single hole. If a hole were to form in the sphere, it would undergo a TPT, changing its genus from 0 to 1 and becoming topologically equivalent to a donut. This process is analogous to the closing and reopening of the energy gap in a material during a TPT, where the change in the Chern number signifies the transition (BEUGELING *et al.*, 2012; LIU *et al.*, 2012; WANG *et al.*, 2016; CHEN; ZHOU, 2017; OWERRE, 2018; ABLOWITZ; COLE, 2019; MOJARRO; ULLOA, 2023; XING *et al.*, 2024). Conversely, transforming a donut into a coffee mug, which also has a genus of $G = 1$, does not change its topological invariant because both shapes have the same number of holes.[15] Thus, the topological invariant remains the same unless there is a fundamental change, such as the creation or annihilation of a hole, reflecting the robustness of topological phases in materials.

1.3 Outline

Throughout the subsequent chapters, we will develop the mathematical framework that helps to investigate the basic electronic properties of the Lieb-Kagome lattice subjected to strain, both with and without ISO coupling. More precisely, we will present the generic TB model applied to Lieb, transition, and Kagome lattices to obtain the effects on the energy spectrum driven by strain, investigating the occurrence of TPT and the evolution of edge states in nanoribbons constructed from Lieb-Kagome lattices. The effects of hypothetical strains and non-topological phase transitions are also analyzed.

In Ch. 2, we develop a generic tight-binding Hamiltonian based on the interconvert-

[15] The deformation of a coffee mug into a donut (torus) can be seen in this gif: https://upload.wikimedia.org/wikipedia/commons/2/26/Mug_and_Torus_morph.gif.

ibility of Lieb-Kagome lattices, discussing the energy spectra obtained when these lattices are subjected to biaxial, pure shear, as well as uniaxial and simple shear strains along the crystallographic x and y directions. The discussion of second neighbor effects, hypothetical strain cases, in which the values of the hopping parameters do not change, and the strain-induced vector pseudopotentials, is also carried out.

In Ch. 3, we present the Hamiltonian with ISO coupling, and subsequently discuss the effects of strain on the electronic spectrum of Lieb and Kagome lattices with ISO coupling, respectively, investigating the opening and closing of energy gaps, the evolution of Berry curvature for each case, and the change of spin Chern numbers, setting up topological phase transitions driven by strain.

In Ch. 4, we investigate the effects of NNN sites and strain on the energy spectrum and DOS of the nanoribbons with three types of edges (straight, bearded, and asymmetric). We also explore the role of strain on edge states.

Finally, we present the main concluding remarks in Ch. 5.

2 EFFECTS OF UNIAXIAL AND SHEAR STRAINS ON THE ELECTRONIC SPECTRUM OF LIEB AND KAGOME LATTICES

We systematically study the effects of the shear and uniaxial strains, applied along different crystallographic directions, on the electronic spectrum of Lieb and Kagome lattices by using the TB model with a general Hamiltonian that describes both lattices by means of only one control parameter. Our findings show that such deformations do not open an energy gap in their electronic spectra, but can cause: (i) approximation of the energy cones, (ii) anisotropy in the energy levels, and (iii) deformation of the nearly-flat band, such that the triply degenerate Dirac point in the Lieb lattice transforms into two doubly degenerate Dirac points. By analyzing hypothetical strain cases in which the values of the hopping parameters do not change, we observe that effects such as deformation in the nearly-flat band and division of the triply degenerate Dirac point are only due to the hopping parameter changes caused by the strain. Moreover, we identify cases in which there are non-null strain-induced pseudovector potentials in Lieb and Kagome lattices.

2.1 Motivation

The discovery of many interesting properties of 2D crystals has led in recent years to a renewed interest on the study of structures such as the Lieb and Kagome lattices. In these systems, a conical Dirac energy band coexists with nearly-flat bands. The development of experimental techniques for the synthesis of electronic and chemical structures with such lattice configurations has motivated research on electronic-based lattices (SLOT *et al.*, 2017; LI *et al.*, 2018), waveguides-based photonic systems (SHEN *et al.*, 2010; GOLDMAN *et al.*, 2011b; GUZMÁN-SILVA *et al.*, 2014; VICENCIO *et al.*, 2015; MUKHERJEE *et al.*, 2015a; MUKHERJEE *et al.*, 2015b; TAIE *et al.*, 2015; XIA *et al.*, 2016; ZONG *et al.*, 2016; DIEBEL *et al.*, 2016; SCHULZ *et al.*, 2017; LI *et al.*, 2018), and even structures formed by organic bonds (ONO *et al.*, 2009; ZHANG *et al.*, 2010; NITA *et al.*, 2013; KEIMER *et al.*, 2015; NAKATSUJI *et al.*, 2015; DOWNIE *et al.*, 2015; CUI *et al.*, 2017; LIU *et al.*, 2018; REICHARDT *et al.*, 2018; JIANG *et al.*, 2019a; YAZYEV, 2019; CUI *et al.*, 2020).

In this context, Yin *et al.* (2022) presents some of such artificial kagome materials connecting the theoretical ideas and experimental observations, as well as the bond between quantum interactions within kagome magnets and kagome superconductors, and their relation to the concepts in topological insulators, topological superconductors, Weyl semimetals, and high-

temperature superconductors, whose topics are at the research cutting-edge of the topological quantum matter. Such experiments have allowed the verification of theoretical predictions (ONSAGER, 1944; LIEB, 1989; MEKATA, 2003), such as the co-existence of Dirac-like cones and flat bands, (GUO; FRANZ, 2009; DEPENBROCK *et al.*, 2012; LI *et al.*, 2016; LU *et al.*, 2017; YIN *et al.*, 2019), and have encouraged theoretical investigations of the effects of deformation on the optoelectronic and magnetic properties of these structures. Recently, there have been investigations of the stability of the flat band and the band-touching points due to breathing anisotropy (ESSAFI *et al.*, 2017) and disordered flat bands in the Kagome lattice (BILITEWSKI; MOESSNER, 2018), as well as multi-functional twisted-Kagome lattices (LIARTE *et al.*, 2020), strain-induced topological magnon phase transitions (OWERRE, 2018) and strain-induced pseudomagnetic field in Kagome crystals (LIU, 2020). Similar studies have explored the dispersion relations of strained and complex Lieb lattices (ZHANG *et al.*, 2016) and strain-induced superconductor-insulator transition on a Lieb lattice (SWAIN; KARMAKAR, 2020).

In addition, it has been shown that the Lieb and Kagome lattices are inter-convertible by the application of strain along the diagonal direction (JIANG *et al.*, 2019c; JIANG *et al.*, 2019a; CUI *et al.*, 2020; LIM *et al.*, 2020). Before the publication of the article derived from this chapter of our thesis (LIMA *et al.*, 2023), there was a lack of studies presenting a generic TB Hamiltonian that describes the effect of strain on both Lieb and Kagome lattices.[1] Jiang *et al.* (2019a), Jiang *et al.* (2019c), Cui *et al.* (2020) and Lim *et al.* (2020) include strain applied along the diagonal direction of the lattice in order to induce the interconversion between Lieb and Kagome lattices, but no strain tensor is used in the Hamiltonian, such that diagonal strains are used as a thought experiment, not being explicit in the methodology of these articles. A TB Hamiltonian with the presence of the strain tensor was reported by Liu (2020), but only for the study of strained Kagome lattices. However, the authors did not use the knowledge of the interconversibility of Lieb and Kagome lattices, which would allow a comparison between the strained Lieb and Kagome lattices. Thus, as a generalization of the previous studies, in this chapter we present a general TB Hamiltonian that not only describes the interconversion between the Lieb and Kagome lattices, but also enables the study of these structures when subject to uniaxial and shear strains along different crystallographic directions. Based on this formalism, we investigate the effects of strain on the energy spectrum of Lieb and Kagome lattices that have

[1] An initial study was conducted in the master's dissertation of the author of the present thesis (LIMA, 2020).

not been previously explored, such as: (i) the appearance of anisotropy in the energy levels, (ii) the variation of the Fermi level, (iii) strain-induced flat band deformations, (iv) a shift of the Dirac points with respect to the location of the high symmetry k-space points, and (v) the appearance of a strain-induced pseudovector potentials. The pseudovector potential terms originated by strain in the Kagome lattice were presented by Liu (2020), but the effects caused by such terms on the energy spectrum were not explored. In the present chapter, on the other hand, we show both the effect of non-zero strain-induced pseudovector potentials on Kagome and Lieb lattices, and make a comparison between these lattices.

Furthermore, inspired by studies that explore the strain effects on graphene based systems (PEREIRA *et al.*, 2009; COCCO *et al.*, 2010; LI *et al.*, 2010; SENA *et al.*, 2012; QU *et al.*, 2014; NAUMIS *et al.*, 2017), we investigate two theoretical methodologies for applying deformations in Lieb and Kagome lattices, namely: real and hypothetical cases. In the former case, we consider that the strain tensor changes the position of the lattice sites, and consequently, it modifies the hopping parameter values that connect the atomic sites. In the latter, we admit that the hopping parameters' values remain unchanged, being independent of the applied lattice deformation (KITT *et al.*, 2012; OLIVA-LEYVA; NAUMIS, 2013; OLIVA-LEYVA; NAUMIS, 2015; KITT *et al.*, 2013; OLIVA-LEYVA; WANG, 2017). Shear and uniaxial strains applied along different crystallographic directions are investigated for Lieb and Kagome lattices, for both real and hypothetical cases.

The chapter is organized as follows. In Sec. 2.2, we describe the generic lattice that enables the study of strain in Lieb and Kagome lattices, as well as present the high symmetry points of the corresponding reciprocal lattices. In Sec. 2.3, we review the strain theory for 2D materials, and in Sec. 2.4 we derive the TB model for the generic lattice within the strain formalism. In Sec. 2.5, we discuss the hopping renormalization adopted in the previously developed model, and in Sec. 2.6 we examine the choice of the n parameter that governs the adopted hopping parameterization. In Secs. 2.7 and 2.8, we discuss the strain effects on Lieb and Kagome lattices, respectively. The results for the hypothetical case are discussed in Sec. 2.9, and in Sec. 2.10 we identify the effects of the strain-induced pseudovector potentials. We present a synthesis of strain effects on Lieb and Kagome lattices in Sec. 2.11. Finally, in Sec. 2.12 we summarize our main findings.

Figure 15 – Real (top panels) and reciprocal (bottom panels) generic lattices: (a) Lieb lattice - $\hat{D}_{4h}$ ($\theta = \pi/2$), (b) transition lattice - $\hat{D}_{2h}$ ($\pi/2 < \theta < 2\pi/3$) and (c) Kagome lattice - $\hat{D}_{6h}$ ($\theta = 2\pi/3$). $\mathbf{a}_1$ and $\mathbf{a}_2$ are the primitive vectors with unit cells denoted by the red dashed lines containing three non-equivalent sites A (blue empty circle), B (yellow filled circle) and C (green circle with dot inside). The distance between NN sites is a_0 and the non-null hopping parameters are represented by t_{BA}, t_{BC}, t_{AC}^{-}, t_{AC}^{+}. For Lieb and Kagome lattices, the NN hopping is $t_{BA} = t_{BC} = t$ and the NNN hopping is $t_{AC}^{-} = t_{AC}^{+} = t'$. BZ of the (d) Lieb, (e) transition, and (f) Kagome lattices denoted by the dashed blue lines. The reciprocal vectors are $\mathbf{b}_1$ and $\mathbf{b}_2$ and the high symmetry points are $\mathbf{\Gamma}$ (filled circle), $\mathbf{X}$ (empty solid circle), $\mathbf{M}$ (circle with dot inside) and $\mathbf{K}$ (empty dashed circle).

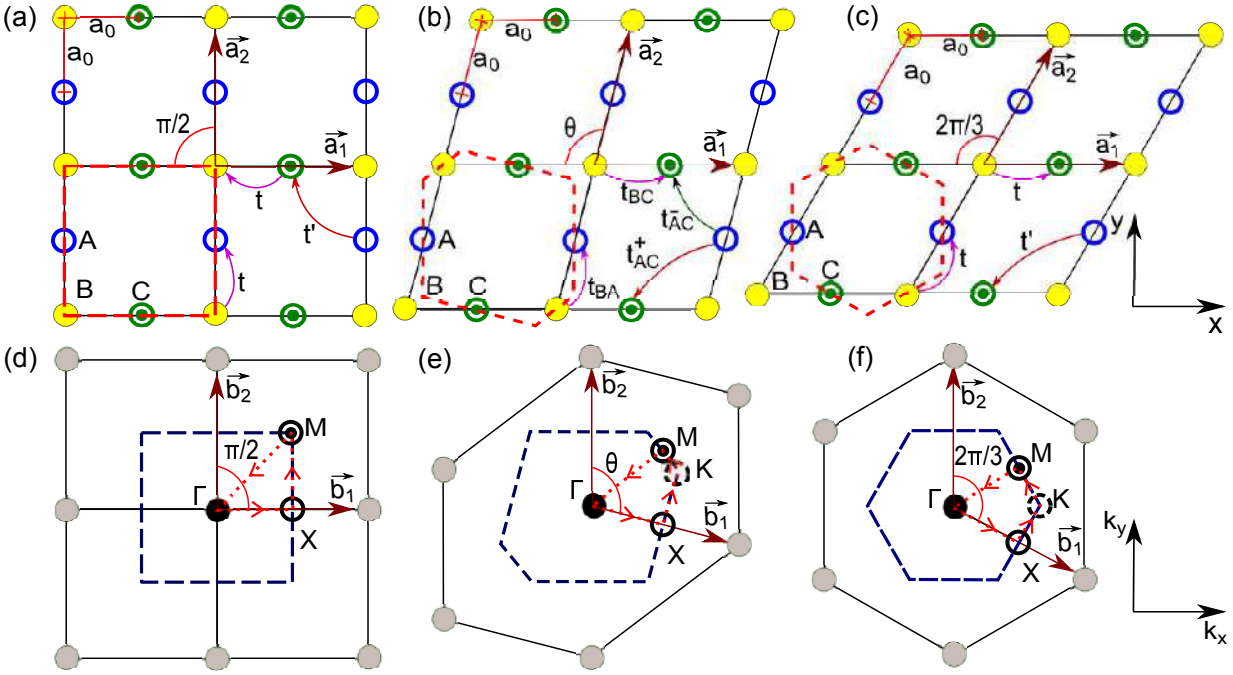

Source: The author Lima *et al.* (2023).

2.2 Generic lattice

We define the generic lattice as a 2D crystalline structure with a unit cell composed by three sites at the basis (labeled by A, B, and C), which may present symmetry $\hat{D}_{4h}$, $\hat{D}_{2h}$ and $\hat{D}_{6h}$ according to the angle choice $\pi/2 \leq \theta \leq 2\pi/3$. As represented in the Figs. 15 (a) and 15 (c), $\theta = \pi/2$ and $\theta = 2\pi/3$ correspond to the Lieb ($\hat{D}_{4h}$) and Kagome ($\hat{D}_{6h}$) lattices, respectively. The 2D crystals obtained with $\pi/2 < \theta < 2\pi/3$ are called transition lattices ($\hat{D}_{2h}$), as shown in Fig. 15 (b), since they represent the evolution stages between Lieb and Kagome lattices in the interconversion process, as well discussed by Jiang *et al.* (2019c), Cui *et al.* (2020), Jiang *et al.* (2019a) and Lim *et al.* (2020).

The generic primitive lattice vectors are

$$\mathbf{a}_1 = a\hat{v}_1, \quad \text{and} \quad \mathbf{a}_2 = a\hat{v}_2, \tag{2.1}$$

with $\hat{v}_1 = (1,0)$ and $\hat{v}_2 = (-\cos\theta, \sin\theta)$. In order to investigate a more generic case, we consider here, without loss of generality, that $a = 1$ Å. The reciprocal lattice in turn, is generated by the following primitive vectors

$$\mathbf{b}_1 = b_1\hat{v}_1, \quad \text{and} \quad \mathbf{b}_2 = b_2\hat{v}_2, \tag{2.2}$$

with $|\mathbf{b}_1| = |\mathbf{b}_2| = 2\pi/(a\sin\theta) \equiv b$, $\hat{v}_1 = (\sin\theta, \cos\theta)$ and $\hat{v}_2 = (0,1)$. The high symmetry points in the BZ are given by

$$\mathbf{\Gamma} = (0,0), \qquad \mathbf{X} = \frac{b}{2}\hat{v}_1, \qquad \mathbf{M} = \frac{b}{2}(\hat{v}_1 + \hat{v}_2), \qquad \mathbf{K} = \frac{1}{2}(b - l\cos\theta)\,\hat{v}_1 + \frac{l}{2}\hat{v}_2, \tag{2.3}$$

with $l = b/(1-\cos\theta)$. The BZ, the high symmetry points in the reciprocal space, and the reciprocal vectors are illustrated in Figs. 15 (d), 15 (e), and 15 (f), for Lieb, transition and Kagome lattices, respectively.

Throughout this chapter, we will use a generic lattice to simultaneously study the strained Lieb and Kagome lattices using a generic TB model as a function of the angle θ.

2.3 Analysis of strain

The application of strain in a crystal modifies the vectors connecting lattice sites and changes the corresponding hopping parameters. Considering $\mathbf{r}$ the position vector of a unstrained site. The new site position on the deformed lattice is written as (OLIVA-LEYVA; NAUMIS, 2013; SI *et al.*, 2016; NAUMIS *et al.*, 2017)

$$\mathbf{r}' = \mathbf{r} + \delta(\mathbf{r}), \tag{2.4}$$

where $\delta(\mathbf{r})$ is the displacement vector usually expressed in terms of the strain tensor $\overline{\varepsilon}$, given by (PEREIRA *et al.*, 2009; OLIVA-LEYVA; NAUMIS, 2013; NAUMIS *et al.*, 2017)

$$\delta(\mathbf{r}) = \overline{\varepsilon}\cdot\mathbf{r}. \tag{2.5}$$

Thus, the sites of the strained lattice are located by (NASCIMENTO *et al.*, 2017; BANDEIRA *et al.*, 2020)

$$\mathbf{r}' = (\mathbb{I} + \overline{\varepsilon})\cdot\mathbf{r}, \tag{2.6}$$

where $(\mathbb{I} + \overline{\varepsilon})$ is the transformation matrix that takes the original lattice vectors and provides the vectors corresponding to the strained lattice. As for instance, by Eqs. (2.1) and (2.6), one

has that the primitive vectors of the generic lattice are transformed as $\mathbf{a'}_1 = (\mathbb{I} + \overline{\varepsilon}) \cdot \mathbf{a}_1$ and $\mathbf{a'}_2 = (\mathbb{I} + \overline{\varepsilon}) \cdot \mathbf{a}_2$.

Any point ($\mathbf{k} = (k_x, k_y)$) in the reciprocal space is transformed by the strain tensor according to the following relation (OLIVA-LEYVA; NAUMIS, 2013; OLIVA-LEYVA; NAUMIS, 2015; NAUMIS *et al.*, 2017; OLIVA-LEYVA; WANG, 2017)

$$\mathbf{k'} = [(\mathbb{I} + \overline{\varepsilon})^{-1}]^T \cdot \mathbf{k}. \tag{2.7}$$

For 2D crystals, the strain tensor is generally of the form (PEREIRA *et al.*, 2009; COCCO *et al.*, 2010; LI *et al.*, 2010; SENA *et al.*, 2012; QU *et al.*, 2014; NAUMIS *et al.*, 2017)

$$\overline{\varepsilon} = \begin{pmatrix} \overline{\varepsilon}_{xx} & \overline{\varepsilon}_{xy} \\ \overline{\varepsilon}_{yx} & \overline{\varepsilon}_{yy} \end{pmatrix} = \begin{pmatrix} \varepsilon_{xx} - \sigma_p \varepsilon_{yy} & \varepsilon_{xy} \\ \varepsilon_{yx} & \varepsilon_{yy} - \sigma_p \varepsilon_{xx} \end{pmatrix}, \tag{2.8}$$

where ε_{ij} refers to a deformation in the i direction that will be multiplied by the j component of the non-deformed vector $\mathbf{r}$, and σ_p denotes the Poisson ratio (BLAKSLEE *et al.*, 1970; PEREIRA *et al.*, 2009), adopted in this thesis as $\sigma_p = 0.1$ in any direction for uniaxial strains.[2]

Figure 16 shows the effects on the unit cell of the generic lattice due to the application of the six different types of strains to the Lieb and Kagome lattices investigated here, which are: (i) uniaxial along the x direction (UX) [Fig. 16 (a)], (ii) uniaxial along the y direction (UY) [Fig. 16 (b)], (iii) biaxial (BI) [Fig. 16 (c)], (iv) simple shear along the x direction (SX) [Fig. 16 (d)], (v) simple shear along the y direction (SY) [Fig. 16 (e)], and (vi) pure shear (PS)-strain [Fig. 16 (f)]. The atomic positions of the strained lattices, $\mathbf{r'} = (r'_x, r'_y)$, are found by Eqs. (2.6) and (3.5), such that the correspondence with the unstrained lattice sites, $\mathbf{r} = (r_x, r_y)$, is given by

$$\begin{pmatrix} r'_x \\ r'_y \end{pmatrix} = \begin{pmatrix} [1 + (\varepsilon_{xx} - \sigma_p \varepsilon_{yy})]\, r_x + \varepsilon_{xy} r_y \\ \varepsilon_{yx} r_x + [1 + (\varepsilon_{yy} - \sigma_p \varepsilon_{xx})]\, r_y \end{pmatrix}, \tag{2.9}$$

with ε_{ij}-values (with $i, j = x, y$) being summarized in the Table 1 for all the six investigated deformations.

The effects of the six types of strain on the Lieb and Kagome lattices are pictorially represented in Figs. 17 and 18, respectively, similar to what is depicted in Fig. 16, but now for a section of the infinite lattice instead of just the unit cell. In both figures, we present a comparison of lattices without strain (black lines) and with strain (red lines) with $\varepsilon > 0$ of the types: (i) UX

[2] The Poisson ratio, when positive (negative), describes how a material contracts (expands) in directions perpendicular to the direction of the applied force. In graphite, $\sigma_p = 0.165$ (BLAKSLEE *et al.*, 1970; PEREIRA *et al.*, 2009). For convenience, we adopt $\sigma_p = 0.1$ in this work, as we are using a generic Lieb and Kagome model not tied to a specific material.

Figure 16 – Comparison of the unstrained ($\varepsilon = 0$) and strained ($\varepsilon \neq 0$) generic lattices subjected to (a) UX, (b) UY, (c) BI, (d) SX and (e) SY, and (f) PS-strain. The generic lattice sites (A, B and C) are represented by black-filled symbols connected by black dashed lines and primitive vectors $\mathbf{a}_1$ and $\mathbf{a}_2$, whereas the strained lattice sites (A′, B′ and C′) are represented by red oppend symbols connected by red dashed lines and primitive vectors $\mathbf{a}'_1$ and $\mathbf{a}'_2$.

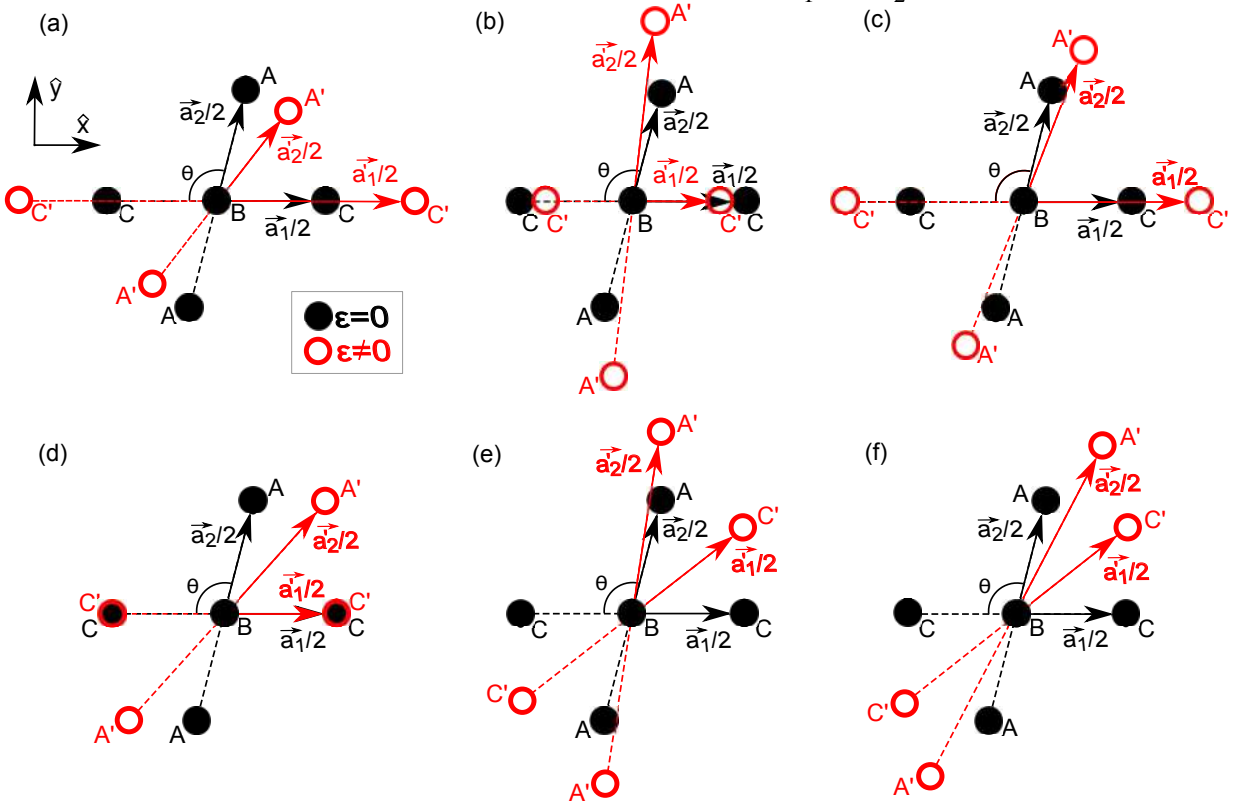

Source: The author Lima *et al.* (2023).

Table 1 – Strain tensor elements [Eq. (3.5)] for each type of strain applied.

Type of strain	ε_{xx}	ε_{xy}	ε_{yx}	ε_{yy}
UX	ε	0	0	0
UY	0	0	0	ε
BI	ε	0	0	ε
SX	0	ε	0	0
SY	0	0	ε	0
PS	0	ε	ε	0

[Figs. 17(a) and 18(a)], (ii) UY [Figs. 17(b) and 18(b)], (iii) BI [Figs. 17(c) and 18(c)], (iv) SX [Figs. 17(d) and 18(d)], (v) SY [Figs. 17(e) and 18(e)], and (vi) PS [Figs. 17(f) and 18(f)].

Figure 17 – Comparison of Lieb lattices without strain (black lines) and with strain (red lines) with $\varepsilon > 0$ of the types: (a) UX, (b) UY, (c) BI, (d) SX, (e) SY, and (f) PS. The non-zero Poisson ratio justifies the compression in the vertical (horizontal) direction for UX (UY) strain.

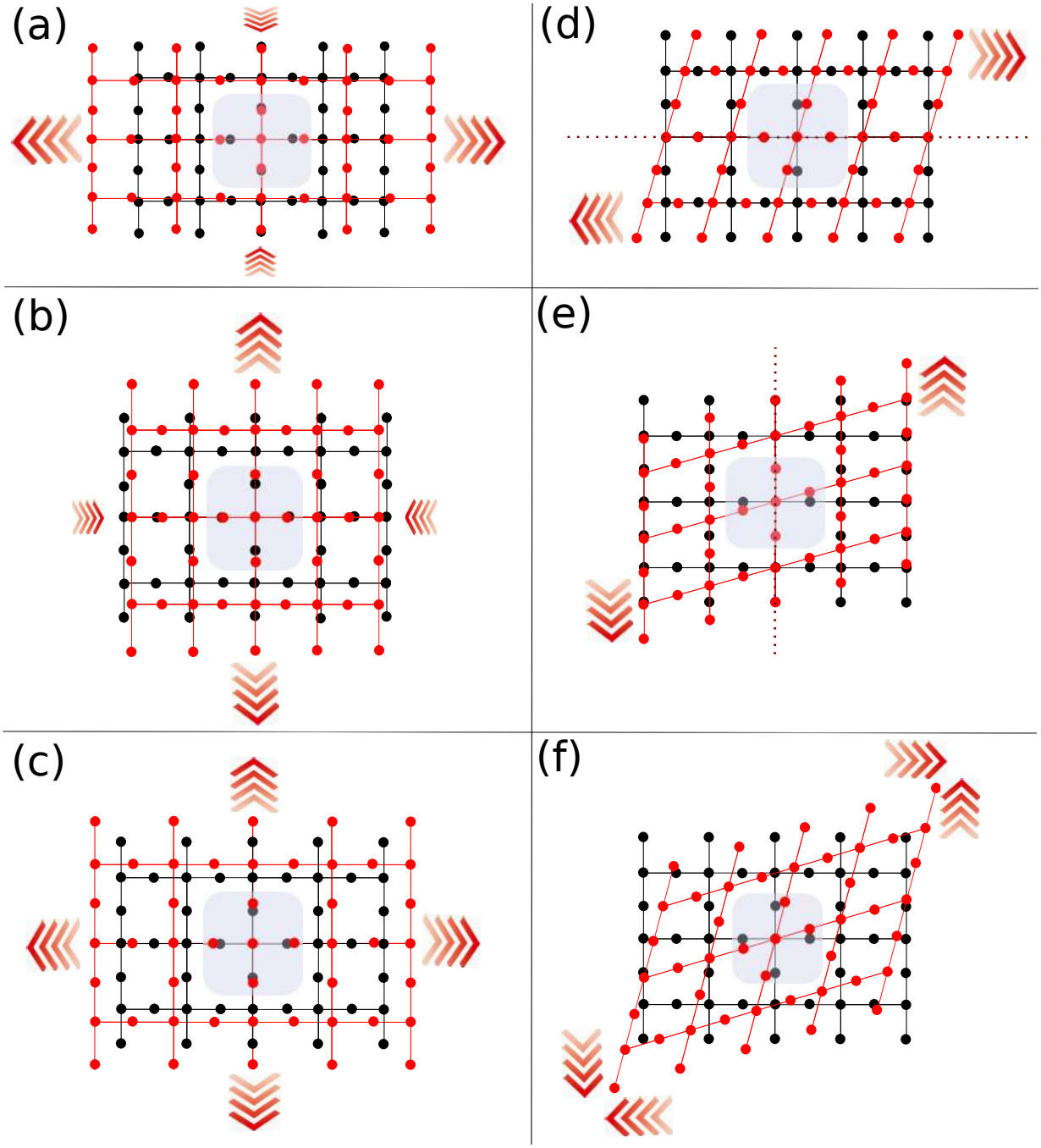

Source: The author.

Figure 18 – Comparison of Kagome lattice without strain (black lines) and with strain (red lines), with $\varepsilon > 0$, for: (a) UX, (b) UY, (c) BI, (d) SX, (e) SY, and (f) PS. The non-zero Poisson ratio justifies the compression in the vertical (horizontal) direction for UX (UY) strain.

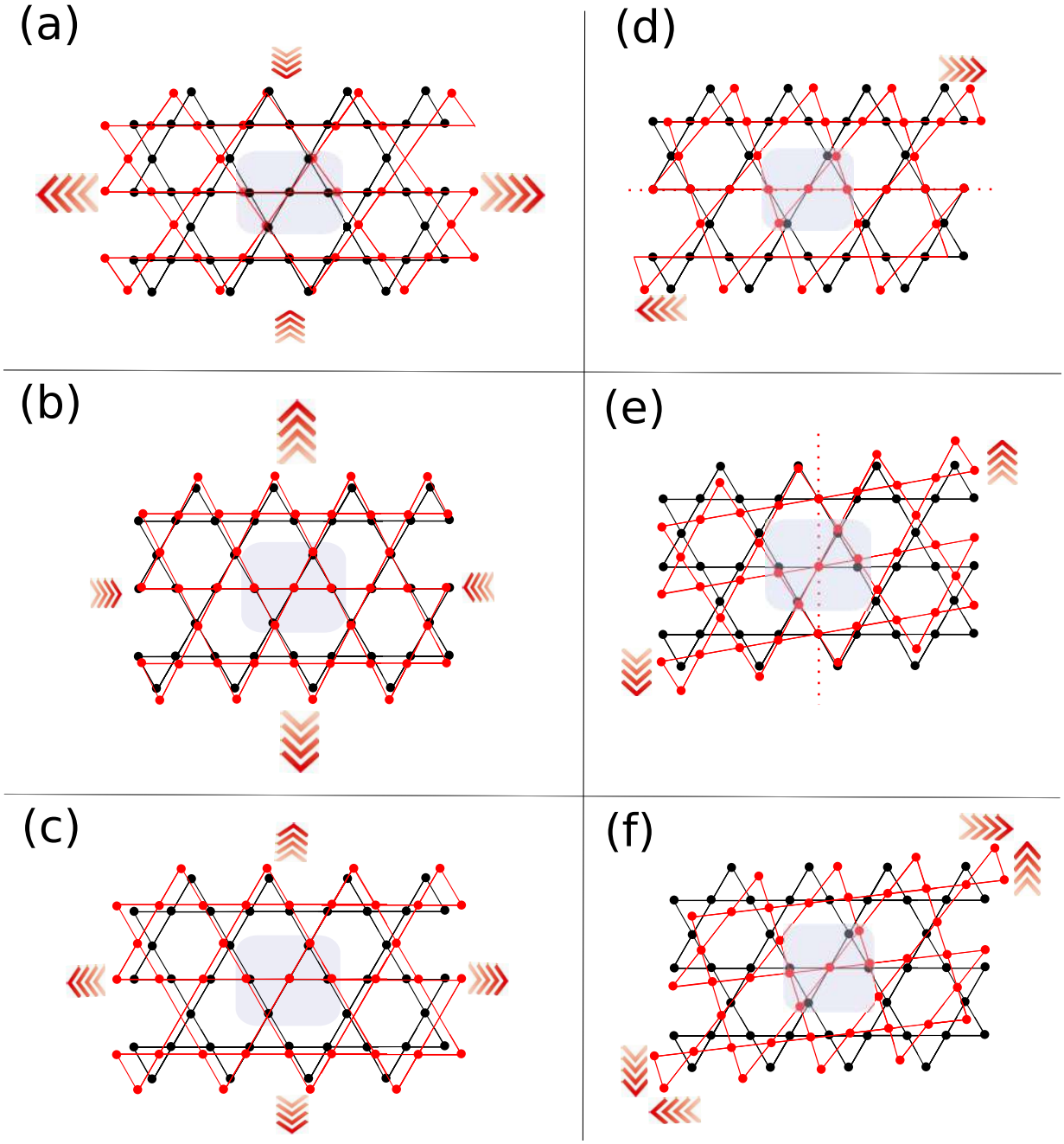

Source: The author.

2.4 Tight-binding model

Since the unit cell of the generic lattice has three distinct sites (A, B, C), as depicted in Fig. 15, the electronic states can be taken as a linear combination of the Bloch's functions Φ_s with $s = A, B, C$, such as

$$\Phi_s(\mathbf{r}) = \frac{1}{\sqrt{N}} \sum_{\mathbf{R}'_s}^{N} e^{i\mathbf{k}\cdot\mathbf{R}'_s} \varphi_s(\mathbf{r} - \mathbf{R}'_s), \tag{2.10}$$

being φ_s the atomic orbitals of the site s and $1/\sqrt{N}$ the normalization term of the wave function.[3] For each site s, the summation is taken over the neighbour sites located on the position $\mathbf{R}'_s$, within the proposed TB approach. In our model, as represented in Fig. 16, we consider the hopping energy contributions due to the neighbours located on $\pm\mathbf{a}'_2/2$, $\pm\mathbf{a}'_1/2$, $\pm(\mathbf{a}'_1 - \mathbf{a}'_2)/2$ and $\pm(\mathbf{a}'_1 + \mathbf{a}'_2)/2$.

Assuming the contribution of one orbital per site, the TB Hamiltonian in first quantization given by $H'_{ss'} = \langle \Phi_s | H'_{\mathbf{k}} | \Phi_{s'} \rangle$, with $s, s' =$ A, B, C, can be written in the matrix format as

$$H'_{\mathbf{k}} = \begin{pmatrix} H'_{AA} & H'_{BA} & H'_{AC} \\ & H'_{BB} & H'_{BC} \\ & & H'_{CC} \end{pmatrix}, \tag{2.11}$$

whose off-diagonal matrix elements are

$$H'_{BA}(\mathbf{k}) = 2t'_{BA} \cos\left(\mathbf{k}\cdot\mathbf{a}'_2/2\right), \tag{2.12a}$$

$$H'_{BC}(\mathbf{k}) = 2t'_{BC} \cos\left(\mathbf{k}\cdot\mathbf{a}'_1/2\right), \tag{2.12b}$$

$$H'_{AC}(\mathbf{k}) = 2t'^{-}_{AC} \cos\left[\mathbf{k}\cdot(\mathbf{a}'_1 - \mathbf{a}'_2)/2\right] + 2t'^{+}_{AC} \cos\left[\mathbf{k}\cdot(\mathbf{a}'_1 + \mathbf{a}'_2)/2\right], \tag{2.12c}$$

and the main diagonal matrix elements $H'_{ss}(\mathbf{k})$, related to the on-site energies, are considered here null. The omitted lower triangle of the matrix in Eq. (2.11) should be filled in according to a hermitian matrix. The hopping parameters present in Eqs. (2.12) (a)–(2.12) (c) are defined as

$$t'_{BA} = \left\langle \varphi_B(\mathbf{r} - \mathbf{R}'_B) \middle| H'_{\mathbf{k}} \middle| \varphi_A(\mathbf{r} - \mathbf{R}'_B \pm \mathbf{a}'_2/2) \right\rangle, \tag{2.13a}$$

$$t'_{BC} = \left\langle \varphi_B(\mathbf{r} - \mathbf{R}'_B) \middle| H'_{\mathbf{k}} \middle| \varphi_C(\mathbf{r} - \mathbf{R}'_B \pm \mathbf{a}'_1/2) \right\rangle, \tag{2.13b}$$

$$t'^{-}_{AC} = \left\langle \varphi_A(\mathbf{r} - \mathbf{R}'_A) \middle| H'_{\mathbf{k}} \middle| \varphi_C(\mathbf{r} - \mathbf{R}'_A \pm (\mathbf{a}'_1 - \mathbf{a}'_2)/2) \right\rangle, \tag{2.13c}$$

$$t'^{+}_{AC} = \left\langle \varphi_A(\mathbf{r} - \mathbf{R}'_A) \middle| H'_{\mathbf{k}} \middle| \varphi_C(\mathbf{r} - \mathbf{R}'_A \pm (\mathbf{a}'_1 + \mathbf{a}'_2)/2) \right\rangle. \tag{2.13d}$$

[3] In our TB model, we adopt one orbital per site, similar to TB models for graphene that consider only the p_z orbital (REICH *et al.*, 2002; PEREIRA *et al.*, 2009). The index s does not refer to the s orbital, but to the type of sublattice, which can be $s =$ A, B, or C.

The Hamiltonian of Eq. (2.11) can be rewritten in the position space by taking $\hat{H} = \sum_{\mathbf{k}} \langle \hat{\Psi}_{\mathbf{k}} | H'_{\mathbf{k}} | \hat{\Psi}_{\mathbf{k}} \rangle$ with $|\hat{\Psi}_{\mathbf{k}}\rangle = \begin{pmatrix} \hat{a}_{\mathbf{k}} & \hat{b}_{\mathbf{k}} & \hat{c}_{\mathbf{k}} \end{pmatrix}^T$, whereby we obtain (LIMA *et al.*, 2022)

$$\begin{aligned}\hat{H} =& \sum_j \left(E_A \hat{a'}^{\dagger}_j \hat{a}'_j + E_B \hat{b'}^{\dagger}_j \hat{b}'_j + E_C \hat{c'}^{\dagger}_j \hat{c}'_j \right) + \sum_{jj'} \left[t_{BA} \left(\hat{b'}^{\dagger}_{j'} \hat{a}'_j + \hat{a'}_j{}^{\dagger} \hat{b}'_{j'} \right) + t_{BC} \left(\hat{b'}^{\dagger}_{j'} \hat{c}'_j + \hat{c'}_j{}^{\dagger} \hat{b}'_{j'} \right) \right] \\ &+ \sum_{jj'} \left[t_{AC} \left(\hat{a'}^{\dagger}_{j'} \hat{c}'_j + \hat{c'}_j{}^{\dagger} \hat{a}'_{j'} \right) \right], \end{aligned} \tag{2.14}$$

where $\hat{a}'_j$ ($\hat{a'}_j{}^{\dagger}$), $\hat{b}'_j$ ($\hat{b'}_j{}^{\dagger}$) and $\hat{c}'_j$ ($\hat{c'}_j{}^{\dagger}$) are annihilation (creation) operators corresponding to the jth-site of sublattice A, B, and C, respectively. These operators are related to the elements of $|\hat{\Psi}_{\mathbf{k}}\rangle$ by the following Fourier expansions

$$\hat{s}_j = \frac{1}{\sqrt{N}} \sum_{\mathbf{k}} e^{i\mathbf{k}\cdot\mathbf{r}_j} \hat{s}_{\mathbf{k}}, \quad \hat{s}^{\dagger}_j = \frac{1}{\sqrt{N}} \sum_{\mathbf{k}} e^{-i\mathbf{k}\cdot\mathbf{r}_j} \hat{s}^{\dagger}_{\mathbf{k}}. \tag{2.15}$$

The TB Hamiltonian for the unstrained lattice is a particular case of Eq. (2.11), obtained when one takes $\varepsilon = 0$, which leads to $|\mathbf{a}_1| = |\mathbf{a}_2|$ in the matrix elements in Eq. (2.12), since this condition is characteristic of the unstrained generic lattice as indicated in Eq. (2.1). It implies that

$$H_{BA}(\mathbf{k}) = 2t_{BA} \cos\left(a_0 \mathbf{k} \cdot \hat{\upsilon}_2\right), \tag{2.16a}$$

$$H_{BC}(\mathbf{k}) = 2t_{BC} \cos\left(a_0 \mathbf{k} \cdot \hat{\upsilon}_1\right), \tag{2.16b}$$

$$H_{AC}(\mathbf{k}) = 2t^{-}_{AC} \cos\left[a_0 \mathbf{k} \cdot (\hat{\upsilon}_1 - \hat{\upsilon}_2)\right] + 2t^{+}_{AC} \cos\left[a_0 \mathbf{k} \cdot (\hat{\upsilon}_1 + \hat{\upsilon}_2)\right]. \tag{2.16c}$$

As expected, the matrix elements in Eq. (2.16) consist exactly the ones for the Hamiltonian reported by Jiang *et al.* (2019c), used to study the interconversion between the Lieb and Kagome lattices for unstrained generic lattice.

2.5 Hopping renormalization

Under strain, as discussed in Sec. 2.3, the interatomic distances change and thus the hopping energies are modified. We assume the value $t = 1.0$ eV for the hopping parameter in a free-standing layer in which the interatomic distance between the NN sites is a_0. The hopping parameters for strained lattices are given by the following transformation

$$t'_{ij} = t e^{-n\left(a'_{ij}/a_0 - 1\right)} a_0 / a'_{ij}, \tag{2.17}$$

where[4] $n = 8$ and a'_{ij} represents the distance between the atomic sites i and j in the strained lattice, that is given, with respect to the undeformed lattice distances a_{ij}, according to $\mathbf{a}'_{ij} = (\mathbb{I} + \overline{\varepsilon})\mathbf{a}_{ij}$,

[4] We adopt $n = 8$ in accordance with Jiang *et al.* (2019c), because this value results in nearly-flat bands in the spectra of Lieb and Kagome characteristic of a TB model of NN-sites. Using $n < 8$ results in the inclusion of NNN-sites effects, as discussed in Sec. 2.6.

with $a'_{ij} = (\mathbf{a}'_{ij} \cdot \mathbf{a}'_{ij})^{1/2}$. Therefore, Eq. (2.17) governs the values admitted by t_{BA}, t_{BC}, t^{-}_{AC} and t^{+}_{AC} for all strains applied in Lieb and Kagome lattices.[5]

For unstrained case, it is evident that Eq. (2.17) becomes

$$t_{ij} = te^{-n\left(a_{ij}/a_0 - 1\right)} a_0/a_{ij}. \tag{2.18}$$

As previously mentioned, we shall also investigate the hypothetical case of strain (Sec. 2.9), in which one assumes that the strain changes the position of the lattice sites, obeying the Eq. (2.6), but it does not modify the values of hopping parameters that are characteristic of the unstrained lattice. Thus, in this hypothetical case the hopping values are given by Eq. (2.18) instead of Eq. (2.17).

The hopping normalization assumed here, Eq. (2.17), is different from those used by Jiang *et al.* (2019a), Jiang *et al.* (2019c), Lima *et al.* (2019a) Cui *et al.* (2020) and Lim *et al.* (2020), which are expressed as follows

$$t'_{ij} = te^{-n\left(a'_{ij}/a_0 - 1\right)}, \qquad n = 8. \tag{2.19}$$

Essentially, in our model, we add a dimensionless multiplicative term a_0/a_{ij} in Eq. (2.19), aiming to ensure the study of deformations that contract the material, *i.e.* compression ($\varepsilon < 0$), and, in turn, that are theoretically inconsistent by using Eq. (2.19). For example, in the case when a_{ij} tends to zero, the hopping value must tend to infinity, which is ensured by Eq. (2.17), but not by Eq. (2.19). Despite this, one can verify that Eqs. (2.17) and (2.19) provide very close hopping values for small deformations. To check it, let us Taylor expand Eqs. (2.17) and (2.19), such as

$$t'_{ij}/t = 1 + \Delta^{(1)}_{ij} + \Delta^{(2)}_{ij} + \mathbb{O}(\varepsilon^3), \tag{2.20}$$

where $\Delta^{(1)}_n$ and $\Delta^{(2)}_n$ are the first and second-order terms in the strain, respectively. To find these contributions, one replaces $a'_{ij} = [(\mathbb{I} + \overline{\varepsilon})\mathbf{a}_{ij} \cdot (\mathbb{I} + \overline{\varepsilon})\mathbf{a}_{ij}]^{1/2}$ into Eqs. (2.17) and (2.19). One ends up with the following terms for Eq. (2.19)

$$\Delta^{(1)}_{ij} = -\frac{n}{a_0^2}\mathbf{a}_{ij} \cdot \overline{\varepsilon}\mathbf{a}_{ij}, \tag{2.21a}$$

$$\Delta^{(2)}_{ij} = -\frac{n}{2a_0^2}|\overline{\varepsilon}\mathbf{a}_{ij}|^2 + \frac{n(n+1)}{a_0^4}\left(\mathbf{a}_{ij} \cdot \overline{\varepsilon}\mathbf{a}_{ij}\right)^2, \tag{2.21b}$$

[5] In this chapter, we will apply strain to the particular cases of Lieb and Kagome lattices, using the transition lattice to explain some effects on the energy spectrum of strained Lieb and Kagome lattices. In Ch. 3 and 4, with the aim of investigating TPT and edge states, we will apply the six types of strain also to transition lattices.

Figure 19 – Band structures along the high symmetry path $\mathbf{\Gamma}-\mathbf{X}-\mathbf{K}-\mathbf{M}-\mathbf{\Gamma}$ in BZ of: (a) the Lieb lattice ($\theta=\pi/2$), (b) the transition lattice ($\theta=7\pi/12$), and (c) the Kagome lattice ($\theta=2\pi/3$), for different parameter n in Eq. (2.18) related to the hopping energy. Results for $n=1$, $n=4$, and $n=8$ are shown in dotted blue, dashed red, and solid black lines, respectively.

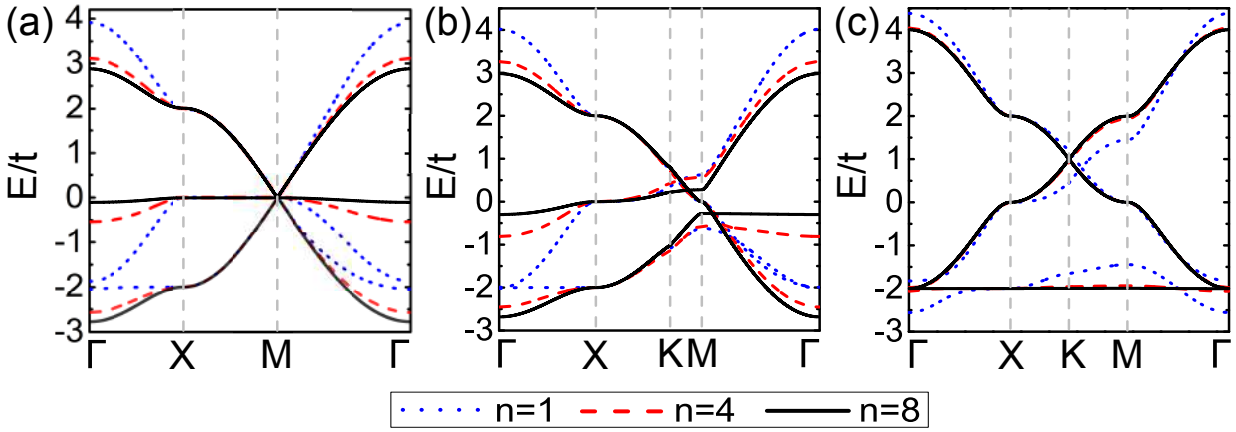

Source: The author Lima *et al.* (2023).

and, similarly by performing the same procedure, one obtains for Eq. (2.17) that

$$\Delta_{ij}^{(1)} = -\frac{n}{a_0^2}\mathbf{a}_{ij}\cdot\bar{\varepsilon}\mathbf{a}_{ij} - \frac{1}{a_0^2}\mathbf{a}_{ij}\cdot\bar{\varepsilon}\mathbf{a}_{ij}, \tag{2.22a}$$

$$\Delta_{ij}^{(2)} = -\frac{n}{2a_0^2}|\bar{\varepsilon}\mathbf{a}_{ij}|^2 + \frac{n(n+1)}{a_0^4}\left(\mathbf{a}_{ij}\cdot\bar{\varepsilon}\mathbf{a}_{ij}\right)^2 - \frac{1}{2a_0^2}|\bar{\varepsilon}\mathbf{a}_{ij}|^2 + \frac{3+2n}{a_0^4}\left(\mathbf{a}_{ij}\cdot\bar{\varepsilon}\mathbf{a}_{ij}\right)^2. \tag{2.22b}$$

By comparing Eqs. (2.22) and (2.21), one notices that the resulting hoppings, obtained by replacing them into Eq. (2.20), are not the same, since both first and second order terms have additional contributions for the hopping case of Eq. (2.17). Although they result in very close values for small deformations, our proposed theoretical model for the renormalized hoppings shows to be more appropriate and not limited to a specific deformation.

2.6 Choice of the n-parameter

Let us now discuss the effects of the parameter n, related to the hopping present in Eq. (2.17), on the energy spectrum of the Lieb-Kagome lattices. According to Eq. (2.17), one can see that the parameter n, at the exponential exponent, dictates how fast the interaction between connected atomic sites decays as a function of the interatomic distance. In order to discuss its effects, we show in Fig. 19 a comparison between the energy bands calculated by taking the parameter $n=1$ (dotted blue curves), $n=4$ (dashed red curves), and $n=8$ (solid black curves), along the high symmetry points of (a) Lieb lattice ($\theta=\pi/2$), (b) transition lattice ($\theta=7\pi/12$) and (c) Kagome lattice ($\theta=2\pi/3$). For a better visualization of how the n-changing affects individually each energy band of the spectrum, one depicts in Fig. 20 the isoenergy curves of

the upper (bottom panels), middle (middle panels) and lower (top panels) bands for (a - left panels) Lieb, (b - middle panels) transition, and (c - right panels) Kagome lattices. Before performing such discussion, let us briefly recall, as reported by Jiang *et al.* (2019c), the behavior of the energy spectrum during the interconversion process between the Lieb and Kagome lattices, showing the well-known coexistence of Dirac bands and nearly-flat bands in the energy spectra of Lieb and Kagome lattices and the energetic location of the nearly-flat band on the spectrum.

Comparing the spectra obtained for $n = 8$ in Fig. 19, one notices that when the angle θ varies from $\pi/2$ [Fig. 19 (a)] to $2\pi/3$ [Fig. 19 (c)], the bands evolve in such a way that the spectrum of Lieb lattice with a nearly-flat band, located at the middle of the band structure, deforms until it forms a nearly-flat band located at the bottom (top) of the energy spectrum in Kagome lattice for the hopping case of $t > 0$ ($t < 0$) (JIANG *et al.*, 2019c). Moreover, the triply degenerate Dirac point (at **M** point) in Lieb lattice transforms into two double-degenerate Dirac points, one of them moving along the $\mathbf{M} - \mathbf{\Gamma}$ direction and the another one moves along the $\mathbf{M} - \mathbf{K}/\mathbf{K}'$ direction, forming the energy band of Kagome lattice. The Dirac cones in the transition stages, *i.e.* for $\pi/2 < \theta < 2\pi/3$, are strongly tilted, showing coexistence of type-I Dirac points, referring to the connection between the middle band and the upper band, and type-II, characterized by the connection between the middle and lower bands, as already discussed by Jiang *et al.* (2019c) and Lim *et al.* (2020).

From Eq. (2.17), it is seen that the hopping energy decreases as the value of the n-parameter increases. Thus, the n-parameter governs the range of the interactions between the atomic sites. That is, the effects of more distant sites are suppressed for $n \geq 8$, and intensified for $n < 8$. Figs. 19 and 20 show that for $n = 8$ the energy bands give a good approximation of the characteristic of the Lieb and Kagome lattices within the NN TB model, since they present almost nearly-flat bands and Dirac cones, as expected for such structures (JIANG *et al.*, 2019c).

From Figs. 19 (a) and 20 (a) for Lieb lattice, one can see that a reduction of the value of n alters the energy dispersion curves by deforming the nearly-flat band, bringing the middle band closer to the lower band at the $\mathbf{\Gamma}$-point, with the energy dispersion along the **X**-**M** remaining unchanged, as well as the triply degenerate Dirac point remaining located at **M**. The latter is due to the NNN sites to be distributed in such a way that the changes in the hopping parameters, resulting from the change of n, can be seen in an equivalent way as a biaxial and symmetric diagonal deformation, maintaining the symmetry of the level curves and changing only the spectrum in the direction of the energy axis. The effects on the energy spectrum of

Figure 20 – Isoenergy curves of the upper, middle, and lower bands (from bottom to top panels) of: (a) the Lieb lattice ($\theta = \pi/2$), (b) the transition lattice ($\pi/2 < \theta < 2\pi/3$), and (c) the Kagome lattice ($\theta = 2\pi/3$), for different parameter n in Eq. (2.18) related to the unstrained hopping energy. Results for $n = 1$, $n = 4$, and $n = 8$ are shown in dotted blue, dashed red, and solid black lines, respectively.

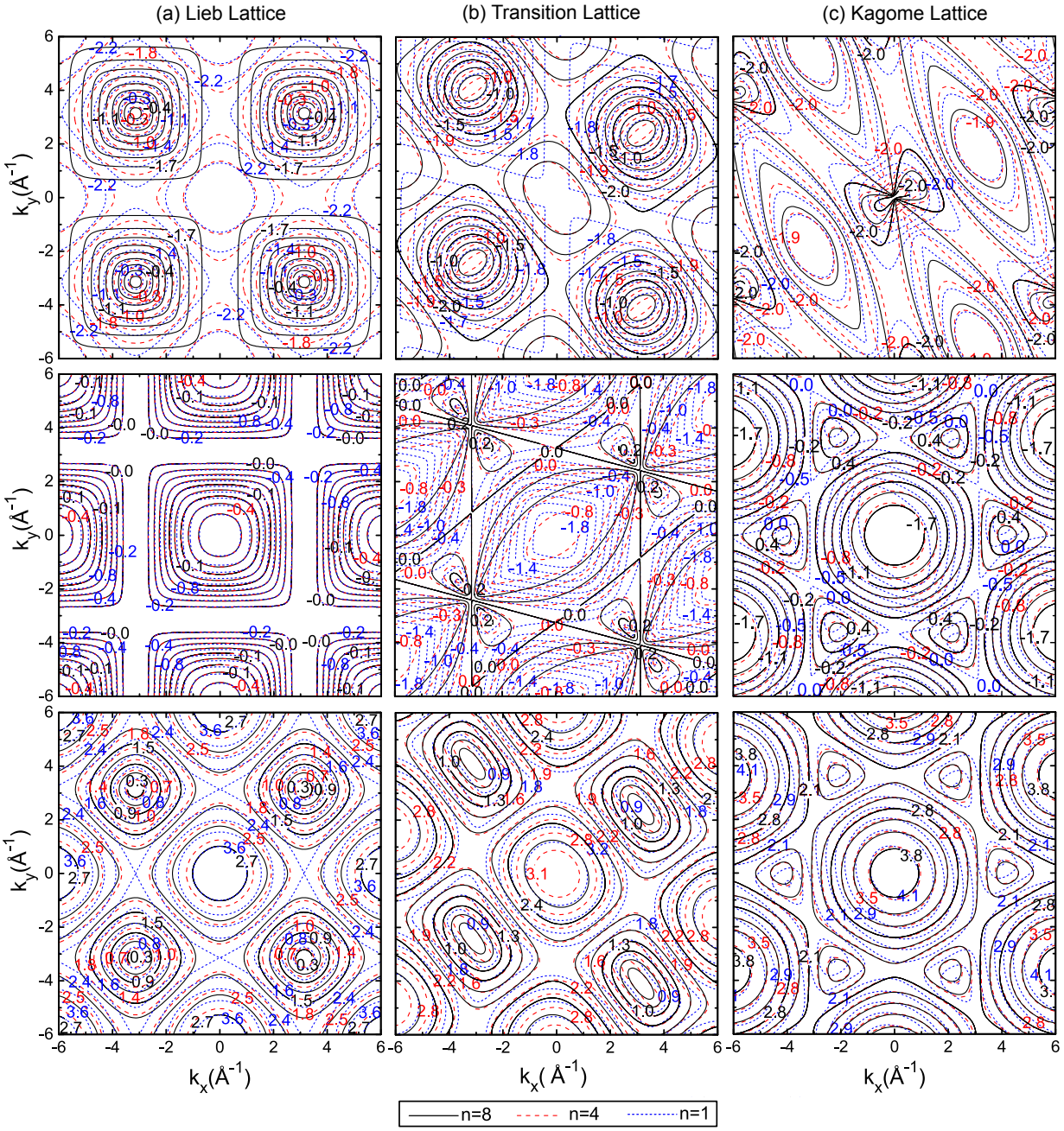

Source: The author Lima *et al.* (2023).

transition lattices are shown in Figs. 19 (b) and 20 (b), in which one can also find diagonal-like strain effects in the reciprocal lattice resulting from the modification of the n-parameter. For the Kagome lattice, Figs. 19 (c) and 20 (c) show that the nearly-flat band is also deformed by decreasing the n-parameter, but now the Dirac point does not keep the same position in reciprocal space coinciding with the **K**-point, but rather it moves along the **K**-**M** direction. Moreover,

for the Kagome lattice, the variation of the n-parameter causes a break of degeneracy at the $\mathbf{\Gamma}$-point between the lower and middle bands. This is because of the fact that the NNN sites in the Kagome lattice, corresponding to non-equivalent sites, are not symmetrically distributed around the NN sites. In fact, they are located diagonally, so that $n < 8$ makes the hopping intensities of the NNN to be more and more expressive, causing diagonal-like strain effects in the Kagome energy spectrum. In addition, we notice a false energy gap in $\mathbf{\Gamma}$-point, as well as a false asymmetry of $\mathbf{X}-\mathbf{K}$ and $\mathbf{K}-\mathbf{M}$.[6] Note that a change in the hopping energies does not change the reciprocal space and the location of the high symmetry points since the real lattice is not changed (ASCROFT; MERMIM, 1976). Thus, for $n < 8$ the energy spectrum is modified so that the position of the Dirac cones is not found along the path $\mathbf{\Gamma}-\mathbf{X}-\mathbf{K}-\mathbf{M}-\mathbf{\Gamma}$ (see the position of the cones moving by comparing the middle and bottom panels of the isoenergy curves in Figs. 20 (c)).

Such results encourage us in the seek to understand the effects of strain in reciprocal space, resulting from the real space deformation, whether the hopping parameter is changed or not. Thus, in the next section, we shall apply uniaxial and biaxial strains, and pure and simple shear strains to Lieb, transition, and Kagome lattices.

[6] In fact, in Fig. 19 (c), for $n < 8$, there is a separation between the lower band and the middle band at the $\mathbf{\Gamma}$-point. However, this occurs because the zero-gap point between these bands is no longer at the $\mathbf{\Gamma}$-point. In other words, we have a false energy gap at the $\mathbf{\Gamma}$-point because there is no gap between the bands for all values of $\mathbf{k}$. Similarly, the asymmetry between the paths $\mathbf{X}-\mathbf{K}$ and $\mathbf{K}-\mathbf{M}$ does not indicate an asymmetry between the $\mathbf{k}$-point of the Dirac cone and the midpoint between two Dirac points, which indeed remains symmetric as seen in Fig. 20 (c).

Figure 21 – Band structures along the high symmetry path $\mathbf{\Gamma}-\mathbf{X}-\mathbf{M}-\mathbf{Y}-\mathbf{\Gamma}$ in the BZ of Lieb lattice submitted to (a) UX and (b) UY strains for different strain amplitudes: $\varepsilon = 0.0$ (solid black), $\varepsilon = 0.1$ (dashed blue), $\varepsilon = 0.7$ (dotted red). Vertical gray lines with their respective line styles linked to the ε-value indicate the position of the high symmetry points for $\varepsilon = 0.0$ (solid), $\varepsilon = 0.1$ (dashed) and $\varepsilon = 0.7$ (dotted).

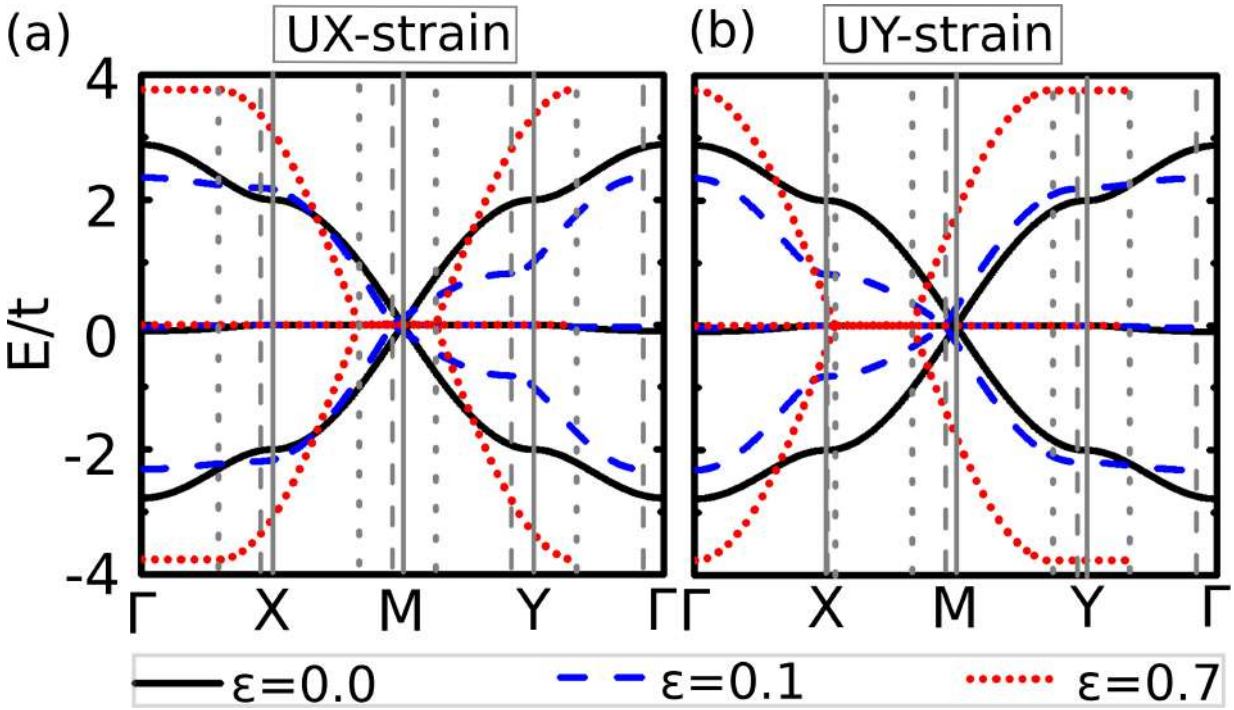

Source: The author Lima *et al.* (2023).

2.7 Strained Lieb lattice

In Fig. 21 (a) [21 (b)] we represent the dispersion relation along the path that connects the high symmetry points $\mathbf{\Gamma}-\mathbf{X}-\mathbf{M}-\mathbf{Y} = \mathbf{b}_2/2-\mathbf{\Gamma}$ in the reciprocal space of Lieb lattice subject to UX-strain [UY-strain] for different strain amplitudes. The isoenergy curves of the upper (right panels), middle (middle panels), and lower (left panels) bands corresponding to these energy spectra are shown in Figs. 22 and 23 for UX-strain and UY-strain, respectively.

Note that even with the strain application, the electron-hole symmetry is nearly preserved. By varying the ε-parameter, one notices that if $\varepsilon > 0$ ($\varepsilon < 0$) the Dirac cones approach (move away) the $\mathbf{M}-\mathbf{Y}$ direction, *i.e.* along the $\mathbf{k}_x$ direction (Fig. 22), and the $\mathbf{X}-\mathbf{M}$ direction, *i.e.* along the $\mathbf{k}_y$ direction (Fig. 23), for UX-strain and UY-strain cases, respectively. As seen in Figs. 21 (a) and 21 (b), such uniaxial strains do not cause an energy gap opening, regardless of the application direction. Instead of the appearance of an energy gap, as shown in strained graphene (PEREIRA *et al.*, 2009), the Lieb lattice under uniaxial strain presents the formation of a triply degenerate linear band, *i.e.* a Dirac line, at the Fermi level along the $\mathbf{M}-\mathbf{Y}$ direction for UX-strain case and along the $\mathbf{X}-\mathbf{M}$ direction for UY-strain case, as shown by

the red dashed curves in Figs. 21 (a) and 21 (b), respectively. It also can be verified in the fifth row (for $\varepsilon = 0.3$) of contour plots in Fig. 22 and in Fig. 24 (d) for the UX-strain case, and in the first row (for $\varepsilon = -0.3$) of contour plots in Fig. 23 in the UY-strain case. Thus, one has the presence of type-III Dirac point (critically tilted), that combines nearly-flat band and linear dispersion, similar to cones emerging from flat bands in photonic orbital graphene (MILIĆEVIĆ *et al.*, 2019). This triply degenerate Dirac strain-induced line state, *i.e.*, triply degenerate nodal line (LIU *et al.*, 2021), is formed by the approach (separation) of the Dirac cones, which is accompanied by a small decrease (increase) in the separation and curvature of the upper and lower energy bands in the energetic line that connects the cones along the k_x (k_y) direction, for a fixed k_y (k_x), near the BZ boundaries for the UX-strain (UY-strain) cases. This trend of the triply degenerate linear band formation can be noticed by comparing panels (b), (c), and (d) in Fig. 24 for the UX-strain case. This evolution of the UX (UY)-strain-induced band deformation increases the energetic distances between the upper and lower bands along the k_y (k_x) direction, for a fixed k_x (k_y) value, reaching the larger value at the $\mathbf{\Gamma}$-point.

As expected, the dispersion relations in Fig. 22 (Fig. 23) are compressed (extended) along the k_x (k_y) direction, by taking UX (UY)-strain amplitudes with positive $\varepsilon > 0$ and oppositely for negative $\varepsilon < 0$ values. In addition, one notices small band distortions along the k_y (k_x) direction due to the considered Poisson ratio, as a less expressive response in the opposite applied strain direction. The consequence of these effects is the flattening of the cones along the k_y (k_x) direction, such that they no longer exhibit circular isoenergy curves, but rather has approximately elliptical shape [see second and fourth panel rows of the contour plots in Fig. 22 (Fig. 23) for lower and top bands, respectively, for UX (UY)-strain case]. This leads to anisotropic Fermi velocities, resulting in anisotropic transport properties that may be relevant to direction-dependent electronic transport devices in a similar way to 2D anisotropic semiconductors such as phosphorene (LI *et al.*, 2014b). It is worth mentioning that an equivalent direct analysis between the results under UX-strain and UY-strain cases can be easily achieved by taking the following transformation $\mathbf{k}_x \to \mathbf{k}_y$ and $x \to y$ for the reciprocal and real spaces, respectively. This is due to the fact that Lieb lattice obeys $\hat{D}_{4h}$-symmetry. Therefore, compression ($\varepsilon < 0$) and extension ($\varepsilon > 0$) for UX-strain can be mapped by extension and compression, respectively, for UY-strain case. This statement can be verified by the correspondence between the panels of the following rows: $1_{UX} \longleftrightarrow 5_{UY}$, $2_{UX} \longleftrightarrow 4_{UY}$, $4_{UX} \longleftrightarrow 2_{UY}$, and $5_{UX} \longleftrightarrow 1_{UY}$ for Fig. 22$\longleftrightarrow$Fig. 23.

In order to verify additive effects due to the combination of uniaxial strains along

x and y directions, viewed as biaxial deformations, Fig. 25 shows the band structures of Lieb lattice under BI-strain for the same strain amplitudes adopted in Figs. 22 and 23. Regardless of the strain amplitude, it is seen in Fig. 25 that the bands' curvatures and their aspect ratios in $\mathbf{k}$-space are kept undeformed, keeping the circular symmetry of the contour lines close to the Fermi level, which indicates that the Fermi velocity remains isotropic under BI-strain. This is easily understood, given that the high symmetry points are also shifted uniformly in both directions in the BI-strain, as a consequence of the modules increase (decrease) of the two lattice vectors for extension $\varepsilon > 0$ (compression $\varepsilon < 0$), leading to the modules reduction (increasing) of the two reciprocal lattice vectors and also to a smaller (larger) first square BZ.

Let us now analyze the energy spectrum of Lieb lattice subjected to shear strain. For SX-strain, Fig. 26 shows that the triply degenerate Dirac point at Fermi energy level in the vicinity of the M-point gives place to two pairs of doubly degenerated Dirac points. The larger the strain amplitude, the more noticeable is the formation of these two pairs of doubly degenerate Dirac points, which arises from the deformation of the nearly-flat band, without a band gap opening, adjusting itself to touch a pair of points in the upper energy band and a pair of points in the lower energy band. This is clearly shown in the 3D plots of Figs. 28 (a) and 28 (b) and through the bands' evolution in Fig. 26. The evolution of the BZ distortion (white dashed line) is shown as the ε-value increases. Moreover, the connecting energetic lines, between the pair of double degenerate points in the upper bands and in the lower bands, that are initially perpendicular in $\mathbf{k}$-space, for high ε-values tend to be aligned in $\mathbf{k}$-space and these double Dirac points move away from each other. This can be clearly seen in Figs. 28 (c) and 28 (d) for $\varepsilon = 0.5$. From these results (Figs. 26 and 28), it becomes evident that the nearly-flat band plays an important role, as it deforms, creating four Dirac points that do not allow the band gap opening. Lim *et al.* (2020) explores the emergence of Dirac points from nearly-flat bands in generic lattices of Lieb and Kagome during their interconversibility process. This can be understood in view of the fact that diagonal deformations inherent to the interconversion process result in structures that can be achieved with a combination of shear and uniaxial deformations.

Figure 22 – Contour plots of the lower (left panels), middle (middle panels), and top (right panels) energy bands for Lieb lattice under UX-strain for different strain amplitudes: $\varepsilon = -0.3,\ -0.1,\ 0.0,\ 0.1,\ 0.3$ from top to bottom panels.

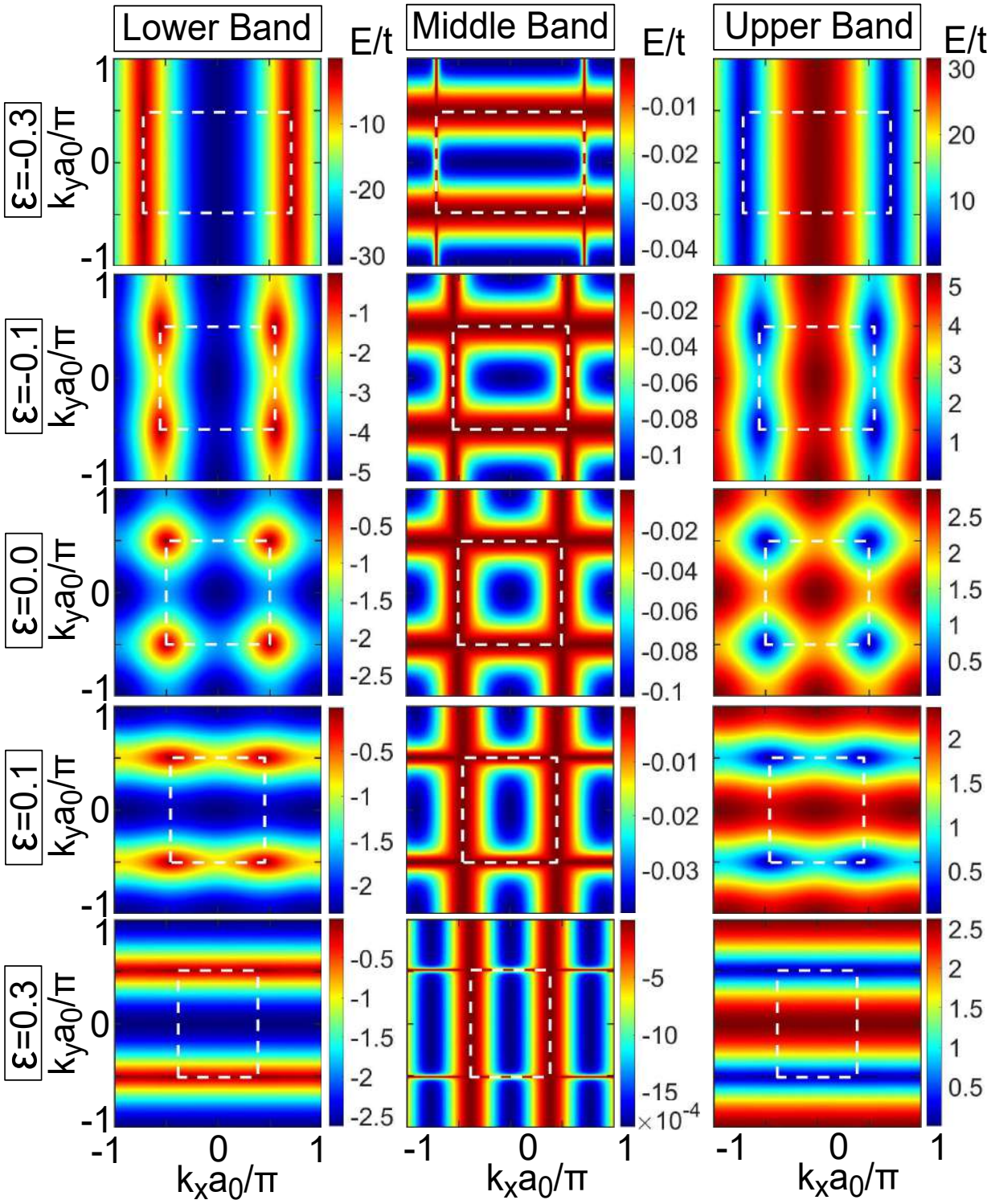

Source: The author Lima *et al.* (2023).

Figure 23 – The same as in Fig. 22, but now for the Lieb lattice under UY-strain.

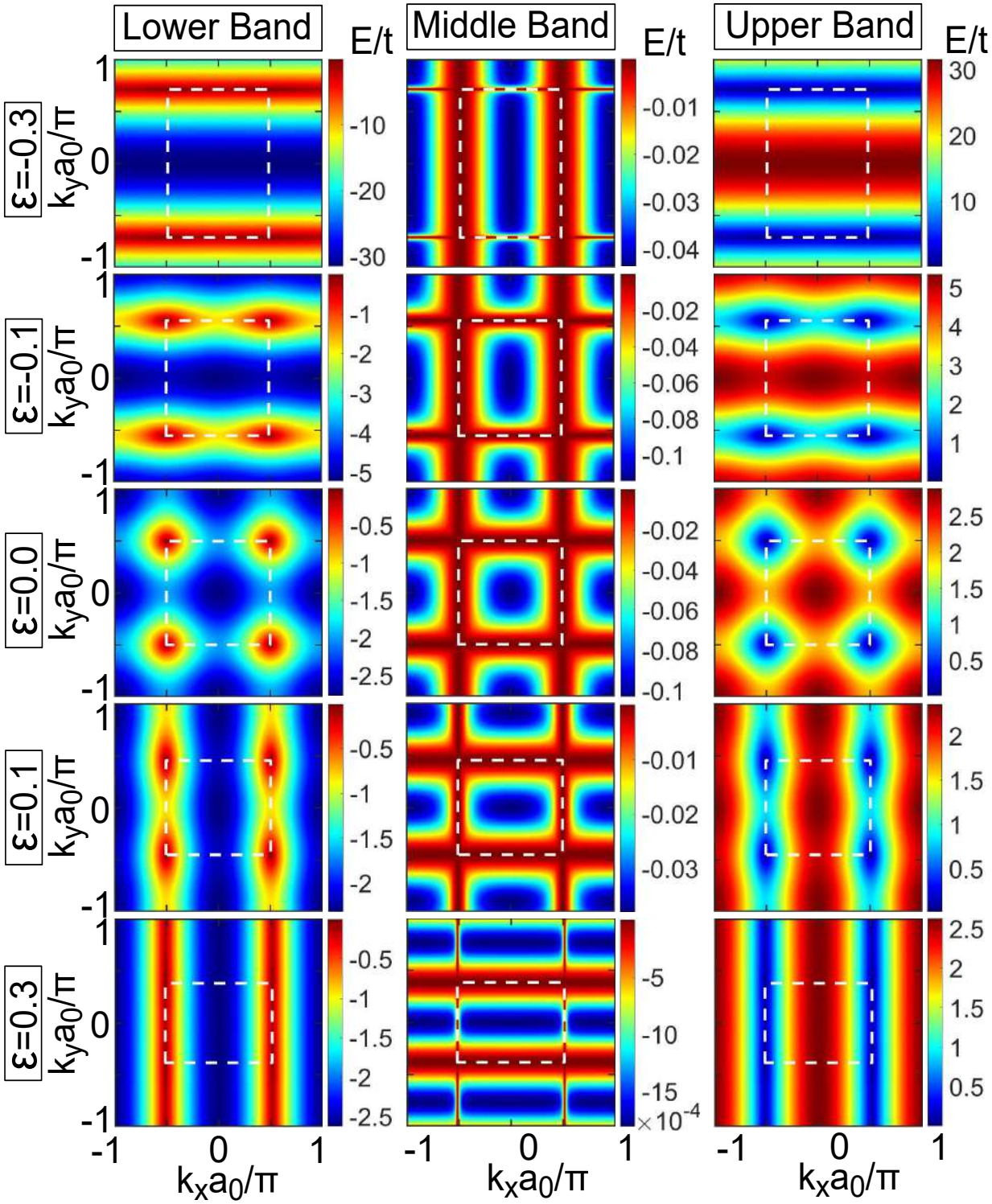

Source: The author Lima *et al.* (2023).

Figure 24 – 3D plots of the band structures for the Lieb lattice under UX-strain for (a) $\varepsilon = -0.1$, (b) $\varepsilon = 0.1$, (c) $\varepsilon = 0.3$, and (d) $\varepsilon = 0.7$, in order to emphasize the strain-induced formation of the triply degenerate linear state.

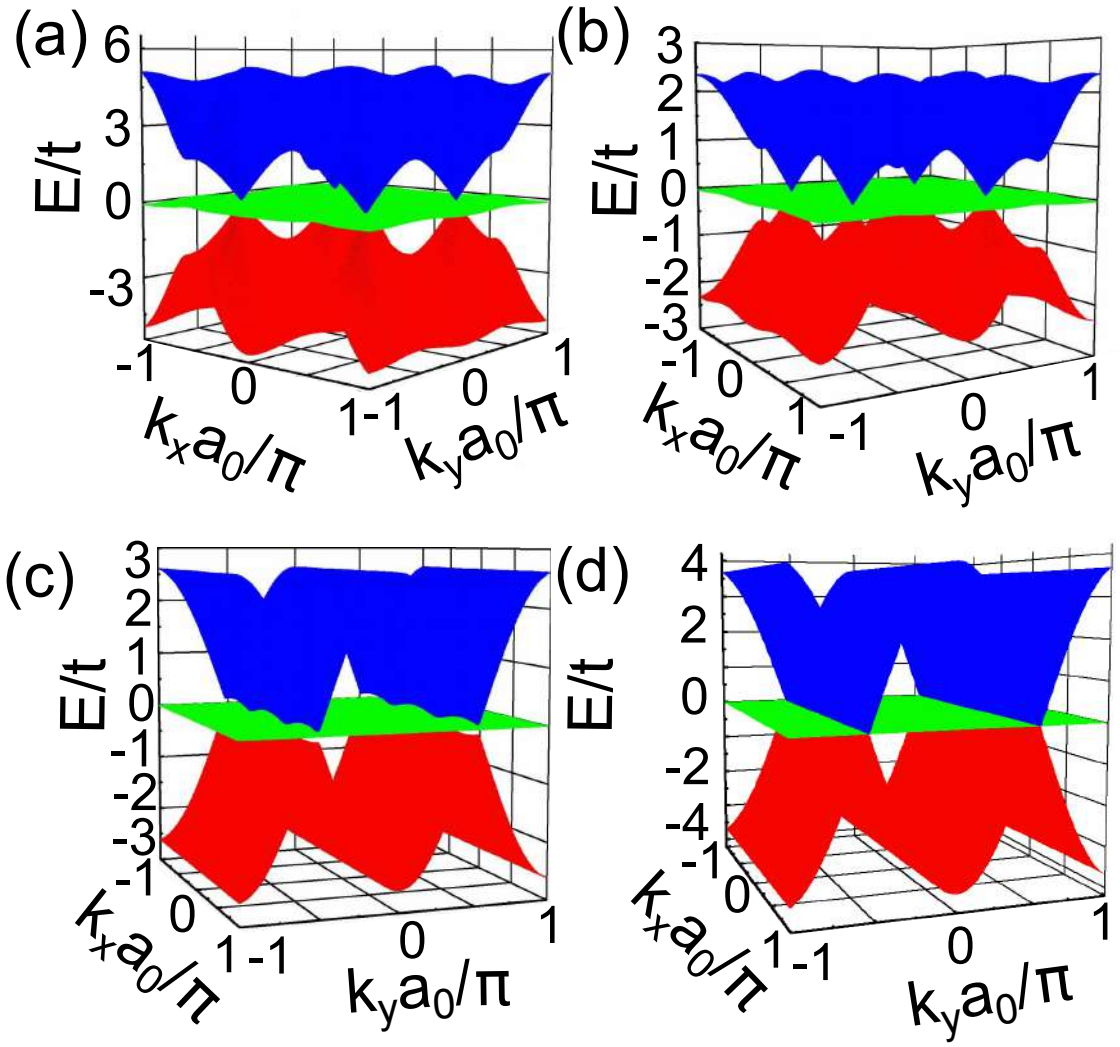

Source: The author Lima *et al.* (2023).

Figure 25 – The same as in Fig. 22, but now for the Lieb lattice under BI-strain.

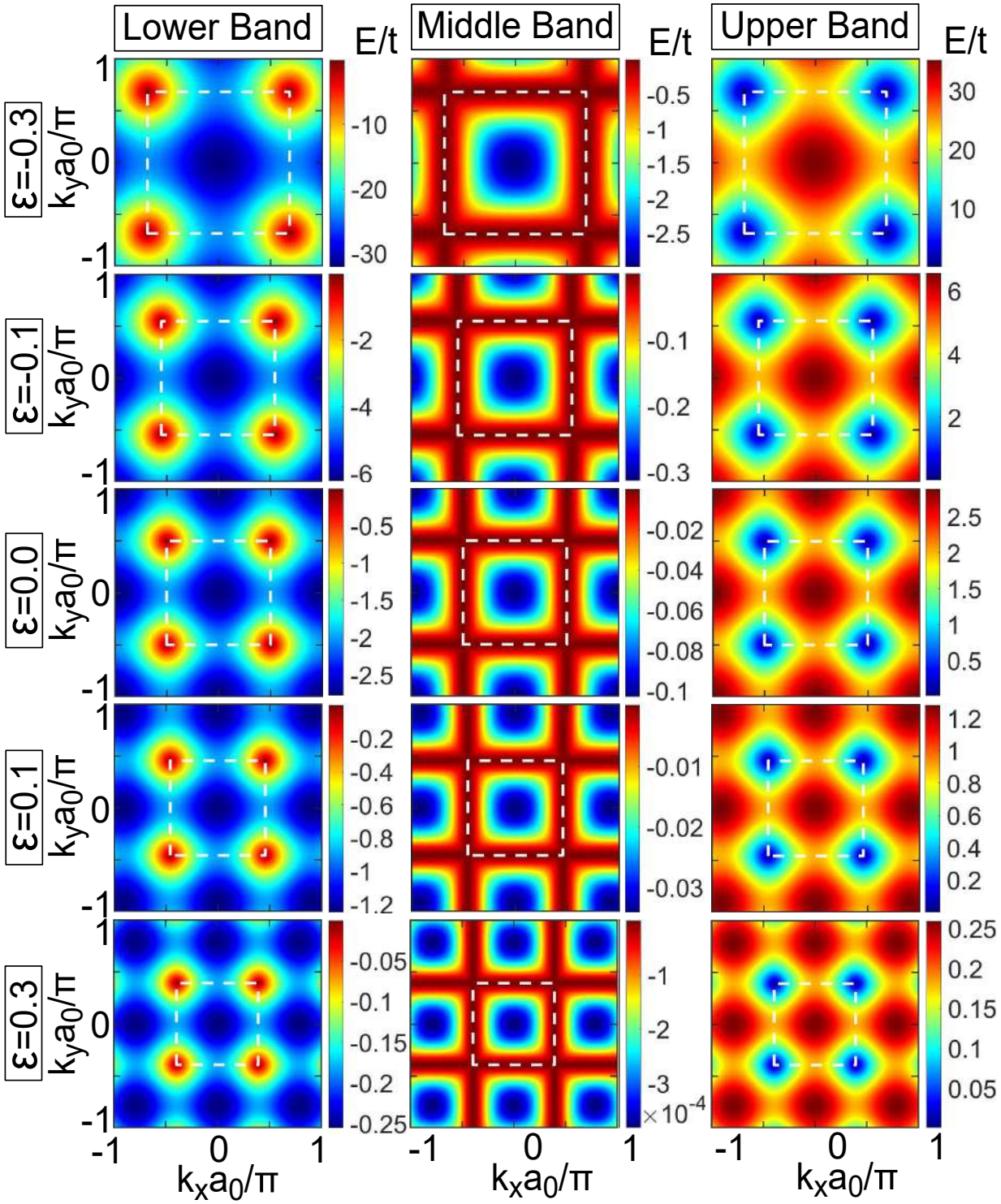

Source: The author Lima *et al.* (2023).

Figure 26 – The same as in Fig. 22, but now for the Lieb lattice under SX-strain and assuming the following order of the strain amplitudes: $\varepsilon = -0.7, -0.5, -0.3, -0.1, 0.0, 0.1, 0.3, 0.5, 0.7$ from top to bottom panels. The strain cases with $\varepsilon > 0$ and $\varepsilon < 0$ are enantiomorphs in absolute values of ε.

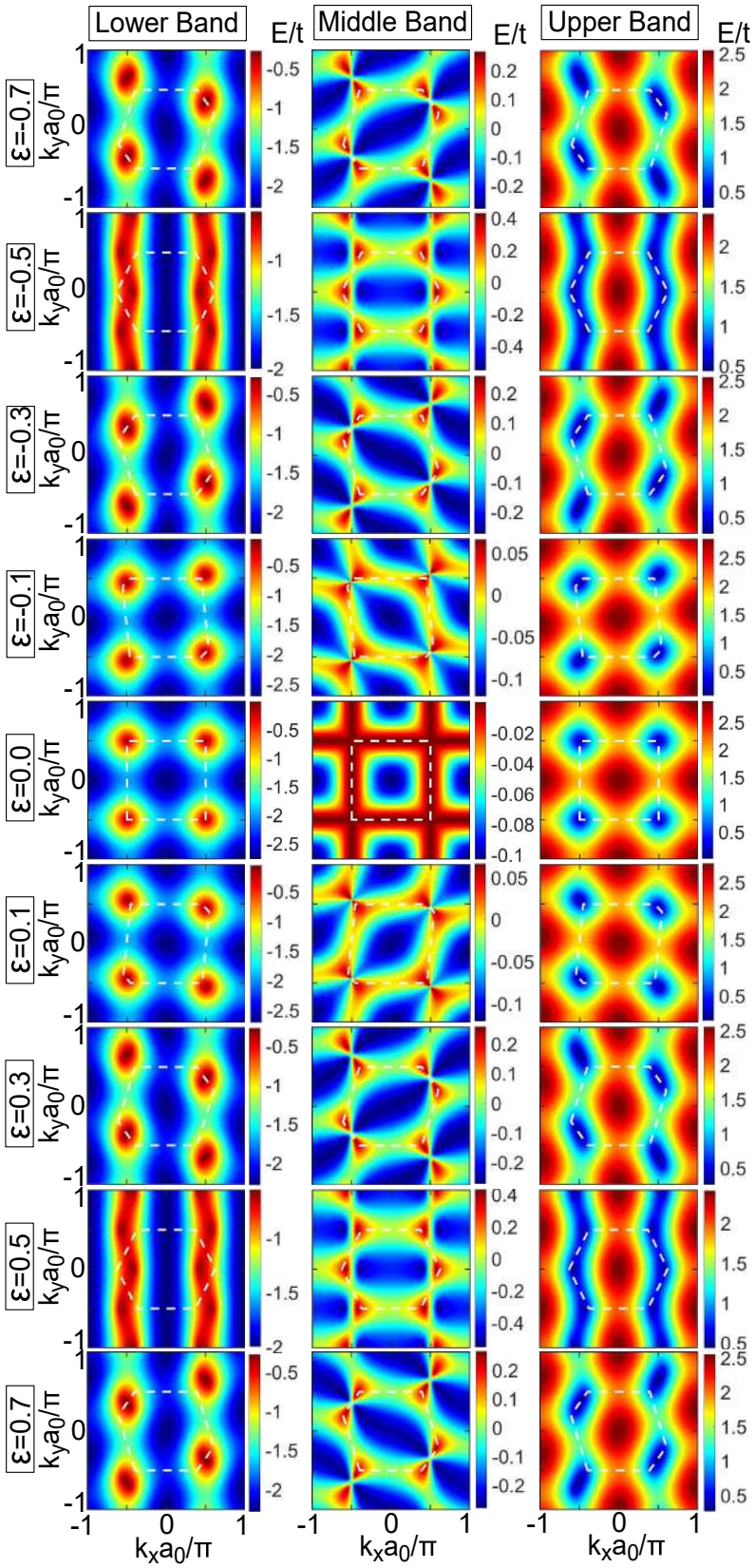

Source: The author Lima *et al.* (2023).

Figure 27 – The same as in Fig. 26, but now for the Lieb lattice under SY-strain.

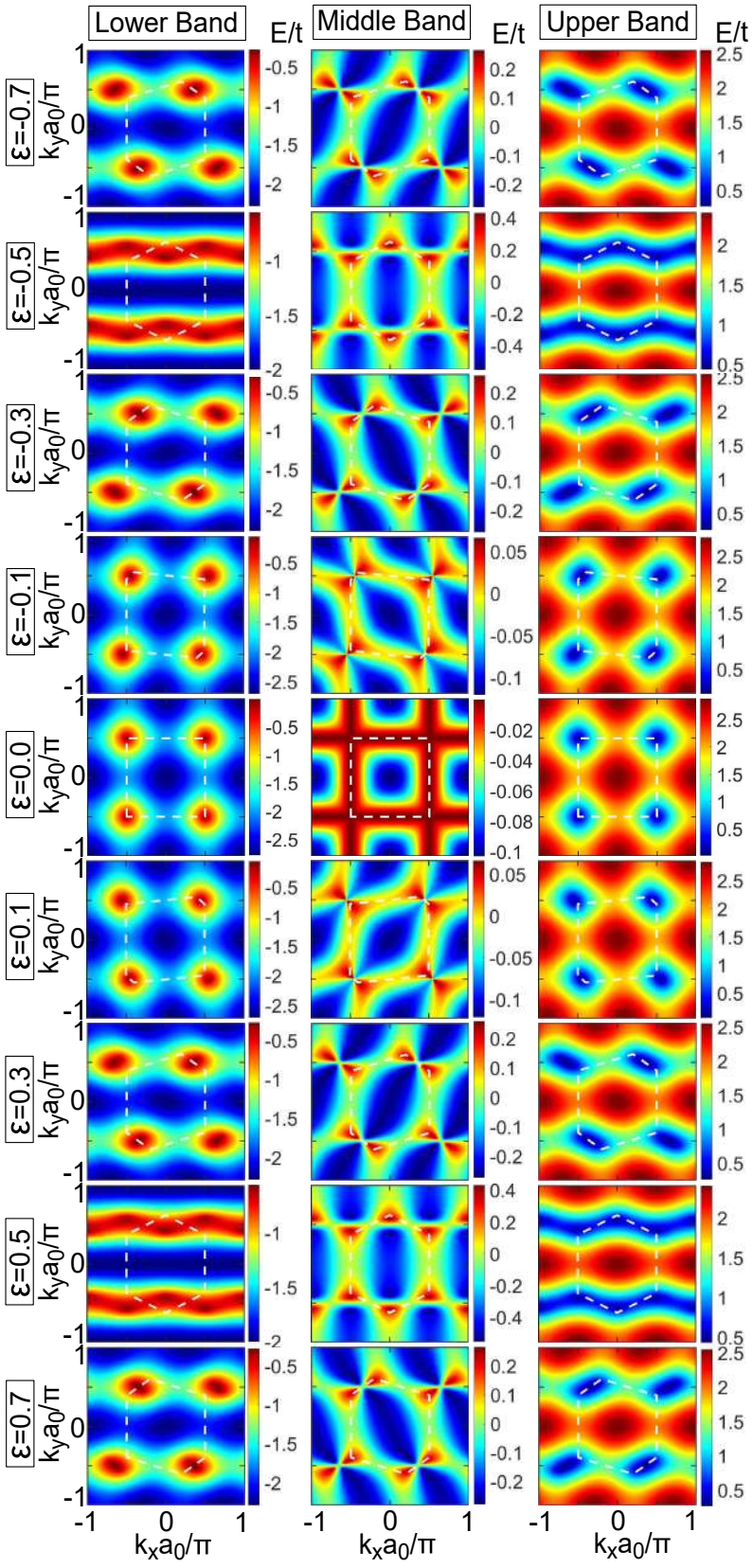

Source: The author Lima *et al.* (2023).

Figure 28 – 3D plots of the band structures for the Lieb lattice under SX-strain for (a, b) $\varepsilon = 0.3$ and (c, d) $\varepsilon = 0.5$. An enlargement at the vicinity of the Fermi energy level for panels (a) and (c) are shown in panels (b) and (d), respectively, in order to emphasize the deformation of the nearly-flat band, emerging two pairs of doubly degenerate points to appear in place of a triply degenerate point, and the absence of the energy gap opening in such spectra.

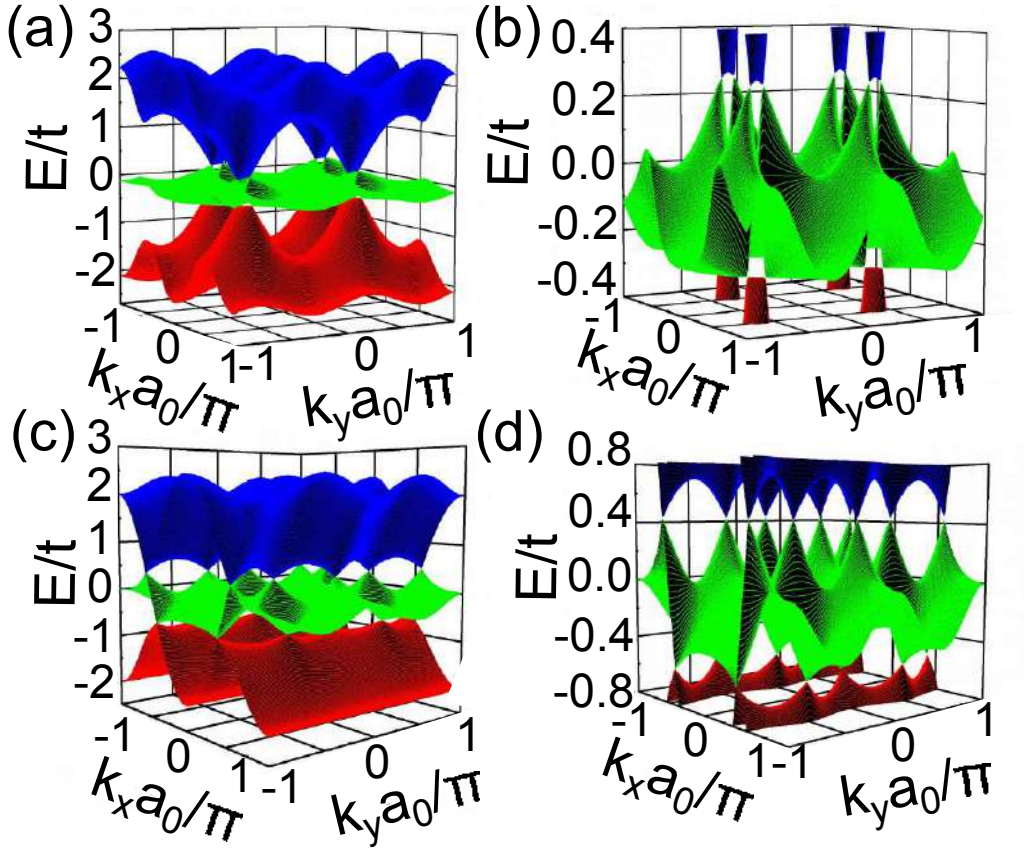

Source: The author Lima *et al.* (2023).

A particular observation can be noticed on the SX-strained case for $\varepsilon = 0.5$ [Figs. 28 (c) and 28 (d)]. For this strain amplitude, the x components of the vectors that locate the A sites in relation to the B sites have exactly half of the distance value that separates the $B-C$ sites. However, perhaps as expected by the analysis of the triangle BAC formed by the sublattices A, B, and C, this strain situation does not lead to the case of the Kagome lattice. This is due to the fact that a simple shear strain in x-direction does not change the y-coordinate of the vector that locates A sublattice, and thus it does not form an equilateral triangle BAC, which in turn does not correspond to the spatial configuration referred to $\theta = 2\pi/3$ case. Therefore, by applying the SX-strain in the Lieb lattice with strain amplitude $\varepsilon = 0.5$, one obtains a lattice structure that resembles the Kagome lattice compressed uniaxially in x-direction, with some $\varepsilon < 0$, as indicated by the contour plots in the eighth row of Fig. 26. This result further confirms the fact that the Lieb and Kagome lattices are interconvertible under diagonal strain, as it is easy

to understand geometrically that the combination of uniaxial strain and simple shear strain can generate deformations similar to those caused by diagonal strain. Moreover, notice that for $\varepsilon > 0.5$, the inversion in the orientation of the isoenergy curves is owing to the fact that A sublattice is closer to the left of sublattice C than the right of sublattice B, generating a spatial configuration of sites that behaves like a simple shear strain with $\varepsilon < 0$, as shown in Fig. 26.

The isoenergy curves for the Lieb lattice under the effect of SY-strain are shown in Fig. 27. Similarly to the SX-strain case (Fig. 26), one notices that the energy spectra for SY-strained Lieb lattice are very similar to those ones for a diagonally strained Kagome lattice when $\varepsilon = 0.5$ (we shall return to this discussed in Sec. 2.8). Moreover, one notes the following equivalence between the results under SX-strain (Fig. 26) and SY-strain (Fig. 27): transformations in the SX-strained (SY-strained) isoenergies composed by a $\pi/2$-rotation in the $\mathbf{k}$-space combined with a compression-to-distension (or vice-verse) exchange lead to the same energetic band curves as the SY-strained (SX-strained) Lieb case with a sign change in the strain amplitude ε, *i.e.* by applying a $\hat{C}_2$ symmetry operation in the momentum space and changing $\varepsilon < 0$ by $\varepsilon > 0$ (or vice-versa), one gets the same energy spectrum for Lieb lattice with shear strain applied in the other direction. This statement can be verified by the correspondence between the panels of the following rows of Fig. 26 (SX) and Fig. 27 (SY): $1_{SX} \equiv \hat{C}_2 9_{SY}$ ($9_{SY} \equiv \hat{C}_2 1_{SX}$), $2_{SX} \equiv \hat{C}_2 8_{SY}$ ($8_{SY} \equiv \hat{C}_2 2_{SX}$), $3_{SX} \equiv \hat{C}_2 7_{SY}$ ($7_{SY} \equiv \hat{C}_2 3_{SX}$), $4_{SX} \equiv \hat{C}_2 6_{SY}$ ($6_{SY} \equiv \hat{C}_2 4_{SX}$).

Therefore, it becomes evident that the cases with $\varepsilon > 0$ and $\varepsilon < 0$ are enantiomorphs in absolute values of ε-parameter, *i.e.* they are mirror images of each other. The energy spectra being enantiomorphs are a consequence of the fact that the displacement of the sites in the simple shear are mirror images of each other for deformations caused by positive and negative values of ε-parameter. The reference line to perform the simple shear must be the same in both cases and the atoms will move on both sides of the reference line in order to form exactly deformed structures enantiomorphs.

To investigate combined effects due to simple shear strains along x and y directions, we present in Fig. 29 the band structures of Lieb lattice under PS strain for the same strain amplitudes adopted in Figs. 26 and 27. Note that, similarly to the simple shear strain cases, the original triple degenerate Dirac point of Lieb lattice is split into two doubly degenerate Dirac points. When this occurs, the lower and upper energy bands are divided into two, such that the connecting energetic lines between the upper and middle bands and middle and lower bands are always perpendicular, regardless of the applied strain amplitude. This situation is opposite to

Figure 29 – The same as in Fig. 26, but now for the Lieb lattice under PS-strain. Note that the cases for $\varepsilon > 0$ and $\varepsilon < 0$ are mirror images of each other in absolute values of the ε-parameter, or equivalently mapped on each other by $\pi/2$-rotation.

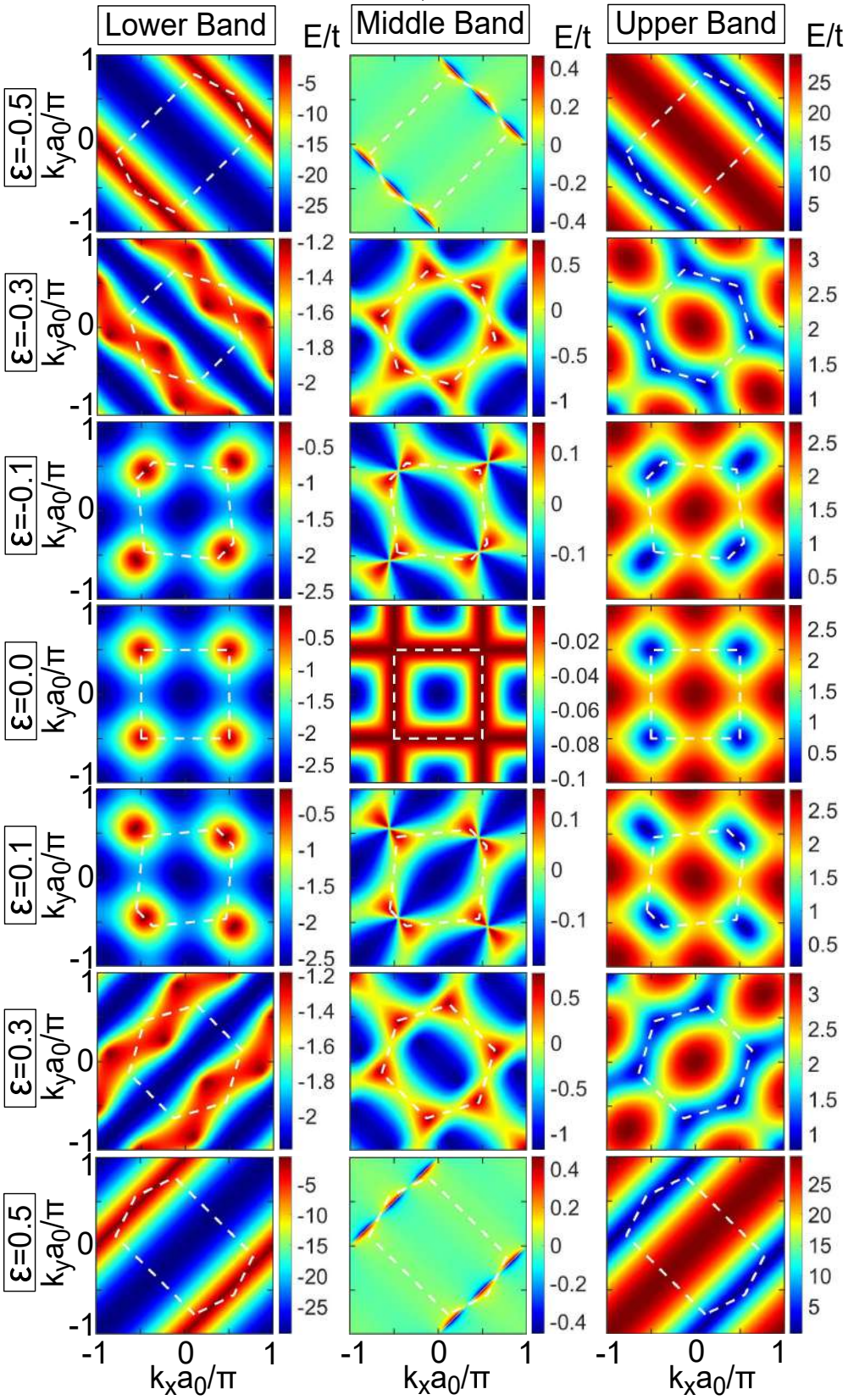

Source: The author Lima *et al.* (2023).

that discussed cases of simple shear strains, where such two energetic lines connecting the par of doubly degenerate points tend to align with each other. The case corresponding to $\varepsilon = 0.5$ ($\varepsilon = -0.5$), shown in the first (seventh) row of Fig. 29, resembles the energy spectrum of the Kagome lattice rotated by $\pi/4$ clockwise (counterclockwise) in relation to to the positive k_x-axis.

From Fig. 29, a diagonal deformation is clearly noticeable caused by the PS strain, but now without any rotation of the energy spectrum as observed for the simple shear strain cases [Figs. 26 and 27]. This can be understood by Eq. (2.9) and Table 1, which for the PS strain case one has that $\mathbf{a}'_1 = (\varepsilon a, 0)$ and $\mathbf{a}'_2 = (0, \varepsilon a)$, leading to $(\mathbf{a}'_1)_x = (\mathbf{a}'_2)_y = \varepsilon a$ and $(\mathbf{a}'_1)_y = (\mathbf{a}'_2)_x = 0$, and which consequently sets a diagonal deformation without any isoenergy curves rotation. On the other hand, the rotation of the isoenergy spectrum for simple shear strain cases occurs because, in these cases, $(\mathbf{a}'_1)_x \neq (\mathbf{a}'_2)_y$ and $(\mathbf{a}'_1)_y \neq (\mathbf{a}'_2)_x = 0$. This discussion also explains the reason why PS strain results for $\varepsilon > 0$ and $\varepsilon < 0$ are mirror images of each other in absolute values of the ε-parameter, *i.e.* they can be mapped on each other by rotations of $\pi/2$ both clockwise and counterclockwise in relation to the energy axis, what no longer occurs in simple shear strain cases whatever the deformation direction.

Figure 30 – The same as in Fig. 22, but now for the Kagome lattice under UX-strain.

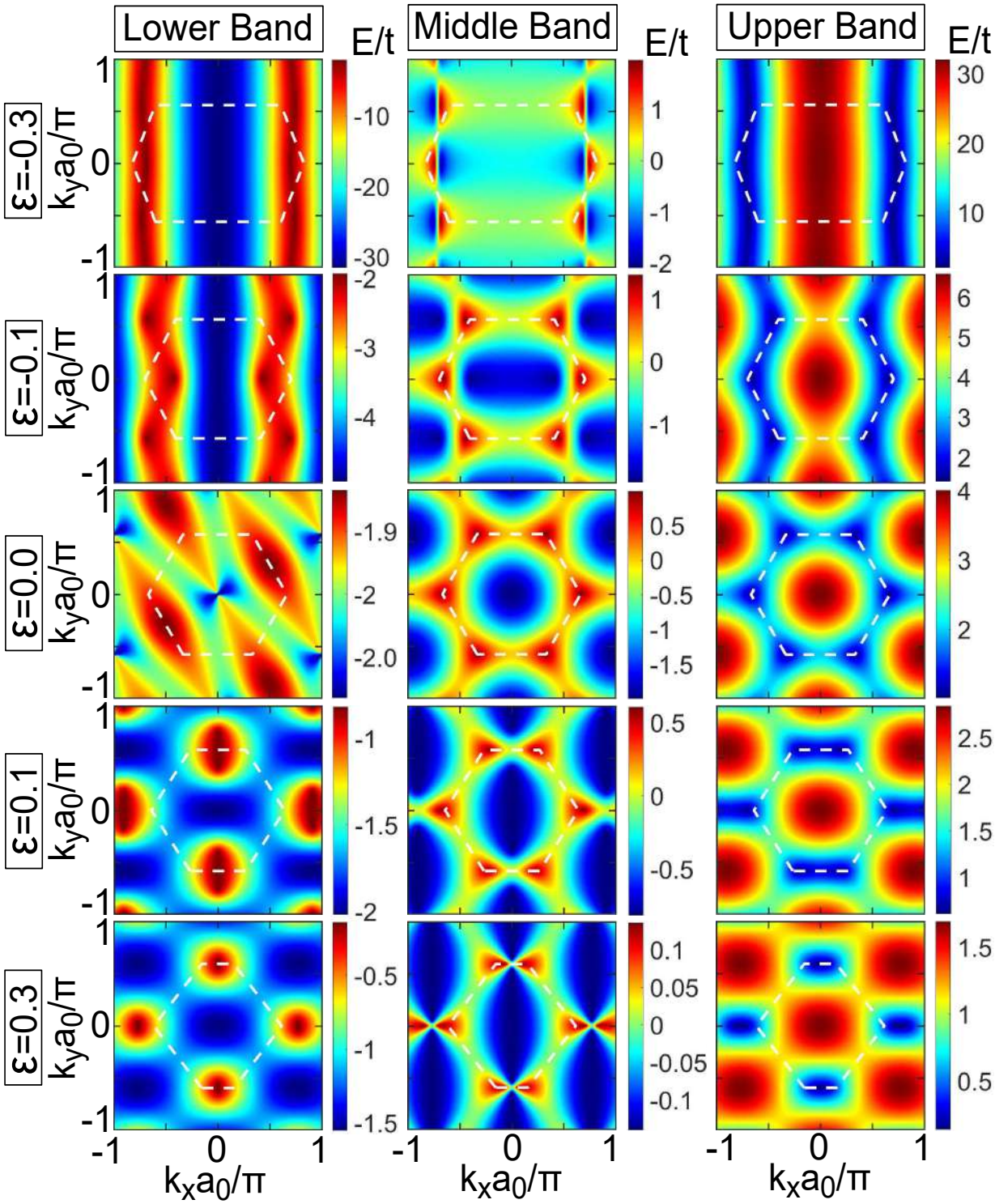

Source: The author Lima *et al.* (2023).

2.8 Strained Kagome lattice

Let us now investigate the effects of the six deformations types illustrated in Fig. 16 and given in Table 1 on the energy spectrum of Kagome lattice. Fig. 30 shows the energy spectrum of Kagome lattice under UX-strain. For $\varepsilon > 0$ (distention), the Dirac cones approach

Figure 31 – Dispersion relation of the Kagome lattice under UX-strain (a) along the k_x direction, keeping $k_y = 0$, and (b) along the k_y direction, keeping $k_x = 0$, for different strain amplitudes: $\varepsilon = 0.0$ (black solid lines), $\varepsilon = 0.1$ (blue dashed lines), $\varepsilon = 0.3$ (green dotted lines), $\varepsilon = 0.5$ (red dash-dotted lines), and $\varepsilon = 0.7$ (purple dash-double-dotted lines). The band-crossing is emphasized by circles with the same strained color lines.

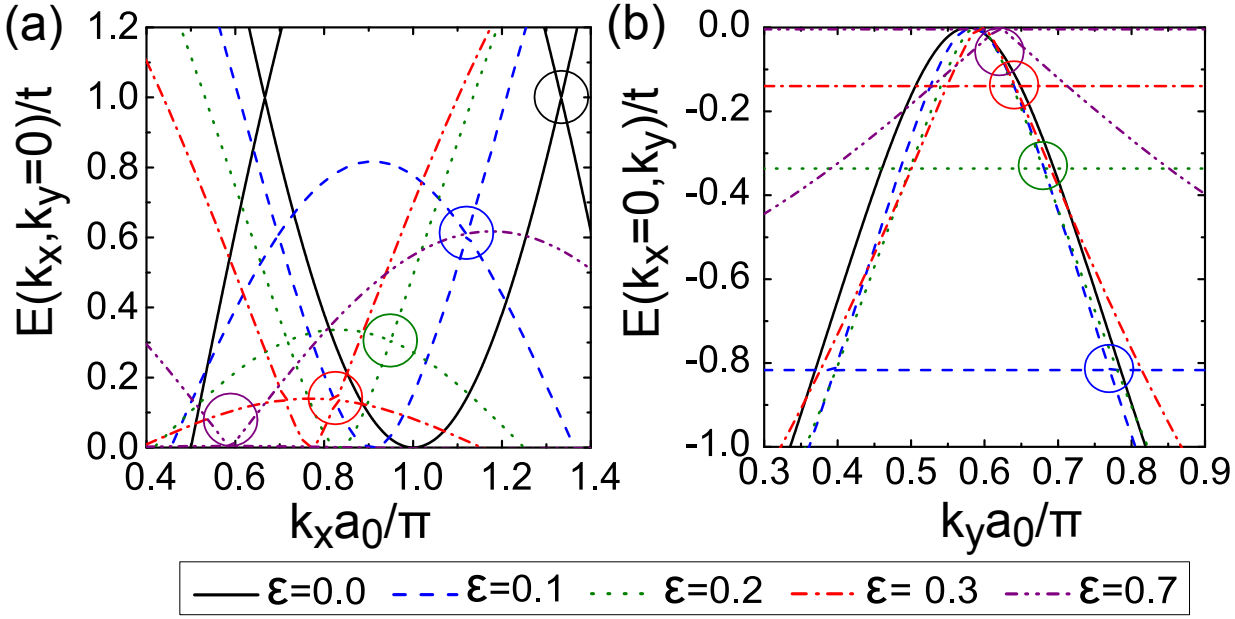

Source: The author Lima *et al.* (2023).

and merge, forming an elliptical isoenergy similar to the situation found for graphene (PEREIRA *et al.*, 2009). However, unlike the latter, the cones in the Kagome lattice approach indefinitely, without opening an energy gap (compare the isoenergies on the fourth and fifth rows of Fig. 30). As ε increases, the Dirac cones approach at the same time that the lower band becomes more dispersive, tending to form a single Dirac cone. This can be noticed by the energy scale increase on the colorbar for the lower bands in Fig. 30 when ε increases. In this process, the lower band creates spikes that form Dirac cones with the middle band, to the point where this middle band tends to become nearly-flat (also note the energy scale decrease on colorbar for the middle bands when ε increases), thus resembling to the Lieb lattice case. The UX-strained dispersion relation for the Kagome lattice (Fig. 30) close to the Fermi level is roughly similar to that for simple shear case applied along the x direction for the Lieb lattice (Fig. 26), as shown in the previous section. These obtained results are in agreement with the evident interconversion between Lieb and Kagome lattices. Furthermore, for $\varepsilon < 0$ (compression), the first and second rows of Fig. 30 show that the Dirac cones move away when the absolute value of ε increases, and consequently, the UX-strained Kagome energy spectrum becomes very similar to that one displayed by the Lieb lattice under simple shear strain along the x direction (compare with the first row of Fig. 22).

To carefully analyze the approaching behavior of the Dirac cones in the Kagome

energy spectrum under UX-strain, we present in Fig. 31 (a) [31 (b)] the dispersion relation along the k_x [k_y] direction and keeping $k_y = 0$ [$k_x = 0$] fixed, *i.e.* it is depicted the spectrum $E(k_x, k_y = 0)$ [$E(k_x = 0, k_y)$], for different strain amplitudes. By Fig. 31 (a), one notices that as ε increases, the Dirac cones deform, exhibiting a tilted cone shape with an asymmetric k_x-projected spectrum. As shown in Fig. 31 (a), the Dirac cone approximation induced by UX-strain results in a total cone immersion when $\varepsilon = 0.7$ (purple dash-double-dotted lines). On the other hand, by Fig. 31 (b) one can realize an unusual behavior (which brings the flat band to the $E = 0$-level as ε increases) of the Dirac cone formed by the crossing between the dispersive band in the hole region and the nearly-flat band. Similar band structure behavior was reported by Montambaux *et al.* (2009a), Montambaux *et al.* (2009b), Gail *et al.* (2012), Montambaux *et al.* (2018), Milićević *et al.* (2019) and Lim *et al.* (2020), which explains this energy bands evolution as a characteristic behavior of Dirac points emerging from nearly-flat bands and merging on nearly-flat bands, being the latter exactly the current case here.

The energy spectra of the Kagome lattice under UY-strain for the same strain amplitudes as in UX-strain case (Fig. 30) are depicted in Fig. 32. Due to Kagome lattice obeys the $\hat{D}_{6h}$ symmetry, which in turn includes $\hat{C}_2$, $\hat{C}_3$, and $\hat{C}_6$ symmetries, it was expected that UX-strain and UY-strain results would indeed be correlated by, roughly speaking, a $\pi/2$-rotation linked to $\hat{C}_2$-symmetry, except by an energy scale difference and a size difference on the aspect ratio of the BZ for each uniaxial strain case (for instance, compare the isoenergies in the first row in Fig. 32 for UY-strain and the fifth row in Fig. 30 for UX-strain). This aspect ratio difference on $\mathbf{k}$-space of the BZ between UX-strain and UY-strain results for Kagome lattice is linked to the combination of the facts that: (i) uniaxial strain causes a larger deformation in the interatomic distances along the applied deformation direction, and (ii) the larger the spatial deformation in a certain direction in the real space the smaller is the BZ dimension along the correspondent direction. For instance, note, by comparing $\varepsilon = 0$ (black symbols) with $\varepsilon \neq 0$ (red symbols) illustrations in Figs. 16 (a) and 16 (b), that the x component of the displacement vectors $\delta(\mathbf{r})$'s in Fig. 16 (a) are greater than in Fig. 16 (b), increasing (decreasing) its modules in the former (latter) situation when one compares the unstrained (black symbols) with the strained (red symbols) cases, which leads to a greater length along the k_x-direction of the BZ for the UY-strain case with $\varepsilon > 0$ in comparison to the UX-strain case with $\varepsilon < 0$ (compare the isoenergies in the first and second rows in Fig. 30 for UX-strain and the fourth and fifth rows in Fig. 32 for UY-strain). A similar analysis for the y-direction can be done by connecting the distension case ($\varepsilon > 0$) for

Figure 32 – The same as in Fig. 22, but now for the Kagome lattice under UY-strain.

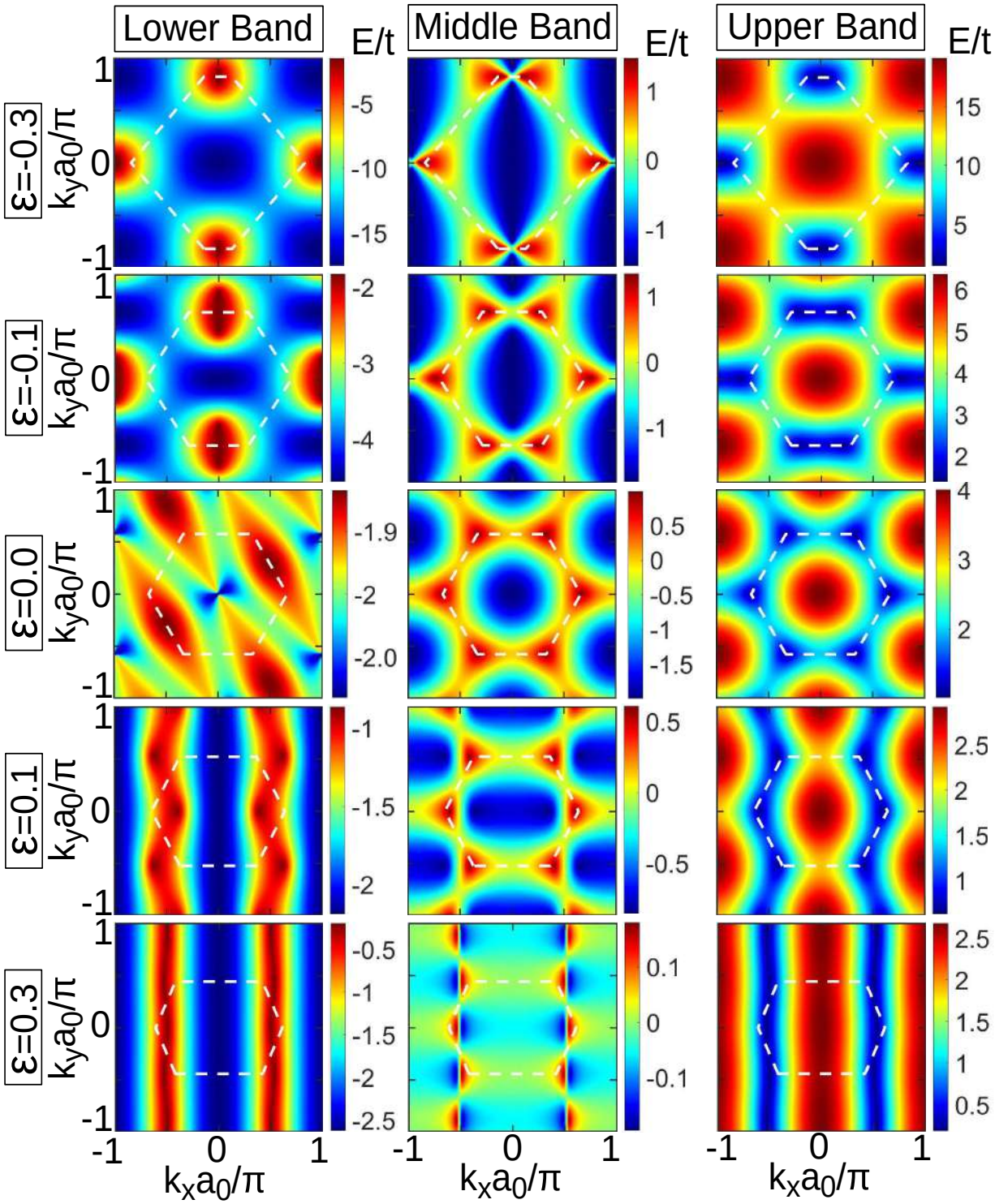

Source: The author Lima *et al.* (2023).

Kagome lattice under UX-strain (Fig. 30) and the compression case ($\varepsilon < 0$) for Kagome lattice under UY-strain (Fig. 32), as can be seen by the isoenergies in the fourth and fifth rows in Fig. 30 for UX-strain and the first and second rows in Fig. 32 for UY-strain. This qualitatively direct analogy is such that compression ($\varepsilon < 0$) and extension ($\varepsilon > 0$) results for Kagome lattice under UX-strain can be mapped by extension and compression, respectively, for the UY-strain case.

Figure 33 – The same as in Fig. 22, but now for the Kagome lattice under BI-strain.

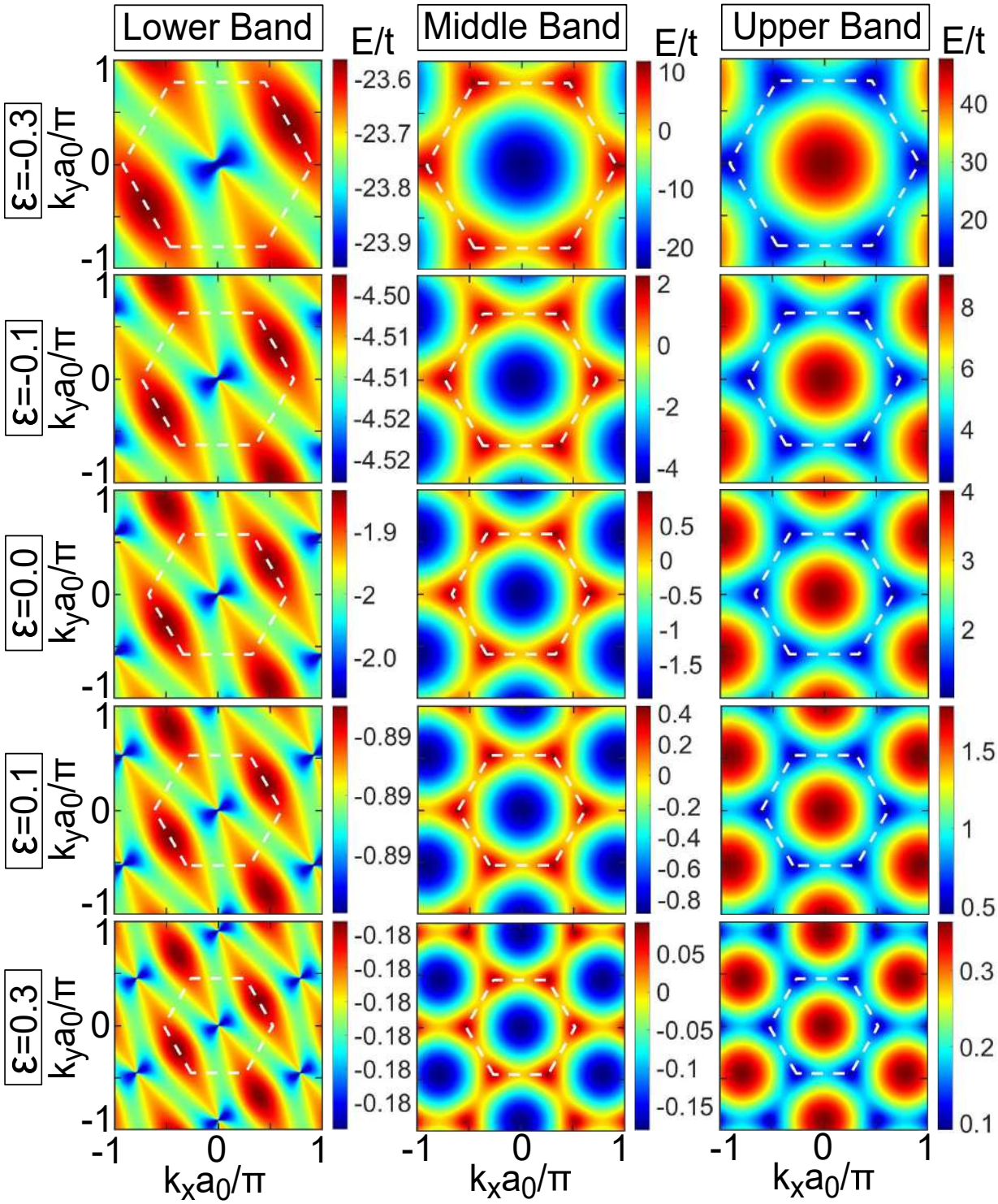

Source: The author Lima *et al.* (2023).

This statement can be viewed by the following correspondence between the rows of Figs. 30 and 32: $1_{UX} \approx 5_{UY}$, $2_{UX} \approx 4_{UY}$, $4_{UX} \approx 2_{UY}$, and $5_{UX} \approx 1_{UY}$.

Additive effects of combined uniaxial strains applied along the x and y directions, *i.e.* BI-strain, in the energy bands of Kagome lattice are shown in Fig. 33. The consequences on the energy spectrum of Kagome lattice under BI-strain are similar to that observed in Fig. 25 for the

Lieb lattice subjected to the same strain type: (i) regardless of the strain amplitude, the bands' curvatures and their aspect ratios in **k**-space are kept undeformed, maintaining in the current case its original hexagonal structure of the unstrained middle and upper bands; and (ii) the biaxial lattice deformation roughly keeps the nearly-flat band without dispersion. On the other hand, unlike the Lieb response to BI-strain (Fig. 25), the Kagome lattice biaxially strained (Fig. 33) presents an energetic shift of the nearly-flat band, as verified by the energy scale change of the lower band colorbar in the left column of Fig. 33 and in Fig. 31 (b). As already discussed in Sec. 2.4, due to strain, the lattice distances change and consequently $t' \equiv t_{ij}$ varies with respect to the ε parameter according to Eq. (2.17). Thus, by increasing the value of the strain amplitude ε for the BI-strain case, the entire nearly-flat band of the Kagome lattice (see the left column in Fig. 33) is energetically shifted up (down) along the energy axis for $\varepsilon > 0$ ($\varepsilon < 0$). This behavior is emphasized in Fig. 34, which shows the evolution of the nearly-flat band at the $\mathbf{\Gamma}$-point as a function of the (a) strain amplitude ε and (b) the strained hopping parameter t_{ij} expressed in Eq. (2.17), that for Kagome lattice case corresponds to $t_{ij} \equiv t'$. In Fig. 34 (a), one notices that the nearly-flat band of the Kagome lattice under BI-strain obeys an exponential tendency given by the fitting function $E/t = a\exp(b\varepsilon - c) + d$ with $a = -399.9$, $b = 8.359$, $c = 5.328$, and $d = -0.043$, being in concordance with the exponential behavior of the hopping in Eq. (2.17). Analyzing Fig. 34 (b), one observes a linear dependence of the energy value of the nearly-flat band on the t'-parameter. This can be understood considering that the energy expression for the nearly-flat band in the non-deformed case (MIZOGUCHI; UDAGAWA, 2019) is given by $E_{flat} \approx -2t$, thus in a similar manner it leads to roughly write an analytical expression for the flat band in the strained Kagome case such as $E_{flat} \approx -2t'$. This is confirmed by the fitting function of the obtained data given by $E_{fit} = at' + b$ with $a = -2.014$ and $b = 0.009257$.

The isoenergy spectra obtained by applying shear strain along the x-direction (SX-strain) and along the y-direction (SY-strain) in the Kagome lattice are shown in Figs. 35 and 36, respectively. By a careful analysis of Fig. 35, one realizes that, similarly to the Lieb lattice subjected to SX-strain (Fig. 26), the strained isoenergies corresponding to distension ($\varepsilon > 0$) and compression ($\varepsilon < 0$) deformations are enantiomorphs in absolute values of ε-parameter, *i. e.* they are mirror images of each other (compare the first, second, third, and fourth rows of Fig. 35 with the ninth, eighth, seventh, and sixth rows of Fig. 35, respectively). This is due to the isotropic lattice structure of Kagome lattice under shear strain for positive and negative values of ε-parameter which has its atomic positions deformed oppositely to both sides with

Figure 34 – Evolution of flat band at the Γ-point for Kagome lattice under BI-strain as a function of (a) the strain parameter ε and (b) the hopping parameter t' between first NN. The red circles correspond to the data associated with the cases of Fig. 33.

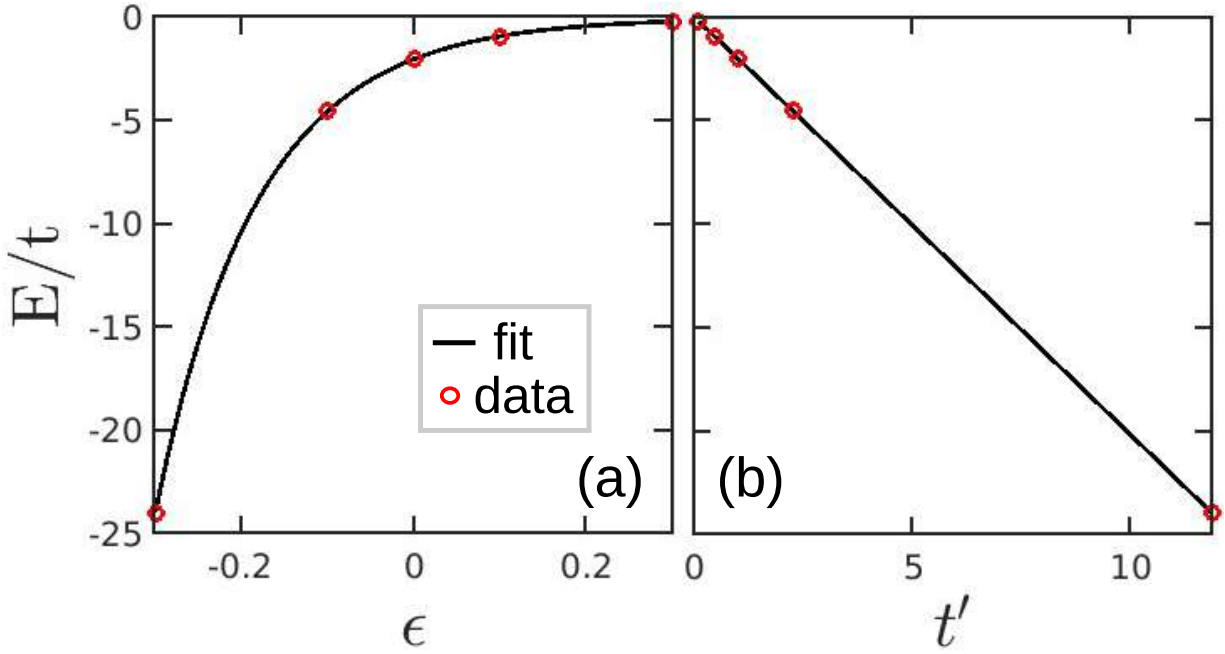

Source: The author Lima *et al.* (2023).

respect to an atomic reference line in the lattice (see a similar discussion in the ante-penultimate paragraph in Sec. 2.7 for Lieb lattice under shear strain). Furthermore, the Kagome lattice under SX-strain with $\varepsilon = 0.5$ roughly resembles the undeformed Lieb lattice as well as the undeformed Kagome lattice roughly resembles the Lieb lattice under UY-strain together with a weakly applied simple shear strain. Although this geometric argument is coherent with respect to the equivalence between these lattice structures, the energy spectra for these two situations are not fully equivalent. On the contrary, it is observed that the obtained isoenergy spectra of the deformed Kagome lattice under SX-strain (Fig. 35) qualitatively resemble that deformed spectra of the Lieb lattice under SY-strain (Fig. 27). For instance, note the similarities between the results of the lower, middle and upper bands in the fifth and sixth rows of Fig. 35 and the correspondent ones in Fig. 26 for $\varepsilon = 0.3$ and $\varepsilon = 0.5$. On the other hand, for high strain amplitudes (see the ninth row of Fig. 35 for $\varepsilon = 0.7$) the BZ (white dashed lines) of Kagome lattice under SX-strain is no longer a six-sided polygon, but rather a parallelogram. In the evolving process of BZ deformation into a parallelogram, the nearly-flat (lower) band becomes more dispersive while the middle band becomes less dispersive, leading to a displacement of the doubly degenerate Dirac points such that for high ε values these doubly degenerate Dirac points start to merge two-by-two connecting the high symmetry points in a parallelogram format.

Figure 35 – The same as in Fig. 26, but now for the Kagome lattice under SX-strain.

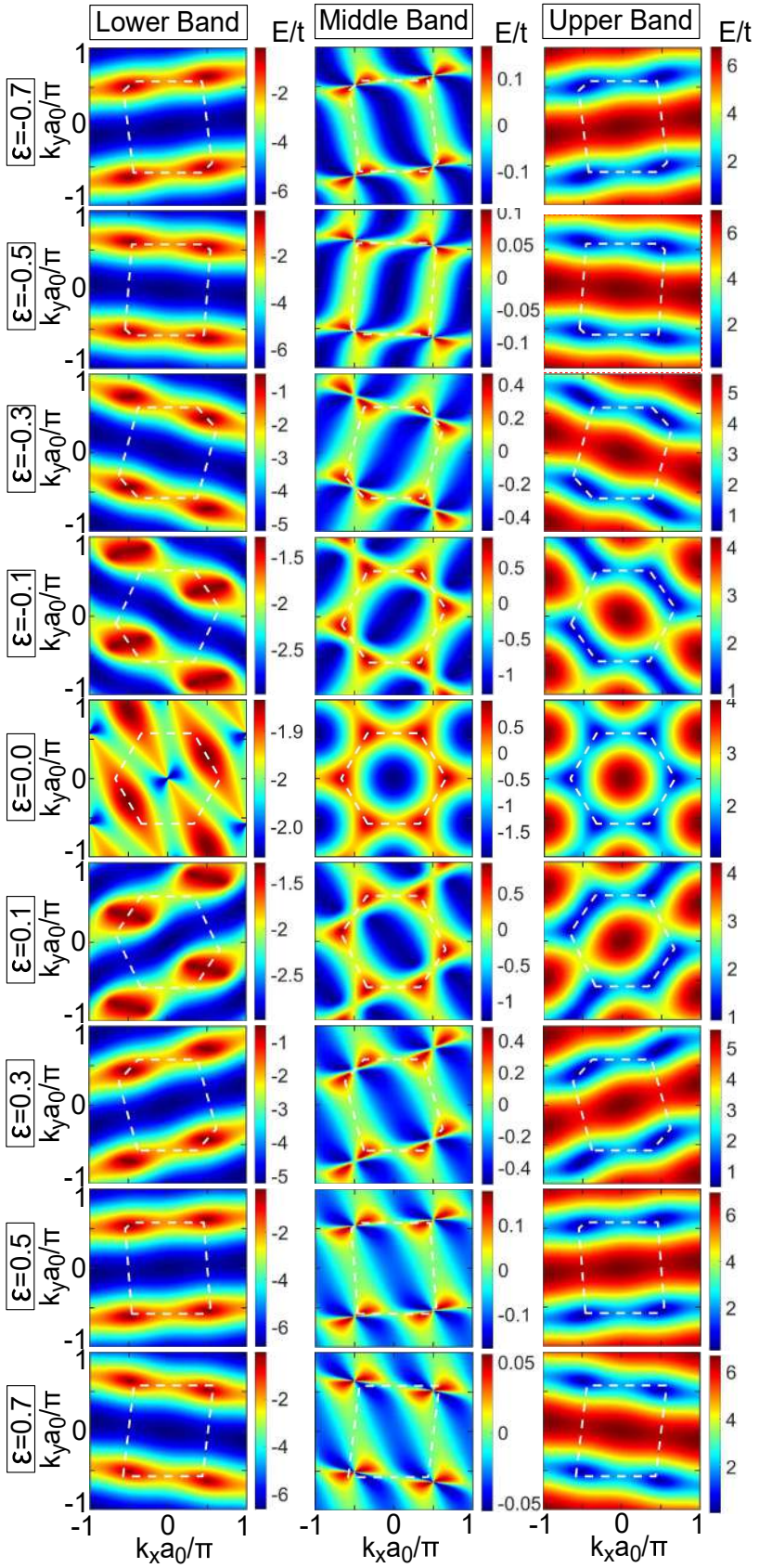

Source: The author Lima *et al.* (2023).

Figure 36 – The same as in Fig. 26, but now for the Kagome lattice under SY-strain.

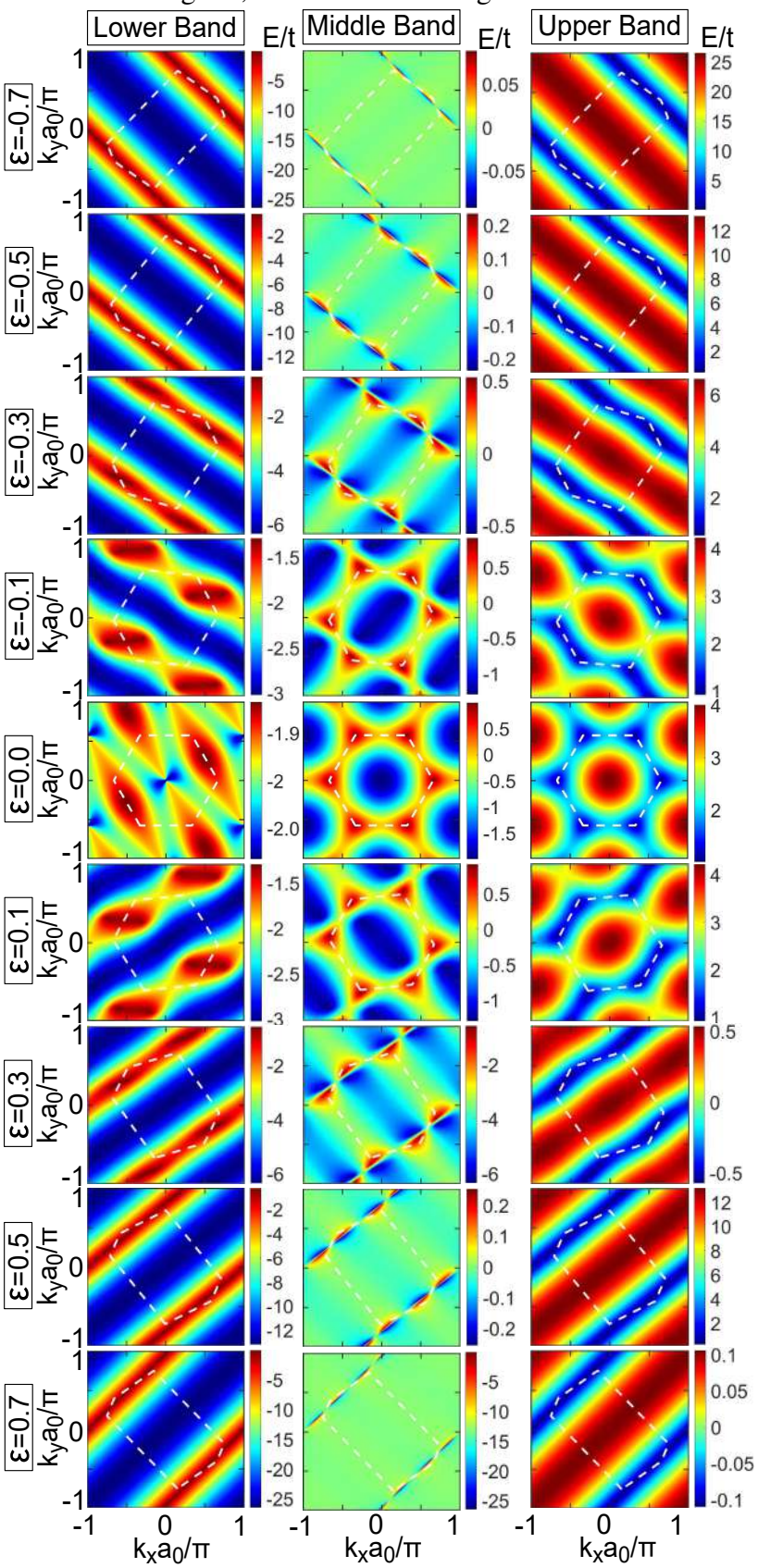

Source: The author Lima *et al.* (2023).

Figure 37 – The same as in Fig. 29, but now for the Kagome lattice under PS-strain.

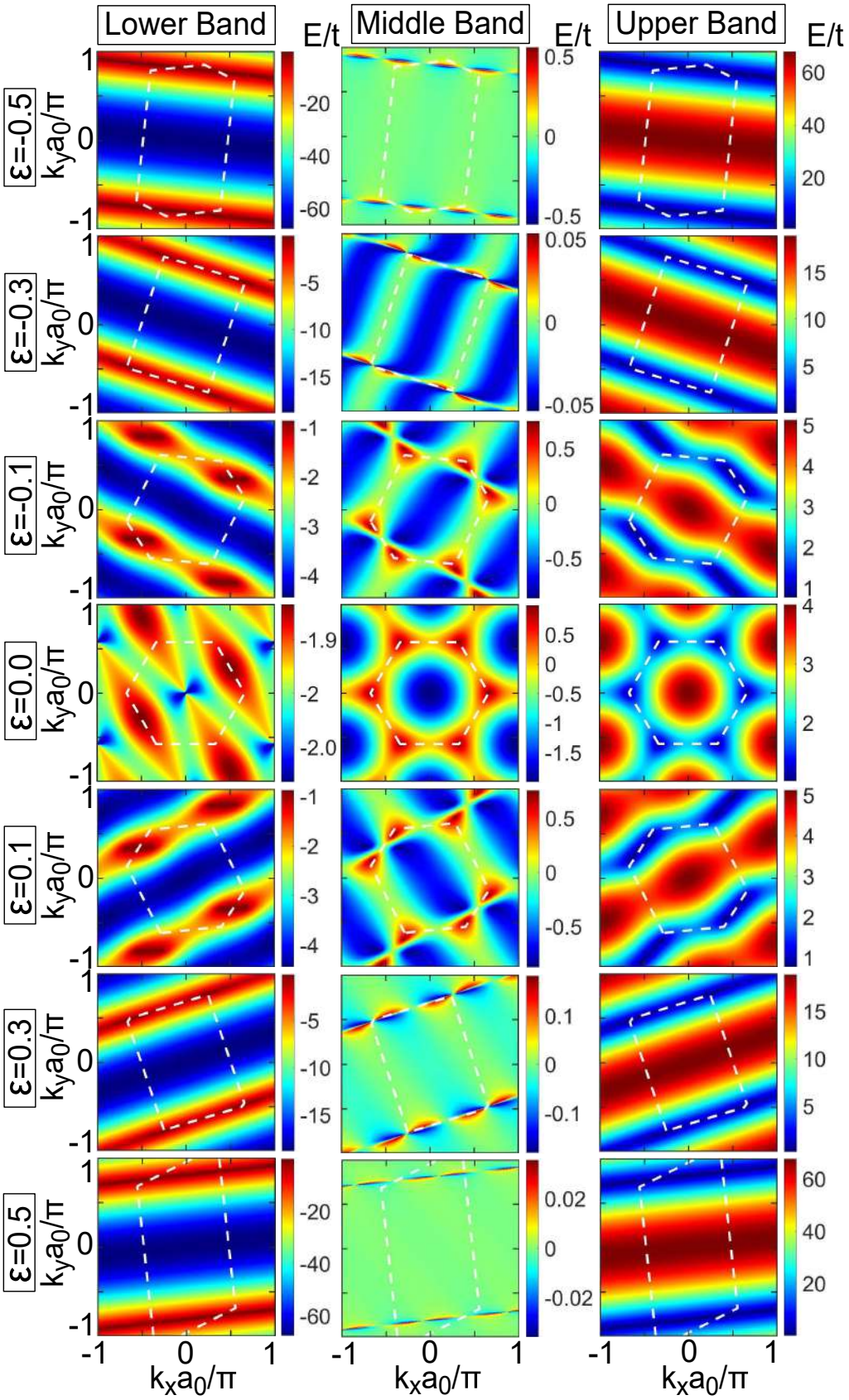

Source: The author Lima *et al.* (2023).

For the Kagome lattice under SY-strain, the isoenergies shown in Fig. 36 present a

very distinct behavior as compared to the previous SX-strain case (Fig. 35). Due to the lattice deformation caused by the SY-strain applied in the Kagome lattice, the band structure is strongly affected, becoming highly (less) dispersive for the lower and middle (upper) bands (compare the energy scale changes on the colorbar in Fig. 36), and also one observes the doubly degenerate points located at the high symmetry points in the BZ being flattened and thus forming energetic lines connecting these degenerate points. Energetically speaking, similar features as the ones obtained in Fig. 36 for deformed Kagome lattice under SY-strain is roughly observed: (i) in the case of the Lieb lattice under pure shear strain (PS-strain) subjected to high strain amplitudes, as can be verified by comparing the seventh row of Fig. 29 for $\varepsilon = 0.5$ with the eighth row in Fig. 36, and (ii) when Kagome lattice is subjected to uniaxial strain along y-direction (UY-strain), as shown in Fig. 32, but being oriented diagonally in the reciprocal space.

In order to verify the combined effects of simple shear strains along x (SX-strain) and y (SY-strain) directions in the Kagome lattice, Fig. 37 shows the strained isoenergy spectra subjected to pure shear deformation. One notices that, unlike the Lieb case subjected to the same strain (Fig. 29) where PS-strain just causes a diagonal-like deformation in the isoenergies, the strained Kagome isoenergies are not only diagonally deformed, but rather present a smoother rotation than those corresponding to simple shear cases in Figs. 35 and 36. According to Eq. (2.9) and Table 1 for the PS strain case and taking the primitive vectors for Kagome lattice, one finds that $(\mathbf{a}'_1)_x \neq (\mathbf{a}'_2)_y$ and $(\mathbf{a}'_1)_y \neq (\mathbf{a}'_2)_x = 0$. This geometric statement of the deformed lattice vectors for each situation explains the nature of the difference between applying PS-strain in Lieb (Fig. 29) and Kagome (Fig. 37) lattices, as well as between PS-strain and SX and SY-strains in Kagome lattice.

2.9 Hypothetical strain

Based on previous works that addressed the origin of strain-induced pseudovector potentials (**A**) in strained graphene (OLIVA-LEYVA; NAUMIS, 2013; OLIVA-LEYVA; NAUMIS, 2015; OLIVA-LEYVA; WANG, 2017), we shall similarly analyze now the existence of a non-null **A** quantity by comparing the obtained energy spectra of strained lattice structures when one assumes strain-dependent and strain-independent hopping parameter cases. Let us label them as real and hypothetical cases, respectively, for the case when one admits or not the ε-dependence on t'_{ij}. Within this nomenclature, one notes that the previous sections have focused on the real strain cases for six different types (UX, UY, BI, SX, SY, and PS) of strain, as shown in Table 1, for the Lieb (Sec. 2.7) and Kagome (Sec. 2.8) lattices, assuming that strain changes both the position of the lattice sites and the hopping parameters. Similarly, we investigate the strain effects on the energy spectra of Lieb and Kagome lattices for all six studied strains but now for the hypothetical case: UX_h, UY_h, BI_h, SX_h, SY_h, and PS_h strain. For each of these cases, we shall identify when there are non-null strain-induced pseudovector potentials. However, we already know that, because we apply only uniform strains, no predicted **A** will be able to generate non-null strain-induced pseudomagnetic fields, since, in the case of uniform strains, one has that $\nabla \times \mathbf{A} = 0$ (KITT *et al.*, 2012; KITT *et al.*, 2013; NAUMIS *et al.*, 2017). Even so, the relevance of understanding when there will be non-null strain-induced pseudovector potentials in uniform strains is that the expression for **A** can be used in cases of non-uniform strains, replacing only the matrix elements of the strain tensor [Eq. (3.5)] for their appropriate position-dependent expansions (KITT *et al.*, 2012; KITT *et al.*, 2013; OLIVA-LEYVA; NAUMIS, 2013; OLIVA-LEYVA; NAUMIS, 2015; NAUMIS *et al.*, 2017; OLIVA-LEYVA; WANG, 2017). Moreover, our main goal in this section is to identify, through an energetic comparison with real cases, the role of lattice deformation, considering or not the changes in hopping. For instance, we examine the emergence of pairs of doubly degenerate Dirac cones or triply degenerate energetic Dirac lines, the breaking of the degeneracy of the triply degenerate Dirac cones, and how the nearly-flat band deforms, if at all.

Concerning such hypothetical cases, what at first glance may seem like fanciful cases, it can be artificially created atom by atom in a scanning tunneling microscope as reported by Slot *et al.* (2019), Gardenier *et al.* (2020), and Broeke *et al.* (2021) for artificial electronic lattices. This experimental platform allows to realize and characterize novel orbital-, position-, and geometric-controlled artificial lattices by designing on Cu(111) surface (copper) with

desired positions for the CO molecules/adatoms which enables to manipulate the geometry of the emerged artificial lattice, the on-site energies, and the inter-site couplings.

Let us start our comparative analysis by the hypothetical uniaxial strains. Fig. 38 presents the isoenergies of the bottom, middle and upper bands for Lieb lattice subjected to UX_h and UY_h strains. As expected for uniaxial strain, the applied deformation direction in real space is the correspondent one distorted in reciprocal space as can be seen by comparing the square-like shape of the BZ for the unstrained case (white line in the third row in Fig. 38) with the rectangular shape with minor axis in the x and y-directions for UX_h and UY_h strain cases in the fourth and fifth rows, and first and second rows in Fig. 38, respectively. In contrast to the real UX and UY strain cases in Lieb lattice as shown in Figs. 22 and 23, respectively, here for both UX_h and UY_h cases, one notices that: (i) the nearly-flat band does not deform, keeping the same energy scale of the colorbar, and (ii) the deformed upper and lower bands in hypothetical strained cases do not form the triply degenerate Dirac strain-induced line state.

Results for the hypothetical biaxial strain (BI_h) for Lieb lattice are depicted in the first ($\varepsilon = 0.3$) and the second ($\varepsilon = 0.1$) rows of Fig. 39, with the third row corresponding to the unstrained case for reference. By comparing the strained BI_h case (Fig. 39) with the strained real BI case (Fig. 25), one notices that in both cases the aspect ratio in $\mathbf{k}$-space of the bands is kept undeformed by changing the strain amplitude, exhibiting a circular symmetry of the contour lines close to the Fermi level, as discussed in Sec. 2.7, since both x and y directions in BI-strain the bands are extended or squeezed equally for positive or negative ε, respectively. In contrast to the real BI-strain case (Fig. 25), where the bands deform in such a way that the colorbar range is clearly altered leading to a maximum energy scale of ten times greater than the unstrained case, this is not the case for the Lieb lattice with BI_h-strain, where the energy scale on the colorbar is unchanged for any strain value and for any of the three bands. This is easily understood by the fact that we are forcing changes in the lattice structure without considering any change in the hopping parameters, which in turn does not allow changes in the energy scale of the bands.

The isoenergies for Lieb lattice under hypothetical PS strain (PS_h), shown in the fourth ($\varepsilon = 0.1$) and the fifth ($\varepsilon = 0.3$) rows of Fig. 39, demonstrate that, unlikely to the real PS-strain case (Fig. 29), in the present case: (i) the triply degenerate Dirac point at Fermi energy level does not split into two pairs of doubly degenerate Dirac points and (ii) the electron-hole symmetry is nearly preserved, as noted by the fact that the lower and upper bands obey the following $E_{lower} = -E_{upper}$ symmetry and the colorbar scale of the nearly-flat band for $\varepsilon > 0$

remains nearly unchanged. Oppositely, one has for the PS-strain case that the lower and upper energy bands are connected to the middle band by energetic lines that are perpendicular between themselves, *i.e.* between the upper and middle bands and middle and lower bands, reinforcing the symmetry-breaking argument for the real PS-strain case. This can be verified by comparing the lower and upper isoenergies around the corners of the BZ (white dashed line) in the fifth and sixth rows of Fig. 29 with the ones in the fourth and the fifth rows of Fig. 39 for the PS_h-strain case, where in the latter case such energetic line band inversion is absent; on the contrary, the format of the isoenergies around the corners of the BZs is elliptically deformed in a similar way for the lower and upper bands. Another very noticeable difference between the two cases is that the hypothetical PS-strain case does not significantly change the energetic scale of the bands with the deformation as happens in the real PS-strain case. Note in the fourth and the fifth rows of Fig. 39 that the colorbar scale ranges for the lower and upper bands are unchanged and the middle band it is just slightly altered for PS_h-strain. This was already expected since in the PS_h case we are assuming hypothetical deformation with strain-independent hopping parameters. Therefore, it demonstrates that the formation of the two pairs of doubly degenerate Dirac cones, instead of the triply degenerate Dirac point, caused by a pronounced deformation of the nearly-flat band, and the lack of electron-hole symmetry in the energetic bands of Lieb lattice under PS-strain is a consequence of both changes in the atomic position and in the hopping parameters. It is important to note that since the atomic positions and real lattice vectors are changing due to strain application, the reciprocal lattice vectors and consequently the BZ must change. Such changes are independent of the hopping parameters changed or not, that is, the BZ will present the same deformation for both real and hypothetical cases. Note that for both real and hypothetical PS-strain cases, the unstrained square-like BZ deforms into a six-sided polygon, leading to the BZ with a hexagonal shape the larger the strain amplitude, which in turn resembles the Kagome lattice BZ.

Let us now discuss the consequences on the energy spectrum of Lieb lattice due to hypothetical simple shear strain applied along x and y-directions, *i.e.* the SX_h and SY_h cases. Results are shown in the first ($\varepsilon = 0.3$) and second ($\varepsilon = 0.1$) rows for SY_h-strain and in the fourth ($\varepsilon = 0.1$) and fifth ($\varepsilon = 0.3$) rows for SX_h-strain of Fig. 40. The isoenergies in the third row correspond to the unstrained case for comparison. Similar consequences in the energetic bands as those observed for the PS_h-strain case (Fig. 39) are also verified here for Lieb lattice subjected to simple shear strain for hypothetical case (Fig. 40), *i.e.*: the electron-hole symmetry

is nearly preserved and the triple degeneracy of the Dirac point is maintained regardless of the applied strain amplitude and direction. This agreement was already expected since the PS_h-strain case can be viewed as a combination of the SX_h and SY_h strains. In addition to these physical statements concerning the differences and similarities raised for the PS_h-strain in Fig. 39 in comparison to the real PS-strain case in Fig. 29, here one also observes for hypothetical simple shear strain (Fig. 40) the absence of the connecting energetic lines between the upper and middle bands and middle and lower bands that are formed for high strain amplitudes when the triply degenerate Dirac cone is divided into two. Such notable differences between the hypothetical shear strain cases and the corresponding real cases can be seen comparing Figs. 26 and 27 for SX and SY strains with Fig. 40 for SX_h and SY_h strains. Therefore, the effects of degeneracy breaking and the non-conservation of the electron-hole symmetry in the energy spectrum of Lieb lattice under simple and pure shear strains are due to the variation of the strain-induced hopping parameters, indicating a non-null term for the vector potential $\mathbf{A}$ for the real cases of SX and SY strains. We shall return to this discussed in more detail in Sec. 2.10.

The consequences on the energy spectra of the Kagome lattice by assuming the six different types of hypothetical strain cases, namely UX_h, UY_h, BI_h, SX_h, SY_h, PS_h, similarly to the ones mentioned for the real strain cases in Table 1, are present in Figs. 41, 42, and 43. Results for hypothetical uniaxially strained Kagome lattice deformed along the y and x directions are shown, respectively, in the first ($\varepsilon = 0.3$) and second ($\varepsilon = 0.1$) rows and in the fourth ($\varepsilon = 0.1$) and fifth ($\varepsilon = 0.3$) rows of Fig. 41. Unlike the results for Kagome lattice subjected to real uniaxial strains shown in Figs. 30 (UX-strain) and 32 (UY-strain), in the current hypothetical case, one observes that: (i) the dispersive character of the bands and, consequently, the colorbar scale ranges are kept unchanged for all the three bands, regardless the strain amplitude and direction; (ii) the approaching of the Dirac cones (for $\varepsilon > 0$ and UX_h case or for $\varepsilon < 0$ UY_h case) and the moving away of the Dirac cones (for $\varepsilon < 0$ and UX_h case or for $\varepsilon > 0$ UY_h case) are less expressive here than in the real case. For instance, compare the location changes of the BZ corners (white dashed curve) in the fifth row of Fig. 30 for UX case with $\varepsilon = 0.3$ and the respective hypothetical case in the fifth row of Fig. 41, where in the former (real) case the cones merge for high ε values, as emphasized in Fig. 31 (a); (iii) the energetic location of the nearly-flat band is not altered in the presence of the hypothetical strain case, whereas in the real UX and UY strain cases it approaches to the $E = 0$-level as ε increases, as depicted in Fig. 31 (b); and (iv) the upper and middle bands are energetically mirror images of each other and such

symmetry is preserved regardless the strain amplitude and direction. Figs. 30 and 32 show that such mirror symmetry between upper and middle bands is lacking in the real UX and UY strains cases. Similarly to the hypothetical cases discussed previously for the Lieb lattice, here for the Kagome lattice one has that the absence of the energy scale change of the bands, as well as of the unaltered dispersion character of the bands; and the lacking of the energetic moving of the nearly-flat band, are due to hypothetical strain does not change the values of the hopping energies. Therefore, it leads us to state that the strain-induced asymmetry on the isoenergies of the middle and upper bands and the deformation of the nearly-flat (lower) band in the Kagome lattice subjected to real uniaxial strain [Figs. 30 and 32] are consequences of the hopping energy variation when the lattice distances change subjected to strain. It is an indication that there is a non-null vector pseudopotential term for real UX and UY strain cases for the Kagome lattice, as we shall discuss more in Sec. 2.10.

In order to verify the combination effect of hypothetical uniaxial strains jointly applied along both x and y directions on the dispersion relation of the Kagome lattice, we present in the first ($\varepsilon = 0.3$) and second ($\varepsilon = 0.1$) rows of Fig. 42 the isoenergies of the lower, middle, and upper bands for the deformed case subjected to hypothetical biaxial strain (BI_h). One observes that the BI_h-strained bands' curvatures and their aspect ratios in $\mathbf{k}$-space are kept unchanged, similarly to the real BI-strain case (Fig. 33), and in addition to that, likewise to each separated hypothetical uniaxial strain case, *i.e.* to UX_h and to UY_h cases for Kagome lattice shown in Fig. 41, one obtains upper and middle bands obeying an energetic mirror-symmetry between themselves without any variation on the energetic scale range for any of the three bands regardless the ε value. Such lack of energetic alteration in the BI_h-strained Kagome energy bands is equally explained, as in the previous hypothetical cases, in view of the no changes in the hopping parameters to be considered.

Comparing the results obtained in the fifth and sixth rows of Fig. 37 for the real PS-strained Kagome lattice with the ones shown in the fourth and fifth rows of Fig. 42 for the hypothetical case (PS_h), one notices that there is a drastic difference between such spectra for the deformed lattices, in which in the hypothetical case almost no alteration with respect to the undeformed lattice (third row of Fig. 42) is seen, except by the bands' diagonal-like bending subjected to strain. The most pronounced difference between the Kagome lattice under PS and PS_h strains is the non-formation of the energetic lines connecting the doubly degenerate points located at the high symmetry points in the BZ caused by the flattening of the middle band. This

is a consequence of the lack of bands' curvature distortion in the PS_h-strain case by keeping the hopping unchanged.

Generally speaking, no pronounced modification on the dispersion relations of the BI_h and PS_h Kagome strained cases, shown in Fig. 42, are observed when compared with the unstrained case, but, on the other hand, the isoenergies of such hypothetical cases present huge differences with respect to the real BI (Fig. 33) and PS (Fig. 37) strained Kagome cases. By such comparison, we understand that the asymmetry of the middle and upper bands, together with the deformation of the nearly-flat band, is also due to the variation of the hopping parameters with the strain, indicating non-null vector pseudopotential terms for BI and PS strains in the Kagome lattice.

As the last two investigated cases, in Fig. 43, we present the isoenergies of the Kagome lattice subjected to SY_h-strain (first and second rows) and SX_h-strain (fourth and fifth rows) for two strain amplitudes: $\varepsilon = 0.1$ and $\varepsilon = 0.3$. Similar remarks as the ones discussed in the previous paragraph for the PS_h-strain case in the Kagome lattice are also obtained here, as expected since the pure shear strain can be viewed as a combination of the simple shear strains jointly applied along the both x and y directions. By a direct comparison between Fig. 43 for hypothetical shear strain SX_h and SY_h cases and Figs. 35 and 36 for SX and SY real cases, respectively, one notices that regardless of the strain amplitude and applied direction, there is no way to get the energetic line in the hypothetical (simple or pure) shear strain cases, as well as the emergence of the doubly degenerate points and the breaking mirror symmetry between the middle and upper bands. In this way, we can state that the variation of the hopping parameters due to strain is the main cause of the drastic changes in the real pure and simple shear strained energy spectra, indicating that a non-null vector pseudopotential term should be associated with the real cases of SX and SY strains in Kagome lattice, as discussed in more details in Sec. 2.10.

In the next section, we shall justify in more detail the existence or not of a non-null pseudovector potentials term associated with the energy spectra changes whose indication of such existence arose when we compared the results obtained in cases of hypothetical and real Kagome and Lieb strained lattices. Our previous discussions suggested us a non-null $\mathbf{A}$ term for all investigated cases of real strain, except for the Lieb lattice subjected to UX and UY strains, owing to the preservation of the nearly-flat band and the triple degenerate Dirac point at zero energy level.

Figure 38 – Contour plots of the lower (left panels), middle (middle panels), and upper (right panels) energy bands for Lieb lattice under hypothetical UY (first and second rows) and UX (fourth and fifth rows) strains applied along the y and x directions, *i.e.* UY_h and UX_h cases, respectively, for two strain amplitudes: $\varepsilon = 0.1$ and $\varepsilon = 0.3$. The third row presents the non-strain case for comparison.

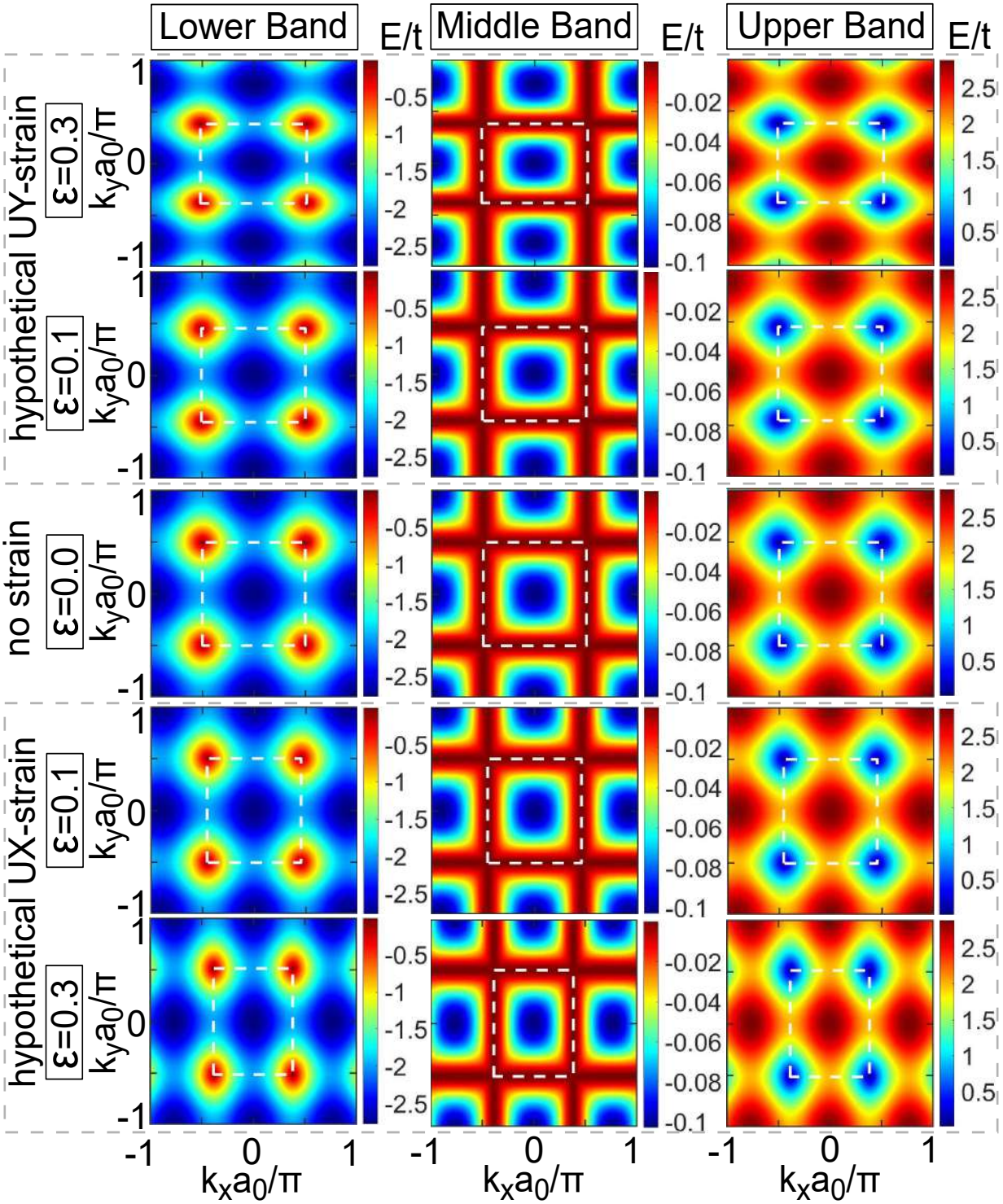

Source: The author Lima *et al.* (2023).

Figure 39 – The same as in Fig. 38, but now for the Lieb lattice under hypothetical BI and PS strains, *i.e.* BI_h and PS_h cases, respectively.

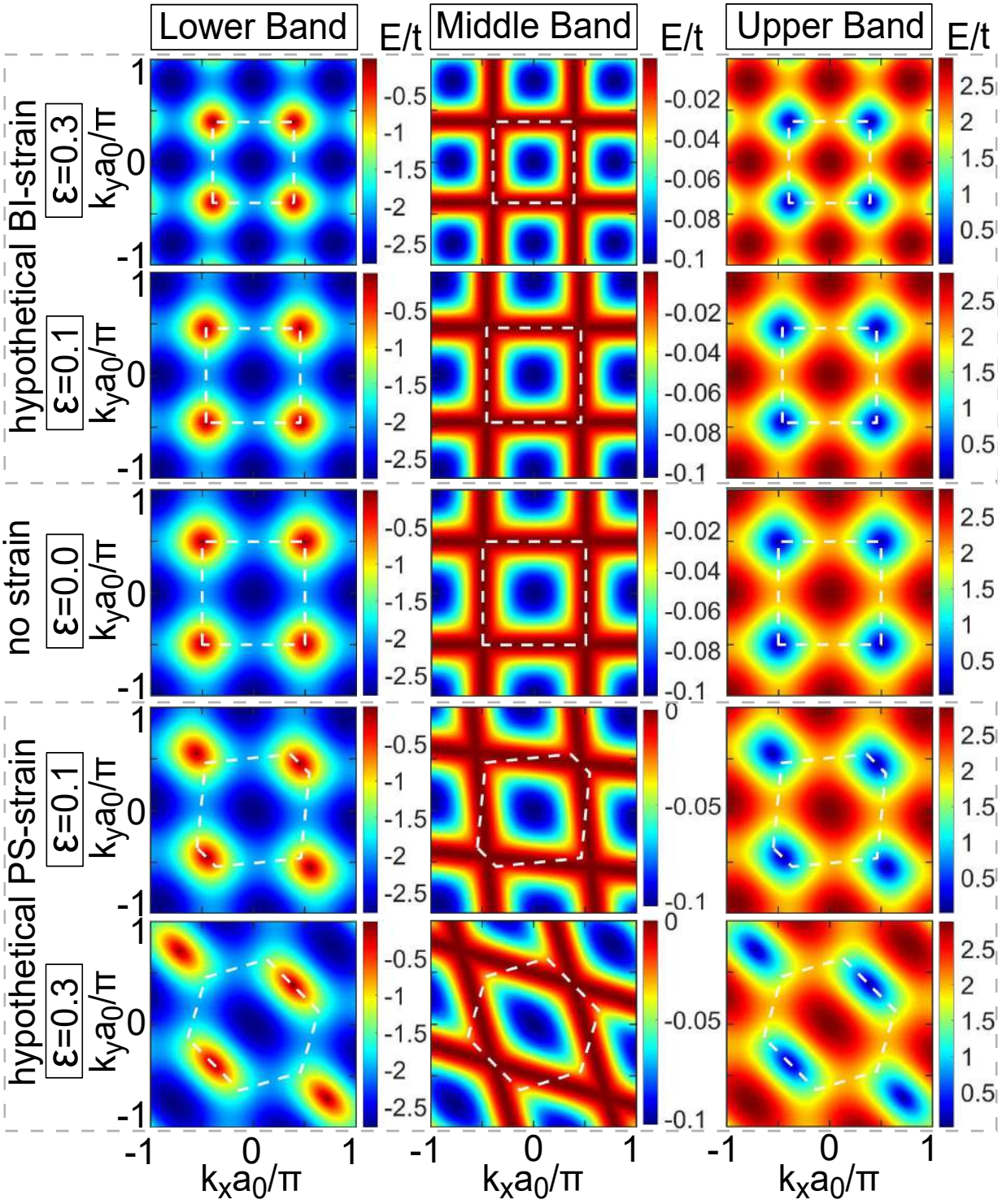

Source: The author Lima *et al.* (2023).

Figure 40 – The same as in Fig. 38, but now for the Lieb lattice under hypothetical SX and SY strains, *i.e.* SX_h and SY_h cases, respectively.

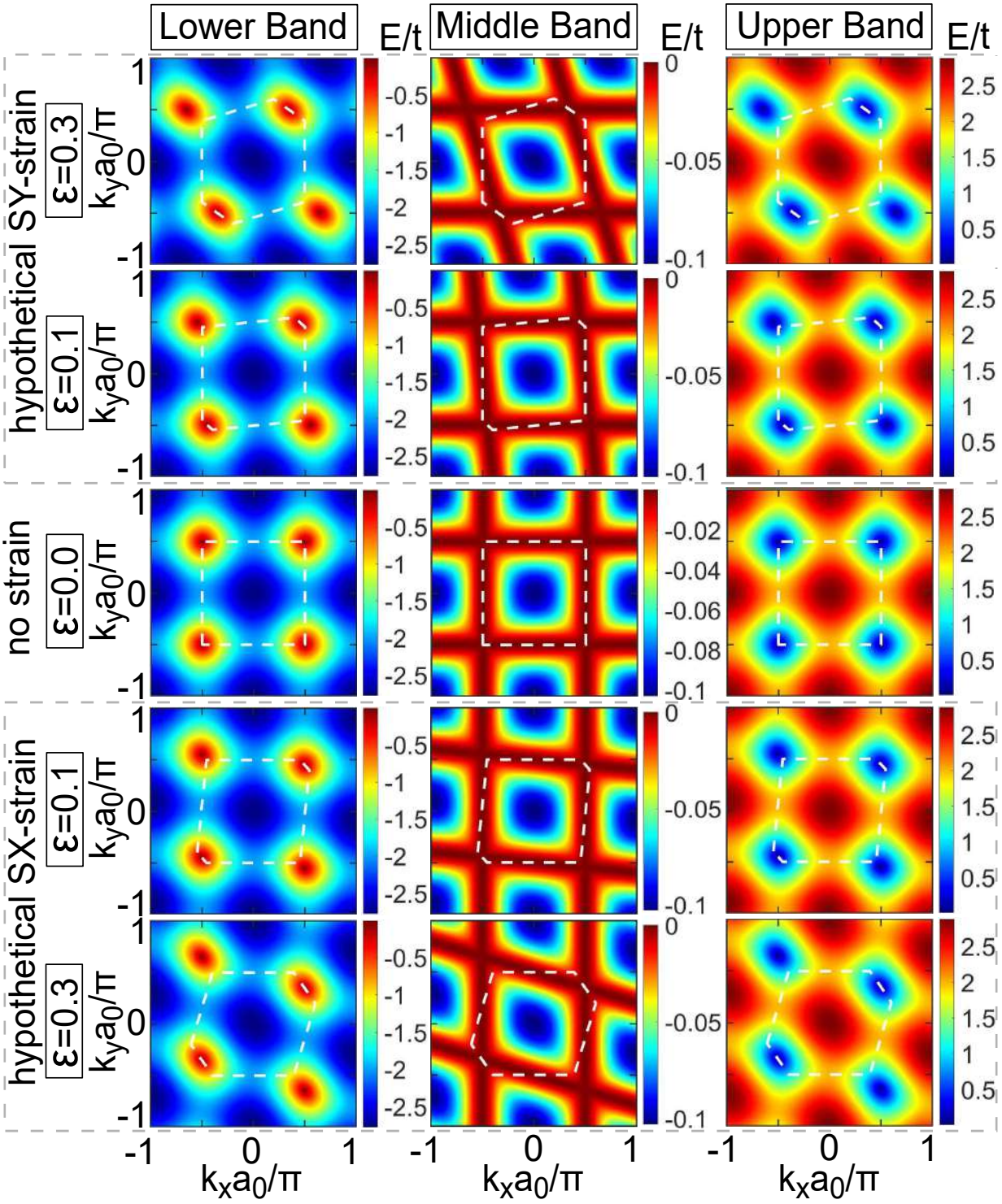

Source: The author Lima *et al.* (2023).

Figure 41 – The same as in Fig. 38, but now for the Kagome lattice under hypothetical UX and UY strains, *i.e.* UX_h and UY_h cases, respectively.

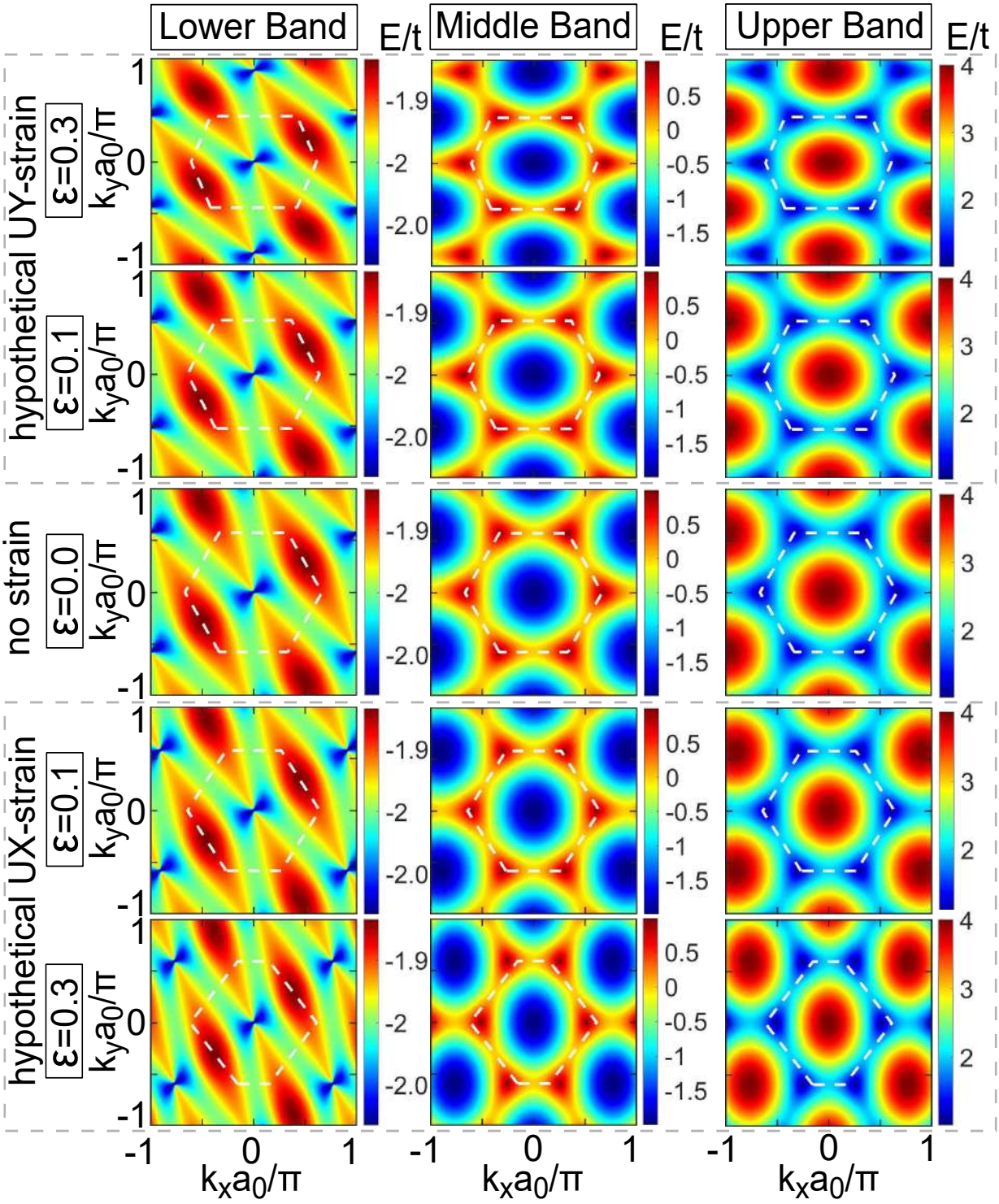

Source: The author Lima *et al.* (2023).

Figure 42 – The same as in Fig. 38, but now for the Kagome lattice under hypothetical BI and PS strains, *i.e.* BI_h and PS_h cases, respectively.

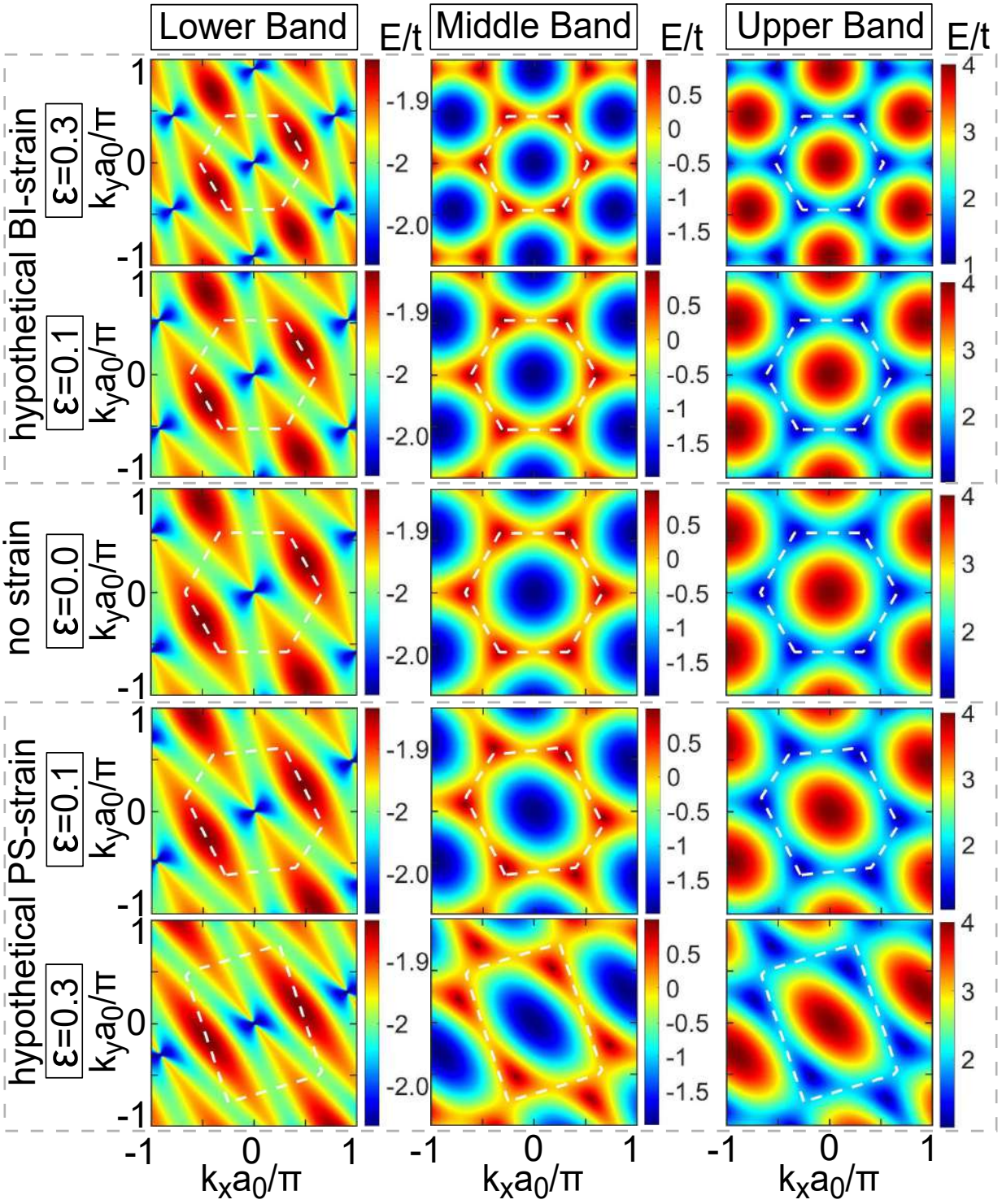

Source: The author Lima *et al.* (2023).

Figure 43 – The same as in Fig. 38, but now for the Kagome lattice under hypothetical SX and SY strains, *i.e.* SX_h and SY_h cases, respectively.

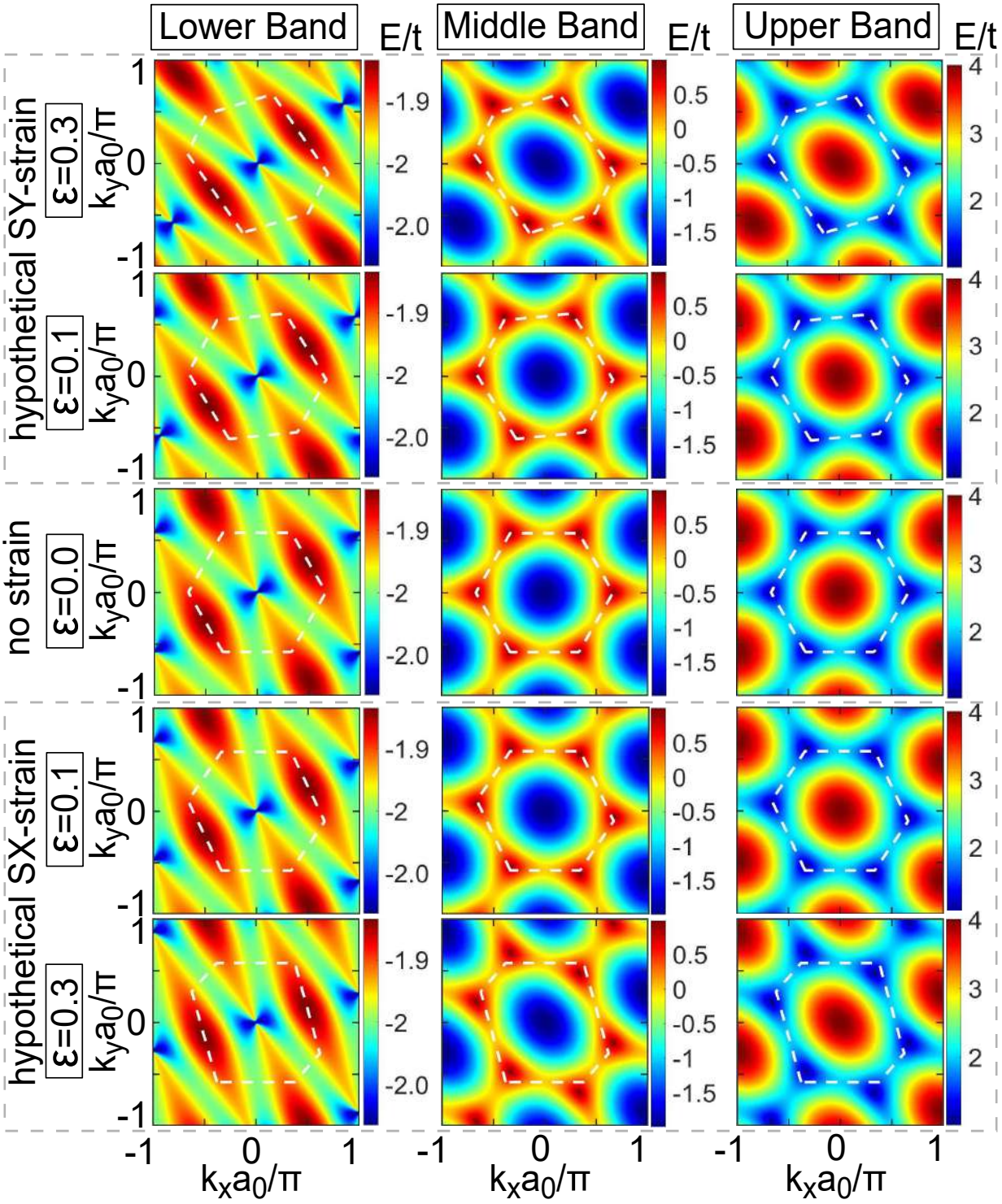

Source: The author Lima *et al.* (2023).

2.10 Strain-induced vector pseudopotentials

Consider the high symmetry point **K** (**M**) in the BZ of the Kagome (Lieb) lattice, in which, for the unstrained lattice, it coincides with the position in the reciprocal space of the Dirac cone, as shown in Figs. 19 and 20. By applying the hypothetical strain, we verified in Sec. 2.9 that the Dirac cones' locations always coincide with the positions of the high symmetry points $\mathbf{K}'$ ($\mathbf{M}'$), being their (k_x, k_y)-coordinates redefined as the strain is applied to the Kagome (Lieb) lattice. On the other hand, the results for real strain cases, presented in Secs. 2.7 and 2.8, revealed that the Dirac points' locations only coincide with the high symmetry points $\mathbf{K}'$ ($\mathbf{M}'$) if there are no non-null vector pseudopotential terms (OLIVA-LEYVA; NAUMIS, 2013; KITT *et al.*, 2013; OLIVA-LEYVA; NAUMIS, 2015; OLIVA-LEYVA; WANG, 2017; NAUMIS *et al.*, 2017). In general, a **A**-term must be added to the $\mathbf{K}'$ ($\mathbf{M}'$) points to provide the correct positions of the Dirac points, such as $\mathbf{K}_D = \mathbf{K}' + \mathbf{A}$ ($\mathbf{M}_D = \mathbf{M}' + \mathbf{A}$). It is important to mention that, for the Lieb lattice cases where Dirac points are split due to strain application, the previous discussion is still valid, being $\mathbf{M}_D$ point at the connecting midpoint distance in the reciprocal space between the two doubly degenerate Dirac points (see Fig. 28).

Owing to check the variation of the Dirac point location in the reciprocal space and thus to confirm the statements raised in the previous sections concerning the existence or not of a non-null **A** term, we present in Fig. 44 (Fig. 45) a comparison between the energy spectra of Lieb (Kagome) lattice for the case (i) without strain ($\varepsilon = 0$ - black solid curves), (ii) subjected to real strain ($\varepsilon = 0.1$ - red dashed curves), and (iii) subjected to hypothetical strain ($\varepsilon = 0.1$ - blue dotted curves). The dispersion relations are shown around the Dirac point in the vicinity of the Fermi energy level for the Lieb lattice subjected to UX [Fig. 44 (a)], UY [Fig. 44 (b)], BI [Fig. 44 (c)], SX [Fig. 44 (d)], SY [Fig. 44 (e)] and PS [Fig. 44 (f)] strains. It is worth remembering that, similarly to Secs. 2.7 and 2.8, for the real strain one considers the variation of both: the atomic positions, $\mathbf{a}'_1$ and $\mathbf{a}'_2$ (see Sec. 2.3), and the hopping parameters $t' \equiv t'(\varepsilon)$ [Eq. (2.17)], whereas for hypothetical strain case, one just assumes the variation of $\mathbf{a}'_1$ and $\mathbf{a}'_2$, keeping the hopping parameters unchanged for any type of strain, *i.e.* one takes $t' = t$.

Analyzing the Dirac cone position in the reciprocal space for Lieb lattice under uniaxial (a, b) and biaxial (c) strains in Fig. 44, one notes that the results for both hypothetical (dotted blue curves) and real (dashed red curves) strain cases exhibit the Dirac point coinciding with the $\mathbf{M}'$ point. This means that such strain types in the Lieb lattice do not require correction terms to make matching the position of the Dirac points and the $\mathbf{M}'$ point of the strained reciprocal

lattice, and consequently, no vector pseudopotential is expected, *i.e.* $\mathbf{A} = 0$ and then $\mathbf{M}_D = \mathbf{M}'$. These results, for the Dirac point position in the reciprocal space, for the Lieb lattice subjected to uniaxial strains along the x [Fig. 44 (a)] end y [Fig. 44 (b)] directions are not similar to the ones for UX and UY strained graphene, whereas the one in Fig. 44 (c) presents identical features as those obtained for the BI-strained graphene, as reported by Kitt *et al.* (2012) (KITT *et al.*, 2013).

As follows, we shall demonstrate that $\mathbf{A} = 0$ in the Lieb lattice subjected to UX, UY, and BI strains. For that, we follow a procedure similar to the one commonly used to find the terms associated with strain-induced pseudovector potentials in strained graphene, as reported by Pereira *et al.* (2009) and Oliva-Leyva e Wang (2017), since similarly to the graphene case, here for uniaxially and biaxially strained Lieb lattice we have the crossing point of the Dirac cone energetically located approximately at the $E = 0$ level, even under the application of strain. This statement can be verified in Figs. 22, 23, and 24. By diagonalizing the Hamiltonian (2.11), with off-diagonal matrix elements given by Eq. (2.12) and assuming the main diagonal matrix elements as zero, one gets for Lieb lattice ($\theta = 90^\circ$) the following expressions for the lower and upper energy bands

$$E_{\substack{lower \\ upper}} = \mp 2\sqrt{t'^2_{BC}\cos^2\left(\mathbf{k}\cdot\frac{\mathbf{a}'_1}{2}\right) + t'^2_{BA}\cos^2\left(\mathbf{k}\cdot\frac{\mathbf{a}'_2}{2}\right)}. \tag{2.23}$$

Setting Eq. (2.23) equal to zero, analytically associating the triple degenerate point with the Dirac point ($\mathbf{M}_D$) where the upper and lower bands touch each other, one obtains

$$0 = \sqrt{t'^2_{BC}\cos^2(\mathbf{M}_D\cdot\mathbf{a}_1/2) + t'^2_{BA}\cos^2(\mathbf{M}_D\cdot\mathbf{a}_2/2)}, \tag{2.24}$$

in which, based on Eq. (2.7), the strain dependence of the strained lattice vectors $\mathbf{a}'_{1,2}$ in Eq. (2.23) is incorporated in the $\mathbf{M}_D$ point in Eq. (2.24), once that $\mathbf{M}_D \approx [(\mathbb{I}+\overline{\varepsilon})^{-1}]^T\cdot(\mathbf{M}+\mathbf{A}) \approx \mathbf{M}'+\mathbf{A}$ (OLIVA-LEYVA; NAUMIS, 2013; OLIVA-LEYVA; NAUMIS, 2015; OLIVA-LEYVA; WANG, 2017). Since the position of the Dirac point depends on the strain parameter ε, one can Taylor expand $\mathbf{M}_D$ around its unstrained value, that for the Lieb lattice is the $\mathbf{M}$ point, such that up to second-order of the ε-parameter, one has

$$\mathbf{M}_D = \mathbf{M} + \mathbf{A}^{(1)} + \mathbf{A}^{(2)} + \mathbb{O}(\varepsilon^3), \tag{2.25}$$

where $\mathbf{A}^{(i)}$ corresponds to the $i-$th order correction term of the $\mathbf{M}_D$ point in relation to the unstrained $\mathbf{M}$ point.

Likewise, once the hopping parameters also depend on the strain parameter ε [see Eq. (2.17)], one can also Taylor expand t'_n around the unstrained hopping value t_0 and in terms of

the ε-parameter, in a similar way to Eq. (2.20), *i. e.*,

$$t'_n/t_0 = 1 + \Delta_n^{(1)} + \Delta_n^{(2)} + \mathbb{O}(\varepsilon^3), \tag{2.26}$$

where $\Delta_n^{(i)}$ is the $i-$th order correction term of the t'_n-parameter in relation to the unstrained value t_0. Replacing the Eqs. (2.25) and (2.26) in Eq. (2.24), and considering expansions up to second order, one obtains

$$\begin{aligned} 0 &= \sqrt{\sum_{n=1}^{2} t'^2_n \cos^2\left(\mathbf{M}_D \cdot \frac{\mathbf{a}_n}{2}\right)} \\ &\approx t_0 \sqrt{\sum_{n=1}^{2} \left[\left(\mathbf{A}^{(1)} + \mathbf{A}^{(2)} + \Delta_n^{(1)}\mathbf{A}^{(1)}\right) \cdot \frac{\mathbf{a}_n}{2}\right]^2}, \end{aligned} \tag{2.27}$$

in which it was used that $\sum_n t_0 e^{i\mathbf{M}\cdot\delta_n} = 0$. In Eq. (2.27), $n = 1$ and $n = 2$ refer to terms related to connections $\overline{BC}$ and $\overline{BA}$, respectively. By taking just the first order in Eq. (2.27), one gets

$$\begin{aligned} 0 &= \sqrt{\sum_{n=1}^{2} \left[\mathbf{A}^{(1)} \cdot \frac{\mathbf{a}_n}{2}\right]^2} \\ &= \sqrt{\left(\frac{\mathbf{A}^{(1)} \cdot \mathbf{a}_1}{2}\right)^2 + \left(\frac{\mathbf{A}^{(1)} \cdot \mathbf{a}_2}{2}\right)^2}, \end{aligned} \tag{2.28}$$

and equivalently that

$$\sqrt{\left(\mathbf{A}_x^{(1)}\right)^2 + \left(\mathbf{A}_y^{(1)}\right)^2} = 0. \tag{2.29}$$

This means that $\mathbf{A}^{(1)} = 0$, *i. e.*, there are no strain-induced vector pseudopotentials at the first order generated by UX and UY strains in the Lieb lattice. We emphasize that the calculation to obtain $\mathbf{A}^{(1)} = 0$ is not valid for other types of strains, since the initial condition for the derivation was that the Dirac point ($\mathbf{M}_D$) remains located at zero energy level when the lattice is subjected to strain. This only occurs for UX, UY, and BI strains in the Lieb lattice, as shown in Fig. 44.

To perform a similar investigation for the Lieb lattice under shear strain, we show in Figs. 44 (d), 44 (e), and 44 (f) the dispersion relations for SX, SY, and PS strains, respectively, around the Dirac point for the real and hypothetical cases. Such results for real strain Lieb lattice (dashed red curves) demonstrate the presence of two false energy gaps around the $\mathbf{M}'$ point, between the upper and middle bands, and between the lower and middle bands. This is because the Dirac cone ($\mathbf{M}_D$-point) for such real strain cases is not found at the M'-point, requiring a strain-induced pseudovector potential term $\mathbf{A}$ to be added to $\mathbf{M}'$ to match with the real position

of the $\mathbf{M}_D$-point. The analytical derivation of such correction term is more complicated to be obtained than the previously analyzed cases of UX and UY strains in the Lieb lattice and also than the correspondent one for graphene since the Fermi level here does not remain fixed at zero energy level, varying energetically as strain is applied. However, by a parallel analysis with those made for the case of strained graphene (KITT *et al.*, 2012; KITT *et al.*, 2013; OLIVA-LEYVA; WANG, 2017; NAUMIS *et al.*, 2017), one expects a general dependence of the strain-induced vector pseudopotentials of the Lieb lattice to be in the form $\mathbf{A} \propto n(0, \overline{\varepsilon}_{xy} + \overline{\varepsilon}_{yx})$, with $\overline{\varepsilon}_{ij}$ given by Eq. (3.5) and the n-parameter governing the hopping variation with the strain [Eq. (2.17)].

Figure 45 shows the dispersion relations of the Kagome lattice under UX [Fig. 45 (a)], UY [Fig. 45 (b)], BI [Fig. 45 (c)], SX [Fig. 45 (d)], SY [Fig. 45 (e)], and PS [Fig. 45 (f)] strains. Note that, for all hypothetical strain cases (blue dotted curves), the Dirac cone is located at the $\mathbf{K}'$ point. This holds true for the real BI case (red dashed curves in Fig. 45 (c)), but on the other hand, it is not the case for others real strains, where one observes two apparent energy gaps around the $\mathbf{K}'$ point. This means that a correction $\mathbf{A} \neq \mathbf{0}$ term should be added to $\mathbf{K}'$ point to match the Dirac point position in the reciprocal space and BI strained Kagome lattice is the only analysed strain case that the vector pseudopotential term must be identically null, similarly to the BI strained graphene (KITT *et al.*, 2012; KITT *et al.*, 2013). Our results lead us to write an analytical strain-induced $\bar{\varepsilon}$-dependent pseudovector potential for the Kagome lattice, based on the model presented by Liu (2020), such as $\mathbf{A} \propto n(\overline{\varepsilon}_{yy} - \overline{\varepsilon}_{xx}, \overline{\varepsilon}_{xy} + \overline{\varepsilon}_{yx})$, where $\overline{\varepsilon}_{ij}$ is given by Eq. (3.5) and the n-parameter governs the strain-dependent hopping variation, given by Eq. (2.17). It is worth mentioning that this $\mathbf{A}$ expression is the same as the one for strained graphene, being this analogy possible due to the hexagonal symmetry shared by the Kagome and graphene lattices.

Figure 44 – Band structures around the Dirac point and in the vicinity of Fermi energy level of the Lieb lattice subjected to the (a) UX, (b) UY, (c) BI, (d) SX, (e) SY, and (f) PS strains. Black solid, blue dotted, and red dashed correspond to the unstrained ($\varepsilon = 0$), hypothetical ($\varepsilon = 0.1$), and real strain ($\varepsilon = 0.1$) cases, respectively. t'_{ij} denotes the strained hopping energies between $s - s'$ sublattices, given by Eq. (2.17) for the real strain case and by $t'_{ij} = t_{ij}$ for the hypothetical strain and unstrained cases.

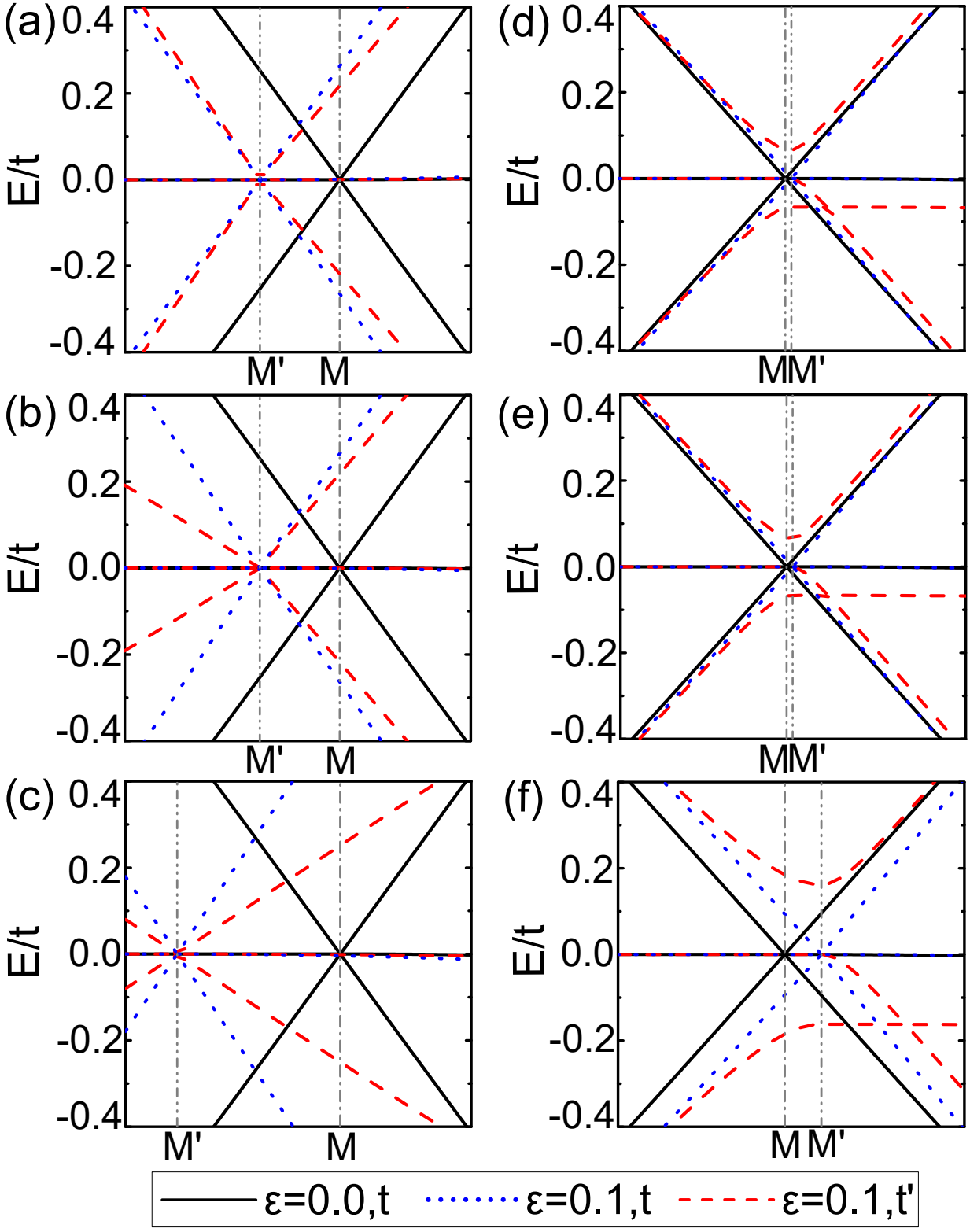

Source: The author Lima *et al.* (2023).

Figure 45 – The same as in Fig. 44, but now for the Kagome lattice.

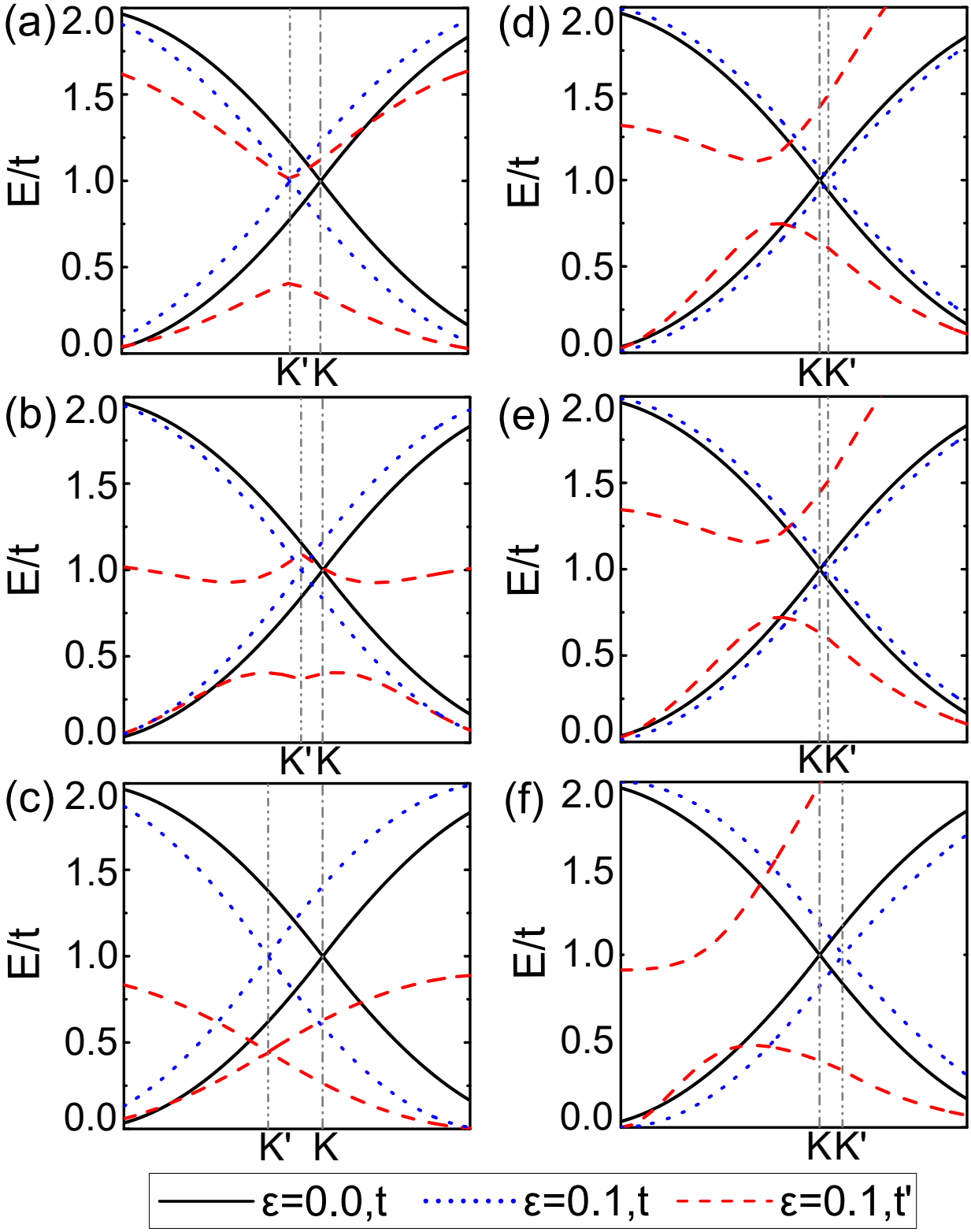

Source: The author Lima *et al.* (2023).

2.11 Synthesis of strain effects on Lieb and Kagome lattices

In Tabs. 2 and 3, we present the main effects of strain on the energy spectrum of the Lieb and Kagome lattices, respectively. We omit some geometric effects, such as the approach or separation of cones and asymmetry in energy levels. Essentially, we list the effects related to the variation of the hopping parameter as a function of strain.

Table 2 – Summary of strain effects on the Lieb lattice.

	UX	**UY**	**BI**	**SX**	**SY**	**PS**
Does it present an energy gap for any strain value?	No	No	No	No	No	No
Does the middle band remain nearly-flat?	Yes	Yes	Yes	No	No	No
Does the triply degenerate point still exist?	Yes	Yes	Yes	No	No	No
Are there two doubly degenerate Dirac points?	No	No	No	Yes	Yes	Yes
Is there the formation of a triply degenerate line?	Yes	Yes	No	No	No	No
Does it indicate a non-zero vector pseudopotential?	No	No	No	Yes	Yes	Yes

Table 3 – Summary of strain effects on the Kagome lattice.

	UX	**UY**	**BI**	**SX**	**SY**	**PS**
Does it present an energy gap for any strain value?	No	No	No	No	No	No
Does the lower band remain nearly-flat?	No	No	Yes	No	No	No
Does it indicate a non-zero vector pseudopotential?	Yes	Yes	No	Yes	Yes	Yes

2.12 Conclusions

In summary, we systematically studied the effects of strain on the electronic properties of the Lieb and Kagome lattices based on a recently proposed TB Hamiltonian reported by Jiang *et al.* (2019c) that takes into account the interconversibility between the Lieb and Kagome lattices by defining a transition lattice that maps such structures by one control parameter. For this purpose, using the concept of a generic lattice (JIANG *et al.*, 2019c; JIANG *et al.*, 2019a; LIM *et al.*, 2020; CUI *et al.*, 2020) and the standard deformation theory, we derived a more general Hamiltonian including the strain tensor for studying in-plane deformation effects on the energy spectra of such structures within the elastic and linear deformation regimes.

Initially, we discussed the evolution of the energy spectra of unstrained Lieb and Kagome lattices in view of their lattice interconversibility. The effects that the variation of the n-parameter, which governs the variation of hoppings parameters, causes on their energy band structures are also investigated. We found that $n = 8$ is the appropriate value to resume the known energy spectra of the unstrained ($\varepsilon = 0$) Lieb and Kagome lattices and, in turn, is the one assumed here to investigate the strained cases ($\varepsilon \neq 0$). We verified that for $n < 8$, the effects of NNN become more evident, causing distortions on the energy spectra, in particular on the nearly-flat band, making it more dispersive. In addition, for Lieb lattice the changes of the n-parameter (taking $n < 8$) do not move the Dirac point, being located in **M** point, that is due to the lattice configuration symmetry of the NNN sites. On the other hand, for Kagome lattice and $n < 8$ the Dirac cone moves away from the **K** point in reciprocal space and the isoenergies become clearly anisotropic.

In general, we observed some effects analogous to those known in the strained graphene literature, such as the presence of anisotropic Fermi velocity, the approach or separation of the Dirac cones, as well as the existence of strain-induced pseudovector potentials for some types of strain. On the other hand, unlike graphene, the strain in the Lieb and Kagome lattices never opens an energy gap. Instead, in general terms, we identified effects such as deformation of the nearly-flat bands, division of the triple degenerate Dirac point in two doubly degenerated Dirac points (in the Lieb lattice), as well as the appearance of non-null vector pseudopotential terms in some types of strain.

The results showed that the nearly-flat band deforms without opening an energy gap for strains applied in the Lieb and Kagome lattices. For the cases of UX, UY, and BI strains in the Lieb lattice, the nearly-flat band deforms such that the original triple degenerate Dirac point

splits into two doubly degenerated Dirac points that shift in opposite directions away from the zero energy level.

In addition, for some cases of strain, we found that there are non-null strain-induced pseudovector potentials, as SX, SY and PS strains in the Lieb lattice, and UX, UY, SX, SY and PS strains in the Kagome lattice. Thus, we conclude that for the Lieb lattice $\mathbf{A} \propto n(0, \overline{\varepsilon}_{xy} + \overline{\varepsilon}_{yx})$, with $\overline{\varepsilon}_{ij}$ given by Eq. (3.5) and the n-parameter being the one that governs the variation of hoppings parameters with the strain [Eq. (2.17)]. On the other hand, the general expression of strain-induced pseudovector potentials for the Kagome lattice must be $\mathbf{A} \propto n(\overline{\varepsilon}_{yy} - \overline{\varepsilon}_{xx}, \overline{\varepsilon}_{xy} + \overline{\varepsilon}_{yx})$, as demonstrated by Liu (2020).

Furthermore, we find that some strain effects in the energy spectra are due exclusively to the variation of the hopping parameters with the strain. Such effects disappear for the hypothetical case, *i. e.*, when we assume that the strain tensor only modifies the configuration of sites of the real lattices, keeping unchanged the hopping parameters. Examples of this are the deformations in the nearly-flat band, the separation of the triple degenerate Dirac point in two doubly degenerated Dirac points (in Lieb lattice), and the formation of the triple degenerate Dirac band with the presence of a type-III Dirac point (critically tilted), combining nearly-flat band and linear dispersions. On the other hand, some effects are seem to arise exclusively from deformations in real space, which are maintained in hypothetical cases of strains, such as: the approximation or separation of Dirac cones and the asymmetry in the energy level curves.

We believe that such a systematic study pertinent to the effects of different types of strains applied in 2D lattices with the coexistence of nearly-flat and conical bands is very interesting for understanding the defects' effects on the optoelectronic properties of nearly-flat band 2D systems. This is, the 2D materials' electrical and optical properties and consequently their band gap tunability and band deformations can be dictated by strain engineering, being one of the various approaches for the proposes aiming to the application of 2D lattices for future 2D device technologies.

3 TOPOLOGICAL PHASE TRANSITIONS IN STRAINED LIEB-KAGOME LATTICES

Lieb and Kagome lattices exhibit 2D TI behavior with $\mathbb{Z}_2$ topological classification when considering ISO coupling. In this chapter, we used a general TB Hamiltonian with a morphological control parameter θ to describe the Lieb ($\theta = \pi/2$), Kagome ($\theta = 2\pi/3$), and transition lattices ($\pi/2 < \theta < 2\pi/3$) while considering ISO coupling. As in the previous chapter, here we systematically investigated the effects of shear and uniaxial strains, applied along different crystallographic directions, on the electronic spectrum of these structures. Our findings reveal that these deformations can induce TPT by modifying the structural lattice angle associated with the interconversibility process between Lieb and Kagome, the amplitude of the strain, and the magnitude of the ISO coupling. These transitions are confirmed by the evolution of Berry curvature and by changes in the Chern number when the gap closes. Additionally, by analyzing hypothetical strain scenarios in which the hopping and ISO coupling parameters remain intentionally unchanged, our results demonstrate that the strain-induced phase transitions arise from simultaneous changes in the hopping and ISO coupling parameters.

3.1 Motivation

In recent years, the investigation of topological phases of matter has emerged as an important subarea of condensed matter physics (BERNEVIG, 2013; BANSIL *et al.*, 2016). Striking examples of these phases of matter are the materials known as TI, which are found to display insulating behavior in bulk, whereas their surface supports conducting states (KANE, 2008; HASAN; KANE, 2010; MOORE, 2010). In 2D TI, the boundaries correspond to edges, where non-trivial topological phases give rise to gapless edge states (KANE; MELE, 2005a; KANE; MELE, 2005b). In general, non-magnetic insulators with preserved TR symmetry are characterized by the $\mathbb{Z}_2$ invariant ν, where an odd ν value represents a 2D TI, *i.e.*, quantum spin Hall insulator (QSHI), and an even ν value represents a trivial insulator (KANE; MELE, 2005a; KANE; MELE, 2005b; FU; KANE, 2007; QI *et al.*, 2008). Alternatively, the spin Chern number is an efficient and convenient way to distinguish different non-trivial topological states; incidentally, the $\mathbb{Z}_2$ invariant can also be calculated using the spin Chern numbers (FU; KANE, 2007).

TPTs are characterized by a change in the spin Chern number calculated for topological invariants of energy bands, typically observed as the closing and reopening of the band

Figure 46 – (a) Lieb-Kagome lattice. $\mathbf{a_{01}}$ and $\mathbf{a_{02}}$ are the primitive vectors of the unstrained lattice, and the shaded unit cell contains three non-equivalent sites: A (blue empty circle), B (yellow filled circle), and C (green circle with a dot inside). The distance between NN sites is a_0, and the non-zero hopping parameters are represented by t_{AB}, t'_{AB}, t_{BC}, t'_{BC}, t_{AC}, and t'_{AC}. The ISO phase is positive ($+i\lambda_{\langle ij\rangle}$) for spin-up electrons moving along the blue ($\lambda_{\langle ij\rangle}$) or red ($\lambda_{\langle\langle ij\rangle\rangle}$) dotted line counterclockwise, since $|\mathbf{e_{ij}}| = +1$. Otherwise, the ISO coupling phase is negative ($-i\lambda_{ij}$) where $|\mathbf{e_{ij}}| = -1$. (b-g) Comparison of the unit cell of the Lieb-Kagome lattice: (i) unstrained (black solid lines), $\varepsilon = 0$, and (ii) strained (red dashed lines), $\varepsilon > 0$, subjected to: (b) UX, (c) UY, (d) BI, (e) SX, (f) SY, and (g) PS strains.

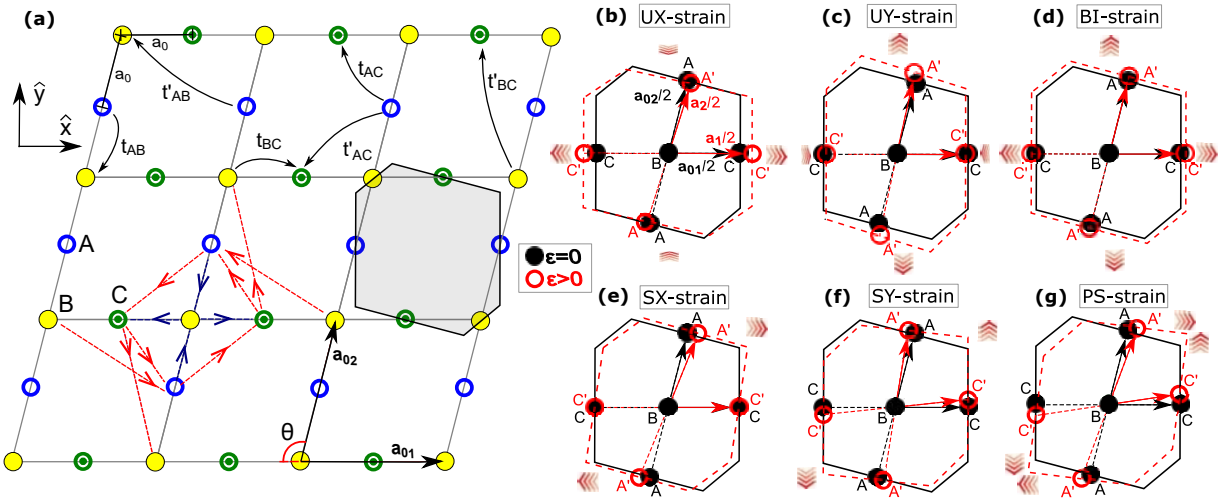

Source: The author.

gap (MURAKAMI, 2007; MURAKAMI *et al.*, 2007; HASAN; KANE, 2010). Theoretical and experimental studies have demonstrated that TPT can be induced by manipulating the band structure through strain (AGAPITO *et al.*, 2013; LIU; XU YONG E WU, 2014; PAL; WAGHMARE, 2014; QIAN *et al.*, 2015; LI *et al.*, 2015; KIRTSCHIG *et al.*, 2016; WANG *et al.*, 2017; KIBIS *et al.*, 2019; MUTCH *et al.*, 2019; TESHOME; DATTA, 2019; JIANG *et al.*, 2020; NICHOLSON *et al.*, 2021; BHATTARAI *et al.*, 2024; XING *et al.*, 2024), as well as through other means, such as chemical substitution, pressure, and electron correlation effects (PESIN; BALENTS, 2010; WAN *et al.*, 2011; WRAY *et al.*, 2011; XU *et al.*, 2011; WU *et al.*, 2013).

In this chapter, we present calculations that demonstrate that TPT can be driven by uniaxial and shear strains in 2D Lieb (WEEKS; FRANZ, 2010; GOLDMAN *et al.*, 2011b) , transitions (JIANG *et al.*, 2019c; JIANG *et al.*, 2019a; CUI *et al.*, 2020; LIM *et al.*, 2020; LANG *et al.*, 2023) and Kagome (GUO; FRANZ, 2009) lattices. These lattices are QSHI, exhibiting characteristic behavior of TI with $\mathbb{Z}_2$ topological classification when the ISO coupling is taken into account (WEEKS; FRANZ, 2010; TITVINIDZE *et al.*, 2021).

In our study, we adopt an approach similar to Ch. 2, with the notable distinction that we incorporate the ISO coupling into the Lieb-Kagome lattice. Our aim is to elucidate the

topological evolution of the Lieb, transition, and Kagome lattices under the six types of strain investigated in Ch. 2 (LIMA *et al.*, 2023) and represented in Fig. 46 (b-g panels).

Previous studies have investigated TPT in Lieb (WANG *et al.*, 2016; CHEN; ZHOU, 2017; JIANG *et al.*, 2020) or Kagome (LIU *et al.*, 2012; BOLENS; NAGAOSA, 2019; TITVINIDZE *et al.*, 2021; ZHAO *et al.*, 2022; DENG *et al.*, 2024; MOJARRO; ULLOA, 2023) lattices, as well as in both types (BEUGELING *et al.*, 2012; ABLOWITZ; COLE, 2019; JIANG *et al.*, 2019c). Typically, these studies consider the inclusion of ISO coupling and have identified several methods to drive TPT, including: (i) adjusting the strength of a real NNN hopping term (BEUGELING *et al.*, 2012), (ii) incorporating RSO coupling with spin-independent and spin-dependent staggered potentials (CHEN; ZHOU, 2017), (iii) tuning the trimerization parameter by considering different hopping amplitudes on two distinct sets of lattices (BOLENS; NAGAOSA, 2019), (iv) decomposing the lattice into three sublattices that can move independently (ABLOWITZ; COLE, 2019), (v) employing artificial gauge fields represented as spin-dependent Peierls phases (TITVINIDZE *et al.*, 2021), (vi) pressure (DENG *et al.*, 2024) and (vii) by applying mechanical strain to these lattices (JIANG *et al.*, 2020; ZHAO *et al.*, 2022; MOJARRO; ULLOA, 2023; XING *et al.*, 2024).

Jiang *et al.* (2020) demonstrated TPT in phthalocyanine-based metal-organic frameworks (MPc-MOFs) with a Lieb band structure via biaxial strain engineering. Similarly, Zhao *et al.* (2022) showed that weaker ISO coupling-induced TPT under uniaxial strain. Mojarro e Ulloa (2023) demonstrated theoretical TPT in Kagome lattices under uniaxial strain, RSO coupling, and site asymmetries. More recently, Xing *et al.* (2024) observed topological edge state modulation in 2D ferromagnetic V_3F_8 under uniaxial strain, highlighting the electronic Kagome lattice's signature transition.

However, it is important to note that these previous studies did not employ a versatile generic TB model to study transition lattices or conduct a comparative analysis of the effects of strain on the TPT of Lieb and Kagome lattices. Furthermore, they primarily focused on uniaxial or biaxial strains and did not explore the full range of strain types that we have incorporated in our model. Thus, to the best of our knowledge, there is a lack of systematic studies exploring the potential TPT driven by uniaxial and shear strains in the Lieb, transition, and Kagome lattices in the existing literature.

The chapter is structured as follows: In Sec. 3.2, we introduce the TB model with ISO coupling for the Lieb-Kagome lattice under strain. In Sec. 3.3 the comparison with previous

models for unstrained lattices, and the evaluation of the Chern numbers in Sec. 3.4. Sec. 3.5 and Sec. 3.6 are dedicated to discussing TPT in the unstrained and strained Lieb-Kagome lattice, respectively. In both sections, we present the closing and reopening of the full[1] and local[2] band gaps for $1/3$ and $2/3$ filling,[3] the evolution of the Berry curvature, and changes in the spin Chern numbers as evidence of TPT. For completeness, as evaluated in the previous chapter, in Sec. 3.7 we discuss the results for hypothetical strains. Finally, in Sec. 3.8, we provide the main concluding remarks.

3.2 Tight-binding model with intrinsic spin-orbit coupling

The general TB Hamiltonian that applies to strained Lieb-Kagome lattices presented in this chapter reads

$$\hat{H} = \hat{H}_0 + \hat{H}_{\mathrm{ISO}}, \tag{3.1}$$

with

$$\hat{H}_0 = \sum_{i,j;\sigma} t_{ij} \hat{s}^{\dagger}_{i,\sigma} \hat{s}_{j,\sigma} + h.c. \tag{3.2a}$$

$$\hat{H}_{\mathrm{ISO}} = \sum_{i,j;\sigma,\sigma'} i\lambda_{ij} \hat{s}^{\dagger}_{i,\sigma} \left(\mathbf{e}_{ij} \cdot \boldsymbol{\sigma}_{\sigma\sigma'} \right) \hat{s}_{j,\sigma'} + h.c., \tag{3.2b}$$

Here, $\hat{s}_{i,\sigma}$ ($\hat{s}^{\dagger}_{i,\sigma}$) represents the annihilation (creation) operator for a particle on-site i with spin σ. The first term, $\hat{H}_0$, describes the hoppings considered in our TB model (see Sec. 2.4). The second term, $\hat{H}_{\mathrm{ISO}}$, represents the ISO coupling Hamiltonian; in this term, we define the unit vector $\mathbf{e}_{ij} = \left(\mathbf{d}_{ik} \times \mathbf{d}_{kj} \right) / \left| \mathbf{d}_{ik} \times \mathbf{d}_{kj} \right|$ in terms of the bond vectors $\mathbf{d}_{ik}$ and $\mathbf{d}_{kj}$, connecting the sites i and j through the unique intermediate site k (BEUGELING *et al.*, 2012). Finally, $\boldsymbol{\sigma} = (\sigma_x, \sigma_y, \sigma_z)$ represents the Pauli matrices.

[1] A full band gap refers to an energy range in an electronic structure where no electronic states can exist. This gap separates the valence band from the conduction band for all k. This means that the maximum energy of the bottom band E_1 is always less than the minimum energy of the middle band E_2, guaranteeing a full gap at $1/3$ filling different from zero for all k values in the BZ, *i.e.*, $\Delta_{12} \neq 0$. Similarly, when the maximum energy of the middle band E_2 is always less than the minimum energy of the upper band E_3, we ensure a full gap at $2/3$ filling different from zero for all k values in the BZ, *i.e.*, $\Delta_{23} \neq 0$.

[2] The local band gap refers to the minimum separation between the bands at each individual point in momentum space. Thus, a non-null local band gap indicates that the bands are separated at each point in the BZ without band crossing. However, the minimum energy of the upper [middle] band is lower than the maximum energy of the middle [bottom] band at different points in momentum space, leading to an indirect band gap at $2/3$ [$1/3$] filling.

[3] The terms $1/3$ filling and $2/3$ filling refer to the proportion of the electronic states that are occupied in the bands. At 1/3 filling, one-third of the available electronic states in the system are occupied, typically filling the lower energy bands. At 2/3 filling, two-thirds of the available electronic states are occupied, filling both the lower and middle energy bands.

In 2D lattices, hopping processes are naturally restricted to in-plane motions, making the ISO coupling effectively proportional to σ_z. Thus, Eq. (3.2b) can be written as (JIANG *et al.*, 2019c)

$$\hat{H}_{\mathrm{ISO}} = \sum_{i,j;\sigma,\sigma'} e_{ij} i\lambda_{ij} \hat{s}^{\dagger}_{i,\sigma} \sigma_z \hat{s}_{j,\sigma'} + h.c.. \tag{3.3}$$

We obtain $e_{ij} = \pm 1$, where the positive value is assigned to the case where the electron shows a leftward deviation (counterclockwise direction) and the negative value when it shows a rightward deviation (clockwise direction). The λ_{ij} represent the amplitudes of the ISO coupling, while t_{ij} are the hopping parameters depicted in Fig. 46 (a), obeying the Eq. (2.17) (LIMA *et al.*, 2022; LIMA *et al.*, 2023),

$$t_{ij} = te^{-n\left(a_{ij}/a_0 - 1\right)} a_0/a_{ij}, \qquad n = 8, \tag{3.4}$$

where t (= 1.0 eV) is the value of the hopping parameter corresponding to the distance between NN sites in the unstrained Lieb-Kagome lattice, *i.e.*, a_0, and a_{ij} is the distance between the sites i and j of types A, B, or C in the strained lattice, calculated by $\mathbf{a_{ij}} = (\mathbb{I} + \overline{\varepsilon})\mathbf{a_{0,ij}}$, with

$$\overline{\varepsilon} = \begin{pmatrix} \varepsilon_{xx} - \sigma_p \varepsilon_{yy} & \varepsilon_{xy} \\ \varepsilon_{yx} & \varepsilon_{yy} - \sigma_p \varepsilon_{xx} \end{pmatrix}, \tag{3.5}$$

where $\sigma_p = 0.1$ denotes the Poisson ratio (PEREIRA *et al.*, 2009), and the ε_{ij} values (with $i, j = x, y$) are summarized in Table 1 for all six investigated deformations, which are depicted in Fig. 46 (b-g).

From Eq. (3.4) it is seen that the value of n controls the magnitude of the hopping parameters. For a given distance between sites, the corresponding hopping value will decrease (increase) as the value of the n-parameter increases (decreases). As discussed by Lima *et al.* (2023), the effects of sites more distant than the NN sites are suppressed for $n \geq 8$ and intensified for $n < 8$. With $n = 8$, we obtain both nearly-flat bands and smooth transitions between the two lattices (JIANG *et al.*, 2019c), thus finding a good approximation for the TB model of NN sites in the specific cases of the Lieb and Kagome lattices (JIANG *et al.*, 2019c; LIMA *et al.*, 2023).

Similarly, we consider λ_{ij} given by (JIANG *et al.*, 2019c)

$$\lambda_{ij} = \lambda_{\mathrm{ISO}} e^{-\left(d_{ij}/a_0 - 1\right)^n} a_0/d_{ij}, \qquad n = 8, \tag{3.6}$$

with $\lambda_{\mathrm{ISO}} = \lambda t$, where λ governs the strength of ISO coupling. We generally consider $\lambda = 0.2$.[4] We admit $n = 8$ in agreement with the expression that governs the hopping parameters [Eq. (3.4)].

[4] We adopt $\lambda = 0.2$ for convenience, as this value provides clear gaps in the Lieb-Kagome energy spectrum, as seen in Fig. 48. Smaller values of λ would result in smaller, less visible gaps. For completeness, we will investigate the evolution of the energy gaps as a function of varying λ in Fig. 54.

In our model, we consider the hopping parameters corresponding to neighboring sites located by $\mathbf{R_{BA}}^{\pm} = \pm\mathbf{a_2}/2$, $\mathbf{R'_{BA}}^{\pm} = \pm(\mathbf{a_2}/2 - \mathbf{a_1})$, $\mathbf{R_{BC}}^{\pm} = \pm\mathbf{a_1}/2$, $\mathbf{R'_{BC}}^{\pm} = \pm(\mathbf{a_1}/2 - \mathbf{a_2})$, $\mathbf{R_{AC}}^{\pm} = \pm(\mathbf{a_1} - \mathbf{a_2})/2$, and $\mathbf{R'_{AC}}^{\pm} = \pm(\mathbf{a_1} + \mathbf{a_2})/2$, as displayed in Fig. 47 (a). Thus, applying a Fourier transformation to the real-space Hamiltonian [Eq. (3.2)],

$$\hat{s}_{i,\sigma} = \frac{1}{\sqrt{N}}\sum_{\mathbf{k}} e^{i\mathbf{k}\cdot\mathbf{r_i}}\hat{s}_{\mathbf{k},\sigma}, \tag{3.7a}$$

$$\hat{s}^{\dagger}{}_{i,\sigma} = \frac{1}{\sqrt{N}}\sum_{\mathbf{k}} e^{-i\mathbf{k}\cdot\mathbf{r_i}}\hat{s}^{\dagger}{}_{\mathbf{k},\sigma}, \tag{3.7b}$$

we find the Hamiltonian in momentum space (LIMA *et al.*, 2022),

$$\hat{H} = \sum_{\mathbf{k}} \hat{\Psi}^{\dagger}_{\mathbf{k}} H(\mathbf{k}) \hat{\Psi}_{\mathbf{k}}, \tag{3.8}$$

with

$$H(\mathbf{k}) = H_0(\mathbf{k}) \otimes \mathbb{1}_{2\times 2} + H_{\mathrm{ISO}}(\mathbf{k}) \otimes \sigma_z, \tag{3.9}$$

where $\hat{\Psi}_{\mathbf{k}} \equiv (\hat{\Psi}_{\mathbf{k},\uparrow}, \hat{\Psi}_{\mathbf{k},\downarrow})^T$ with $\hat{\Psi}_{\mathbf{k},\sigma} \equiv (\hat{a}_{\mathbf{k},\sigma}, \hat{b}_{\mathbf{k},\sigma}, \hat{c}_{\mathbf{k},\sigma})^T$, where $H_0(\mathbf{k})$ and $H_{\mathrm{ISO}}(\mathbf{k})$ are 3×3 matrices presented below (BEUGELING *et al.*, 2012).

The $H_0(\mathbf{k})$ is given by (see Sec. 2.4)

$$H_0(\mathbf{k}) = \begin{pmatrix} H_{\mathbf{0}}^{AA}(\mathbf{k}) & H_{\mathbf{0}}^{AB}(\mathbf{k}) & H_{\mathbf{0}}^{AC}(\mathbf{k}) \\ & H_{\mathbf{0}}^{BB}(\mathbf{k}) & H_{\mathbf{0}}^{BC}(\mathbf{k}) \\ & & H_{\mathbf{0}}^{CC}(\mathbf{k}) \end{pmatrix}, \tag{3.10}$$

where

$$H_{\mathbf{0}}^{AB}(\mathbf{k}) = 2t_{AB}\cos(\mathbf{k}\cdot\mathbf{a_2}/2) + 2t'_{AB}\cos[\mathbf{k}\cdot(\mathbf{a_2}/2 - \mathbf{a_1})], \tag{3.11a}$$

$$H_{\mathbf{0}}^{BC}(\mathbf{k}) = 2t_{BC}\cos(\mathbf{k}\cdot\mathbf{a_1}/2) + 2t'_{BC}\cos[\mathbf{k}\cdot(\mathbf{a_1}/2 - \mathbf{a_2})], \tag{3.11b}$$

$$H_{\mathbf{0}}^{AC}(\mathbf{k}) = 2t_{AC}\cos[\mathbf{k}\cdot(\mathbf{a_1} - \mathbf{a_2})/2] + 2t'_{AC}\cos[\mathbf{k}\cdot(\mathbf{a_1} + \mathbf{a_2})/2]. \tag{3.11c}$$

The lower triangle of the matrix should be filled accordingly for a Hermitian matrix, which is not shown. The hopping parameters t_{ij} (t'_{ij}) are shown in Fig. 46 (a), whose values are governed by Eq. (3.4).

As in the previous chapter, the on-site energies and the hopping parameters between equivalent sites are considered null throughout this thesis, such that $H_{\mathbf{0}}^{AA}(\mathbf{k}) = H_{\mathbf{0}}^{BB}(\mathbf{k}) = H_{\mathbf{0}}^{CC}(\mathbf{k}) = 0$.

Figure 47 – (a) Transition lattice - D_{2h} with $\theta = 105°$, (b) Lieb lattice - D_{4h} ($\theta = 90°$), and (c) Kagome lattice - D_{6h} ($\theta = 120°$). The primitive vectors are $\mathbf{a_1}$ and $\mathbf{a_2}$, and the unit cells contain three non-equivalent sites A (blue empty circle), B (yellow filled circle), and C (green circle with a dot inside). Neighboring sites are denoted by $\mathbf{R}^{\pm}_{\mathbf{BA}} = \pm\mathbf{a_2}/2$ (solid black vectors), $\mathbf{R'}^{\pm}_{\mathbf{BA}} = \pm(\mathbf{a_2}/2 - \mathbf{a_1})$ (green dot-dashed vectors), $\mathbf{R}^{\pm}_{\mathbf{BC}} = \pm\mathbf{a_1}/2$ (solid black vectors), $\mathbf{R'}^{\pm}_{\mathbf{BC}} = \pm(\mathbf{a_1}/2 - \mathbf{a_2})$ (blue dotted vectors), $\mathbf{R}^{\pm}_{\mathbf{AC}} = \pm(\mathbf{a_1} - \mathbf{a_2})/2$ (dashed orange vectors), and $\mathbf{R'}^{\pm}_{\mathbf{AC}} = \pm(\mathbf{a_1} + \mathbf{a_2})/2$ (red short dashed vectors). (b-c) The ISO phase is positive ($+i\lambda_{\langle ij\rangle}$) for spin-up electrons moving counterclockwise along the blue solid ($+i\lambda_{\langle ij\rangle}$), red dashed ($+i\lambda_{\langle\langle ij\rangle\rangle}$), or green dot-dashed ($+i\lambda_{\langle\langle\langle ij\rangle\rangle\rangle}$) lines, where $|\mathbf{e_{ij}}| = +1$. Conversely, the ISO coupling phase is negative ($-i\lambda_{ij}$) where $|\mathbf{e_{ij}}| = -1$. In Lieb and transition lattices, the term ($+i\lambda_{\langle ij\rangle}$) remains in the Lieb-Kagome lattice Hamiltonian as complex hoppings connecting NN sites for completeness, aimed at observing their effects on the energy evolution when transitioning from Kagome to Lieb, through stages of evolution. The terms ($+i\lambda_{\langle\langle\langle ij\rangle\rangle\rangle}$) are effectively null in Lieb lattice, due to Eq. (3.6), but are retained in the Lieb-Kagome model as they become ($+i\lambda_{\langle\langle ij\rangle\rangle}$) in Kagome lattice.

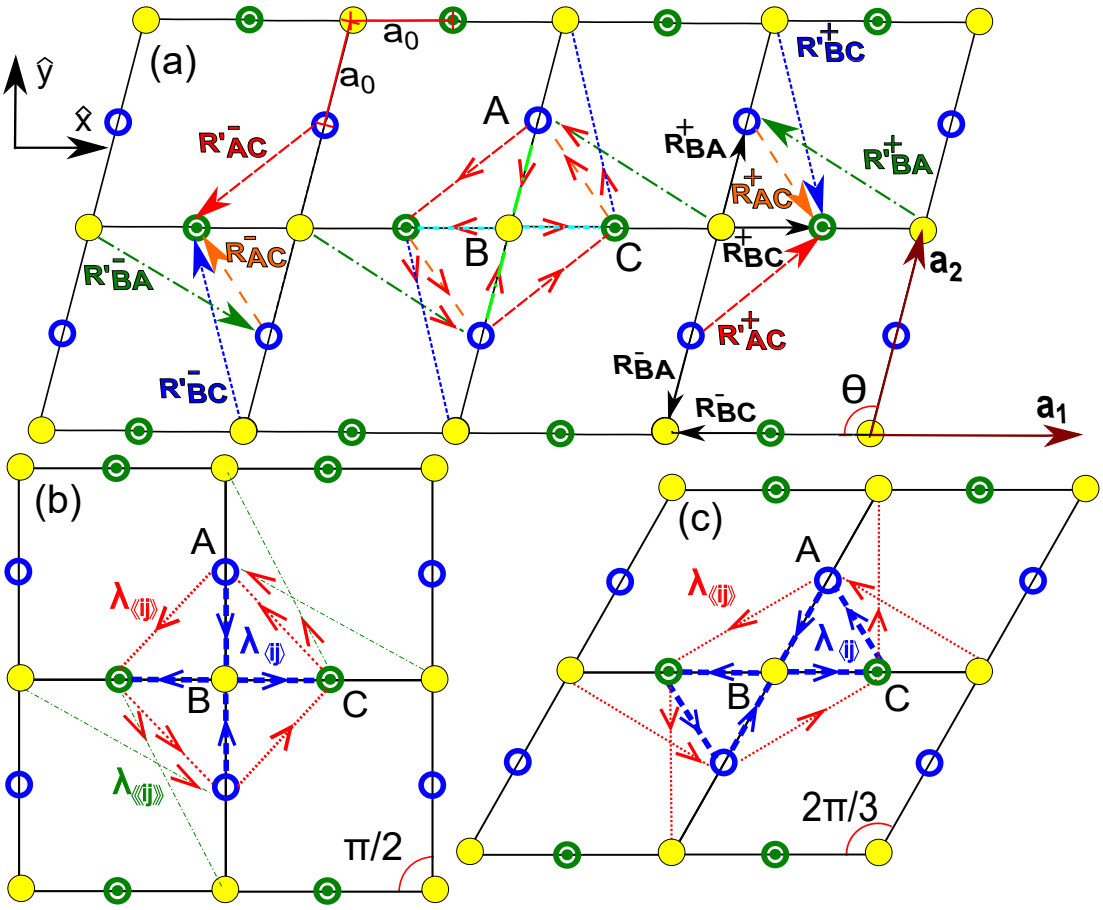

Source: The author.

The $H_{\mathrm{ISO}}(\mathbf{k})$ is given by

$$H_{\mathrm{ISO}}(\mathbf{k}) = \begin{pmatrix} 0 & H^{AB}_{\mathrm{ISO}}(\mathbf{k}) & H^{AC}_{\mathrm{ISO}}(\mathbf{k}) \\ & 0 & H^{BC}_{\mathrm{ISO}}(\mathbf{k}) \\ & & 0 \end{pmatrix}, \tag{3.12}$$

with

$$H_{\mathrm{ISO}}^{AB}(\mathbf{k}) = -2i\lambda_{AB}\cos\left(\mathbf{k}\cdot\mathbf{a_2}/2\right) + 2i\lambda'_{AB}\cos\left[\mathbf{k}\cdot\left(\mathbf{a_2}/2-\mathbf{a_1}\right)\right], \tag{3.13a}$$

$$H_{\mathrm{ISO}}^{BC}(\mathbf{k}) = -2i\lambda_{BC}\cos\left(\mathbf{k}\cdot\mathbf{a_1}/2\right) + 2i\lambda'_{BC}\cos\left[\mathbf{k}\cdot\left(\mathbf{a_1}/2-\mathbf{a_2}\right)\right], \tag{3.13b}$$

$$H_{\mathrm{ISO}}^{AC}(\mathbf{k}) = 2i\lambda_{AC}\cos\left[\mathbf{k}\cdot\left(\mathbf{a_1}-\mathbf{a_2}\right)/2\right] - 2i\lambda'_{AC}\cos\left[\mathbf{k}\cdot\left(\mathbf{a_1}+\mathbf{a_2}\right)/2\right]. \tag{3.13c}$$

The λ_{ij} (λ'_{ij}) correspond to the distances between the sites located by $\mathbf{R_{ij}}^{\pm}$ ($\mathbf{R'_{ij}}^{\pm}$), represented in Fig. 47.

The Hamiltonian matrix $H(\mathbf{k})$ consists of two uncoupled blocks corresponding to the spin-up and spin-down projections, related by TR symmetry, i.e., $H_{\mathrm{ISO}}^{\downarrow}(\mathbf{k}) = \left[H_{\mathrm{ISO}}^{\uparrow}(-\mathbf{k})\right]^{*}$. Due to the TR and inversion symmetries, the ISO coupling is unable to lift the spin degeneracy. For the calculation of the energy spectrum, it thus suffices to restrict our attention to one spin component, while keeping in mind that the resulting bands are doubly degenerate (BEUGELING *et al.*, 2012).

3.3 Comparison with previous models for unstrained lattices

Due to the generality of our model, which includes deformations in the lattices by variation of θ and application of strain, we admit $\mathbf{d}_{ik}$ and $\mathbf{d}_{kj}$ equal to $\mathbf{R_{BA}}^{\pm}$ ($=\pm\mathbf{a_2}/2$), $\mathbf{R_{BC}}^{\pm}$ ($=\pm\mathbf{a_1}/2$) and $\mathbf{R_{AC}}^{\pm}$ ($=\pm\left(\mathbf{a_1}-\mathbf{a_2}\right)/2$). Thus, we evaluated the amplitudes of ISO coupling λ_{ij} given by Eq. (3.6), with d_{ij} equal to module of $\mathbf{R_{BA}}^{\pm}$ ($=\pm\mathbf{a_2}/2$), $\mathbf{R'_{BA}}^{\pm}$ $[=\pm\left(\mathbf{a_1}-\mathbf{a_2}/2\right)]$, $\mathbf{R_{BC}}^{\pm}$ ($=\pm\mathbf{a_1}/2$), $\mathbf{R'_{BC}}^{\pm}$ $[=\pm\left(\mathbf{a_2}-\mathbf{a_1}/2\right)]$, $\mathbf{R_{AC}}^{\pm}$ $[=\pm\left(\mathbf{a_1}-\mathbf{a_2}\right)/2]$, $\mathbf{R'_{AC}}^{\pm}$ $[=\pm\left(\mathbf{a_1}+\mathbf{a_2}\right)/2]$ [see Fig. 47 (a)]. Specifically, we note that: (i) $\mathbf{R_{BA}}^{\pm}$ and $\mathbf{R_{BC}}^{\pm}$ provides the amplitude of ISO coupling calculated with $d_{ij} = \{|\mathbf{R_{AC}}^{\pm}|, |\mathbf{R'_{AC}}^{\pm}|\}$, (ii) $\mathbf{R_{BA}}^{\pm}$ and $\mathbf{R_{AC}}^{\pm}$ corresponds to $d_{ij} = \{|\mathbf{R_{BC}}^{\pm}|, |\mathbf{R'_{BC}}^{\pm}|\}$, and (iii) $\mathbf{R_{BC}}^{\pm}$ and $\mathbf{R_{AC}}^{\pm}$ leads to $d_{ij} = \{|\mathbf{R_{BA}}^{\pm}|, |\mathbf{R'_{BA}}^{\pm}|\}$.

Previous theoretical models for the particular cases of unstrained Lieb and Kagome lattices usually admitted $\mathbf{d}_{ik}$ and $\mathbf{d}_{kj}$ vectors that localize only NN sites, such that $\mathbf{d}_{ij}$ connect only NNN sites (GUO; FRANZ, 2009; GOLDMAN *et al.*, 2011b; BEUGELING *et al.*, 2012). In order to better compare the present model with previous works, we express the Hamiltonian $H_{\mathbf{0}}(\mathbf{k})$ and $H_{\mathrm{ISO}}(\mathbf{k})$ in terms of $\pi/2 \leq \theta \leq 2\pi/3$, for the unstrained Lieb-Kagome lattice,

$$H_{\mathbf{0}}^{AB}(\mathbf{k}) = 2t_{AB}\cos[-k_x a_0\cos\theta + k_y a_0\sin\theta] + 2t'_{AB}\cos[k_x a(1+\cos\theta/2) - k_y a_0\sin\theta], \quad (3.14a)$$

$$H_{\mathbf{0}}^{BC}(\mathbf{k}) = 2t_{BC}\cos(k_x a_0) + 2t'_{BC}\cos[-k_x a(1/2+\cos\theta) + k_y a\sin\theta], \quad (3.14b)$$

$$H_{\mathbf{0}}^{AC}(\mathbf{k}) = 2t_{AC}\cos[k_x a_0(1+\cos\theta) - k_y a_0\sin\theta] + 2t'_{AC}\cos[k_x a_0(1-\cos\theta) + k_y a_0\sin\theta], \quad (3.14c)$$

and

$$H_{\mathrm{ISO}}^{AB}(\mathbf{k}) = 2i\left[-\lambda_{AB}\cos(-k_x a_0\cos\theta + k_y a_0\sin\theta) + \lambda'_{AB}\cos(-k_x a(1+\cos\theta/2) + k_y a_0\sin\theta)\right], \quad (3.15a)$$

$$H_{\mathrm{ISO}}^{BC}(\mathbf{k}) = 2i\left[-\lambda_{BC}\cos(a_0 k_x) + \lambda'_{BC}\cos(k_x a(1/2+\cos\theta) - k_y a\sin\theta)\right], \quad (3.15b)$$

$$H_{\mathrm{ISO}}^{AC}(\mathbf{k}) = 2i\left[\lambda_{AC}\cos(k_x a_0(1+\cos\theta) - k_y a_0\sin\theta) - \lambda'_{AC}\cos(k_x a_0(1-\cos\theta) + k_y a_0\sin\theta)\right], \quad (3.15c)$$

where we use $a_0 = a/2$ and $\mathbf{a_1} = a(1,0)$ and $\mathbf{a_2} = a(-\cos\theta, \sin\theta)$ for the cases of unstrained lattices, i.e, with $\varepsilon = 0$.

For the Lieb lattice with $\theta = \pi/2$, the Hamiltonian $H_{\mathbf{0},L}$ becomes

$$H_{\mathbf{0},L}^{AB}(\mathbf{k}) = 2t_{AB}\cos(k_y a_0) + 2t'_{AB}\cos\left[a(k_x - k_y/2)\right], \quad (3.16a)$$

$$H_{\mathbf{0},L}^{BC}(\mathbf{k}) = 2t_{BC}\cos\left(k_x a_0\right) + 2t'_{BC}\cos\left[a(k_y - k_x/2)\right], \quad (3.16b)$$

$$H_{\mathbf{0},L}^{AC}(\mathbf{k}) = 2t_{AC}\cos\left[a_0(k_x - k_y)\right] + 2t'_{AC}\cos\left[a_0(k_x + k_y)\right], \quad (3.16c)$$

and the Hamiltonian of ISO coupling, $H_{\mathbf{ISO},L}$, expressed by the elements:

$$H_{\mathrm{ISO},L}^{AB}(\mathbf{k}) = 2i\left[-\lambda_{AB}\cos(k_y a_0) + \lambda'_{AB}\cos[a(k_x - k_y/2)]\right], \quad (3.17a)$$

$$H_{\mathrm{ISO},L}^{BC}(\mathbf{k}) = 2i\left[-\lambda_{BC}\cos(a_0 k_x) + \lambda'_{BC}\cos[a(k_y - k_x/2)]\right], \quad (3.17b)$$

$$H_{\mathrm{ISO},L}^{AC}(\mathbf{k}) = 2i\left[\lambda_{AC}\cos[a_0(k_x - k_y)] - \lambda'_{AC}\cos[a_0(k_x + k_y)]\right]. \quad (3.17c)$$

Equations (3.16) and (3.17) show that in this model the unstrained Lieb lattice [see Fig. 47 (b)], *i.e.* with $\theta = \pi/2$ and $\varepsilon = 0$, has $\mathbf{d}_{ik}$ and $\mathbf{d}_{kj}$ that are (i) NN sites ($\mathbf{R_{BA}}^{\pm}$, $\mathbf{R_{BC}}^{\pm}$) and (ii) NNN sites ($\mathbf{R_{AC}}^{\pm}$, $\mathbf{R'_{AC}}^{\pm}$), such that $\mathbf{d}_{ij}$ connect (i') NNN sites ($\mathbf{R_{AC}}^{\pm}$, $\mathbf{R'_{AC}}^{\pm}$), but also connect (ii') fourth NN sites ($\mathbf{R'_{BA}}^{\pm}$, $\mathbf{R'_{BC}}^{\pm}$). The hopping parameters between third NN correspond to equivalents sites that are disregarded in our model together with the on-site energies, similarly to the models of Beugeling *et al.* (2012) and Jiang *et al.* (2019c). Firstly, since Eq. (3.4) automatically makes t_{AC}, t'_{AC}, t'_{AB} and t'_{BC} negligible, similar to TB models of first neighbors for these particular case, *i.e.* with only t_{AB} and t_{BC} significantly non-null. Secondly,

due to the fact that Eq. (3.6) makes λ'_{AB} and λ'_{BC} negligible as well, while only λ_{AC} and λ'_{AC} are significant in accordance with previous models for these particular case (GOLDMAN *et al.*, 2011b; BEUGELING *et al.*, 2012). The λ_{AB} and λ_{BC} are spin orbit amplitudes of NN sites, included in the present model for completeness. Therefore, assuming $t_{AC} = t'_{AC} = t'_{AB} = t'_{BC} = 0$, $\lambda'_{AB} = \lambda'_{BC} = 0$, knowing that $t_{AB} = t_{BC} = t$ and $\lambda_{AC} = \lambda'_{AC} = \lambda_{ISO}$, and disregarding the ISO coupling parameters of NN sites ($\lambda_{AB} = \lambda_{BC} = 0$), the Hamiltonian $H_{\mathbf{0},L}$ and $H^{AB}_{\mathrm{ISO},L}$ from the Goldman *et al.* (2011b) and Beugeling *et al.* (2012) result, given by

$$H^{AB}_{\mathbf{0},L}(\mathbf{k}) = 2t\cos(k_y a_0), \tag{3.18a}$$

$$H^{BC}_{\mathbf{0},L}(\mathbf{k}) = 2t\cos\left(k_x a_0\right), \tag{3.18b}$$

$$H^{AC}_{\mathbf{0},L}(\mathbf{k}) = 0. \tag{3.18c}$$

and

$$H^{AB}_{\mathrm{ISO},L}(\mathbf{k}) = 0, \tag{3.19a}$$

$$H^{BC}_{\mathrm{ISO},L}(\mathbf{k}) = 0, \tag{3.19b}$$

$$H^{AC}_{\mathrm{ISO},L}(\mathbf{k}) = 2i\lambda_{ISO}\cos\left[a_0(k_x - k_y)\right] - 2i\lambda_{ISO}\cos\left[a_0(k_x + k_y)\right]. \tag{3.19c}$$

For the case of unstrained Kagome lattice with $\theta = 2\pi/3$ and $\varepsilon = 0$ (see Fig. 47c) we obtain the Hamiltonian $H_{\mathbf{0},K}$ given by

$$H^{AB}_{\mathbf{0},K}(\mathbf{k}) = 2t_{AB}\cos\left[a_0/2(k_x + \sqrt{3}k_y)\right] + 2t'_{AB}\cos\left[a_0/2(3k_x - \sqrt{3}k_y)\right], \tag{3.20a}$$

$$H^{BC}_{\mathbf{0},K}(\mathbf{k}) = 2t_{BC}\cos(a_0 k_x) + 2t'_{BC}\cos\left(\sqrt{3}a_0 k_y\right), \tag{3.20b}$$

$$H^{AC}_{\mathbf{0},K}(\mathbf{k}) = 2t_{AC}\cos\left[a_0/2(k_x - \sqrt{3}k_y)\right] + 2t'_{AC}\cos\left[a_0/2(3k_x + \sqrt{3}k_y)\right], \tag{3.20c}$$

and $H_{\mathrm{ISO},K}(\mathbf{k})$, whose elements are given by

$$H^{AB}_{\mathrm{ISO},K}(\mathbf{k}) = -2i\lambda_{AB}\cos\left[a_0/2(k_x + \sqrt{3}k_y)\right] + 2i\lambda'_{AB}\cos\left[a_0/2(3k_x - \sqrt{3}k_y)\right], \tag{3.21a}$$

$$H^{BC}_{\mathrm{ISO},K}(\mathbf{k}) = -2i\lambda_{BC}\cos(a_0 k_x) + 2i\lambda'_{BC}\cos\left(\sqrt{3}a_0 k_y\right), \tag{3.21b}$$

$$H^{AC}_{\mathrm{ISO},K}(\mathbf{k}) = 2i\lambda_{AC}\cos\left[a_0/2(k_x - \sqrt{3}k_y)\right] - 2i\lambda'_{AC}\cos\left[a_0/2(3k_x + \sqrt{3}k_y)\right]. \tag{3.21c}$$

So, the generic model for this is case entails $\mathbf{d}_{ik}$ and $\mathbf{d}_{kj}$ that are NN sites ($\mathbf{R_{BA}}^{\mp}$, $\mathbf{R_{BC}}^{\pm}$, $\mathbf{R_{AC}}^{\pm}$), such that $\mathbf{d}_{ij}$ connect: (i) NNN sites ($\mathbf{R'_{BA}}^{\pm}$, $\mathbf{R'_{BC}}^{\pm}$, $\mathbf{R'_{AC}}^{\pm}$) and (ii) NN sites ($\mathbf{R_{AC}}^{\pm}$, $\mathbf{R_{BA}}^{\pm}$, $\mathbf{R_{BC}}^{\pm}$). Explicitly, this last point occurs because the (i) $\mathbf{d}_{ik} = \mathbf{R_{AB}}^{\pm} \equiv \mathbf{R_{BA}}^{\mp}$ and $\mathbf{d}_{kj} = \mathbf{R_{BC}}^{\pm}$ correspond to $\mathbf{d}_{ij} = \mathbf{R_{AC}}^{\pm}$; (ii) $\mathbf{d}_{ik} = \mathbf{R_{BA}}^{\pm}$ and $\mathbf{d}_{kj} = \mathbf{R_{AC}}^{\pm}$ correspond to $\mathbf{d}_{ij} = \mathbf{R_{BC}}^{\pm}$; and (iii) $\mathbf{d}_{ik} = \mathbf{R_{BC}}^{\pm}$ and $\mathbf{d}_{kj} = \mathbf{R_{CA}}^{\pm} \equiv \mathbf{R_{AC}}^{\mp}$ correspond to $\mathbf{d}_{ij} = \mathbf{R_{BA}}^{\pm}$.

Beugeling *et al.* (2012) employs a theoretical model that considers only the ISO coupling amplitude corresponding to $\mathbf{d}_{ij}$ that connect NNN sites on Kagome lattice, *i.e.* $\lambda_{\langle\langle ij\rangle\rangle} = \{\lambda'_{AB}, \lambda'_{BC}, \lambda'_{AC}\}$, as usually accepted to determine the ISO coupling contribution in Hamiltonian (GUO; FRANZ, 2009; BEUGELING *et al.*, 2012). On the other hand, Liu *et al.* (2010) admitted only $\mathbf{d}_{ij}$ that connect NN sites, *i.e.* $\lambda_{\langle ij\rangle}$, and the usual amplitudes $\lambda_{\langle\langle ij\rangle\rangle}$ are neglected for the unstrained Kagome lattice. Jiang *et al.* (2019c) also considers only $\lambda_{\langle ij\rangle}$, but differently of Liu *et al.* (2010), it is admitted $\lambda_{AB} = \lambda_{BC} = 0$, i.e, only λ_{AC} is non-null. The present model includes both terms that are admitted separately by Liu *et al.* (2010), Beugeling *et al.* (2012), Jiang *et al.* (2019c). Therefore, naming $t_{AC} = t_{AB} = t_{BC} = t$ and $t'_{AC} = t'_{AB} = t'_{BC} = t'$, we obtain exactly the Hamiltonian $H_{\mathbf{0},K}$ of the Guo e Franz (2009) and Beugeling *et al.* (2012),

$$H^{AB}_{\mathbf{0},K}(\mathbf{k}) = 2t\cos\left[a_0/2(k_x+\sqrt{3}k_y)\right] + 2t'\cos\left[a_0/2(3k_x-\sqrt{3}k_y)\right], \tag{3.22a}$$

$$H^{BC}_{\mathbf{0},K}(\mathbf{k}) = 2t\cos(a_0k_x) + 2t'\cos\left(\sqrt{3}a_0k_y\right), \tag{3.22b}$$

$$H^{AC}_{\mathbf{0},K}(\mathbf{k}) = 2t\cos\left[a_0/2(k_x-\sqrt{3}k_y)\right] + 2t'\cos\left[a_0/2(3k_x+\sqrt{3}k_y)\right], \tag{3.22c}$$

Assuming $t' = 0$ we find the $H_{\mathbf{0},K}$ of Liu *et al.* (2010). Furthermore, considering $\lambda_{AB} = \lambda_{BC} = \lambda_{AC} = 0$ and naming $\lambda'_{AB} = \lambda'_{BC} = \lambda'_{AC} = \lambda_{\mathrm{ISO}}$ we obtain exactly the Hamiltonian $H_{\mathbf{ISO},K}$ of Guo e Franz (2009) and Beugeling *et al.* (2012),

$$H^{AB}_{\mathrm{ISO},K}(\mathbf{k}) = 2i\lambda_{ISO}\cos\left[a_0/2(3k_x-\sqrt{3}k_y)\right], \tag{3.23a}$$

$$H^{BC}_{\mathrm{ISO},K}(\mathbf{k}) = 2i\lambda_{\mathrm{ISO}}\cos\left(\sqrt{3}a_0k_y\right), \tag{3.23b}$$

$$H^{AC}_{\mathrm{ISO},K}(\mathbf{k}) = -2i\lambda_{ISO}\cos\left[a_0/2(3k_x+\sqrt{3}k_y)\right]. \tag{3.23c}$$

On the other hand, admitting $\lambda'_{AB} = \lambda''_{BC} = \lambda'_{AC} = 0$ and naming $\lambda_{AB} = \lambda_{BC} = \lambda_{AC} = \lambda_{\mathrm{ISO}}$ we obtain exactly the Hamiltonian $H_{\mathbf{ISO},K}$ of Liu *et al.* (2010),

$$H^{AB}_{\mathrm{ISO},K}(\mathbf{k}) = -2i\lambda_{ISO}\cos\left[a_0/2(k_x+\sqrt{3}k_y)\right], \tag{3.24a}$$

$$H^{BC}_{\mathrm{ISO},K}(\mathbf{k}) = -2i\lambda_{ISO}\cos\left(a_0k_x\right), \tag{3.24b}$$

$$H^{AC}_{\mathrm{ISO},K}(\mathbf{k}) = 2i\lambda_{ISO}\cos\left[a_0/2(k_x-\sqrt{3}k_y)\right]. \tag{3.24c}$$

Having discussed the correspondences between the generic Hamiltonian we developed and those presented in the literature for unstrained Lieb or Kagome lattices, it is worth mentioning that the configuration $C^{\uparrow} = (-1, 2, -1)$ obtained for the Kagome lattice corroborates

the models presented by Beugeling *et al.* (2012) and Guo e Franz (2009) which consider only NNN ISO coupling in the Kagome lattice. This means that the ISO coupling amplitudes of NN sites ($\lambda_{\langle ij\rangle} = \lambda_{AC}$ and λ_{AB} and λ_{BC}) do not modify the $\mathbf{C}^{\uparrow} = (-1,2,-1)$ configuration of the unstrained Kagome lattice if the ISO coupling amplitudes of NNN sites being considered are $\lambda_{\langle\langle ij\rangle\rangle} = \{\lambda'_{AC}, \lambda'_{AB}, \lambda'_{BC}\}$.

Jiang *et al.* (2019c) argue that the Chern numbers for the unstrained Lieb-Kagome lattice remain invariant for values of θ ranging from $\theta = \pi/2$ (Lieb lattice) to $\theta = 2\pi/3$ (Kagome lattice). Our results do not agree that that statement is always valid in the Lieb and Kagome lattices since the Chern numbers for the three bands of the unstrained Lieb and Kagome lattices are, in fact, different if $\lambda_{AB} = \lambda_{BC} = 0$. That shows that one cannot neglect the terms $\lambda_{\langle\langle ij\rangle\rangle}$ in the calculation of the energy spectrum of the Kagome lattice if one seeks to compare it to the Lieb spectra with $\lambda_{\langle\langle ij\rangle\rangle}$, as done by Jiang *et al.* (2019c). Thus, if the goal is to assess the possibility of phase transitions due to angle variations, then one must consider both $\lambda_{\langle\langle ij\rangle\rangle}$. Thus, our calculations show that there is a change in the Chern numbers of the three energy bands of the unstrained Lieb-Kagome lattice when θ is varied from $\theta = \pi/2$ to $\theta = 2\pi/3$, such that the unstrained Lieb and Kagome lattices have different Chern numbers per energy band.

3.4 Evaluation of the Chern Numbers

The Chern number C_n associated to the band n is an integer topological index defined as the integral of the Berry curvature over the BZ (BEUGELING *et al.*, 2012; VANDERBILT, 2018)

$$C_n = \frac{1}{2\pi}\int_{\mathrm{BZ}} d\mathbf{k}\left[\partial_{kx}A_n^y(\mathbf{k}) - \partial_{ky}A_n^x(\mathbf{k})\right], \tag{3.25}$$

where $A_n^{\mu} = -i\left\langle \psi_{n,\mathbf{k}}\middle|\partial_{k\mu}\middle|\psi_{n,\mathbf{k}}\right\rangle$ ($\mu = \{x,y\}$) is the Berry connection, defined in terms of the eigenstates $|\psi_{n,\mathbf{k}}\rangle$ (see App. A). Using the Kubo formula (HOR *et al.*, 2009; XIA *et al.*, 2009; HSIEH *et al.*, 2009; VANDERBILT, 2018; JIANG *et al.*, 2019c)

$$C_n = \frac{1}{2\pi}\int_{\mathrm{BZ}} d^2\mathbf{k}\,\Omega(\mathbf{k}), \quad \Omega(\mathbf{k}) = \sum_n f_n\Omega_n(\mathbf{k}), \tag{3.26}$$

$$\Omega_n(\mathbf{k}) = -\sum_{n'\neq n} 2\mathrm{Im}\frac{\left\langle \psi_{n,\mathbf{k}}\middle|\hat{v}_x\middle|\psi_{n',\mathbf{k}}\right\rangle\left\langle \psi_{n',\mathbf{k}}\middle|\hat{v}_y\middle|\psi_{n,\mathbf{k}}\right\rangle}{\left(E_{n',\mathbf{k}} - E_{n,\mathbf{k}}\right)^2}, \tag{3.27}$$

where $\psi_{n,\mathbf{k}}$ and $E_{n,\mathbf{k}}$ are the eigenstates and eigenvalue of band n, respectively. f_n is the Fermi distribution function, and $\hat{v}_{\mu}$ ($\mu = \{x,y\}$) is the velocity operator.

Degeneracies in the spectrum are forbidden in order for the Chern number to be well defined. The spin degeneracy problem of the three bands in this model is solved by projecting the system onto a single spin component. Thus, we obtain separate Chern numbers for the spin-up and the spin-down bands, which we write as $C_n^{\uparrow}$ and $C_n^{\downarrow}$, respectively. Thus, the nontrivial topology of the systems can be further confirmed through the calculation of the topological invariant, i.e., the spin Chern number by band n, $C_n^s = C_n^{\uparrow} - C_n^{\downarrow}$ (BEUGELING *et al.*, 2012; JIANG *et al.*, 2019c).

Alternatively, the spin Chern number is an efficient and convenient way to distinguish different non-trivial topological states, incidentally, the Z_2 invariant can also be calculated using the spin Chern numbers (FU; KANE, 2007).

The spin-up Chern numbers are denoted as $C^{\uparrow} = (C^{\uparrow}_{\text{lower}}, C^{\uparrow}_{\text{middle}}, C^{\uparrow}_{\text{upper}})$ for the lower, middle, and upper bands, respectively. For the spin-down component, we define $C^{\downarrow} = -C^{\uparrow}$. This relationship allows us to straightforwardly derive the Chern numbers for $\lambda_{\text{ISO}} < 0$ from those for $\lambda_{\text{ISO}} > 0$ by swapping the roles of spin-up and spin-down.

Since the Hamiltonian is diagonal in spin space, the spin Chern number is defined as $C_{\text{spin}} = C^{\uparrow} - C^{\downarrow}$ (SHENG *et al.*, 2006). Due to the symmetry between the two spin components, it follows that $C_{\text{spin}} = 2C^{\uparrow}$ (GOLDMAN *et al.*, 2011b; BEUGELING *et al.*, 2012).

By virtue of the bulk-boundary correspondence, the spin Hall conductivity (in units of the spin conductivity quantum $e/4\pi$) is given by

$$\sigma_{\text{SH}} = \sum_{s:\varepsilon_s<E_{\text{F}}} C_{\text{spin},s}, \tag{3.28}$$

where the summation includes all filled bands (E_{F} represents the Fermi energy). The $\mathbb{Z}_2$ index ν, defined as 0 for an even and 1 for an odd number of edge-state pairs, is then related to the spin Hall conductivity by (SHENG *et al.*, 2006; FUKUI; HATSUGAI, 2007; GOLDMAN *et al.*, 2011b; BEUGELING *et al.*, 2012)

$$\nu = \frac{\sigma_{\text{SH}}}{2} \mod 2. \tag{3.29}$$

An alternative approach to determine the Chern numbers and the spin Hall conductivities involves diagonalizing the system in a ribbon geometry and counting the number of edge states that appear inside the bulk gaps (HATSUGAI, 1993; FUKUI *et al.*, 2005; VANDERBILT, 2018). Remarkably, for systems that preserve inversion symmetry, the $\mathbb{Z}_2$ invariant can also be calculated using the parity eigenvalues at the TR symmetric momenta (FU; KANE, 2007). The

advantage of calculating the spin Chern numbers, as we have done here, is that they are directly related to the quantized spin Hall conductivity in the band gaps (BEUGELING *et al.*, 2012).

3.5 Phase transition in the unstrained Lieb-Kagome lattice

3.5.1 Lieb-Kagome lattice with intrinsic spin-orbit coupling

In this section, we investigate TPT on the unstrained Lieb-Kagome lattice. For this, we initially analyze the effects of ISO coupling on the energy spectra of the Lieb, transition ($\theta = 105^\circ$), and Kagome lattices. In Fig. 48, we compare the energy bands obtained in the case without ISO coupling, $\lambda_{\mathrm{ISO}} = 0$ (panels d-f), with all ISO coupling parameters different from zero, including the NN ISO coupling, $\lambda_{AB} \neq 0$, $\lambda_{BC} \neq 0$ (panels g-l), and considering these as zero, $\lambda_{AB} = \lambda_{BC} = 0$ (panels j-l).

Let us first consider $\lambda_{\mathrm{ISO}} = 0$. For the Lieb and Kagome lattices, we identify the well-known coexistence of Dirac bands and nearly-flat bands. In the Lieb lattice, the nearly-flat band is located in the middle of the Dirac bands, while in the Kagome lattice, it is situated at the bottom (top) of the energy spectrum for hopping cases of $t > 0$ ($t < 0$), as shown in Fig. 49. This effect of shifting the location of the nearly-flat bands in Lieb-Kagome lattices can be understood by considering the local magnetic flux (OHGUSHI *et al.*, 2000; GUO; FRANZ, 2009; JIANG *et al.*, 2019c). On the other hand, in the band structure of the transition lattices, the nearly-flat band has disappeared, as the lattice distortion breaks the required symmetry for flat band formation in the Lieb and Kagome lattices. This is attributed to the destructive interference or phase cancellation of Bloch wave functions caused by lattice symmetry (LI *et al.*, 2018; JIANG *et al.*, 2019c).

Indeed, without ISO coupling, the singular nearly-flat bands of the Lieb and Kagome lattices unavoidably cross with dispersive bands due to a symmetry representation (SR) mismatch between the compact localized state (CLS) and its constituent atomic orbitals under unitary symmetry, as demonstrated by Hwang *et al.* (2021). In the Lieb lattice, while the atomic orbitals constituting the CLS occupy only the sublattices A and C, and do not occupy the B sublattice, the SR of CLS under C_4 alone enforces a band crossing at **M**. Besides the two-fold degeneracy enforced by SR for C_4, which belongs to the wallpaper group $p4mm$, there exists an accidental degeneracy that can be broken by the inclusion of a nonzero onsite potential at the B sublattice (HWANG *et al.*, 2021). In the Kagome lattice, all atomic orbitals contribute to the hybrid orbital

Figure 48 – (a-c) Energy dispersion along the high-symmetry points **Γ**, **X**, **K**, and **M** of the BZ, as shown in the insets, is presented for (a) Lieb, (b) transition, and (c) Kagome lattices. Cases (i) without ISO coupling $\lambda_{\mathrm{ISO}} = 0$ [solid black lines], (ii) with ISO coupling, *i.e.*, $\lambda_{AB} \neq 0$, $\lambda_{BC} \neq 0$ [dashed blue lines], and (iii) with ISO coupling but without the following NN ISO coupling terms $\lambda_{AB} = \lambda_{BC} = 0$ [dotted red lines] are presented. The bottom, middle, and top bands are identified as E_1, E_2, and E_3, respectively. The full energy spectra are also depicted (see panels d-l).

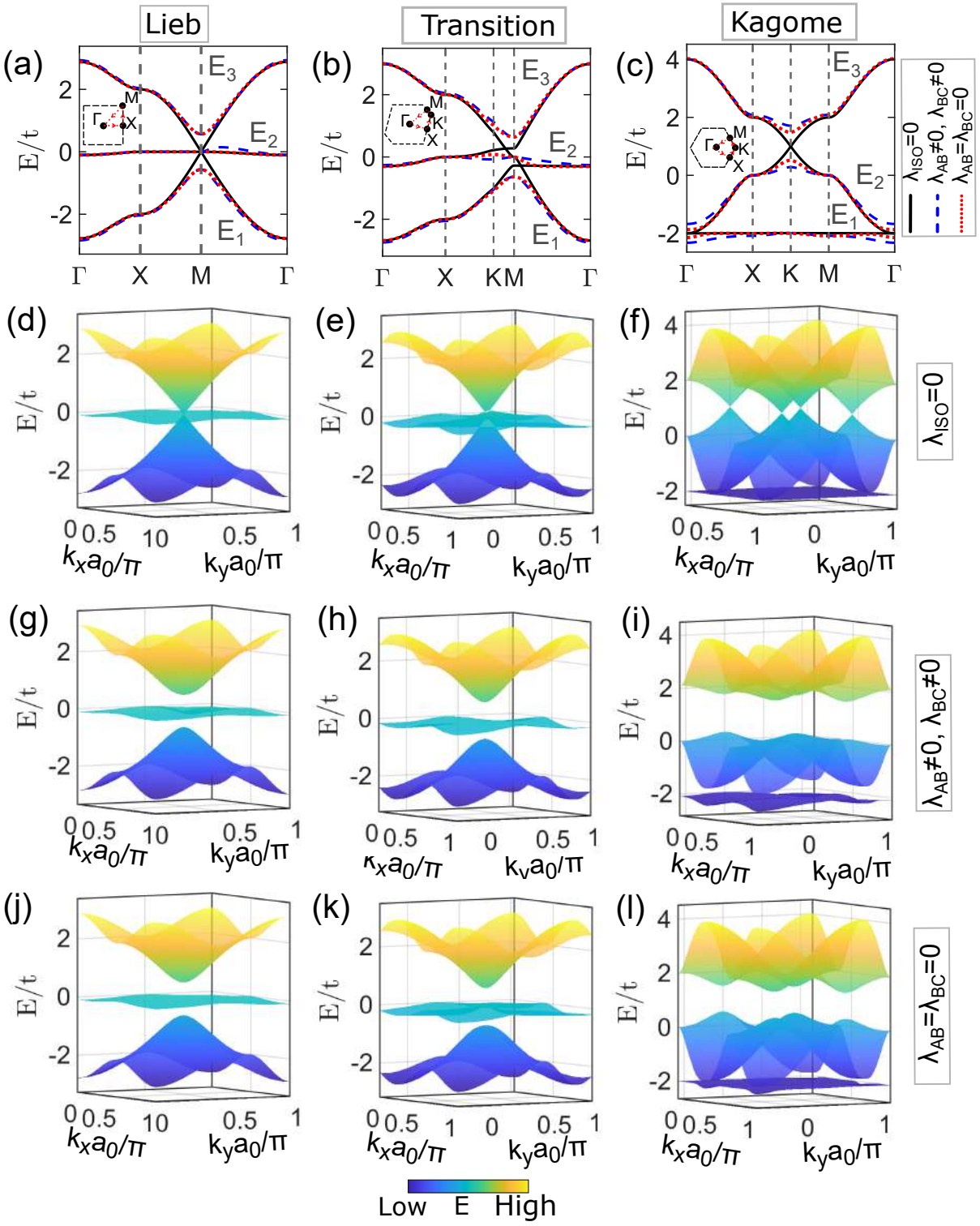

Source: The author.

Figure 49 – Comparison between the energy bands obtained for $t > 0$ (left panels) and $t < 0$ (right panels) along the high-symmetry points **Γ**, **X**, **K**, and **M** of the BZ, as shown in the insets. Presented are (a-b) Lieb, (c-d) transition, and (e-f) Kagome lattices. Cases are: (i) without ISO coupling $\lambda_{\text{ISO}} = 0$ [solid black lines], (ii) with ISO coupling, i.e., $\lambda_{AB} \neq 0$, $\lambda_{BC} \neq 0$ [dashed blue lines], and (iii) with ISO coupling but without the following NN ISO coupling terms $\lambda_{AB} = \lambda_{BC} = 0$ [dotted red lines].

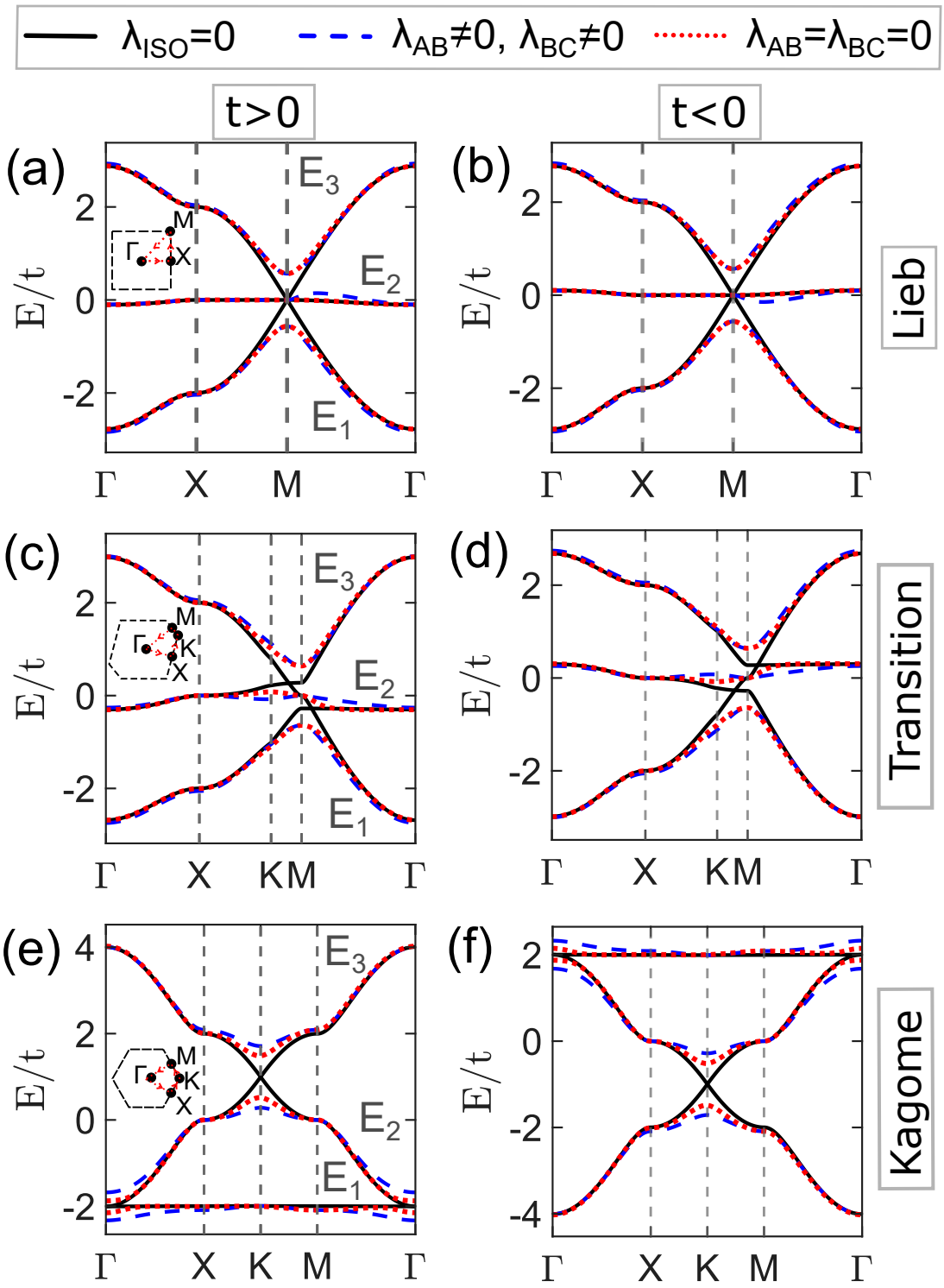

Source: The author.

of the CLS, and the band crossing point of the nearly-flat band can be explained by the SR of the CLS under C_6, which belongs to the wallpaper group *p6mm*. Notably, these degeneracies can be lifted by the inclusion of ISO coupling in Lieb-Kagome lattices [Fig. 48 (g-l)].

Assuming $\lambda_{\mathrm{ISO}} \neq 0$, we observe the opening of two full band gaps in the Lieb-Kagome spectra, denoted by Δ_{12} and Δ_{23}, between bands E_1 and E_2 ($1/3$ filling), and E_2 and E_3 ($2/3$ filling), respectively, as illustrated in Fig. 48 (a-c). In the Lieb lattice, the NN ISO coupling maintains the four-fold rotational symmetry, D_{4h} [see Fig. 47 (b)], without creating a gap at the Dirac point, as depicted in Fig. 50 (JIANG *et al.*, 2019c). This occurs due to the preservation of both the double degeneracy, resulting from the SR coupled with the CLS of the flat band, which remain composed solely of atomic orbitals located on sublattices A and C, and the accidental degeneracy that arises from maintaining the symmetry of the face sublattice sites in relation to the corner sites (HWANG *et al.*, 2021). Additionally, the Lieb lattice with NNN ISO coupling breaks the D_{4h} symmetry, leading to the formation of gaps as illustrated in Fig. 48 (g,j). In this case, C_4 exists while the CLS occupies the B sublattice, resulting in a nearly-flat band with a zero Chern number. Hwang *et al.* (2021) demonstrates that a nonzero Chern number for the nearly-flat band is achieved only when the Lieb lattice undergoes a perturbation that preserves C_4 symmetry while ensuring that the CLS are occupied solely by the A and C sublattices. This investigation is beyond the scope of this thesis. What we can confirm is that, despite the Chern number of the nearly-flat band being zero, the Lieb lattice becomes a non-trivial TI when the ISO coupling is included [Fig. 51 (a-b)] (JIANG *et al.*, 2019c).

In the transition (D_{2h}) and Kagome (D_{6h}) lattices, even NN ISO coupling alone results in the appearance of gaps at both Dirac points. In this case, the inversion symmetry is preserved, ensuring that as Lieb-Kagome lattices remain in the same topological phase as the Lieb lattice during the interconvertibility process, as demonstrated by Jiang *et al.* (2019c) and verified in Fig. 50 (JIANG *et al.*, 2019c). Moreover, Hwang *et al.* (2021) showed that in the case of the Kagome lattice, the inclusion of NN and NNN ISO coupling preserves C_6 but breaks other irrelevant symmetries such as mirror symmetries. Then, all the bands are gapped, and the flat band becomes a nearly-flat band with a Chern number $C_1^{\uparrow} = \pm 1$ [Fig. 51 (e_4 and f_4)]. As we will see, the change in the sign of the spin Chern number of the lower band of the Kagome spectrum, due to the inclusion [Fig. 51 (e_4)] or cancellation [Fig. 51 (f_4)] of the NN ISO coupling terms λ_{AB} and λ_{BC}, indicates TPT.

In all cases, the opening of gaps due to the ISO coupling effect indicates that the

Figure 50 – Evolution of the energy spectrum (1st and 2nd column of panels) and Berry curvature per energy band (3rd to 5th columns of panels) for fillings 1/3 (6th column of panels) and 2/3 (7th column of panels) for Lieb (1st row of panels), transition (2nd row of panels), and Kagome (3rd row of panels) lattices. Obtained considering only NN ISO coupling, i.e., only $\lambda_{AB} \neq 0$ and $\lambda_{BC} \neq 0$ for Lieb and transition lattices, and $\lambda_{AB} \neq 0$, $\lambda_{BC} \neq 0$, and $\lambda_{AC}^{-} \neq 0$ for Kagome lattices. It is noted that there is no gap opening in the Lieb lattice, such that only NNN ISO coupling opens a gap in this lattice as shown in Fig. 48.

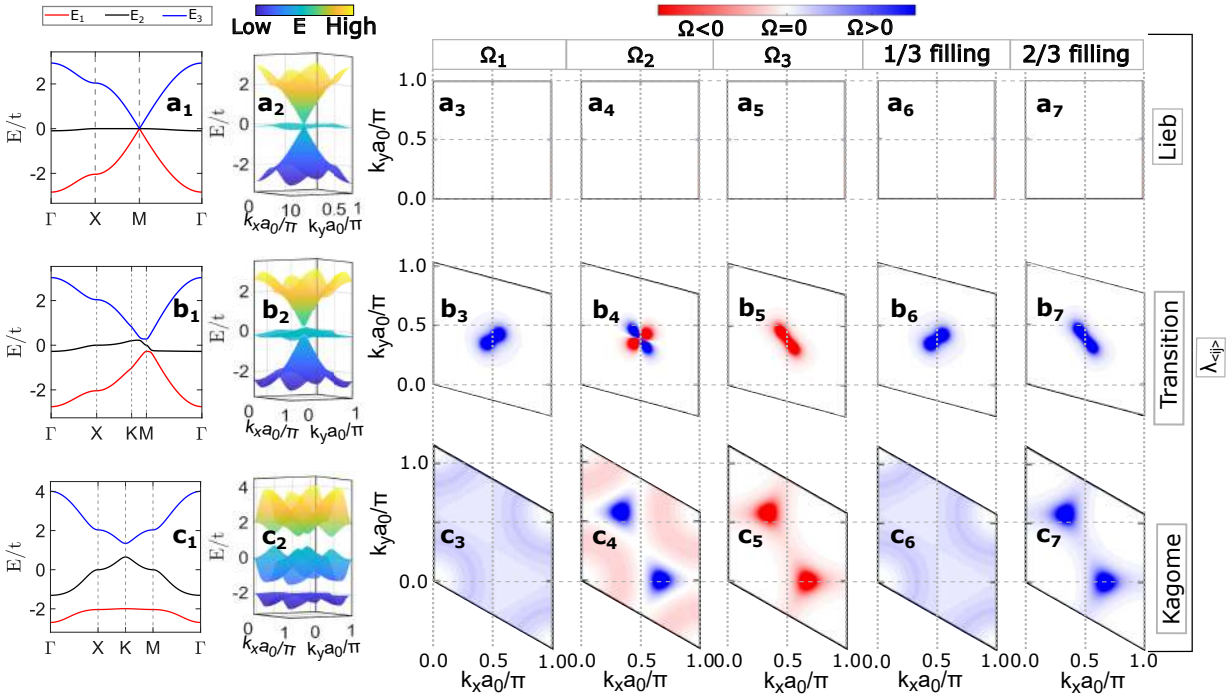

Source: The author.

lattice is topologically nontrivial, regardless of the value of the Chern number of the nearly-flat band. All the TPT identified are confirmed by the gap closing and reopening, evolution of the Berry curvature, and the calculation of the Chern number per energy band, as shown in Fig. 51.

We will initially discuss the evolution of the Berry curvature of the lower (Ω_1), middle (Ω_2), and upper (Ω_3) bands, as presented in Fig. 51. Note that the nonzero Berry curvatures are primarily localized around the Dirac points, which become gapped due to the influence of the ISO coupling effect. Consequently, the evolution of the Dirac points can also be directly visualized through the changes in Berry curvatures for the three bands (JIANG *et al.*, 2019c). This becomes evident when we evaluate the Berry curvatures in the lower (1/3 filling) and upper (2/3 filling) gaps (BEUGELING *et al.*, 2012; JIANG *et al.*, 2019c), which are presented in Fig. 52.

Let us evaluate the cases where $\lambda_{AB} = \lambda_{BC} = 0$ (panels (b), (d), and (f) in Fig. 51), focusing on the evolution of the Berry curvature. Ω_1 and Ω_3 exhibit circularly symmetric peaks around the **M** point, which are positive and negative, respectively [Fig. 51 (b_1 and b_3)], while Ω_2

Figure 51 – Contour plots of Berry curvature Ω_1 (panels 1), Ω_2 (panels 2), and Ω_3 (panels 3) corresponding to the lower, middle, and upper bands presented in panels 4 for (a) Lieb, (c) transition, and (e) Kagome lattices with $\lambda_{AB} \neq 0$, $\lambda_{BC} \neq 0$. The cases where $\lambda_{AB} = \lambda_{BC} = 0$ are shown in panels (b), (d), and (f), respectively. Parallelograms indicate the region of reciprocal space with an area numerically equal to the BZ of each case.

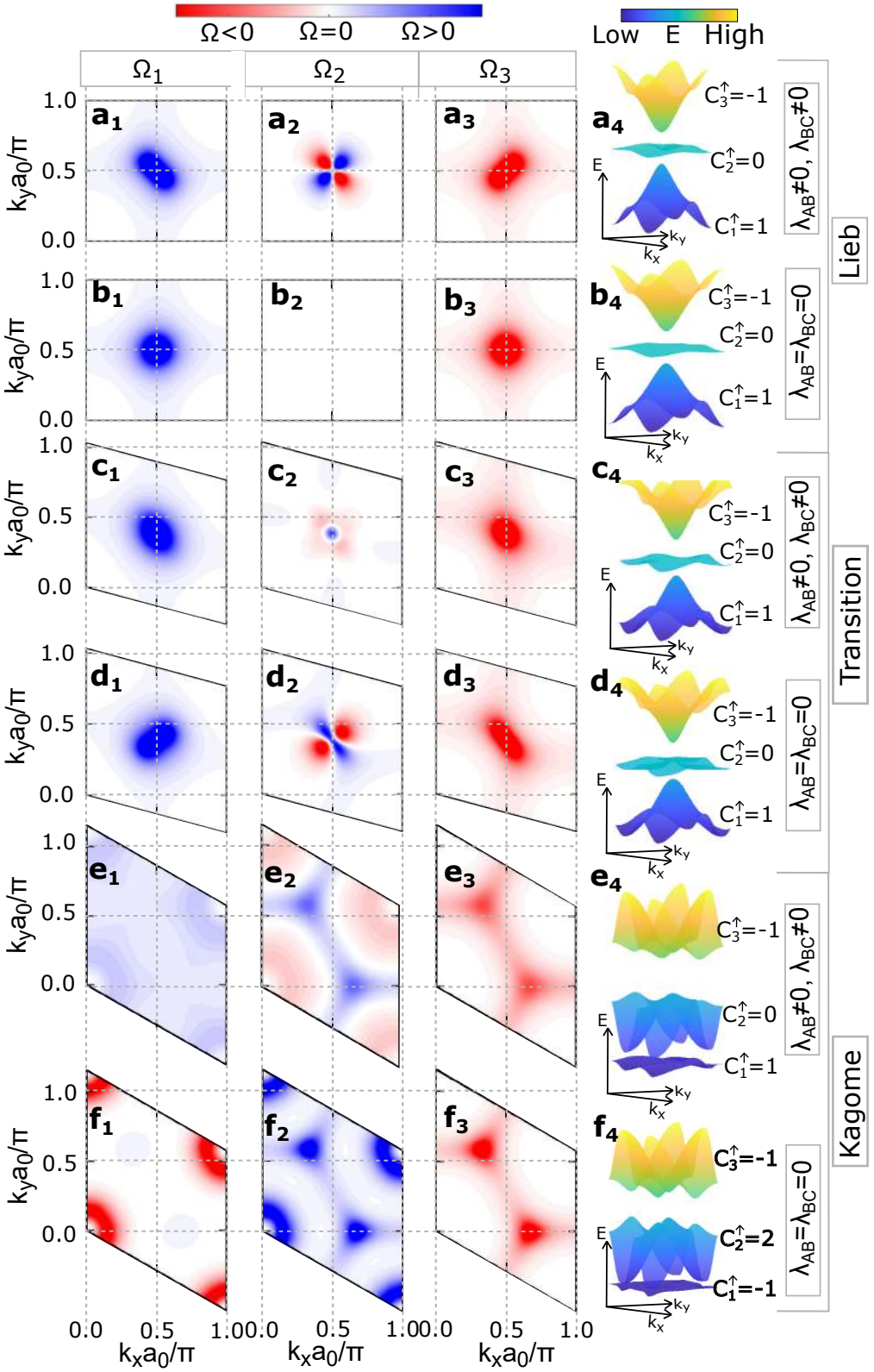

Source: The author.

is negligible due to the flatness of the flat band [Fig. 51 (b_2)]. In the transition lattice ($\theta = 105^\circ$), Ω_1 and Ω_3 retain their signs from the $\theta = 90^\circ$ case but show asymmetric peaks around the **M** point. The former is distributed along the diagonal direction, $k_y = (\cos\theta + 1)/\sin\theta k_x$ [Fig. 51 (d_1)], while the latter is along the antidiagonal direction, $k_y = (\cos\theta - 1)/\sin\theta k_x$, perpendicular to the former. This also occurs with 1/3 and 2/3 filling, respectively [Fig. 52 (d_3 and f_3)]. Interestingly, Ω_2 exhibits four peaks at the **M** point, with two negative along the diagonal direction and two positive in the antidiagonal direction, forming Berry dipoles (ZHANG; SUN YAN E YAN, 2018; BATTILOMO *et al.*, 2019). This is linked to the formation of two doubly degenerate Dirac points, located along the $\mathbf{\Gamma} - \mathbf{M}$ and $\mathbf{M} - \mathbf{K}/\mathbf{K}'$ paths, originating from the triply degenerate point at the **M** point of the BZ of the Lieb lattice when the ISO coupling is zero (JIANG *et al.*, 2019c). According to Fig. 53, we confirm that the behavior of the Berry curvature contours is equivalent to that of the energy spectrum contours, particularly with respect to asymmetries around the **M** point.

The cases with $\lambda_{AB} \neq 0$ and $\lambda_{BC} \neq 0$ are presented in panels (a), (c), and (e) of Fig. 51. We see that the Berry curvatures of the upper and lower bands of the Lieb lattice, which were circularly symmetric around the **M** point (JIANG *et al.*, 2019c), are now asymmetric such that the Berry curvature of the lower (upper) band is similar to the curvature of the upper (lower) band of the transition lattice with $\lambda_{AB} = \lambda_{BC} = 0$. This behavior is also evidenced in the energy spectrum shown in Fig. 53 (d_1). Another surprising point is that the consideration of $\lambda_{AB} \neq 0$ and $\lambda_{BC} \neq 0$ originates Berry dipoles (BATTILOMO *et al.*, 2019) in the Berry curvature of the middle band of the Lieb spectrum [Fig. 52 (a_2)], while the transition lattice ceases to present them [Fig. 52 (c_2)].

Figure 52 – Evolution of the Berry curvature per band (1st and 2nd column of panels) and with fillings 1/3 (3rd column of panels) and 2/3 (4th column of panels) for (a) Lieb, (c) transition, and (e) Kagome lattices with $\lambda_{AB} \neq 0$, $\lambda_{BC} \neq 0$. The cases where $\lambda_{AB} = \lambda_{BC} = 0$ are shown in panels (b), (d), and (f), respectively. Parallelograms indicate the region of reciprocal space with an area numerically equal to the BZ of each case as shown in Fig. 51.

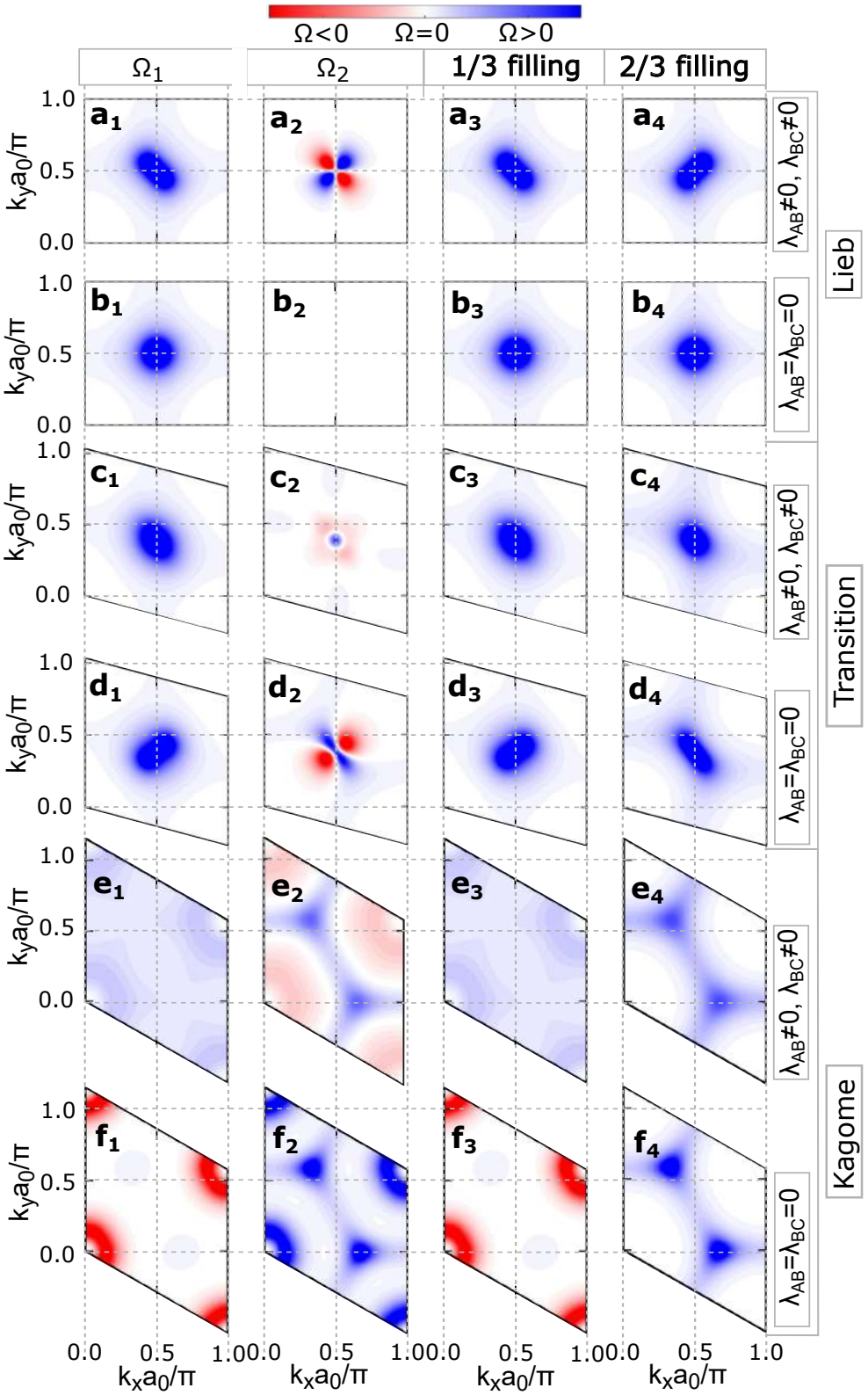

Source: The author.

Figure 53 – Contour plots of (a) lower, (b) middle, and (c) upper bands of Lieb (1st row of panels), transition (2nd row of panels), and Kagome (3rd row of panels) lattices, for the cases (i) $\lambda_{\mathrm{ISO}} = 0$ [solid black line], (ii) $\lambda_{AB} \neq 0$, $\lambda_{BC} \neq 0$ [dashed blue line], and (iii) $\lambda_{AB} = \lambda_{BC} = 0$ [dotted red line]. The regions (i-vi) shaded in blue or red are depicted in an enlarged form in panels (d).

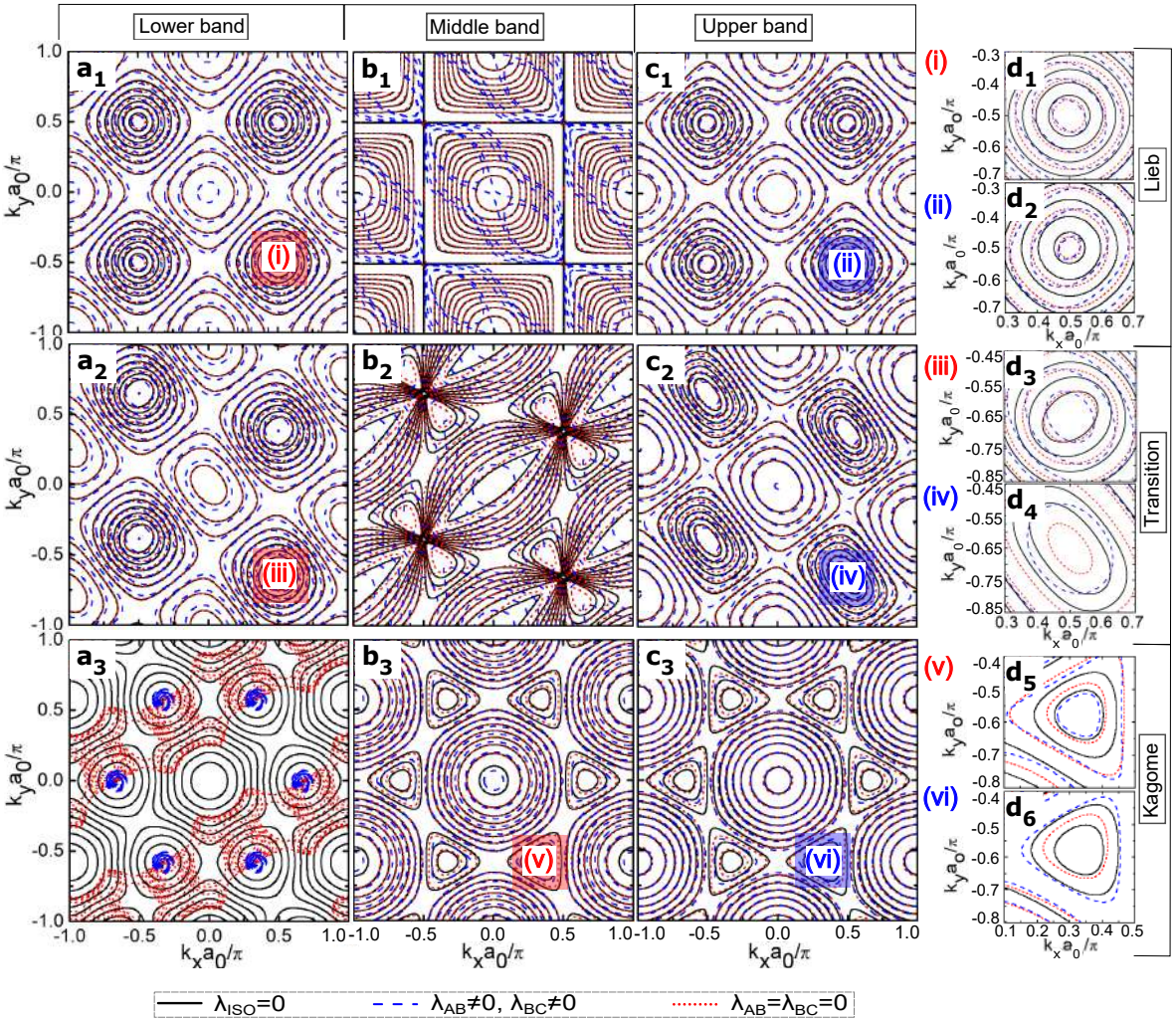

Source: The author.

3.5.2 *Topological phase transitions driven by θ - evolution*

Now, let us evaluate the existence of TPT due to the interconvertibility process between the Lieb and Kagome lattices. Initially, we observe that there is no change in the Chern numbers or in the sign of the Berry curvature between the Lieb and Kagome lattices when we assume $\lambda_{AB} \neq 0$ and $\lambda_{BC} \neq 0$ [Fig. 51 (a,c,e)], indicating that there are no TPT driven by θ in this configuration. The evolution of the full band gaps as a function of the n term, which controls the inclusion of NNN sites in Eq. (3.4), reveals that the topological phase classified by $C^{\uparrow} = (1, 0, -1)$ is robust against the inclusion of NNN sites ($n < 8$), provided we maintain $\lambda = 0.2$ [Fig. 54 (a-b)]. Indeed, we do not identify any closing and reopening of the full band

gaps at any point in Fig. 54 (a-b), which means there are no TPT. However, we note regions with full band gaps that close and do not reopen, depicted in blue in this figure. In these regions the spectrum exhibits a negative indirect gap, as explicitly shown in Fig. 56, such that at 1/3 filling, the system is in a semimetallic regime, characterized by partially filled bands and non-quantized spin Hall conductivity. At 2/3 filling, the system behaves as an insulator, and the spin Hall conductivity carried by the helical edge states becomes observable experimentally (BEUGELING *et al.*, 2012).

Comparing the evolution of the full band gaps presented in Fig. 54 with the local band gaps Δ'_{12} and Δ'_{23} shown in Fig. 55, we observe that $\Delta'_{12} \neq 0$ for the range of n where $\Delta_{12} = 0$. This indicates that E_1 and E_2 do not possess $\mathbf{k}$ points of degeneracy in the region where $\Delta_{12} = 0$.

In general, a null full band gap in Fig. 54, paired with a nonzero corresponding local band gap for the same configuration (n, θ) or (n, λ) in Fig. 55, suggests that the maximum of the valence band exceeds the minimum of the conduction band at a different momentum. This condition is indicative of a spectrum with a negative indirect gap, as explicitly demonstrated in Fig. 56 (BEUGELING *et al.*, 2012). With $\Delta'_{12} \neq 0$, the Chern numbers of the bands remain well-defined, as they do not intersect, precluding the occurrence of TPT. Notably, Δ'_{12} closes and reopens for small n values, leading to a change in $C_1^{\uparrow}$ and $C_2^{\uparrow}$ [Fig. 56 (a-b)]. However, in a 1/3-filled system, both the lower and middle bands will be partially filled, categorizing the bulk as a semimetal and thereby impeding the detection of helical edge states. In this semimetallic phase with partially filled bands, the spin Hall conductivity remains unquantized. It is crucial for the quantization of the spin Hall conductivity that the spectrum possesses a full gap, establishing a range of Fermi energies where only edge states are present, excluding any bulk states (BEUGELING *et al.*, 2012). This condition is met at 2/3 filling, where the system acts as an insulator, allowing the spin Hall conductivity associated with helical edge states to be experimentally observed (BEUGELING *et al.*, 2012).

This discussion also applies to subsequent cases involving strain application. Whenever Δ_{12} and Δ_{23} nullify while Δ'_{12} and Δ'_{23} remain nonzero, the same principles hold.

For $\lambda_{AB} = \lambda_{BC} = 0$, interestingly, we observe that the Berry curvature of the lower band of the Kagome lattice is negative [Fig. 51 (f_1)], in contrast to the positive curvatures of the lower bands of the Lieb [Fig. 51 (b_1)] and transition [Fig. 51 (d_1)] lattices. Similarly, the middle band of the Kagome lattice becomes entirely positive [Fig. 51 (f_2)], unlike at $\theta = 90^\circ$

Figure 54 – Contour plot of the full band gap Δ_{12} [Δ_{23}] between bands E_1 [E_2] and E_2 [E_3] as a function of n and θ with $\lambda = 0.2$ (1st row of panels), and as a function of n and λ for Lieb (2nd row of panels), transition (3rd row of panels), and Kagome (4th row of panels) lattices. Results are presented considering all ISO coupling parameters (1st and 2nd columns of panels), as well as assuming the following NN ISO coupling parameters equal to zero, $\lambda_{AB} = \lambda_{BC} = 0$ (3rd and 4th columns of panels). The regions simultaneously exhibiting the closure of the full band gap and the local band gap, *i.e.*, the touching of bands at a certain point **k** (shown in Fig. 55), indicate TPT.

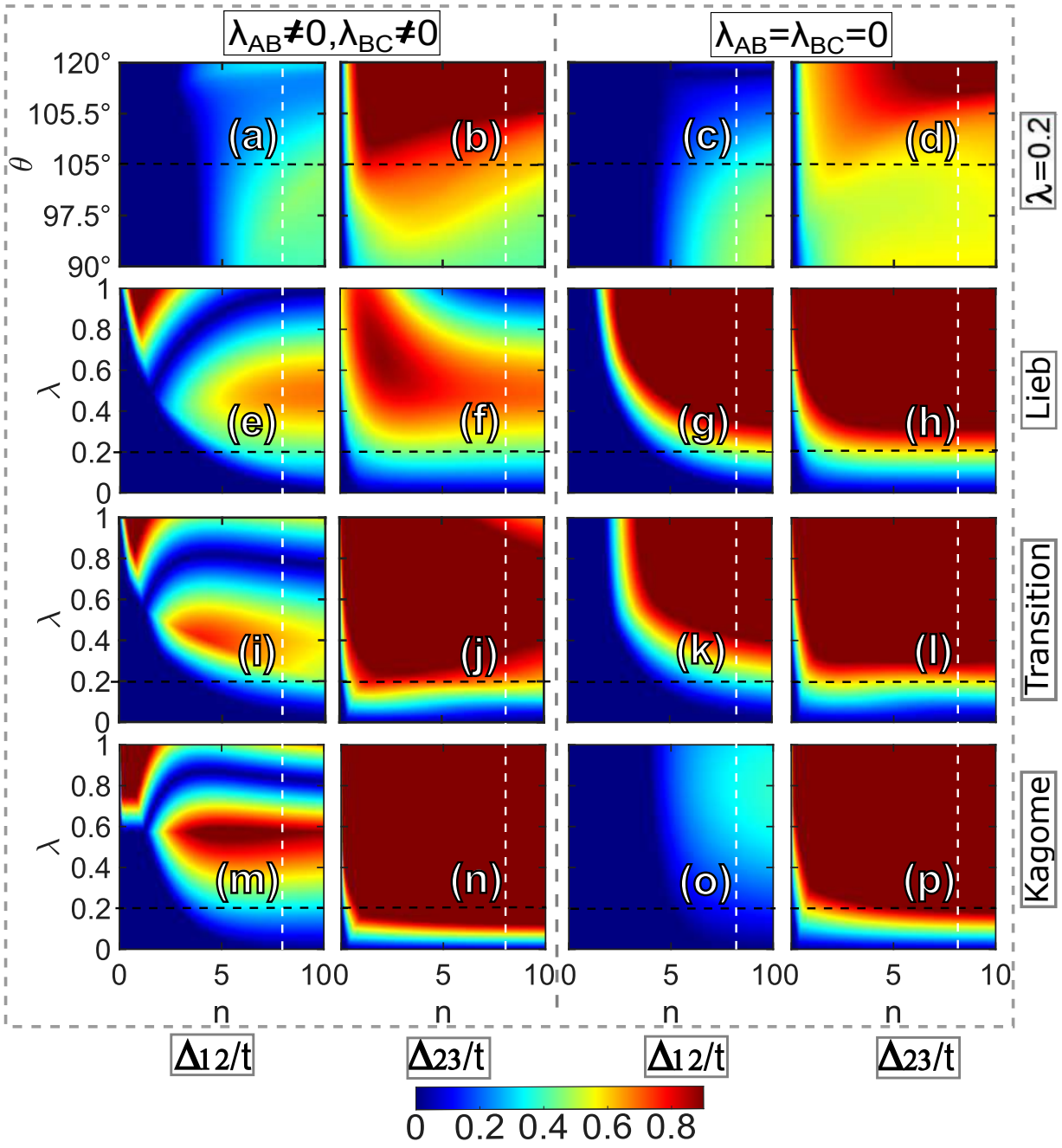

Source: The author.

[Fig. 51 (b_2)] and $\theta = 105°$ [Fig. 51 (d_2)], which exhibit an equal volume of positive and negative phases in the BZ, resulting in a null Chern number. However, we note that the Kagome lattice now presents $C^{\uparrow} = (-1, 2, -1)$, while the Lieb and transition ($\theta = 105°$) lattices show

Figure 55 – Contour plots of the full band gap Δ_{12} [Δ_{23}] presented in Fig. 54 are contrasted with contour plots of the local band gaps Δ'_{12} [Δ'_{23}], which refer to the minimum separation between the bands at each individual point in their momentum space. At points where the bands intersect or touch, the local band gap reduces to zero, indicating TPT.

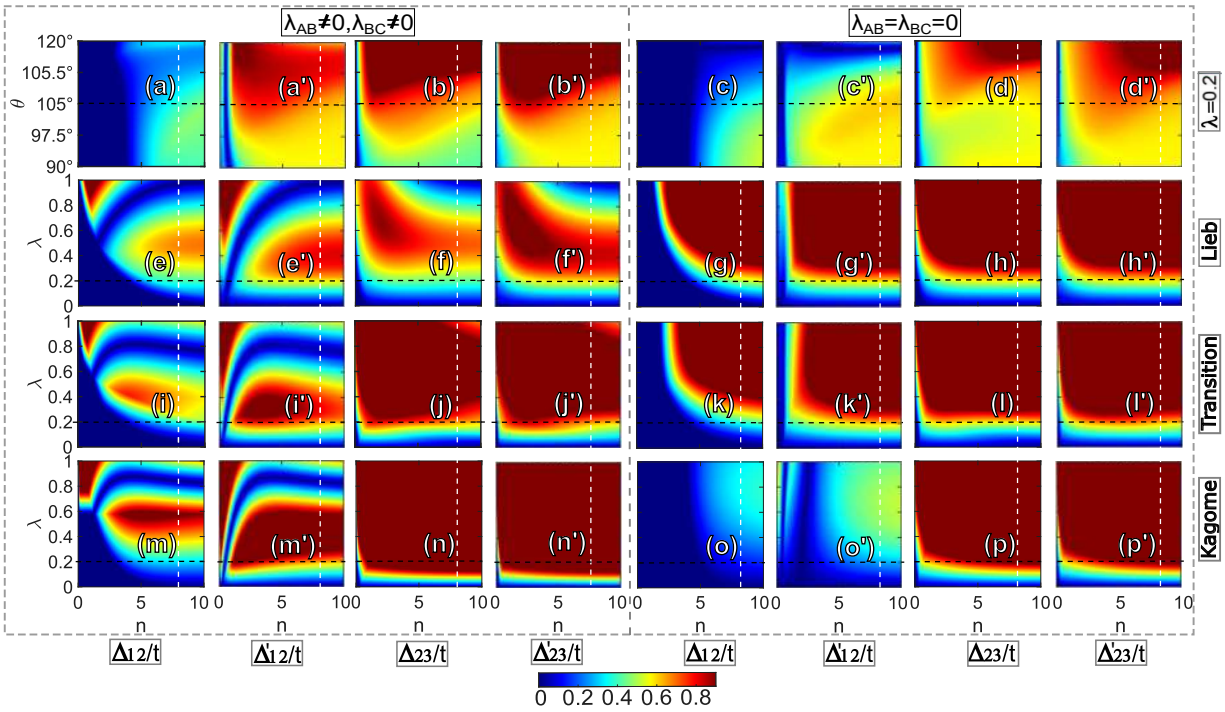

Source: The author.

$C^{\uparrow} = (1, 0, -1)$.

The critical point of the TPT is at $\theta = 118.3°$, where band touchings are indicated by red dotted lines in the phase diagram of Fig. 57 (d). Additionally, we have shaded the regime $C^{\uparrow} = (1, 0, -1)$ in blue, and $C^{\uparrow} = (-1, 2, -1)$ in green. In all open gaps, the system behaves as a QSHI, with a spin Hall conductivity of $\sigma_{\mathrm{SH}} = \pm 1$ (BEUGELING *et al.*, 2012). For $\theta < 118.3°$, the conductivities in the lower (1/3 filling) and upper (2/3 filling) gaps are the same, owing to the zero Chern number of the middle band. For $\theta > 118.3°$, the two bands exhibit opposite conductivities (BEUGELING *et al.*, 2012). From Fig. 54 (c) and Fig. 55 (c'), it is evident that the TPT during the interconvertibility process with $\lambda_{AB} = \lambda_{BC} = 0$ remains robust for $n \neq 8$ values.

Prior to this TPT [Fig. 59 (f)], Ω_1 displays two positive peaks along the diagonal direction. Ω_3 is characterized by two negative peaks along the antidiagonal direction. These peaks evolve from the asymmetric peak near the **M** point at $\theta = 105°$, as demonstrated in Fig. 51 (d_1 and d_3). Ω_2 exhibits two positive peaks in the antidiagonal direction and two negative peaks in the diagonal direction, which are perpendicular to the former. The TPT inverts the signs of the two peaks in Ω_1 and Ω_3, and in Ω_2, this transformation results in the emergence of four positive peaks, eliminating the Berry dipole [Fig. 59 (g)] (ZHANG; SUN YAN E YAN, 2018).

Figure 56 – Evolution of the local band gap for regions of Fig. 55 that exhibit a negative indirect gap. Before and after the touching of the bottom and middle bands, the Chern numbers of the bands are well defined since they do not touch anywhere. However, no TPT occurs due to it being a region of a null full band gap.

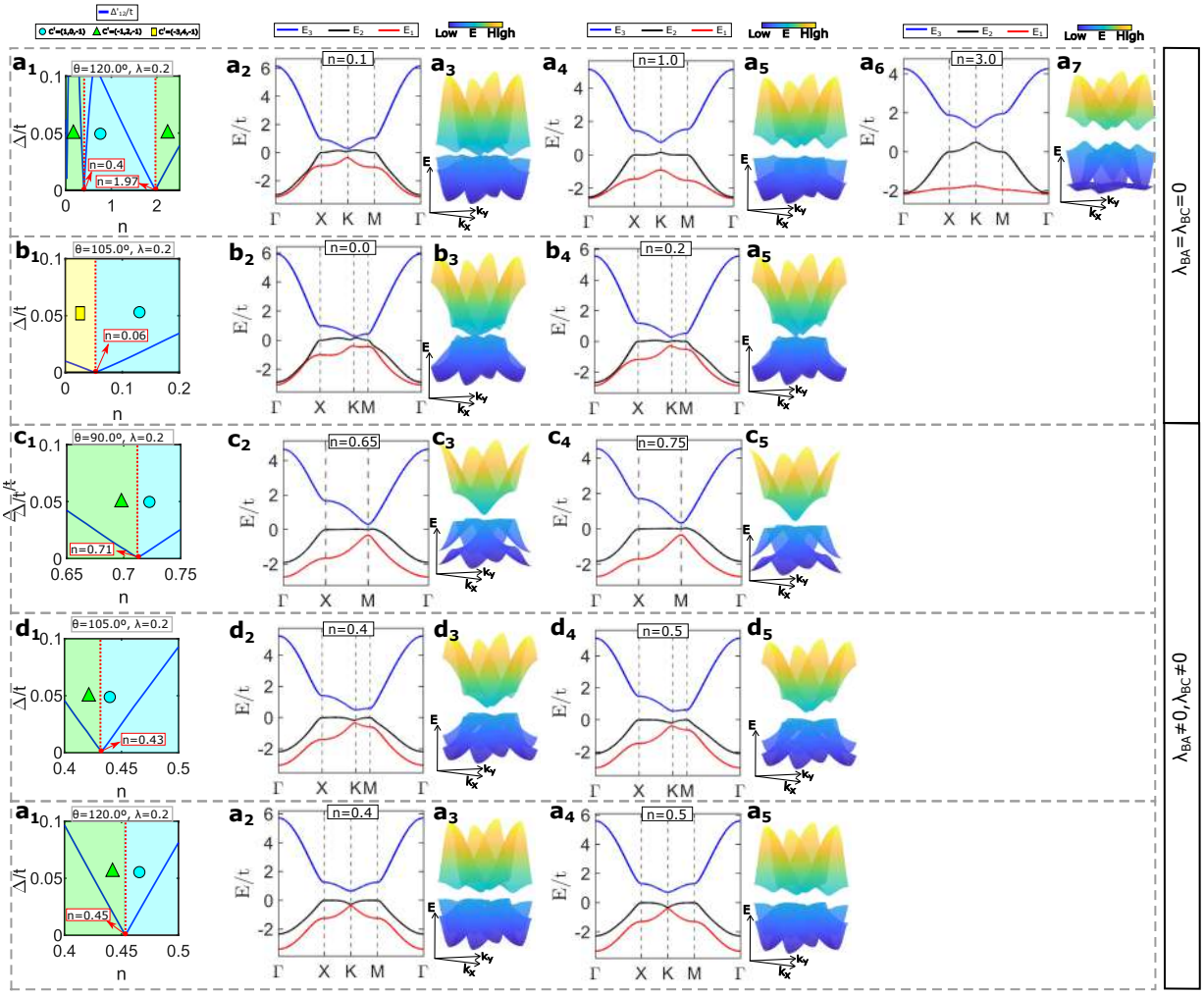

Source: The author.

The TPT that occur at 1/3 filling in the transition [Fig. 57 (b)] and Kagome [Fig. 57 (c)] lattices at the critical points $\lambda = 0.78$ and $\lambda = 0.84$, respectively, are analogous to the TPT in Fig. 57 (d). Specifically, $\Delta C^{\uparrow} = (1,0,-1) - (-1,2,-1) = (2,-2,0)$. The evolution of the Berry curvature for the transition lattice [Fig. 60 (d-e)] is similar to that of the Lieb lattice [Fig. 59 (a-c)]. In the Kagome lattice [Fig. 59 (d-e)], Ω_3 indeed does not exhibit a sign change, remaining negative, but now it does not show localized peaks, analogous to Ω_1 before the TPT [Fig. 51 (e)]. In fact, after the TPT, the Chern nearly-flat band is E_3 (HWANG *et al.*, 2021).

Every TPT in the phase diagram can be understood in terms of the difference in the Chern numbers of the phases on either side of the transition. For the transition defined by the line $\theta < 118.3°$, the lower gap closes, and the system behaves as a metal at the gap closing

Figure 57 – Evolution of the full band gaps Δ_{12} [black solid line] and Δ_{23} [red dashed line] as a function of the parameter λ (panels a-c), or θ (panel d) assuming $\lambda_{AB} \neq 0$ and $\lambda_{BC} \neq 0$ (panels a-c) or $\lambda_{AB} = \lambda_{BC} = 0$ (panels d), which highlights TPT at gap closing points. Regions with distinct Chern numbers for the bands, $C^{\uparrow} = (C_1^{\uparrow}, C_2^{\uparrow}, C_3^{\uparrow})$, have been indicated by different colors, where (1,0,-1), (-1,2,-1), and (-1,0,1) correspond to the blue, green, and red regions, respectively. The remaining cases are presented in Fig. 58.

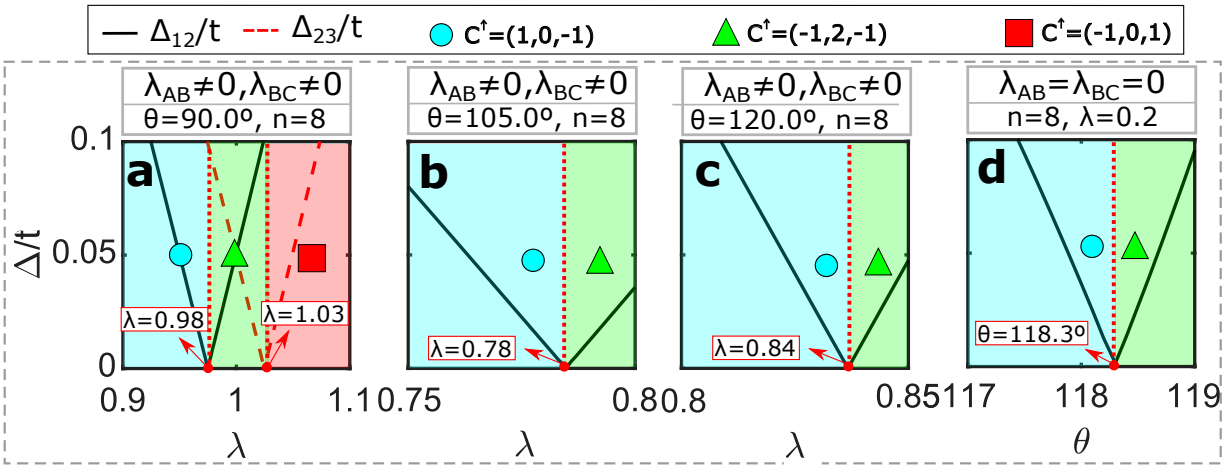

Source: The author.

energy, while the upper gap remains helical. Note that the difference in the Chern numbers is $\Delta C^{\uparrow} = (1,0,-1) - (-1,2,-1) = (2,-2,0)$. We observe that the change in the Chern numbers of the two touching bands is ± 2. This change can be attributed to the fact that the bands touch at the $\mathbf{\Gamma}$ point and exhibit quadratic behavior around this point, implying a Berry phase of 4π associated with this touching point, in accordance with Beugeling *et al.* (2012).

As shown in Fig. 54 (c), when compared with Fig. 55 (c'), it is also revealed that the double degeneracy at the $\mathbf{\Gamma}$ point between bands E_1 and E_2 for $\theta < 118.3^{\circ}$ can be lifted by either including ($n < 8$) or further suppressing ($n > 8$) the effects of NNN hoppings [see Eqs. (3.4) and (3.6)], as elucidated in the phase diagram of Fig. 58 (e). TPT occur at $n = 4.18$ with $C^{\uparrow} = (1,0,-1) - (-1,2,-1) = (2,-2,0)$ and at $n = 8$ with $C^{\uparrow} = (-1,2,-1) - (1,0,-1) = (-2,2,0)$. Furthermore, the phase diagram in Fig. 58 (f) shows that Δ_{12} can be opened while maintaining $n = 8$ and evolving the intensity of the ISO coupling, such that a TPT occurs at $\lambda = 0.2$ with $C^{\uparrow} = (1,0,-1) - (-1,2,-1) = (2,-2,0)$.

Interestingly, the TPT driven by θ evolution is the only phase transition observed in Sec. 3.7 that evaluates the case of hypothetical strains that modify the positions of the lattice sites while keeping the hopping and ISO coupling parameters constant. Other phase transitions that are discussed in Sec. 3.6 are essentially due to changes in the values of the hopping parameters and ISO coupling parameters that vary with the strain parameter.

Indeed, the TPT, as well as the non-TPT to be discussed in Sec. 3.6, are related to the

Figure 58 – Comparison between the full band gap Δ_{12} [Δ_{23}] and the local band gaps Δ'_{12} [Δ'_{23}], as shown in Fig. 57. Before and after the touching of the bottom and middle bands, the Chern numbers of the bands are well defined since they do not touch anywhere. TPT occur only if the full band gap also closes together with the local band gap at the same point, and both are different from zero before and after the TPTs points.

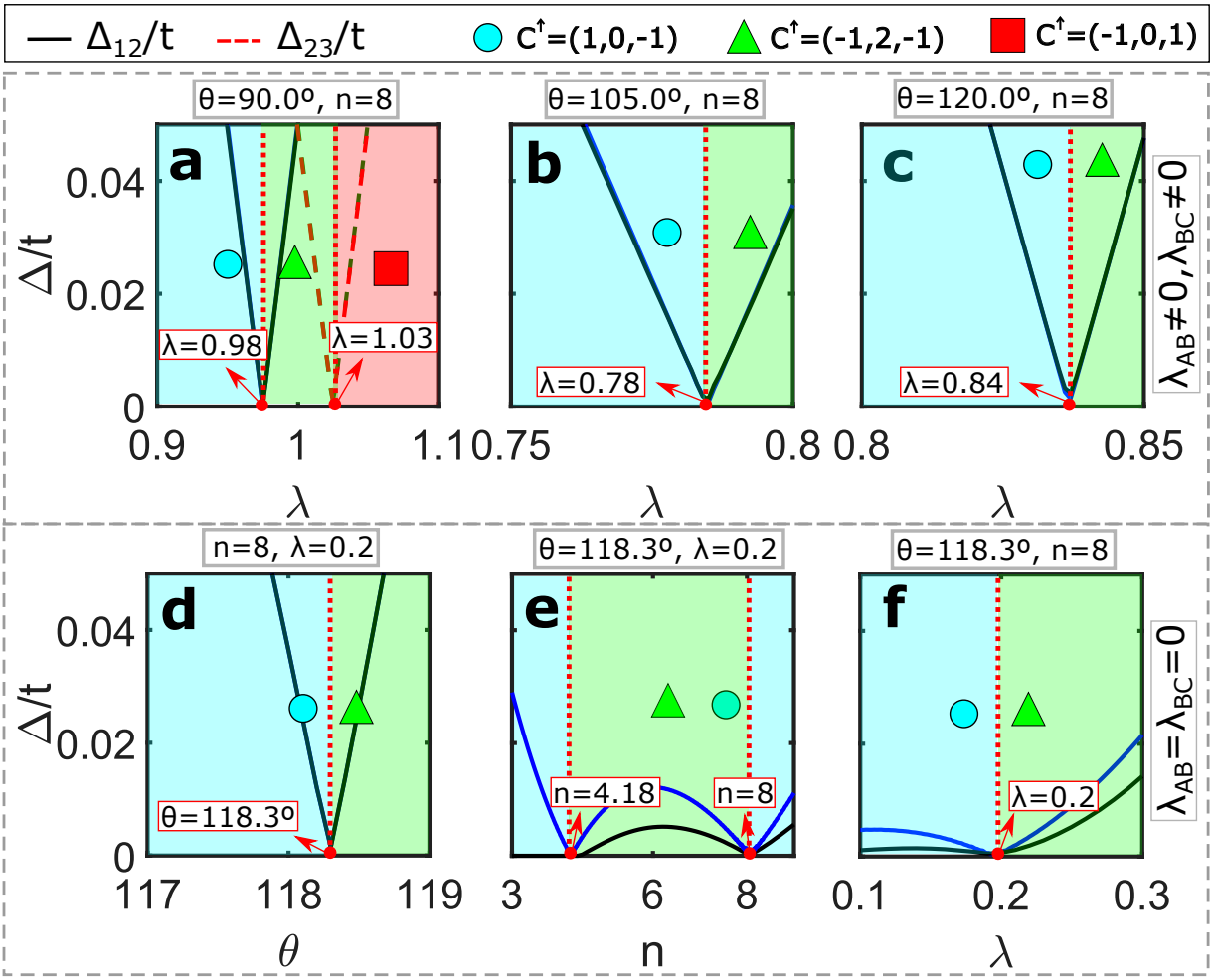

Source: The author.

evolution of energetic parameters that vary due to diagonal strains during the interconvertibility process, or due to the application of uniaxial, biaxial, simple shear, or pure strains. They are not merely a geometric effect resulting from the alteration of the positions of the Lieb-Kagome lattice sites. Thus, it is possible to find TPT at fixed values of θ without strain, simply by altering n and λ parameters as shown in Fig. 54.

3.5.3 Topological phase transitions driven by the evolution of the λ or n parameters

In Fig. 54, we present the evolution of full band gaps in response to the variation of λ and n for Lieb, transition ($\theta = 105°$), and Kagome lattices. By comparing this with the evolution of the local band gaps in Fig. 55, we highlight the TPT arising from the variation of λ

with $n = 8$ in the phase diagrams of Fig. 57 (a-c), corroborated by the phase diagrams in Fig. 58 (a-c) which demonstrate the closing and reopening of Δ_{12} or Δ_{23} at the same values of λ where Δ'_{12} or Δ'_{23} also vanish.

In the Lieb lattice, for the transition defined by the points $\lambda = 0.98$ and $\lambda = 1.03$, the lower and upper gaps respectively close, and the system behaves like a metal at the gap-closing energy; meanwhile, the other gap remains helical. The differences in the Chern numbers can be expressed as $\Delta C^{\uparrow} = (1,0,-1) - (-1,2,-1) = (2,-2,0)$ and $\Delta C^{\uparrow} = (-1,2,-1) - (-1,0,1) = (0,2,-2)$, respectively.

At $\lambda = 0.9$, before the TPT, Ω_1 (Ω_3) features two positive (negative) peaks aligned in the antidiagonal (diagonal) direction, *i.e.*,, $k_x = -k_y$ ($k_x = k_y$) [Fig. 59 (a)]. These evolved from the asymmetric peak located around the **M** point at $\lambda = 0.2$, as shown in Fig. 51 (a_1 and a_3). Ω_2 shows two positive peaks in the diagonal direction and two negative peaks in the antidiagonal direction, perpendicular to the first. The TPT at $1/3$ ($2/3$) filling changes the signs of the two peaks of Ω_1 (Ω_3). Regarding Ω_2, the TPT in the lower gap results in four positive peaks [Fig. 59 (b)], so that it is the TPT in the upper gap that restores the dipole with the two peaks being negative (positive) in the diagonal (antidiagonal) direction [Fig. 59 (c)] (ZHANG; SUN YAN E YAN, 2018).

The TPT that occur at 1/3 filling in the transition [Fig. 57 (b)] and Kagome [Fig. 57 (c)] lattices at the critical points $\lambda = 0.78$ and $\lambda = 0.84$, respectively, are analogous to the TPT in Fig. 57 (d). Specifically, $\Delta C^{\uparrow} = (1,0,-1) - (-1,2,-1) = (2,-2,0)$. The evolution of the Berry curvature for the transition lattice [Fig. 60 (d-e)] is similar to that of the Lieb lattice [Fig. 59 (a-c)]. In the Kagome lattice [Fig. 59 (d-e)], Ω_3 indeed does not exhibit a sign change, remaining negative, but now it does not show localized peaks, analogous to Ω_1 before the TPT [Fig. 51 (e)]. In fact, after the TPT, the Chern nearly-flat band is E_3 (HWANG *et al.*, 2021).

In summary, our results clearly indicate TPT due exclusively to the variation of n and/or λ, without the need for additional factors. With this knowledge, in the next section, we will investigate TPT driven by the six types of strains presented in Fig. 46 (b-g), while maintaining $\lambda = 0.2$ and $n = 8$.

Figure 59 – Contour plots of Berry curvature (as in Fig. 51), before and after the TPTs identified in Fig. 57. Specifically, panels (a-c), (d-e), and (f-g) correspond to the cases depicted in panels a, c, and e of Fig. 57. The remaining cases are presented in Fig. 60. It is noteworthy that the TPT cause a change in the sign of the Berry curvature.

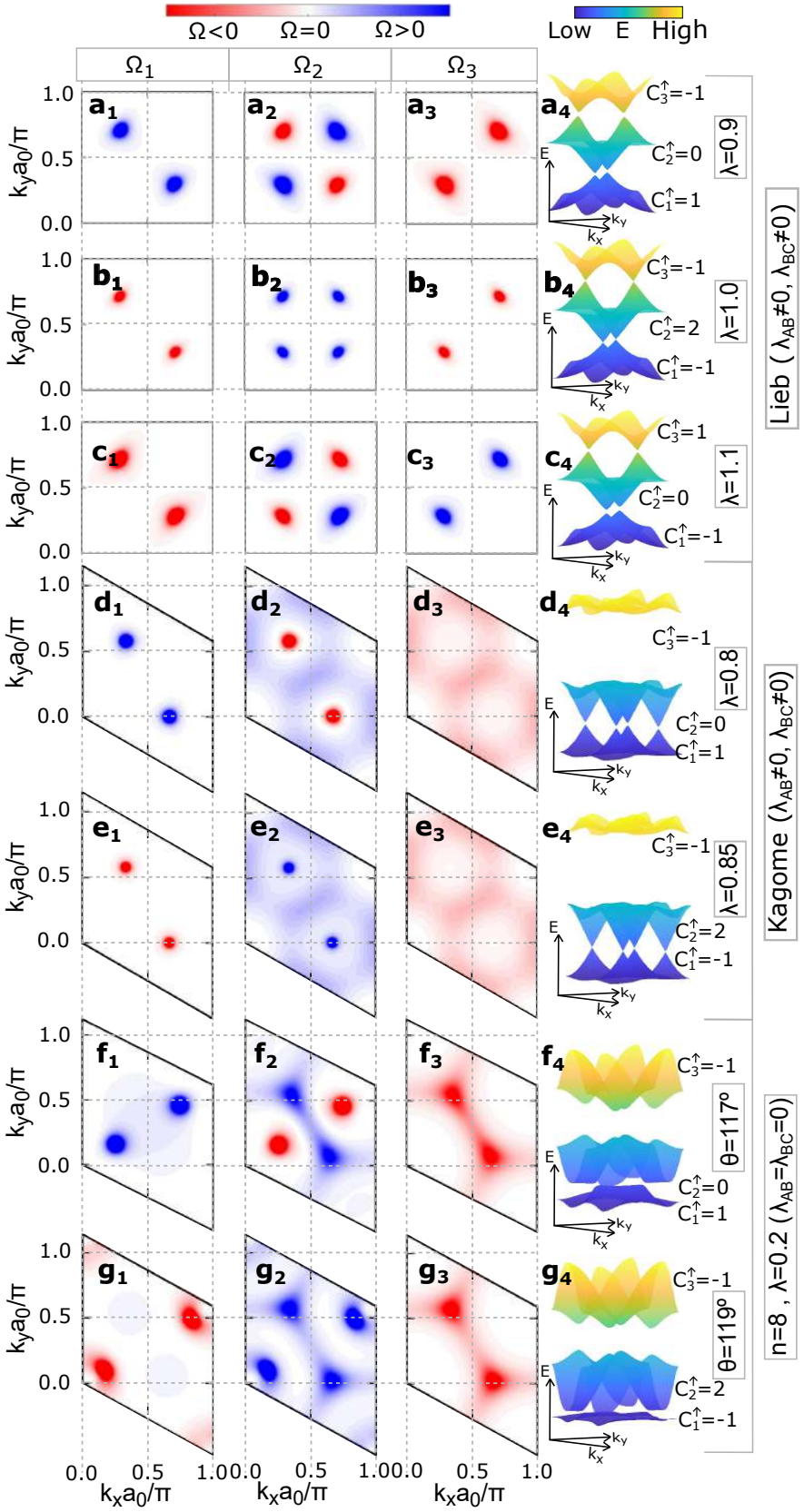

Source: The author.

Figure 60 – Contour plots of the Berry curvature (as shown in Fig. 59), before and after the TPTs identified in Fig. 57. It is noteworthy that the TPT cause a change in the sign of the Berry curvature.

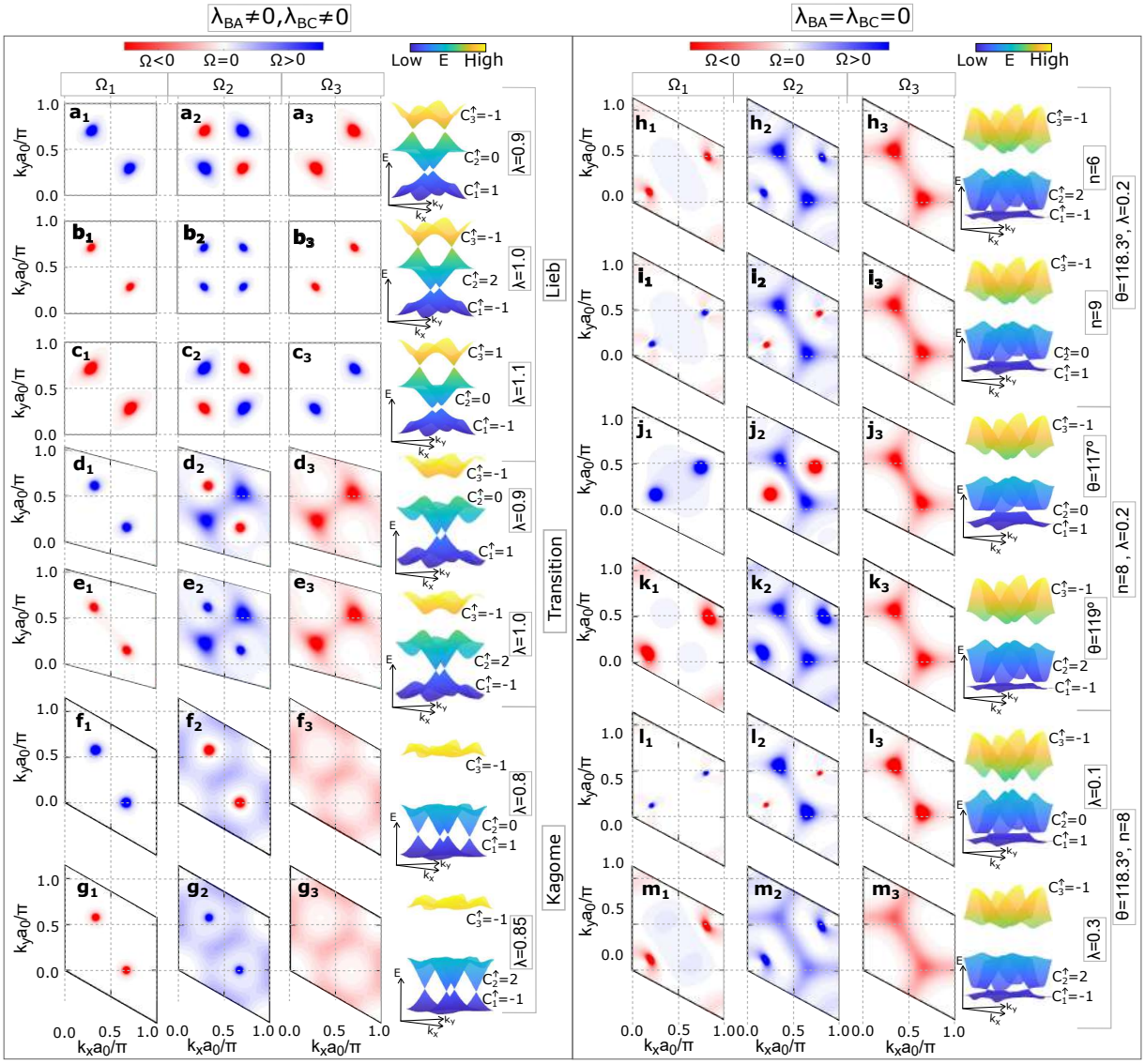

Source: The author.

Figure 61 – Contour plot of the full band gap as in Fig. 54, but now as a function of ε and θ, for UX-strain (1st column of panels), UY-strain (2nd column of panels), BI-strain (3rd column of panels), SX-strain (4th column of panels), SY-strain (5th column of panels), and PS-strain (6th column of panels). Results are presented considering all ISO coupling parameters (1st and 2nd rows of panels), as well as assuming $\lambda_{AB} = \lambda_{BC} = 0$ (3rd and 4th rows of panels). For comparison, Fig. 62 shows the evolution of the local band gap in each case.

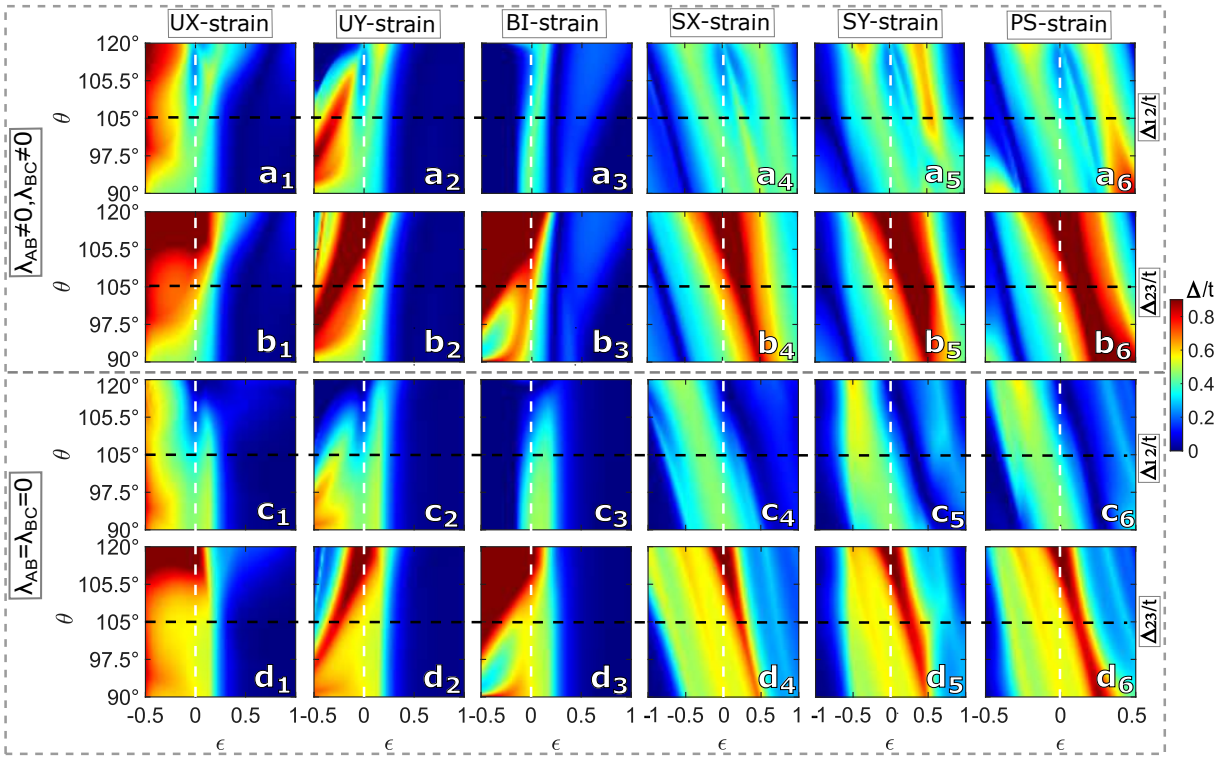

Source: The author.

3.6 Phase transition driven by strain

In this section, we investigate the occurrence of phase transition induced by six distinct types of strains, as depicted in Fig. 46 (b-g). Figure 61 illustrates the evolution of the full band gaps as the angle θ varies from 90° to 120°, in relation to the strain parameter, ε. For comparative analysis, the evolution of the local band gaps is presented in Fig. 62.

In both scenarios, while our theoretical model is not constrained by the elasticity limits of specific real materials, we impose a limitation for uniaxial and biaxial compressive strains at $\varepsilon = -0.5$ (demonstrated in Fig. 61 and Fig. 62, panels 1, 2, and 3). This constraint is set to prevent situations where the distance between NN sites in the strained lattice is much smaller than in the unstrained lattice ($a_0' \ll a_0$), potentially resulting in Δ_1 and $\Delta_2 \to \infty$. This condition is anticipated in the limit where lattice sites overlap.

For simple shear strains, the overlap of site positions is not a concern, as negative ε values do not induce compression but represent shear in the opposite direction to $\varepsilon > 0$. Thus, we

allow $-1 \leq \varepsilon \leq 1$ for these cases (shown in Fig. 61 and Fig. 62, panels 4 and 5). For PS-strains, we consider $-0.5 \leq \varepsilon \leq 0.5$ (Fig. 61 and Fig. 62, panel 6), to facilitate direct comparison with simple shear cases, since $\varepsilon^{PS} = \varepsilon^{SX}/2 = \varepsilon^{SY}/2$ (THIEL *et al.*, 2019).

Figure 63 presents the phase diagrams with a direct comparison between the evolution of full band gaps and local band gaps in specific cases of Lieb lattices [see Fig. 63 (a,d)], the transition state ($\theta = 105^{\circ}$) [see Fig. 63 (b,e)], and Kagome lattices [see Fig. 63 (c,f)]. We explore the TPT points ε_c, where closure and reopening of both full and local band gaps at 1/3 and/or 2/3 filling are observed, attributable to the band crossing of E_1 and E_2 and/or E_2 and E_3 as a function of ε.

The TPT identified in Fig. 63 are system atized in the phase diagrams of Fig. 64. As in Fig. 57, the TPT points ε_c are indicated by red dotted lines, delineating the regimes $C^{\uparrow} = (1,0,-1)$ in blue, $C^{\uparrow} = (-1,2,-1)$ in green, and $C^{\uparrow} = (-1,0,1)$ in red. In all cases of open gaps, the system exhibits behavior characteristic of a QSHI, with spin Hall conductivity $\sigma_{\mathrm{SH}} = \pm 1$ (BEUGELING *et al.*, 2012). When the middle band has a zero Chern number, the conductivities at 1/3 filling and 2/3 filling are the same, being opposite otherwise (BEUGELING *et al.*, 2012).

Figure 62 – Contour plots of the full band gap Δ_{12} [Δ_{23}] presented in Fig. 61 are contrasted with contour plots of the local band gaps Δ'_{12} [Δ'_{23}], which refer to the minimum separation between the bands at each individual point in their momentum space. At points where the bands touch, the local band gap reduces to zero, indicating TPT.

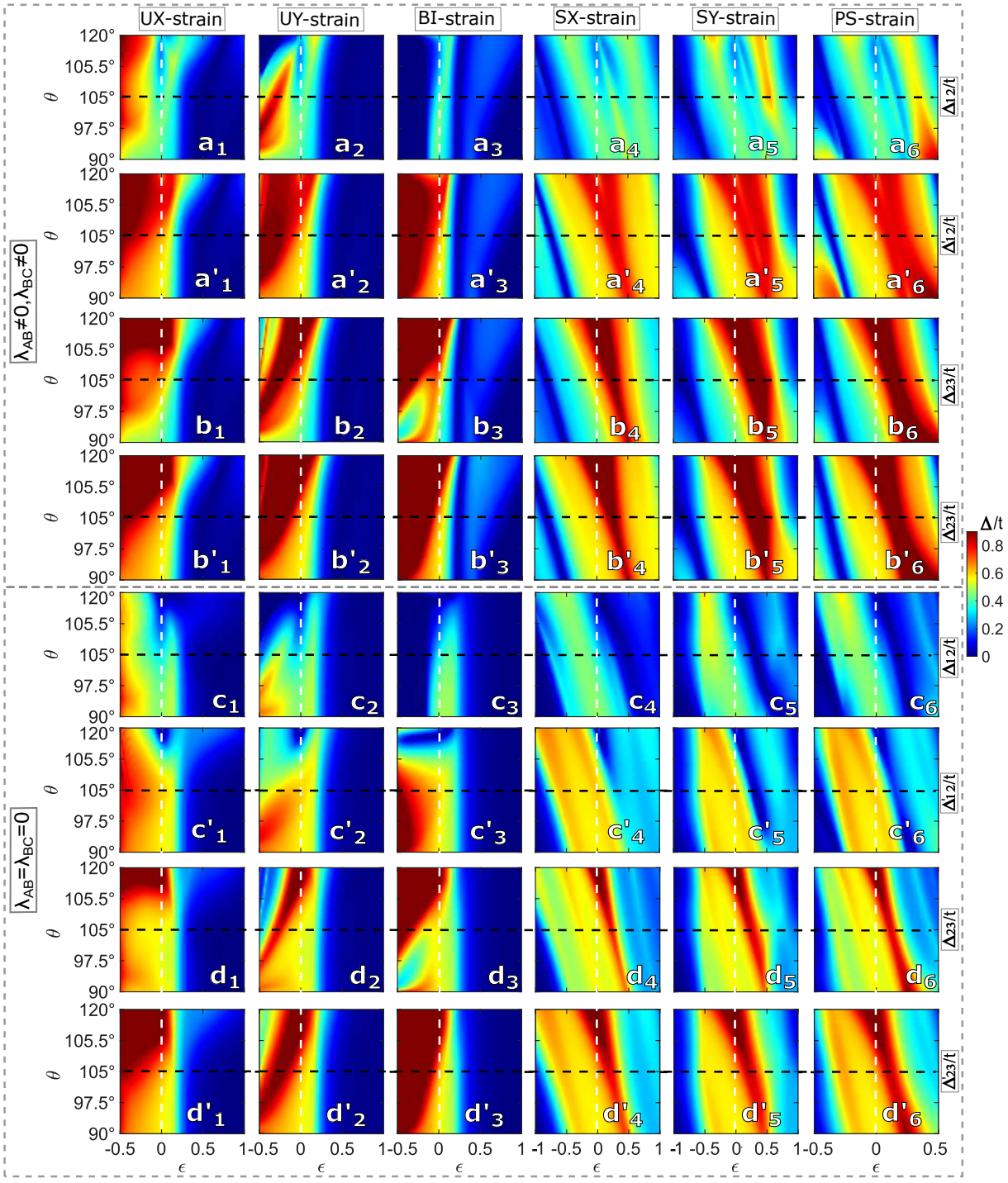

Source: The author.

Figure 63 – The evolution of the full band gap Δ_{12} [Δ_{23}] and local band gaps Δ'_{12} [Δ'_{23}] for the specific cases in Fig. 62 with $\theta = 90°$ (Lieb lattice), $\theta = 105°$ (transition lattice), and $\theta = 120°$ (Kagome lattice) is depicted. The points of non-topological phase transition, linking the TI phase with a semimetallic or metallic phase at 1/3 filling, are indicated by open circles with central dots or simple open circles, respectively. The points ε of TPT that connect two TI phases are highlighted in Fig. 64.

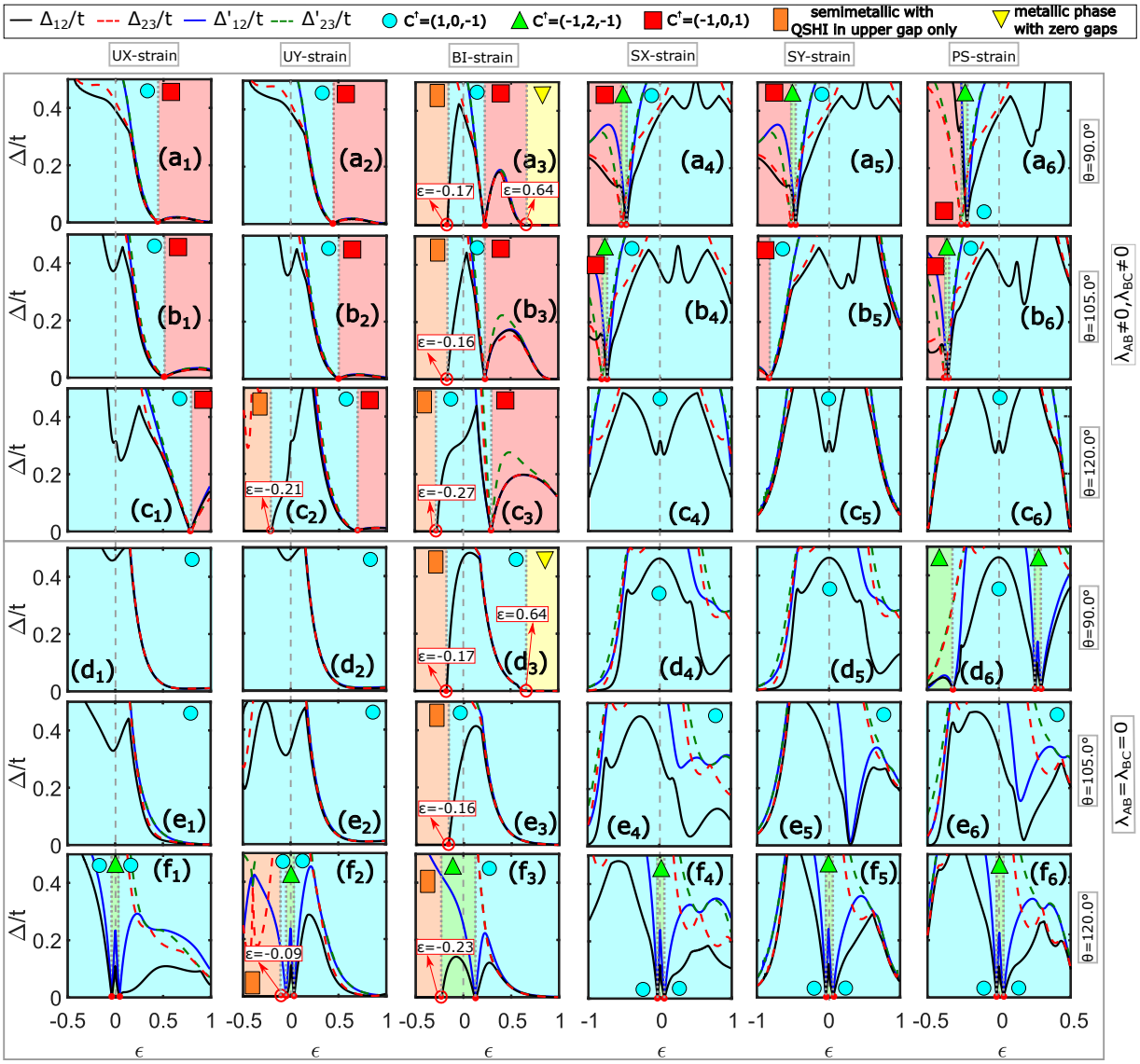

Source: The author.

Figure 64 – Evolution of the full band gaps as in Fig. 57, but now as a function of ϵ for the cases from Fig. 61 where we identified TPT. Fig. 63 shows the evolution of the local band gap, confirming the TPT.

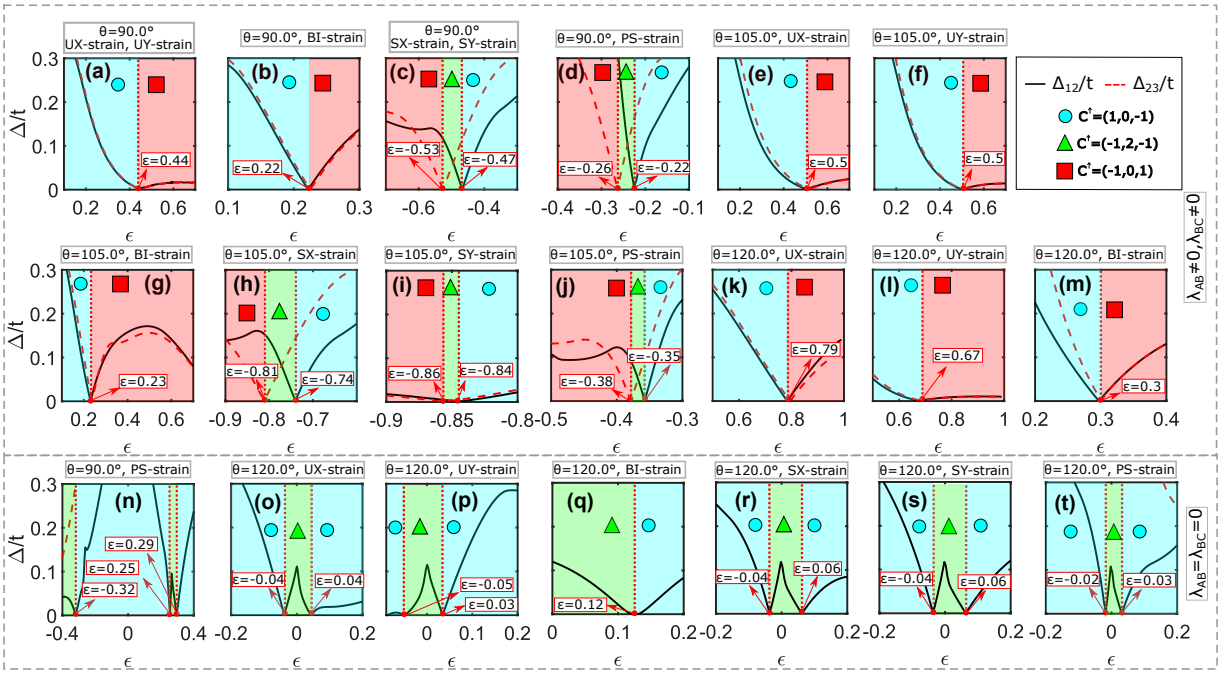

Source: The author.

3.6.1 *Uniaxial and biaxial strain-driven topological phase transitions with* $\lambda_{AB} \neq 0$ *and* $\lambda_{BC} \neq 0$

Initially, we will evaluate the TPT driven by uniaxial and biaxial strains for $\lambda_{AB} \neq 0$ and $\lambda_{BC} \neq 0$. Figure 64 shows that the Lieb [Fig. 64 (a-b)], transition ($\theta = 105^{\circ}$) [Fig. 64 (e-g)], and Kagome [Fig. 64 (k-m)] lattices undergo a TPT characterized by $\Delta C^{\uparrow} = (1,0,-1) - (-1,0,1) = (2,0,-2)$. In the Lieb lattice, this TPT occurs at $\varepsilon_c = 0.44$ when subjected to UX and UY-strains [Fig. 64 (a)], and at $\varepsilon_c = 0.22$ when under BI-strain [Fig. 64 (b)]. In transition lattices with $\theta = 105^{\circ}$, the TPT occurs at $\varepsilon_c = 0.5$ when subjected to UX [Fig. 64 (e)] and UY-strains [Fig. 64 (f)], and at $\varepsilon_c = 0.23$ under BI-strain [Fig. 64 (g)]. In the Kagome lattice, this TPT occurs at $\varepsilon_c = 0.79$ for the UX-strain [Fig. 64 (k)], $\varepsilon_c = 0.67$ for the UY-strain [Fig. 64 (l)], and $\varepsilon_c = 0.3$ for the BI-strain [Fig. 64 (m)]. In all cases, at $\varepsilon = \varepsilon_c$, Δ_1 and Δ_2 close, thereby preventing the emergence of helical states at 1/3 or 2/3 filling. These TPTs are not observed in unstrained Lieb-Kagome lattices [Fig. 57].

These TPTs are confirmed by the evolution of the Berry curvatures, as presented in Figs. 65, 66, and 67 for the Lieb, transition, and Kagome lattices, respectively. We highlight in Fig. 68 (a-b, i-j, k-l) the configurations non-equivalent for strain-driven TPT with $\lambda_{AB} \neq 0$ and $\lambda_{BC} \neq 0$, including the cases of SX, SY, and PS strain, which will be discussed in Subsec. 3.6.2.

Figure 65 – Contour plots of the Berry curvature, before and after the TPTs identified in panels a and b of Fig. 64 (Lieb lattice). It is noteworthy that the TPT cause a change in the sign of the Berry curvature.

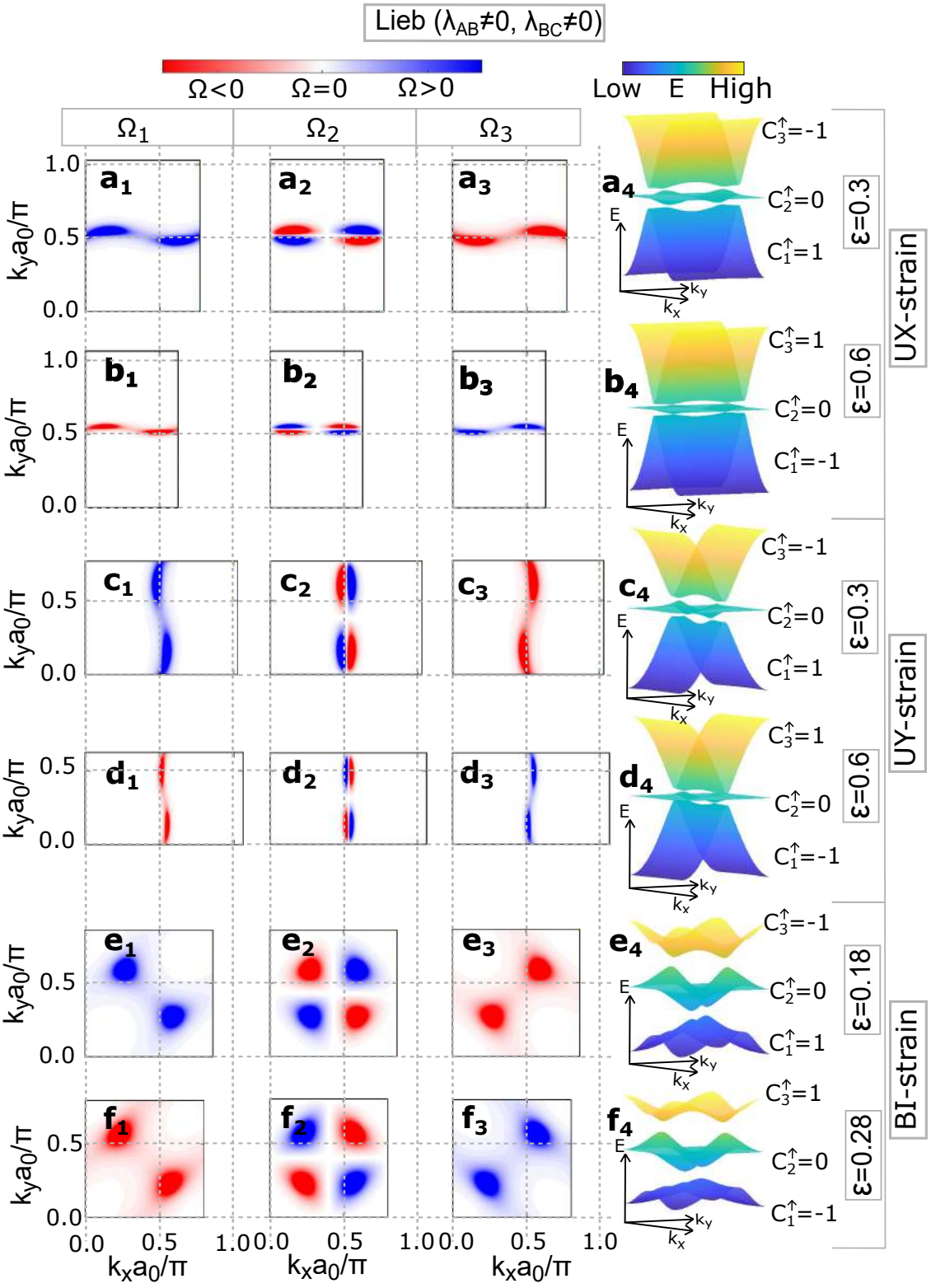

Source: The author.

Figure 66 – Contour plots of the Berry curvature, before and after the TPTs identified in panels (e), (f), and (g) of Fig. 64 (transition lattice). It is noteworthy that the TPT cause a change in the sign of the Berry curvature.

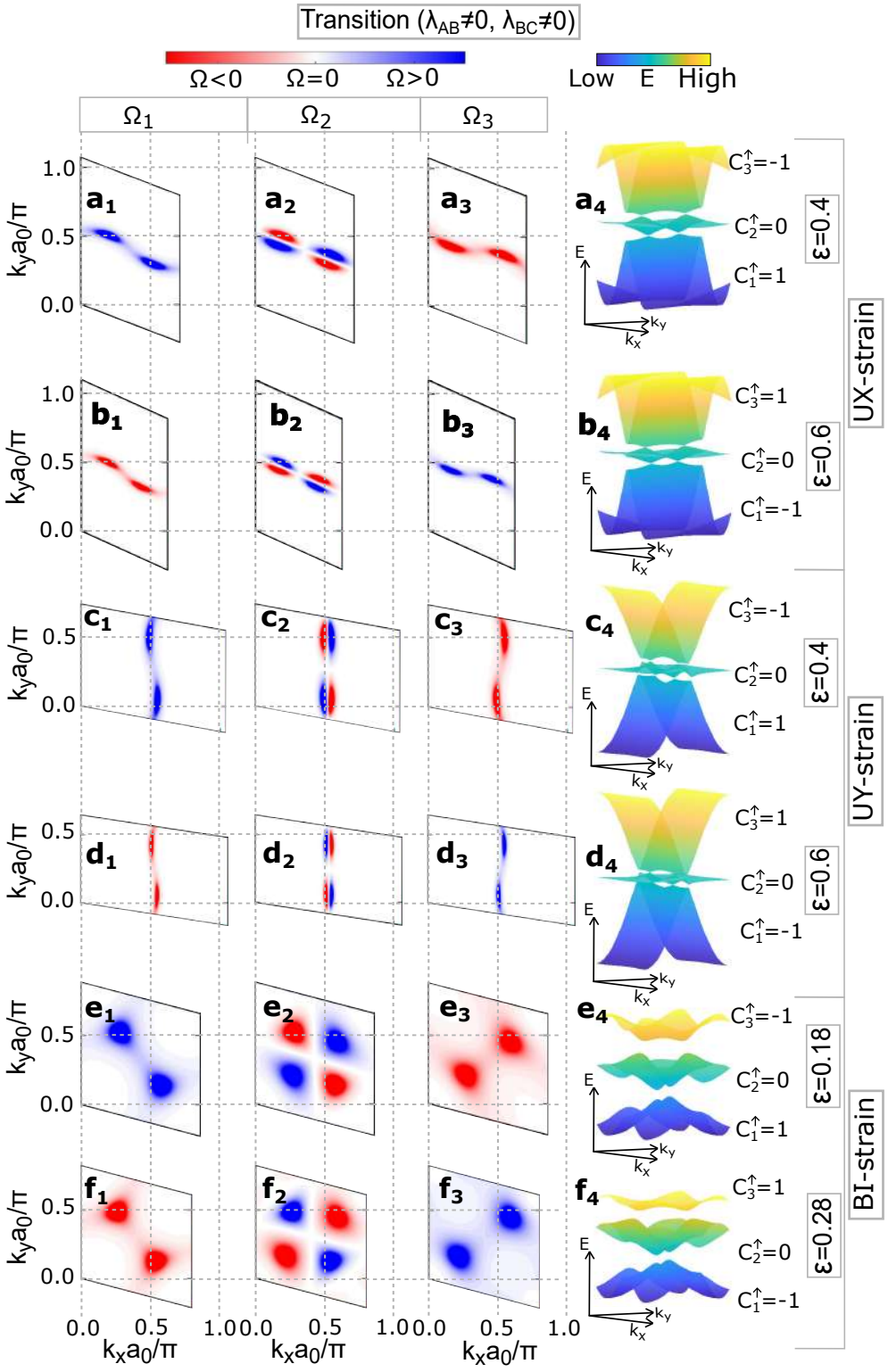

Source: The author.

Figure 67 – Contour plots of the Berry curvature, before and after the TPTs identified in panels (k), (l), and (m) of Fig. 64 (Kagome lattice). It is noteworthy that the TPT cause a change in the sign of the Berry curvature.

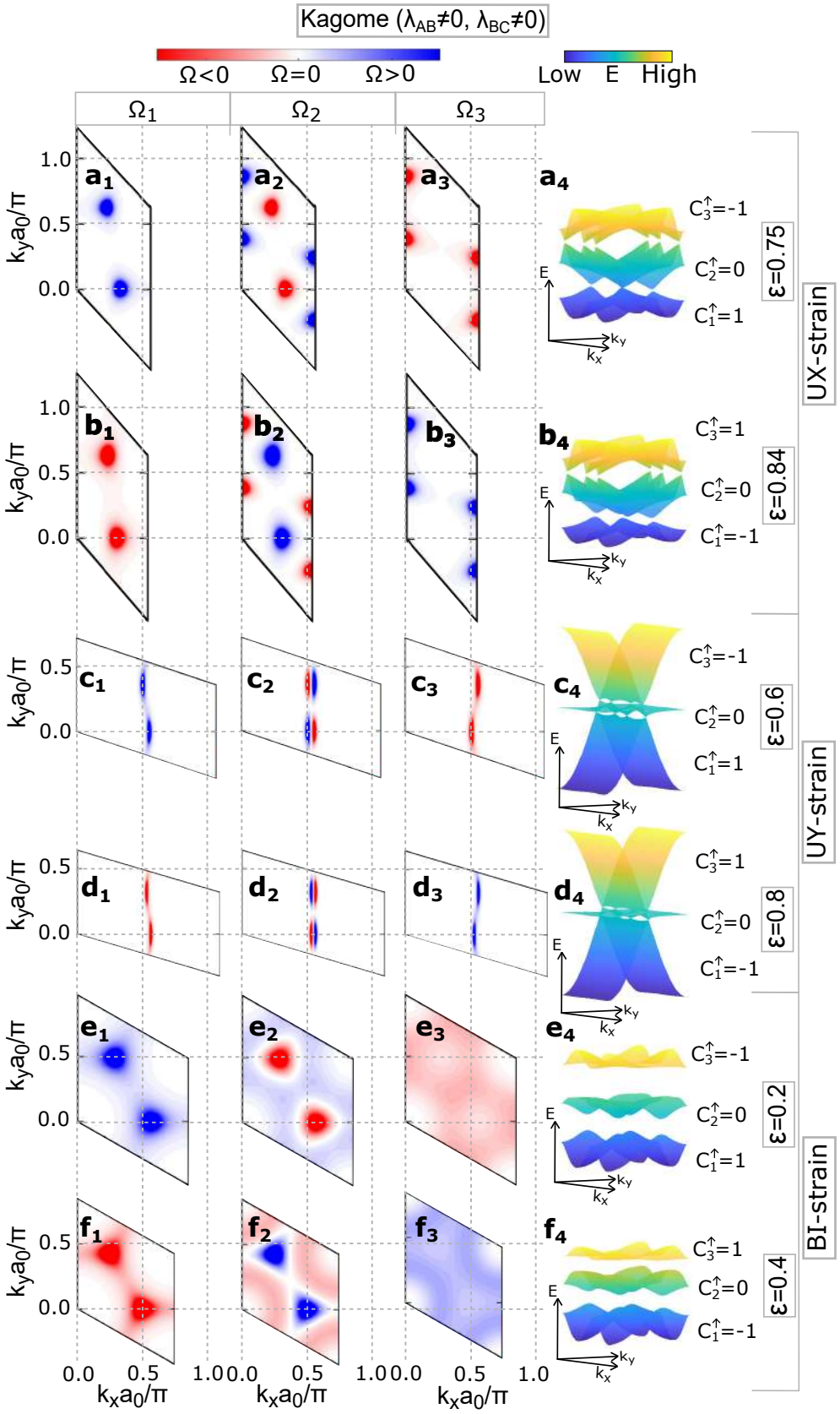

Source: The author.

Figure 68 – Contour plots of Berry curvature (as in Fig. 51), before and after the TPTs identified in Fig. 64 for some cases with $\lambda_{AB} \neq 0$ and $\lambda_{BC} \neq 0$ (see Figs. 75 and 72).

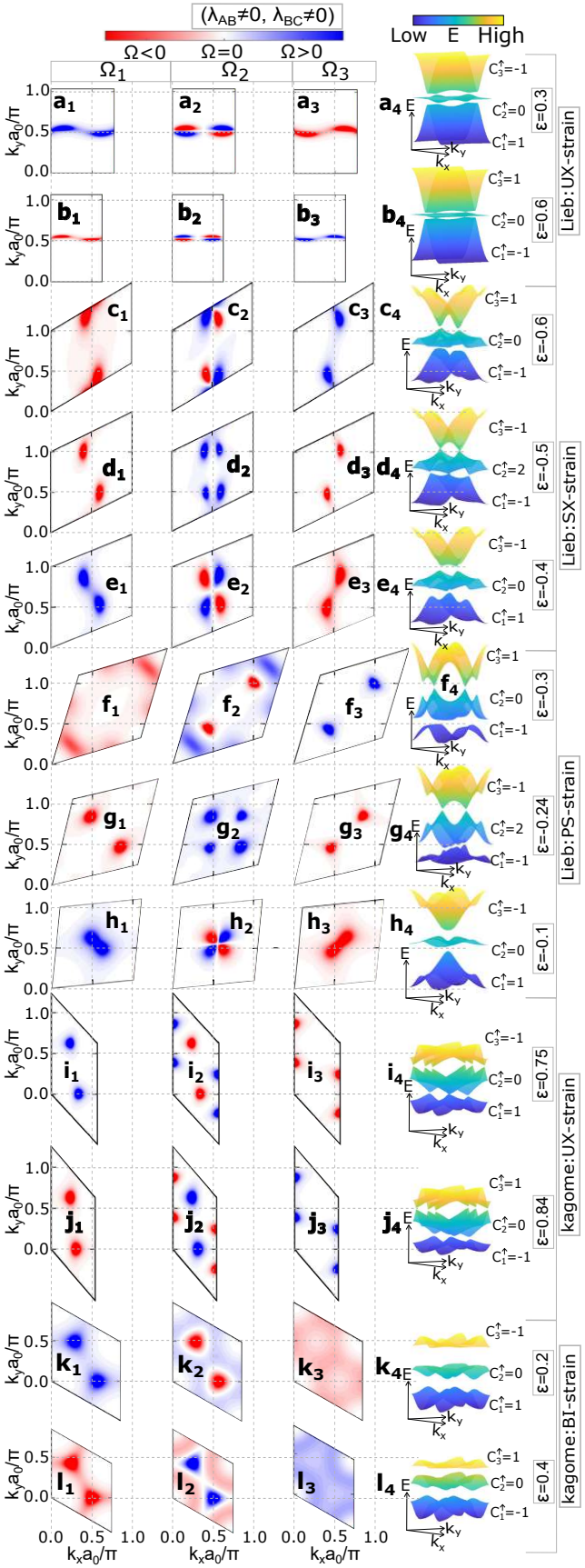

Source: The author.

The Lieb lattice under UX-strain [see Fig. 68 (a-b)] demonstrates that Ω_1^{UX} displays two positive peaks, while Ω_3^{UX} exhibits two negative peaks, which reverse signs when comparing the states before and after ε_c (LANG *et al.*, 2023). Meanwhile, Ω_2^{UX} retains its dipole characteristic, swapping the signs of the two positive and two negative peaks before and after the TPTs (ZHANG; SUN YAN E YAN, 2018). Indeed, the Berry curvatures of Lieb lattices under UY-strain [see Fig. 65 (c-d)] or BI-strain [see Fig. 65 (e-f)], and of the transition lattice ($\theta = 105^\circ$) under UX, UY, and BI-strains [see Fig. 66] are analogous to those of the UX-strained Lieb lattice. For Kagome lattices, the three Berry curvatures for UY-strain, and Ω_1 for both UX and UY-strains, also follow a similar pattern [see Fig. 67].

It is noteworthy that this similarity pertains to the sign configuration before and after the TPTs as well as to the peak distribution of the curvature, with differences in shape and orientation. Specifically, BI-strained Lieb-Kagome lattices exhibit Ω_1^{BI} with non-tilted peaks localized along the antidiagonal direction, defined as $k_y = ((\mathbf{b}_1 - \mathbf{b}_2)_y/(\mathbf{b}_1 - \mathbf{b}_2)_x)k_x$, and Ω_3^{BI} with non-tilted peaks along the diagonal direction, defined as $k_y = ((\mathbf{b}_1 + \mathbf{b}_2)_y/(\mathbf{b}_1 + \mathbf{b}_2)_x)k_x$. Meanwhile, Ω_2^{BI} shows two peaks each along the antidiagonal and diagonal directions. It is important to remember that $\mathbf{b}_1$ and $\mathbf{b}_2$ are dependent on θ . In contrast, UX and UY-strained Lieb-Kagome lattices display tilted peaks, aligning with the direction of the reciprocal lattice vectors $\mathbf{b}_1$ and $\mathbf{b}_2$, respectively. This behavior is analogous to the type III tilted cones observed in the energy spectrum without ISO coupling (LIMA *et al.*, 2023).

The cases of Ω_2 and Ω_3 in UX and UY-strained Kagome lattice exhibit the same number of peaks with the sign configurations seen in the previous cases, but with different peak distributions. In UX-strained Kagome, we find four 1/2 peaks at the edges of the considered reciprocal space area [see Fig. 68 ($i_{2,3}$,$j_{2,3}$)], as opposed to two full peaks outside the edges. In the case of BI-strained Kagome, we do not identify peaks in the diagonal direction as in Lieb and transition cases, but we observe a Berry curvature distribution characteristic of a Chern nearly-flat band [see Fig. 68 ($k_{2,3}$,$l_{2,3}$)].

Regardless of the characteristic format of the Berry curvatures for each band, we note that the TPT driven by uniaxial and biaxial strains for $\lambda_{AB} \neq 0$ and $\lambda_{BC} \neq 0$ within the admitted ε region in Fig. 61 ensure the existence of a Berry curvature with both positive and negative parts calculated for the middle band, and only positive or negative curvature for the lower and upper bands. This indicates that a TPT always inverts these signs when compared with configurations before and after ε_c in Lieb-Kagome lattices.

Figure 69 – Comparison between the full band gap Δ_{12} [Δ_{23}] and the local band gaps Δ'_{12} [Δ'_{23}], versus ε as shown in Fig. 64, for TPT identified for values of ε not presented in Figs. 61 and 62.

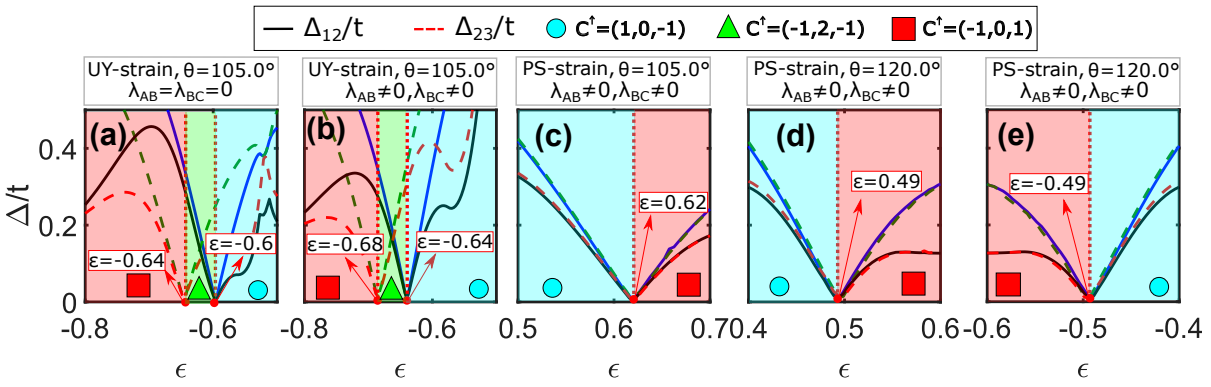

Source: The author.

Outside the admitted ε region in Fig. 61, we identify two TPT in the UY-strained transition lattice [see Fig. 69 (b)], which do not follow this pattern [see Fig. 70]. As observed in Fig. 69 (b), one occurs at $\varepsilon_c = -0.64$ at 1/3 filling (preserving the topological insulating phase at 2/3 filling), characterized by a Chern number change of $\Delta C^{\uparrow} = (1,0,-1) - (-1,2,-1) = (2,-2,0)$. This change is accompanied by the alteration of the sign of the two peaks in Ω_1^{UY}, the disruption of the Berry dipole in Ω_2^{UY} resulting in four positive peaks, and the preservation of the sign of the two peaks in Ω_3^{UY} [see Fig. 70 (b-c)]. Another TPT occurs at $\varepsilon_c = -0.68$ at 2/3 filling (maintaining the topological insulating phase at 1/3 filling), with a Chern number change of $\Delta C^{\uparrow} = (-1,2,-1) - (-1,0,1) = (0,2,-2)$, marked by a sign change in the two peaks of Ω_3^{UY}, the restoration of the Berry dipole in Ω_2^{UY}, and the constant sign of the two peaks of Ω_1^{UY}. As we will see next, this behavior is characteristic of TPT subjected to pure and simple shear strains within the ε range established in Fig. 61.

Figure 70 – Contour plots of the Berry curvature, before and after the TPTs identified in panel b of Fig. 69. It is noteworthy that the TPT cause a change in the sign of the Berry curvature.

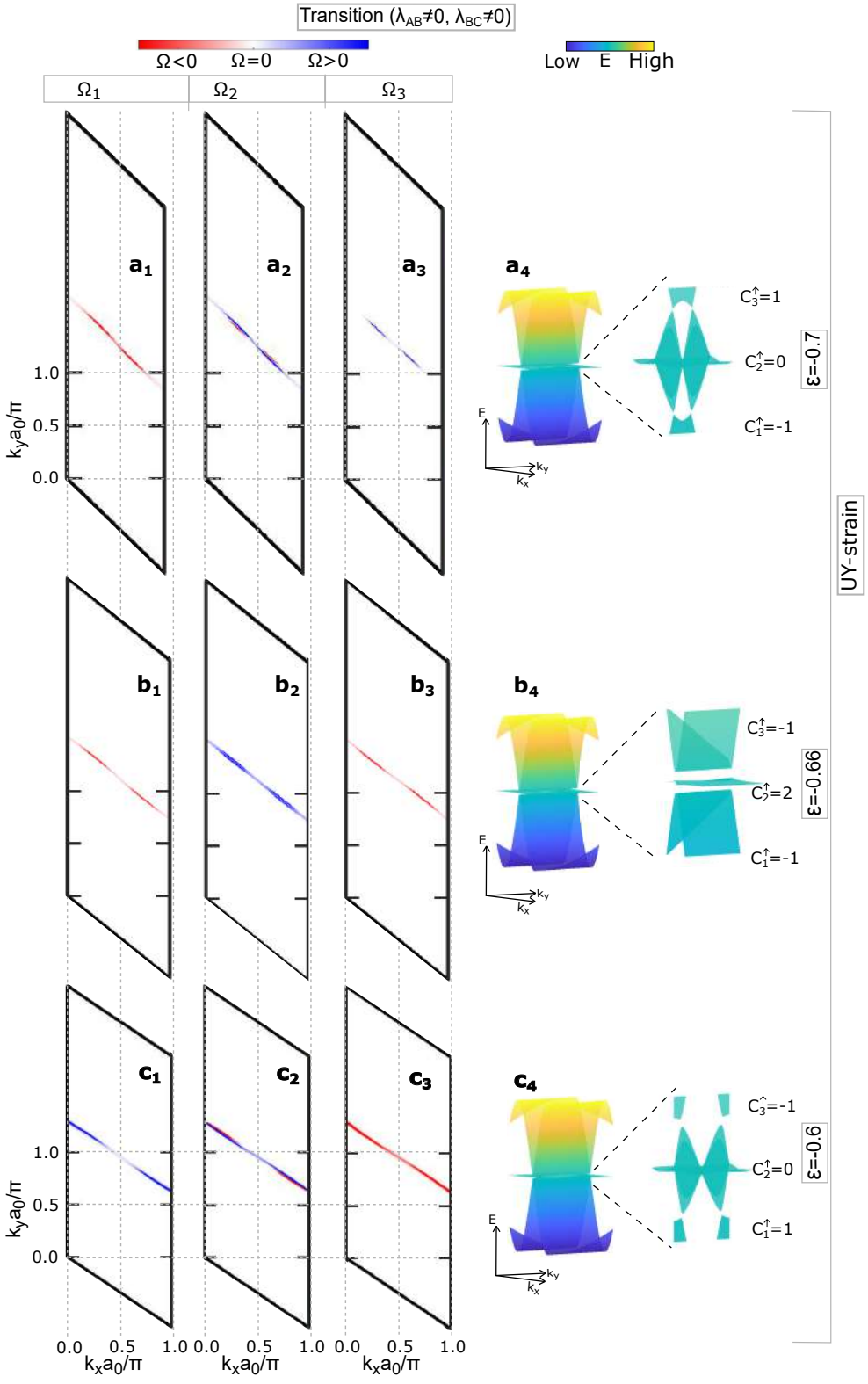

Source: The author.

3.6.2 *Simple and pure shear strain-driven topological phase transitions with $\lambda_{AB} \neq 0$ and $\lambda_{BC} \neq 0$*

Now, let us examine TPT driven by simple and pure shear strains, when $\lambda_{AB} \neq 0$ and $\lambda_{BC} \neq 0$. Reducing ε from zero results in TPT at two distinct values of ε_c in the Lieb lattice [see Fig. 64 (c-d)] and transition lattices [see Fig. 64 (h-j)] when ε falls within the range covered in Fig. 63 (a_{4-6},b_{4-6}), whereas the Kagome lattice remains robust against TPT in this scenario [see Fig. 63 (c_{4-6})]. The first TPT occurs at 1/3 filling, with $\Delta C^{\uparrow} = (1,0,-1) - (-1,2,-1) = (2,-2,0)$, such that the two positive peaks in Ω_1 become negative, the characteristic Berry dipole present in Ω_2^{SX} with two positive and two negative peaks is destroyed by the emergence of four positive peaks, and the two negative peaks of Ω_3^{SX} maintain their sign. The second TPT occurs at 2/3 filling with $\Delta C^{\uparrow} = (-1,2,-1) - (-1,0,1) = (0,2,-2)$, such that the two negative peaks of Ω_3 turn positive, the Berry dipole characteristic is restored in Ω_2, presenting two positive and two negative peaks (with opposite signs to the initial Berry dipole), and the sign of the two negative peaks of Ω_1 is maintained [see Figs. 71 and 72].

Specifically, in the Lieb lattice, TPT occur at 1/3 filling for $\varepsilon_c^{SX} = \varepsilon_c^{SY} = -0.47$ and at $\varepsilon_c^{PS} = -0.22$ under PS-strain. At 2/3 filling, TPTs are observed at $\varepsilon_c^{SX} = \varepsilon_c^{SY} = -0.53$ and at $\varepsilon_c^{PS} = -0.26$ [Fig. 71]. In the transition lattice with $\theta = 105°$, TPT at 1/3 filling occur at $\varepsilon_c^{SX} = -0.74$, $\varepsilon_c^{SY} = -0.84$, and $\varepsilon_c^{PS} = -0.35$. Meanwhile, at 2/3 filling, TPT take place at $\varepsilon_c^{SX} = -0.81$, $\varepsilon_c^{SY} = -0.86$, and $\varepsilon_c^{PS} = -0.38$ [Fig. 72].

Due to the D_{4h} symmetry of the unstrained Lieb lattice, the Berry curvatures of the SY-strained Lieb lattice, Ω_1^{SY}, Ω_2^{SY}, and Ω_3^{SY} [see Fig. 71 (d-f)], are analogous to the Berry curvatures of the SX-strained Lieb lattice, Ω_1^{SX}, Ω_2^{SX}, and Ω_3^{SX} [see Fig. 71 (a-c)]. To establish the connection between these Berry curvatures, we first apply a $\pi/2$-rotation using the operator $\hat{C}_4$, followed by the application of the mirror symmetry operator σ_y to reflect the graph across the k_y axis. This process inversely maps points such that those with $k_y > 0$ are mapped to $k_y < 0$ and vice versa. Therefore, we can express the Berry curvatures for the SY case as $\Omega_1^{SY} = \sigma_y \hat{C}_4 \Omega_1^{SX}$, $\Omega_2^{SY} = \sigma_y \hat{C}_4 \Omega_2^{SX}$, and $\Omega_3^{SY} = \sigma_y \hat{C}_4 \Omega_3^{SX}$. Analogously, the relationships for the UY-strain can be described as $\Omega_1^{UY} = \sigma_y \hat{C}_4 \Omega_1^{UX}$, $\Omega_2^{UY} = \sigma_y \hat{C}_4 \Omega_2^{UX}$, and $\Omega_3^{UY} = \sigma_y \hat{C}_4 \Omega_3^{UX}$ [see Fig. 65 (a-d)]. Indeed, the transition lattices do not exhibit such relations between SX and SY or between UX and UY-strains [Fig. 72 (a-b)].

The evolution of the Berry curvatures for the PS-strained Lieb lattice, before and after the TPTs at 1/3 filling [see Fig. 68 (g-h)], is analogous to that of the SX and SY-strained

Figure 71 – Contour plots of the Berry curvature (which complement those presented in Fig. 68), before and after the TPTs identified in panels c and d of Fig. 64. It is noteworthy that the TPT cause a change in the sign of the Berry curvature.

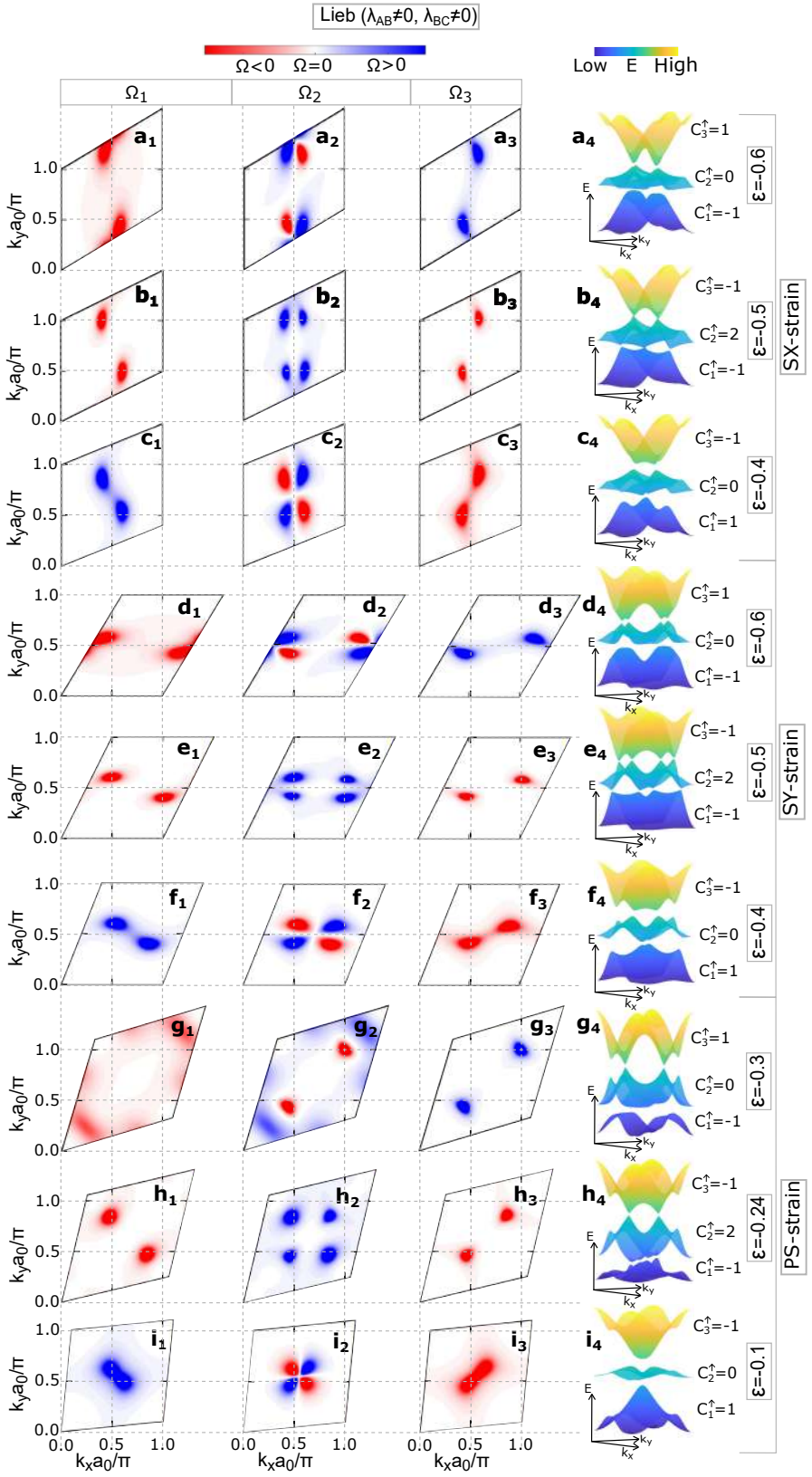

Source: The author.

Figure 72 – Contour plots of the Berry curvature (which complement those presented in Fig. 68), before and after the TPTs identified in panels (h), (i), and (j) of Fig. 64. It is noteworthy that the TPT cause a change in the sign of the Berry curvature.

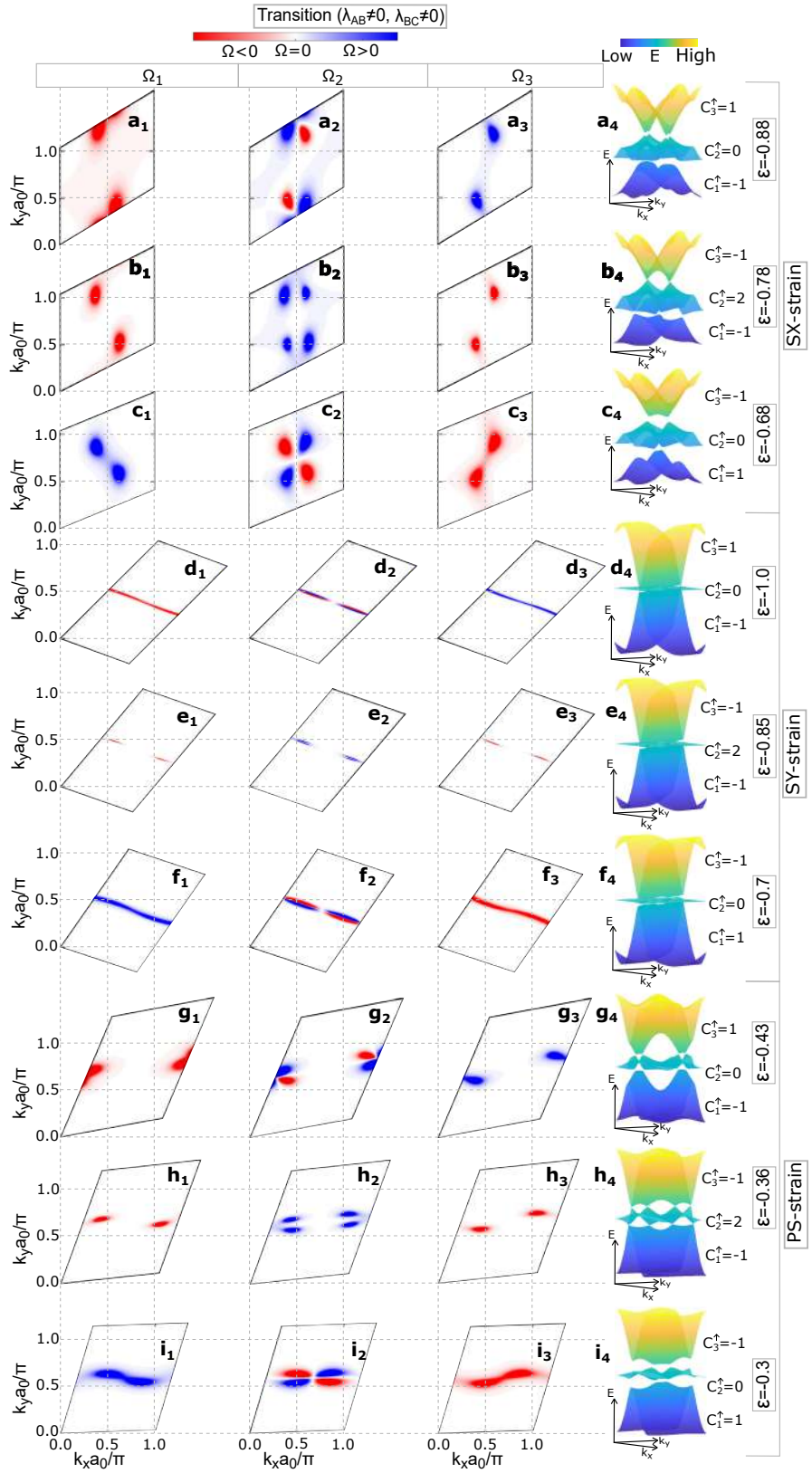

Source: The author.

Figure 73 – Contour plots of the Berry curvature, before and after the TPTs identified in panel c of Fig. 69. It is noteworthy that the TPT cause a change in the sign of the Berry curvature.

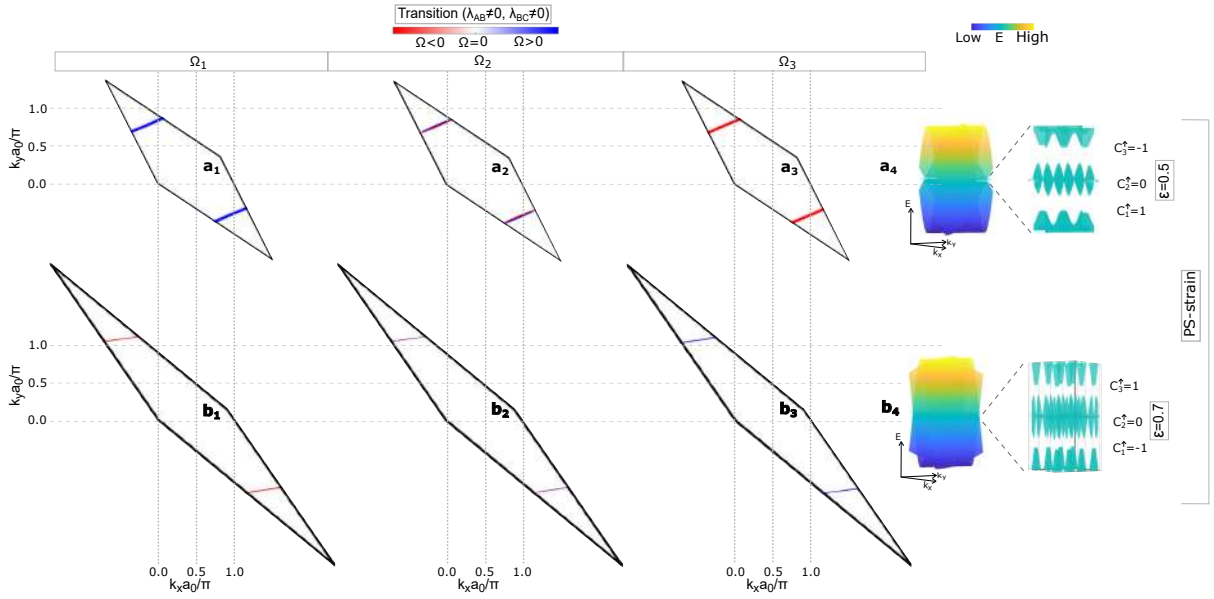

Source: The author.

Lieb lattices [see Fig. 71 (a-f)], with the caveat that it now exhibits mirror symmetry relative to both the diagonal and antidiagonal axes in the presented reciprocal space region. This attribute is also due to the D_{4h} symmetry of the unstrained Lieb lattice. As such, the Berry curvatures of the BI-strained Lieb lattice exhibit this symmetry [see Fig. 65 (e-f)], whereas those of the PS-strained transition lattice do not [see Fig. 71 (g-i)]. A notable difference in the SY-strained Lieb lattice occurs due to the TPT at 2/3 filling, which presents Ω_1^{PS} [see Fig. 68 (f_1)] with two extremely tilted peaks that differ in shape, orientation, and position from the peaks observed in the corresponding SX-strain case [see Fig. 68 (c_1)]. This distinction is also evident in the positive part of Ω_2 [compare Fig. 68 (f_2) with Fig. 68 (c_2)].

In contrast to the shear strain cases of Fig. 64 with $\lambda_{AB} \neq 0$ and $\lambda_{BC} \neq 0$, where TPT occurred when either Δ_{12} or Δ_{23} closed at different ε_c, the transition lattice with PS-strain exhibits a TPT when both the upper and lower gaps close and reopen at $\varepsilon_c = 0.62$ with $\Delta C^{\uparrow} = (1,0,-1) - (-1,0,1) = (2,0,-2)$ [see Fig. 69 (c)]. Similarly, for the Kagome lattice with PS-strain, a TPT occurs at $\varepsilon_c = \pm 0.49$ [see Fig. 69 (d-e)]. The corresponding Berry curvatures are shown in Figs. 73 and 74, respectively, which feature extremely tilted peaks that simply change sign as in the TPT driven by uniaxial and biaxial strains in Figs. 68 (a-b), 65 and 66.

Notably, only the cases involving pure and simple shear in Kagome lattices exhibit mirror symmetry across $\varepsilon = 0$ in the evolution of both full and local band gaps, with respect to positive strain ($\varepsilon > 0$) and negative strain ($\varepsilon < 0$) relative to $\varepsilon = 0$, as observed in Fig. 63 (c4-6).

Figure 74 – Contour plots of the Berry curvature, before and after the TPTs identified in panels d and e of Fig. 69. It is noteworthy that the TPT cause a change in the sign of the Berry curvature.

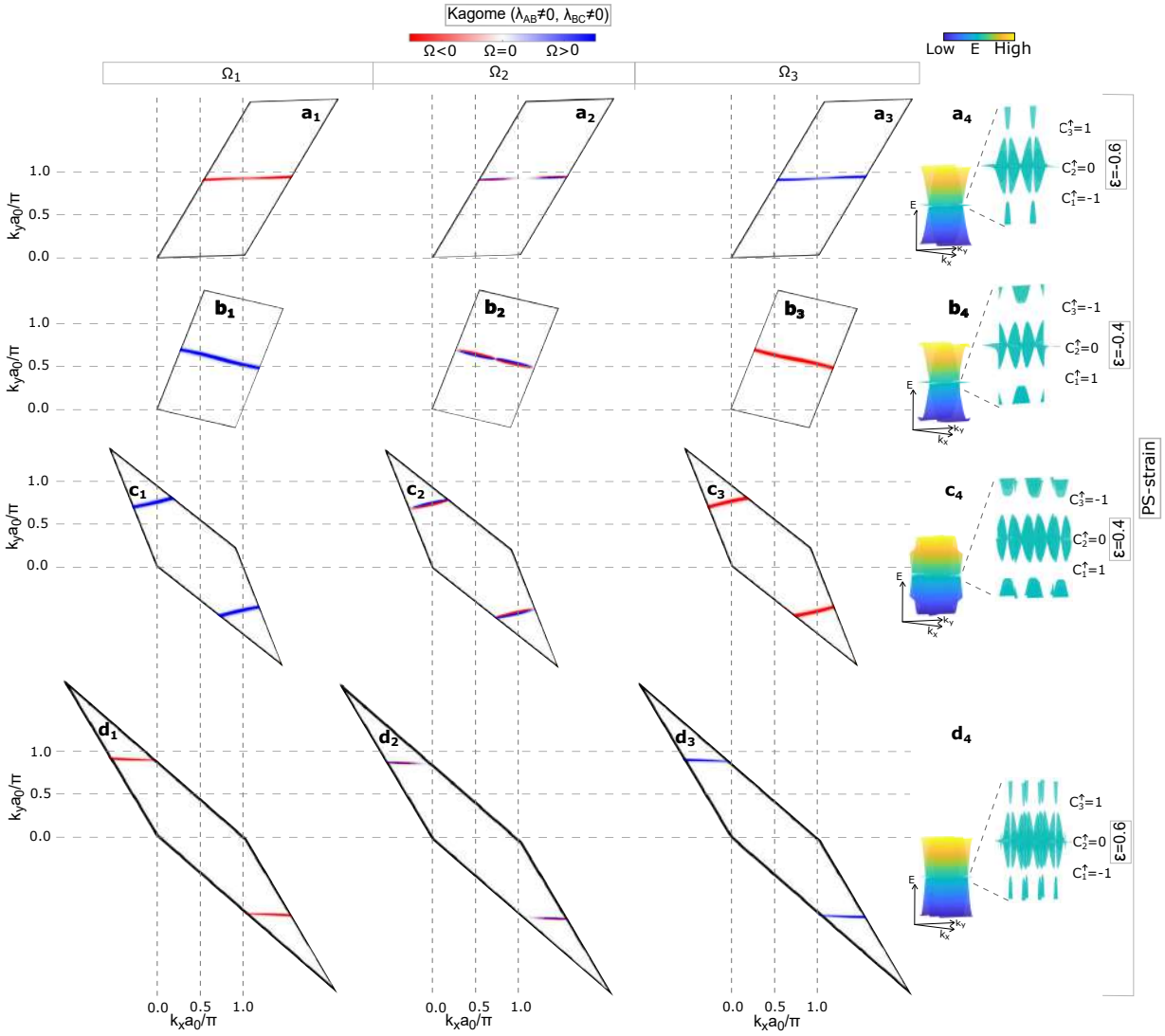

Source: The author.

The Lieb lattice demonstrates this symmetry when considering only NNN ISO coupling, $\lambda_{\langle\langle ij\rangle\rangle}$ [Fig. 75 (d-f)], represented by the red dashed lines in Fig. 47 (b). This symmetry is also observed in Kagome lattices, which include only NNN ISO coupling, $\lambda_{\langle\langle ij\rangle\rangle}$ [Fig. 75 (j-l)] or only NN ISO coupling $\lambda_{\langle ij\rangle}$ [Fig. 75 (p-r)], represented by red dashed and blue dash-dotted lines, respectively, in Fig. 47 (c)].

Indeed, the TPT we find for the Kagome lattice with $\lambda_{AB} \neq 0$ and $\lambda_{BC} \neq 0$ are obtained in the Kagome lattice model with only NN ISO coupling [compare the third row of panels in Fig. 63 with the panels in the third row of Fig. 75]. Meanwhile, the cases of Lieb and Kagome with only NNN-ISO coupling exhibit TPT identified in the cases with $\lambda_{AB} = \lambda_{BC} = 0$ discussed in the following subsection [compare the fourth and sixth row of panels in Fig. 63 with the panels in the first and second row of Fig. 75]. The non-TPT found in Figs. 63 and 75 are

Figure 75 – Comparison between the full band gap Δ_{12} [Δ_{23}] and the local band gaps Δ'_{12} [Δ'_{23}], versus ε as shown in Fig. 63, but now for the case of Lieb only with $\lambda_{\langle\langle ij\rangle\rangle}$ (first row of panels), and the cases of Kagome only with $\lambda_{\langle\langle ij\rangle\rangle}$ (second row of panels) and with only [$\lambda_{\langle ij\rangle}$] (third row of panels). The six columns of figure panels represent the six types of strain applied. It is noteworthy that in points where the full band gap is zero, the bands indeed touch because the local band gap is also zero, corroborating the indication of TPT.

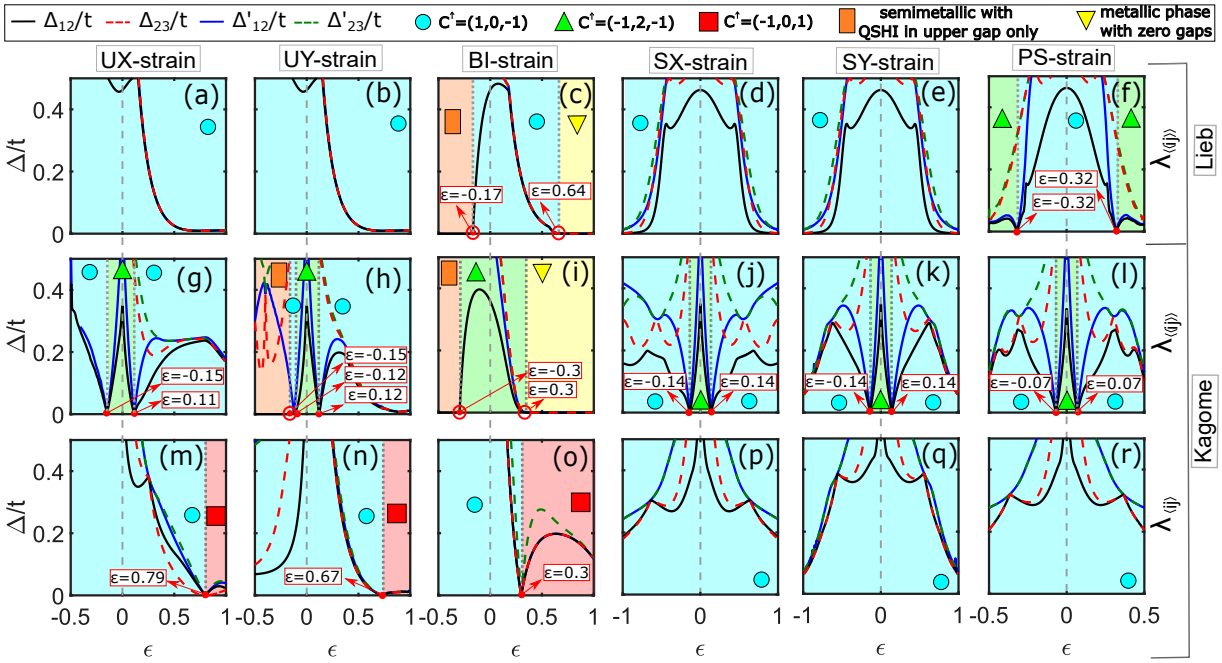

Source: The author.

discussed in subsection 3.6.4.

3.6.3 Strain-driven topological phase transitions with $\lambda_{AB} = \lambda_{BC} = 0$

When $\lambda_{AB} = \lambda_{BC} = 0$, Fig. 64 (n-t) demonstrates that TPT occur exclusively at 1/3 filling within the ε range covered in Fig. 63. This is observed in the case of PS-strained Lieb [Fig. 64 (n)] and Kagome lattices subjected to six types of strain [Fig. 64 (o-t)]. In these instances, we only identify TPT with $\Delta C^{\uparrow} = (1,0,-1) - (-1,2,-1) = (2,-2,0)$ or $\Delta C^{\uparrow} = (-1,2,-1) - (1,0,-1) = (-2,2,0)$, resulting in a change of sign in the Berry curvatures Ω_1 and Ω_2, while Ω_3 remains negative, as depicted in Fig. 76 (panels with subscript 3).

Indeed, the Lieb lattice with $\lambda_{AB} = \lambda_{BC} = 0$, when subjected to uniaxial strains along the UX-strain and UY-strain directions, shows a gradual reduction in the energy gap as ε increases from zero to 1. However, a complete closure of the gap does not occur within the examined parameter range [see Fig. 63 (d_1 and d_2)]. Conversely, in the case of biaxial strain (BI-strain), gap closure is observed at a critical strain value of $\varepsilon = 0.68$. Beyond this critical point, the system exhibits a closed gap for $\varepsilon > 0.68$, indicating a transition to a metallic phase

[refer to Fig. 63 (d_3)]. Notably, neither the SX-strain [Fig. 63 (d_4)] nor the SY-strain [Fig. 63 (d_5)] leads to gap closure at any value of ε.

In the PS-strained Lieb lattice, as shown in Fig. 64 (n), increasing ε from $\varepsilon = 0$ to $\varepsilon > 0$ leads to the first TPT at $\varepsilon = 0.25$ with $\Delta C^{\uparrow} = (1,0,-1) - (-1,2,-1) = (2,-2,0)$, and a second TPT at $\varepsilon = 0.29$ with $\Delta C^{\uparrow} = (-1,2,-1) - (1,0,-1) = (-2,2,0)$. Conversely, when reducing ε from $\varepsilon = 0$ to $\varepsilon < 0$, one TPT is observed at $\varepsilon = -0.32$ with $\Delta C^{\uparrow} = (1,0,-1) - (-1,2,-1) = (2,-2,0)$. Interestingly, when considering only NN ISO coupling in PS-strained Lieb lattice, TPTs are obtained at $\varepsilon = \pm 0.32$ [Fig. 75 (f)]. This indicates that the TPT at $\varepsilon = 0.25$ and $\varepsilon = 0.29$ are due to the effects of ISO coupling between more distant neighbors, mainly the NNN ISO coupling terms.

The evolution of the Berry curvatures presented in Fig. 76 (b) shows that applying PS-strain with $0 < \varepsilon < 0.2$ does not result in TPT, but causes the splitting of the positive (negative) peak of Ω_1 (Ω_3) into two peaks distributed along the diagonal (antidiagonal) direction, when compared to the Berry curvatures of the unstrained lattice [Fig. 51 (b)]. Furthermore, Ω_2 begins to exhibit two negative peaks in the diagonal direction and two positive peaks in the antidiagonal direction. The TPT at $\varepsilon = 0.25$ leads to a configuration of Berry curvatures [Fig. 76 (c)] analogous to that of the unstrained Kagome lattice [Fig. 51 (f)], with Ω_1^{PS} showing negative peaks localized at the $\mathbf{\Gamma}$ points and Ω_2^{PS} being entirely positive. Subsequently, the TPT at $\varepsilon = 0.29$ reverses the signs of the peaks of Ω_1^{PS} and Ω_2^{PS} back to positive and mixed (two positive and two negative), respectively, as observed for $\varepsilon = 0.4$ in Fig. 76 (d). However, now they are significantly tilted compared to the case at $\varepsilon = 0.2$ in Fig. 76 (b). On the other hand, the TPT at $\varepsilon = -0.32$ results in Berry curvatures as shown in Fig. 76 (a), which exhibit highly tilted peaks similar to those in Fig. 76 (d), but with a sign configuration observed in Fig. 76 (c), due to having the same Chern numbers per band.

Turning our attention to the transition lattice with a configuration angle of $\theta = 105^{\circ}$ and $\lambda_{AB} = \lambda_{BC} = 0$, we find that UX-strain does not result in gap closure [Fig. 63 (e_1)]. Similarly, UY-strain does not induce the closure of Δ_{12} within the considered ε range [Fig. 63 (e_2)]. When considering the biaxial BI-strain [Fig. 63 (e_3)], we observe a reduction in the gap for increasingly positive values of ε, though gap closure does not occur definitively. Both SX-strain [Fig. 63 (e_4)] and SY-strain [Fig. 63 (e_5)] do not lead to gap closure. Notably, under SY-strain at $\varepsilon = 0.3$, the gap Δ_{12} reaches a minimum of $\Delta_{12}/t = 0.01$, while maintaining consistent Chern numbers before and after this value. Similarly, the PS-strain [Fig. 63 (e_6)] case does not result in gap

Figure 76 – Contour plots of Berry curvature (as in Fig. 51), before and after the TPTs identified in Fig. 64 for some cases with $\lambda_{AB} = \lambda_{BC} = 0$ (see Figs. 73 and 77).

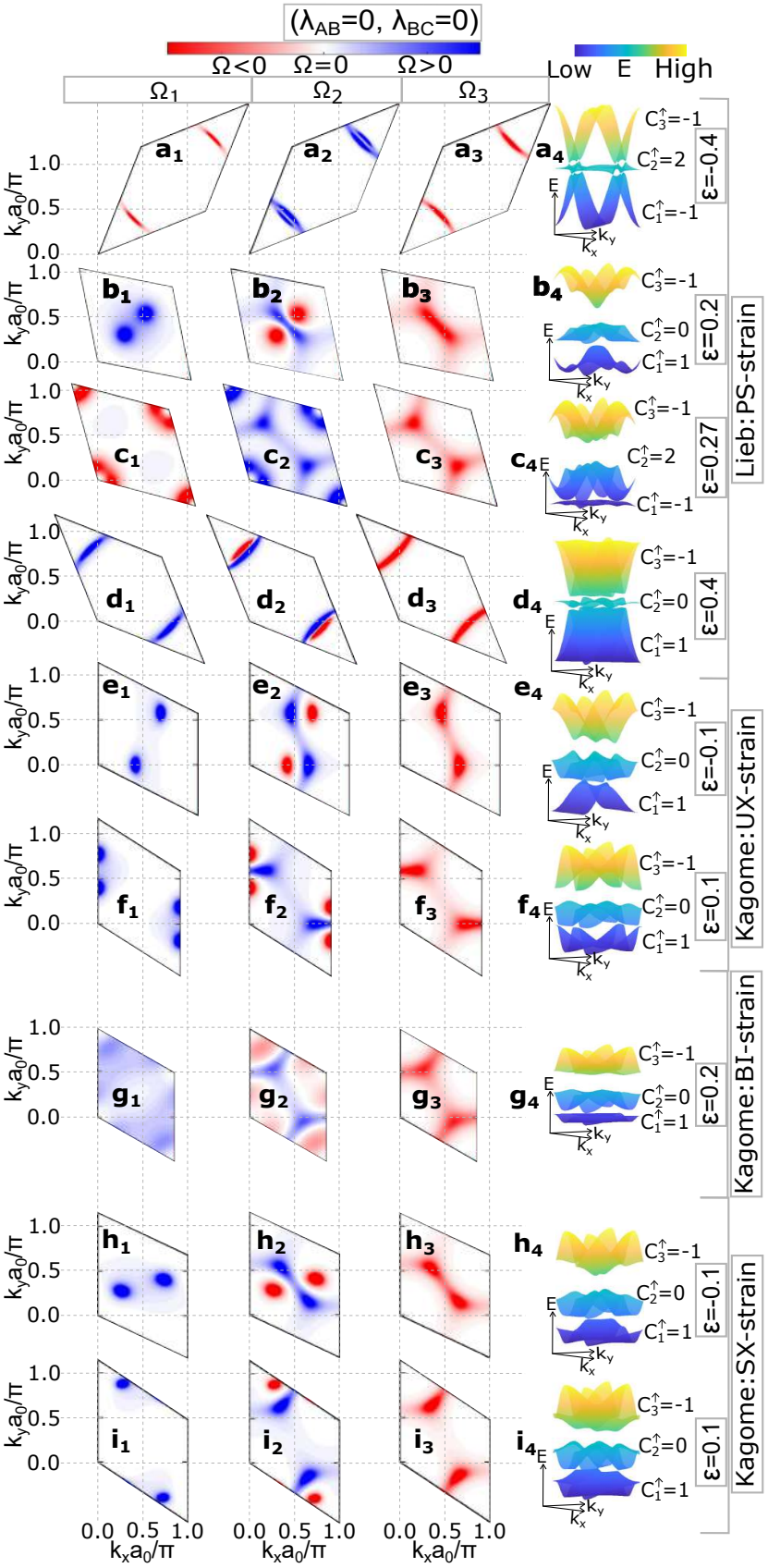

Source: The author.

closure within the examined range.

Indeed, in the case of transition lattices, TPT were only observed beyond the considered range of ε, as shown in Fig. 69 (a), presenting TPT at $\varepsilon_c = -0.6$ at 1/3 filling with $\Delta C^{\uparrow} = (1,0,-1) - (-1,2,-1) = (2,-2,0)$ and at $\varepsilon_c = -0.64$ at 2/3 filling with $\Delta C^{\uparrow} = (-1,2,-1) - (-1,0,1) = (0,2,-2)$, analogous to the TPT in the corresponding case with $\lambda_{AB} \neq 0$ and $\lambda_{BC} \neq 0$ already discussed in the previous subsection [Fig. 69 (b)]. The evolution of the Berry curvatures corresponding to these TPT shown in Fig. 77 is also analogous to those already discussed in Fig. 70, for the equivalent case mentioned.

The Kagome lattice exhibits a heightened susceptibility to TPT with $\Delta C^{\uparrow} = (-1,2,-1) - (1,0,-1) = (-2,2,0)$, when varying ε from its initial value of zero, with $\lambda_{AB} = \lambda_{BC} = 0$. For UX-strain, TPT occur at $\varepsilon_c^{UX} = \pm 0.04$ [see Fig. 64 (o)]. In the case of UY-strain, transitions are observed at $\varepsilon_c^{UY} = 0.03$ and $\varepsilon_c^{UY} = -0.05$ [see Fig. 64 (p)], while for BI-strain, a single TPT manifests at $\varepsilon_c^{BI} = 0.12$ [see Fig. 64 (q)]. SX and SY-strains induce TPT at $\varepsilon_c^{SX} = 0.06$ and $\varepsilon_c^{SY} = -0.04$ respectively [see Fig. 64 (r,s)], and PS-strain leads to transitions at $\varepsilon_c^{PS} = 0.03$ and $\varepsilon_c^{PS} = -0.02$ [see Fig. 64 (t)].

The TPT observed in uniaxially strained or simply and purely sheared Kagome lattices also occur when admitting only NNN ISO coupling, but at different ε_c values. Specifically, at $\varepsilon_c^{UX} = -0.15$ and $\varepsilon_c^{UX} = 0.11$ [Fig. 75 (g)], at $\varepsilon_c^{UY} = \pm 0.12$ [Fig. 75 (h)], at $\varepsilon_c^{SX} = \varepsilon_c^{SY} = \pm 0.14$ [Fig. 75 (j,k)], and at $\varepsilon_c^{PS} = \pm 0.7$ [Fig. 75 (l)]. Intriguingly, the TPT identified at 1/3 filling in the BI-strained Kagome lattice ceases to occur when all NN ISO coupling are nullified [Fig. 75 (i)]. We conclude that this is due to the NN ISO coupling parameter λ_{AC}, which remains nonzero in Fig. 64 (q).

The TPT driven by uniaxial and biaxial strain are confirmed by the Berry curvatures shown in Fig. 78. The UX-strain stretch causes the negative peaks of Ω_1 at the $\mathbf{\Gamma}$ points in the unstrained Kagome lattice [see Fig. 51 (f_1)], to transform into four positive half-peaks. These half-peaks are distributed as two per face in the admitted reciprocal space area, along the $\mathbf{b_2}$ direction [Fig. 76 (f_1)]. Similarly, Ω_2 begins to exhibit the same four half-peaks but as negatives, in addition to two positive peaks outside the faces [Fig. 76 (f_2)]. Conversely, the compressed UX-strain leads to two positive (negative) peaks outside the faces in Ω_1 (Ω_2), diverging from the four half-peak pattern. This behavior is reversed in the case of UY-strain, such that the Berry curvatures for stretched UX-strain correspond to those for compressed UY-strain, and vice versa. This can be observed by comparing $a_1 \longleftrightarrow g_1$, $a_2 \longleftrightarrow g_2$, $a_3 \longleftrightarrow g_3$ and $c_1 \longleftrightarrow e_1$, $c_2 \longleftrightarrow e_2$,

Figure 77 – Contour plots of the Berry curvature, before and after the TPTs identified in panel a of Fig. 69. It is noteworthy that the TPT cause a change in the sign of the Berry curvature.

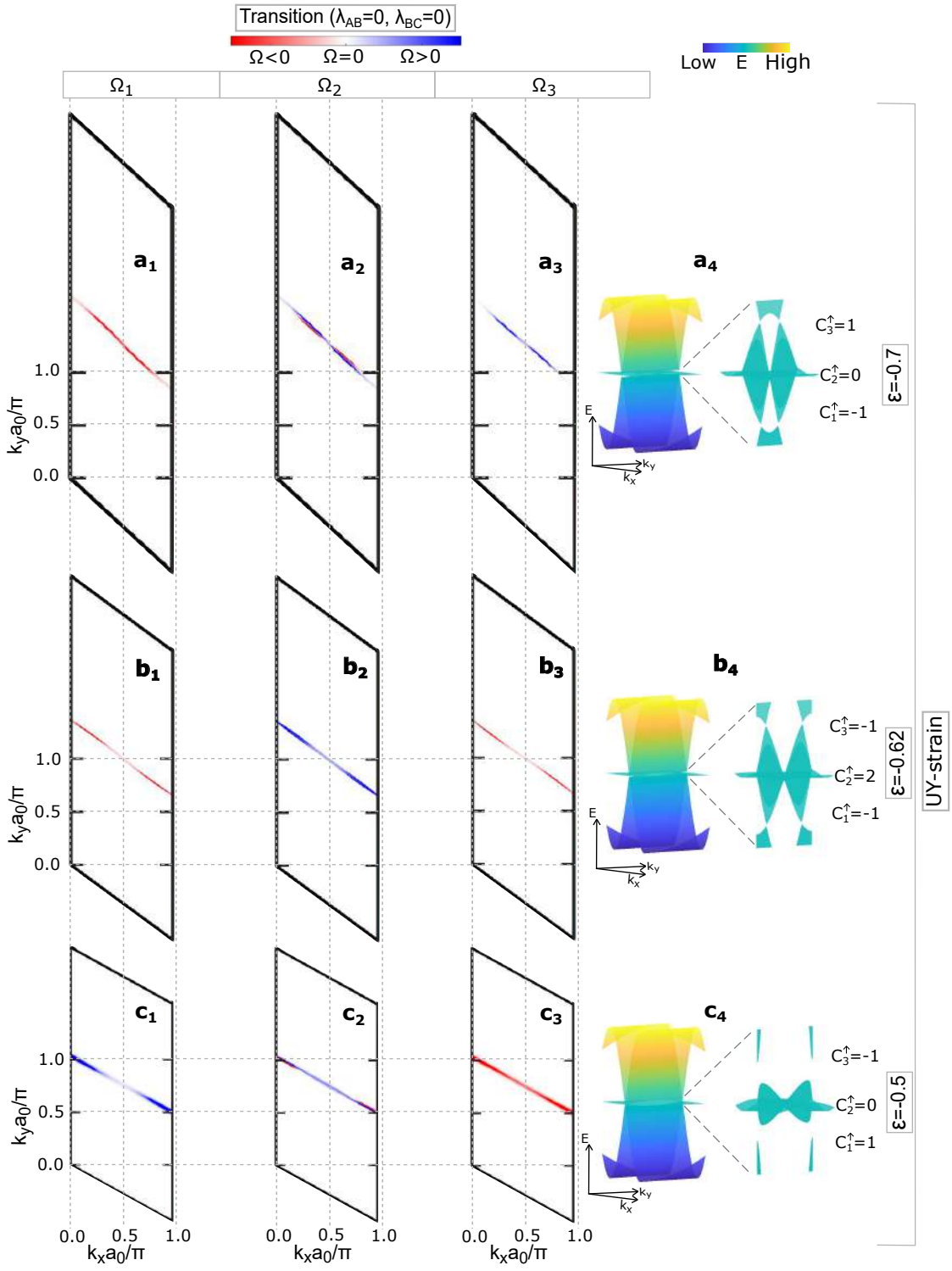

Source: The author.

$c_3 \longleftrightarrow e_3$ in Fig. 78.

Interestingly, the TPT in BI-strained Kagome lattice with $\lambda_{AB} = \lambda_{BC} = 0$ results in Berry curvatures similar to those of the unstrained Kagome lattice with $\lambda_{AB} \neq 0$ and $\lambda_{BC} \neq 0$. This can be observed by comparing the panels in Fig. 76 (g_1, g_2, and g_3) with those in Fig. 51 (e_1, e_2, and e_3), respectively.

In a SX-strained Kagome lattice, the TPT occurring at $\varepsilon < 0$ results in Berry curvatures [Fig. 76 (h)] analogous to those observed in the compressed UX-strained Kagome lattice [Fig. 76 (e)]. Conversely, the TPT at $\varepsilon > 0$ differs from those in the stretch UX-strained Kagome, as Ω_1^{SX} and Ω_2^{SX} display two complete peaks touching both the upper and lower faces in the considered reciprocal space region [Fig. 76 ($i_{1,2}$)], instead of four half-peaks on the right and left faces, as seen in Ω_1^{UX} and Ω_2^{UX} [Fig. 76 ($f_{1,2}$)]. The SY and PS-strained Kagome cases are analogous to the SX-strained Kagome, as shown in Fig. 79.

We emphasize that usually one needs strains of at least $\varepsilon = 0.2$ in order to close the band gap. Furthermore, the cases with $\lambda_{AB} \neq 0$ and $\lambda_{BC} \neq 0$ show more difficulty in closing the gap for the Lieb lattice when compared to the case $\lambda_{AB} = \lambda_{BC} = 0$. Also, smaller strains are sufficient to close (increase) the gap with extension (compression) than with compression (extension).

3.6.4 Strain-driven non-topological phase transitions

We did not exclusively identify TPT when applying strain to the Lieb-Kagome lattices; non-TPT were also observed. When both band gaps, Δ_{12} and Δ_{23}, as well as Δ'_{12} and Δ'_{23}, close at ε_c and do not reopen, the system transitions to a metallic state, thereby losing its QSHI characteristics [yellow regions in Figs. 63 and 75]. This occurs in the BI-strained Lieb lattice for $\varepsilon > 0.64$, regardless of the inclusion of λ_{AB} and λ_{BC} terms [Fig. 63 (a_3,d_3)], and remains the case when considering only NNN ISO coupling [Fig. 75 (c)]. Interestingly, this phase is also observed at $\varepsilon > 0.3$ in the BI-strained Kagome lattice when only NNN ISO coupling are admitted in the model [Fig. 75 (i)]. When the NN ISO coupling term λ_{AC} is introduced in this case, instead of a metallic phase, we have a TI phase due to the TPT at $\varepsilon_c^{BI} = 0.12$ discussed in the previous subsection [Fig. 64 (q)].

Conversely, when only the full band gap Δ_{12} closes while the corresponding local band gap Δ'_{12} remains nonzero, the spectrum starts exhibiting a negative indirect gap at 1/3 filling [orange regions in Figs. 63 and 75]. This phenomenon classifies the bulk as a semimetal,

Figure 78 – Contour plots of the Berry curvature (which complement those presented in Fig. 76), before and after the TPTs identified in panels o, p, and q of Fig. 64. It is noteworthy that the TPT cause a change in the sign of the Berry curvature.

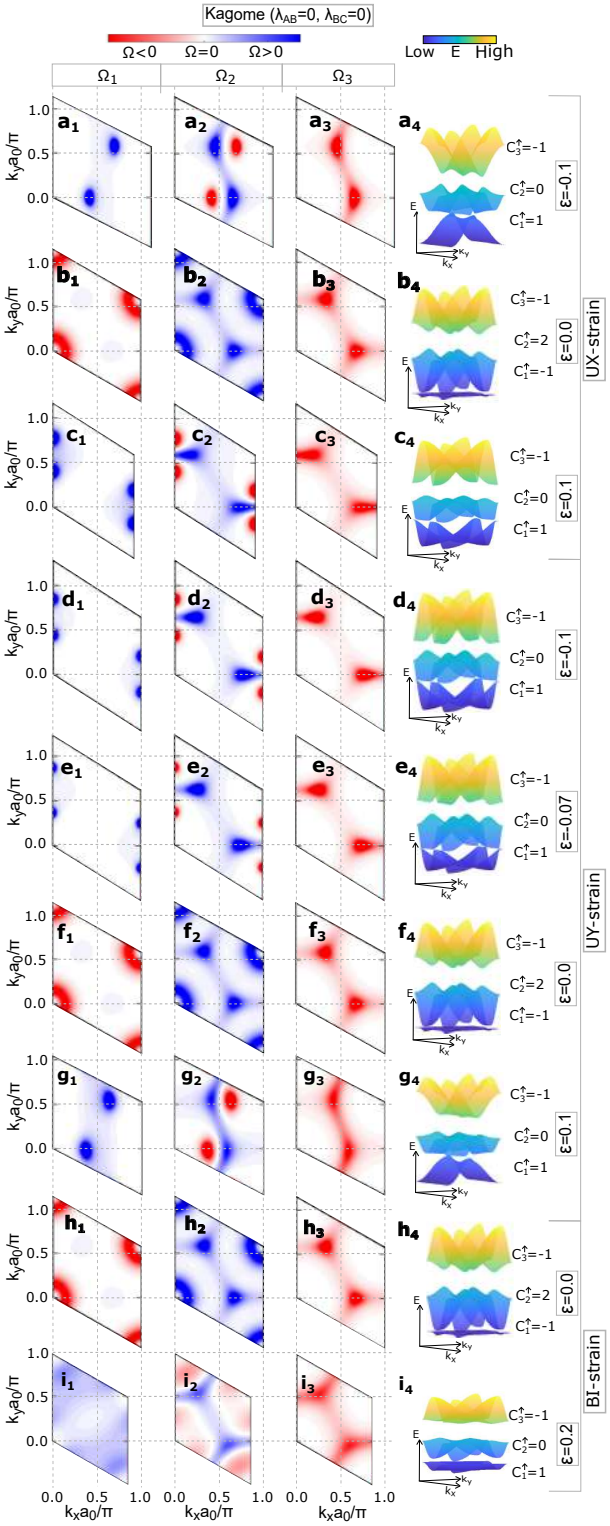

Source: The author.

Figure 79 – Contour plots of the Berry curvature (which complement those presented in Fig. 76), before and after the TPTs identified in panels r, s, and t of Fig. 64. It is noteworthy that the TPT cause a change in the sign of the Berry curvature.

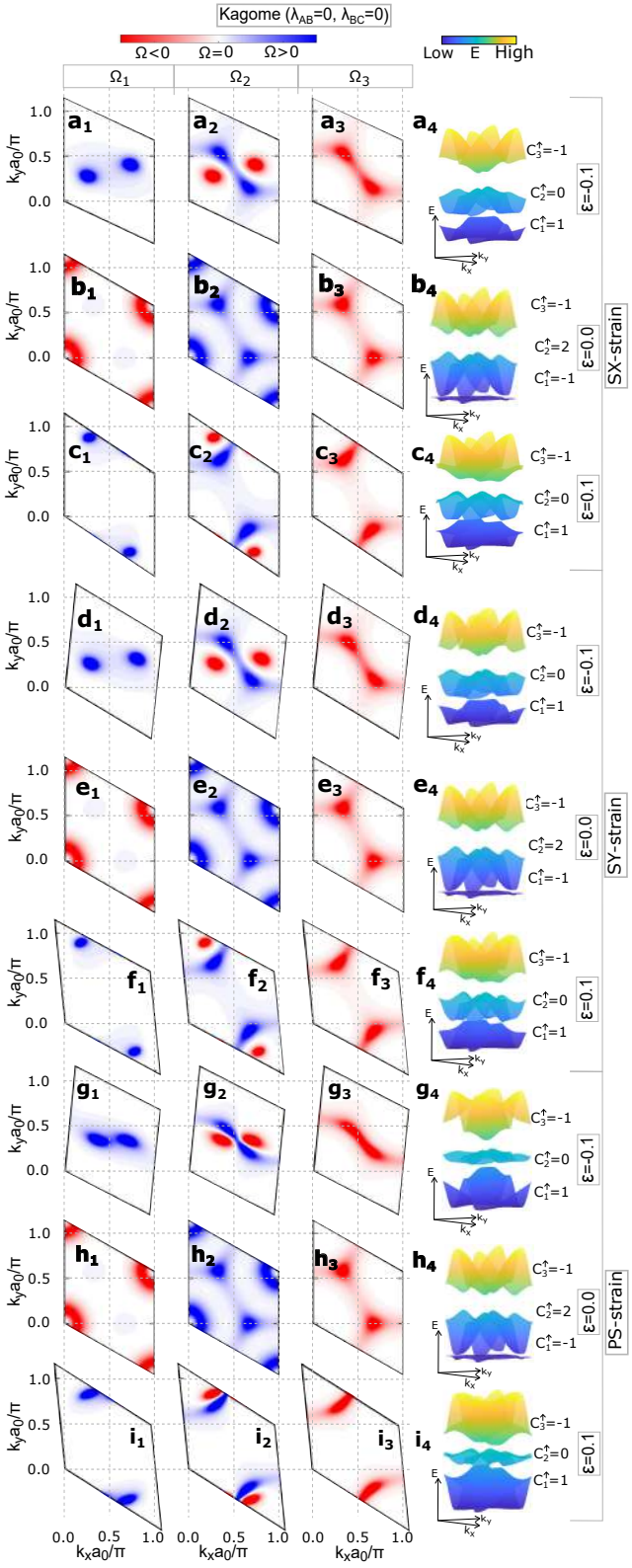

Source: The author.

wherein the QSHI state is only present in the upper gap. In this case, either the lower and middle bands are partially filled, precluding the formation of helical edge states at 1/3 filling.

When $\lambda_{AB} \neq 0$ and $\lambda_{BC} \neq 0$, a semimetallic phase with QSHI in the upper gap occurs for $\varepsilon < -0.17$ in BI-strained Lieb [Fig. 63 (a_3)], $\varepsilon < -0.16$ in BI-strained transition [Fig. 63 (b_3)], $\varepsilon < -0.27$ in BI-strained Kagome [Fig. 63 (c_3)] and for $\varepsilon < -0.21$ in UY-strained Kagome [Fig. 63 (c_2)]. Conversely, when $\lambda_{AB} = \lambda_{BC} = 0$, this phase occurs for $\varepsilon < -0.17$ in BI-strained Lieb [Fig. 63 (d_3)], for $\varepsilon < -0.16$ in BI-strained transition [Fig. 63 (e_3)], for $\varepsilon < -0.23$ in BI-strained Kagome [Fig. 63 (f_3)], and for $\varepsilon < -0.09$ in UY-strained Kagome [Fig. 63 (f_2)].

When comparing the phase diagrams obtained with $\lambda_{AB} = \lambda_{BC} = 0$ with those considering only NNN ISO coupling, we conclude that the aforementioned phase continues to occur in the same region $\varepsilon < -0.17$ in Lieb [Fig. 75 (c)], while it continues to occur in Kagome lattices under UY [Fig. 75 (h)] and BI [Fig. 75 (i)] strain, but in different regions, $\varepsilon^{UY} < -0.15$ and $\varepsilon^{BI} < -0.3$, respectively.

Interestingly, when admitting only NN ISO coupling in Kagome lattice, the semimetallic phase with QSHI in the upper gap ceases to exist [Fig. 75 (n,o)], compared to the corresponding case of $\lambda_{AB} \neq 0$ and $\lambda_{BC} \neq 0$ [Fig. 63 (c_2,c_3)]. This shows that the NNN ISO coupling terms are responsible for this non-topological phase transition in the Kagome lattice.

3.7 Hypothetical strain

In accordance with Sec. 2.9, certain strain effects in the energy spectra are due exclusively to the variation of the hopping parameters with the strain, when the ISO coupling is disregarded. Now, let us investigate the evolution of the energy gap as a function of θ and ε in cases where both the hopping parameters and the ISO coupling parameters remain constant as the strain is applied, so that the six types of deformations only change the positions of the lattice sites.

Curiously, we identified that the six types of strain show the same evolution of the full band gaps as presented in Fig. 80. We observe that the gaps do not close solely as a consequence of strain, presenting only the TPT occurring due to the interconvertibility process at $\theta = 118.3^\circ$ when $\lambda_{AB} = \lambda_{BC} = 0$, as discussed in Sec. 3.5.2. All other strain-induced topological or non- TPTs are energetic effects resulting solely from the changes in values of hopping and ISO coupling parameters that depend on the distances between sites in the strained lattice.

Figure 80 – Contour plot of energy gap Δ_{12} [Δ_{23}] between the bands 1[2] and 2[3] as a function of ε and θ for (a) $\lambda_{AB} \neq 0$ and $\lambda_{BC} \neq 0$ and (b) $\lambda_{AB} = \lambda_{BC} = 0$, considering the ISO coupling and hopping parameters independent of the strain.

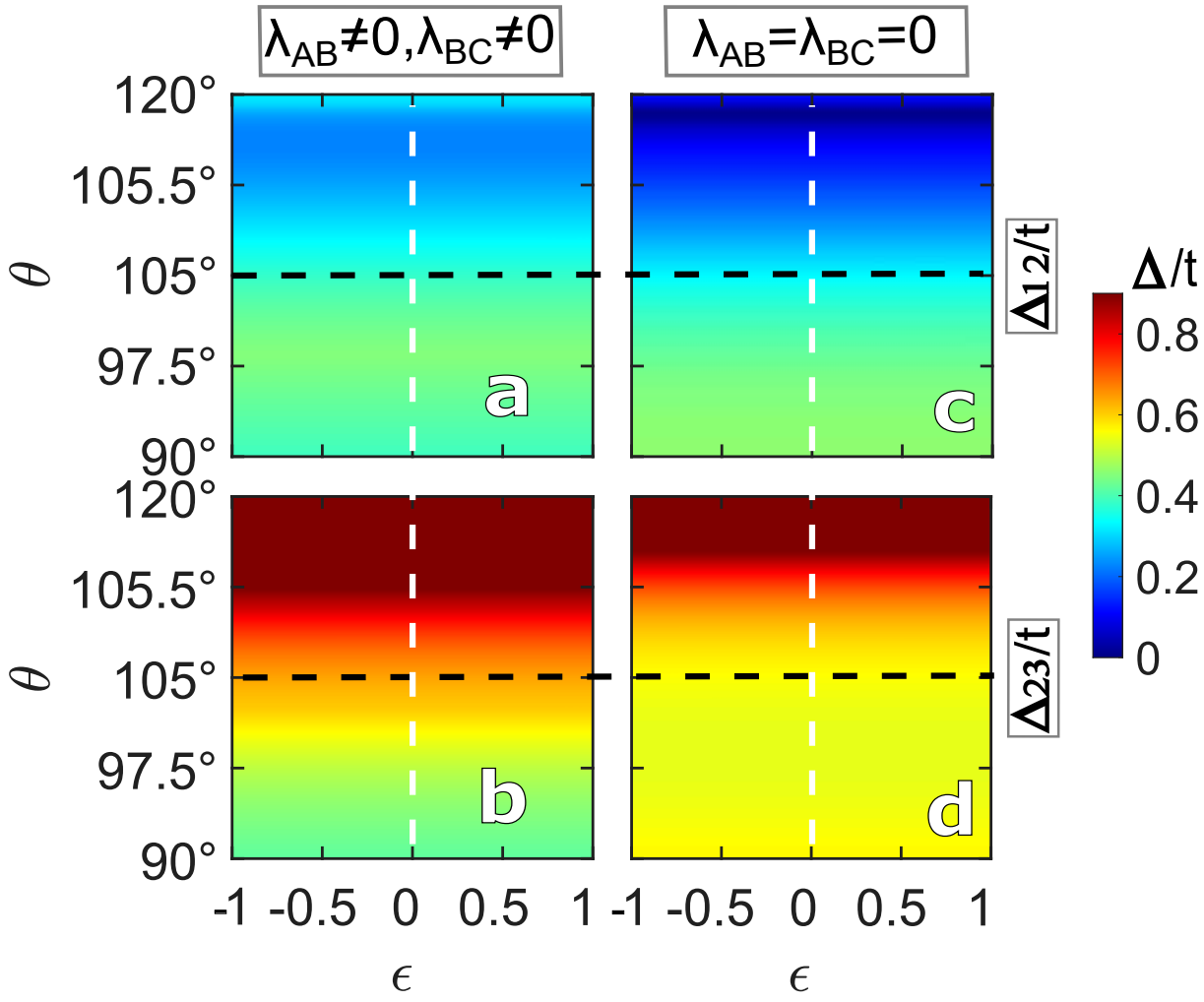

Source: The author.

3.8 Conclusions

In summary, we systematically studied the TPT driven by strain on the Lieb-Kagome lattices with ISO coupling, based on a recently proposed TB Hamiltonian reported by Lima *et al.* (2023) that takes into account uniaxial strains and shear applied in different crystallographic directions of the Lieb-Kagome lattice defined in terms of the interconvertibility discovered by Jiang *et al.* (2019c) between the Lieb and Kagome lattices by defining a transition lattice that maps such structures by one control parameter. For this purpose, using the concept of a strained generic lattice (JIANG *et al.*, 2019a; JIANG *et al.*, 2019c; LIM *et al.*, 2020; CUI *et al.*, 2020; LIMA *et al.*, 2023), we derived a more general Hamiltonian including the ISO coupling.

Initially, we focused on understanding the emergence of two band gaps in the energy spectrum of unstrained Lieb-Kagome lattices, particularly related to the introduction of ISO

coupling. We demonstrated that NN ISO coupling alone does not induce band gaps in the Lieb lattice. Instead, it is the incorporation of NNN ISO coupling that disrupts the D_{4h} symmetry, leading to the formation of a nearly-flat band with Chern number equal to zero (JIANG *et al.*, 2019c; HWANG *et al.*, 2021). In both transition and Kagome lattices, band gaps are produced by NN ISO coupling terms, NNN ISO coupling terms, or a combination of both. Specifically, in the Kagome lattice, the emergence of a Chern nearly-flat band with Chern number equal to ± 1 is observed. The process of these band gaps closing and then reopening is indicative of TPT, confirmed by changes in the Spin Chern number and the Berry curvature, each calculated for the three energy bands.

The first TPT we identified occurred in the unstrained Lieb-Kagome lattice, specifically during the interconvertibility process at the point $\varepsilon = 118.3°$. This transition point is marked by the NN ISO coupling terms λ_{AB} and λ_{BC} becoming null. Uniquely, this TPT represents a singular phase transition driven by hypothetical strains, where the hopping and ISO coupling parameters remain strain-invariant. This finding underscores that the phase transitions induced by strain are not solely due to geometric alterations in the lattice. Instead, they are primarily driven by changes in the Hamiltonian parameters, t_{ij} and λ_{ij}, as governed by Eqs. (3.4) and (3.6), respectively.

Overall, phase transitions were identified when varying the λ or n parameters, as well as upon applying the six types of strain to the Lieb-Kagome lattices. TPT connecting two TI phases occur when both full band gaps, along with their corresponding local band gaps, close and then reopen at the same ε_c. If the lower full band gap closes and does not reopen, while the corresponding local band gap remains non-zero, a negative indirect gap is observed. In this scenario, the system undergoes a non-topological phase transition into a semimetallic regime at 1/3 filling, characterized by partially filled bands and non-quantized spin Hall conductivity. At 2/3 filling, the system behaves as an insulator, with the spin Hall conductivity carried by the helical edge states becoming experimentally observable (BEUGELING *et al.*, 2012). Conversely, if both full band gaps close and do not reopen, the system transitions to a metallic state, inhibiting any spin Hall conductivity.

The difference in the Chern numbers of the phases on either side of the TPT identified in this chapter were $\Delta C^{\uparrow} = \pm(2,-2,0)$ or $\Delta C^{\uparrow} = \pm(2,0,-2)$. We observe that the change in the Chern numbers of the two touching bands is ± 2. Consequently, in all configurations with open gaps, the system behaves as a QSH insulator with spin Hall conductivity equal to $\sigma_{SH} = \pm 1$,

implying a Berry phase of 4π associated with this touching point, in accordance with Beugeling *et al.* (2012).

The Berry curvature for each band changes sign when the corresponding Chern number transitions from positive to negative, or vice versa. Remarkably, the total number of Berry curvature peaks per band is strain invariant within the BZ, despite changes in their shape and distribution. In general, the Berry curvatures corresponding to the lower and/or upper bands exhibit two positive peaks when $C^{\uparrow}_{\text{lower}} = +1$ and/or $C^{\uparrow}_{\text{upper}} = +1$, while they show two negative peaks when $C^{\uparrow}_{\text{lower}} = -1$ or $C^{\uparrow}_{\text{upper}} = -1$. The Berry curvature associated with the middle band displays two positive and two negative peaks when $C^{\uparrow}_{\text{middle}} = 0$, which transform into four positive peaks when $C^{\uparrow}_{\text{middle}} = +2$.

We believe that such a systematic study pertinent to the effects of different types of strains applied in 2D lattices, as demonstrated in the phase transitions in Lieb-Kagome lattices with ISO coupling, is crucial for advancing the field of 2D TI. This research underscores the ability of strain engineering to fine-tune electrical and optical properties, offering new avenues for controlling band gap tunability and band deformations. Such advancements are pivotal for the future of 2D lattice-based device technologies, marking a significant contribution to both the fundamental understanding and practical applications of these materials in nanoscale electronics and photonics.

4 STRAIN-INDUCED TOPOLOGICAL PHASE TRANSITION IN LIEB-KAGOME NANORIBBONS

The combination of ISO coupling and strain can drive TPT in Lieb, Kagome, and transition lattices, as confirmed by the evolution of Berry curvature and Chern numbers in Ch.3. Here, we theoretically study the finite-size effects on the topological properties of these structures, using a TB Hamiltonian that describes nanoribbons of Lieb ($\theta = \pi/2$), Kagome ($\theta = 2\pi/3$), and transition ($\pi/2 < \theta < 2\pi/3$) lattices with ISO coupling and under shear and uniaxial strains applied along different crystallographic directions. The energy spectrum and DOS for nanoribbons with three types of edges (straight, bearded, and asymmetric) are discussed. Our results confirm TPT driven by strain engineering in these structures, based on the bulk-edge correspondence. Furthermore, the evolution of edge states indicates that such deformations can generate opposite spin currents under strain.

4.1 Motivation

As presented in previous chapters, 2D TI, such as the Lieb (LIEB, 1989; WEEKS; FRANZ, 2010; GOLDMAN *et al.*, 2011b) and Kagome lattices (MIELKE, 1992; GUO; FRANZ, 2009) with $\mathbb{Z}_2$ topological classification (KANE; MELE, 2005a; KANE; MELE, 2005b; QI *et al.*, 2008; FU; KANE, 2007), have attracted the attention of the scientific community due to their interesting physical properties with potential applications in tunable spintronics and optoelectronic devices. In the infinite layer energy spectrum, these lattices already present conical Dirac energy bands coexisting with flat (non-dispersive) bands. This suggests the combination of the exciting physics of the linear dispersive bands of graphene, such as massless relativistic particles and a semimetallic state with extremely high electron mobility, with the promising physics of flat bands, encompassing phenomena such as the ferromagnetic superconductivity (LIN *et al.*, 2018), spin liquid (BLOCK *et al.*, 2020), and topological states (DEPENBROCK *et al.*, 2012; HAN *et al.*, 2012; JIANG *et al.*, 2019d; YIN *et al.*, 2019; LEYKAM *et al.*, 2018).

Other exciting phenomena, which we will explore in this chapter, occur at the edges of the nanoribbons formed by this class of TI. Due to their $\mathbb{Z}_2$ classification (KANE, 2008; HASAN; KANE, 2010; MOORE, 2010), Lieb (GOLDMAN *et al.*, 2011a; CHEN; ZHOU, 2016; ZHANG *et al.*, 2016; JIANG *et al.*, 2019c; BINH *et al.*, 2019) and Kagome (DEY *et al.*, 2011; ZHANG; TONG, 2019; JIANG *et al.*, 2019c) nanoribbons display gapless edge states when the ISO coupling is considered. The spin-up and spin-down states propagate in

opposite directions along the edge of the system, generating spin-filtered edge states in the gap region of the bulk energy spectrum (KANE; MELE, 2005a; KANE; MELE, 2005b). According to the bulk-edge correspondence, this interesting behavior only occurs in cases of non-trivial topology, characterized by a non-null spin Chern number C^s (KANE; MELE, 2005a; KANE; MELE, 2005b; FU; KANE, 2007; QI *et al.*, 2008), where $C^s = (C^{\uparrow} - C^{\downarrow})/2$ and C^{σ}, $\sigma = \{\uparrow,\downarrow\}$, represents the Chern number associated with the individual spins (FUKUI *et al.*, 2005; SHENG *et al.*, 2006; FUKUI; HATSUGAI, 2007).

In addition to studying the bulk and boundary properties of these TI, mechanisms capable of changing the topological invariant, resulting in TPT, have been investigated. This is because obtaining new topological configurations can result in the maintenance, loss, or enhancement of the optoelectronic and transport properties of the sample. In Ch. 3, we show that TPT can be driven by uniaxial and shear strains in Lieb, Kagome, and transition lattices. This was confirmed by the evolution of Berry curvature and Chern numbers, but the bulk-edge correspondence of these phase transitions in nanoribbons constructed from these structures was not investigated. In fact, Zhao *et al.* (2022) investigated the evolution of edge states in Kagome nanoribbons under uniaxial strain and ISO coupling. However, the authors did not apply other types of possible strains, such as shear and biaxial strains. Also, we did not identify analogous studies for the strained Lieb nanoribbon with ISO coupling. Thus, as a generalization of previous studies, in this work, we investigate the strain effects on the electronic properties of Lieb and Kagome nanoribbons with ISO coupling.

To achieve our objectives, we developed a general TB Hamiltonian that describes both Lieb and Kagome nanoribbons, with ISO coupling, under uniaxial and shear strains along different crystallographic directions. This Hamiltonian is based on the interconvertibility of Lieb and Kagome lattices, initially proposed by Jiang *et al.* (2019c). The authors presented a Hamiltonian that describes the Lieb ($\theta = \pi/2$), Kagome ($\theta = 2\pi/3$), and transition lattices $\pi/2 < \theta < 2\pi/3$ (JIANG *et al.*, 2019a; CUI *et al.*, 2020; LIM *et al.*, 2020). Subsequently, we included the strain tensor in this Hamiltonian for the cases without (LIMA *et al.*, 2023) and with ISO coupling in Chs. 2 and 3, respectively. Furthermore, a Hamiltonian for Lieb, Kagome, and transition nanoribbons was proposed by Uchoa (2023), but without considering strain and ISO coupling, which are already included in our theoretical model.

The chapter is organized as follows. In Sec. 4.2, we derive the TB model that describes the generic nanoribbon, enabling the study of strain in Lieb and Kagome nanoribbons

Figure 81 – Sketches of generic nanoribbons with (b) straight, (c) bearded, and (d) asymmetric edges, emphasizing their unit cells (red dashed lines), edge terminations, and the row count in each case are shown. The non-equivalent sites are: A (blue empty circle), B (yellow filled circle), and C (green circle with a dot inside), as in Figs. 15 (a-c) and 46 (a). N is the total number of lines defining the ribbon size $W = (N-1)|\mathbf{a}_2|/2$, which is always odd for straight or bearded edges and even for asymmetric edges.

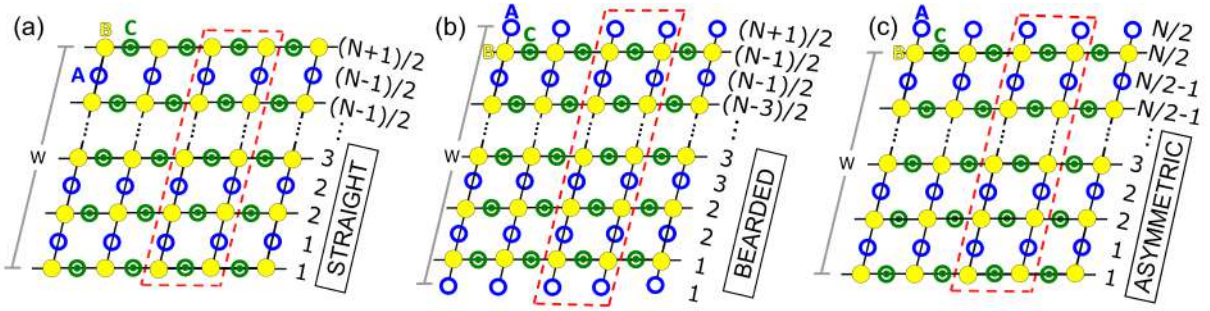

Source: The author.

with ISO coupling. In Sec. 4.3, we examine the choice of the n parameter that governs the adopted hopping parameterization. In Sec. 4.4, we discuss the effects of ISO coupling on the energy spectrum and DOS for nanoribbons with three types of edges (straight, bearded, and asymmetric). In Sec. 4.5, we present the effects of TPT driven by λ and θ on the edge states of Lieb-Kagome nanoribbons, while in Sec. 4.6, we discuss the strain effects on these nanoribbons, showing the edge states before and after the occurrence of TPT in both sections. Finally, in Sec. 4.7, we summarize our main findings.

4.2 Theoretical model

4.2.1 Crystalographic lattice structure for generic Lieb-Kagome nanoribbons

We will consider Lieb ($\theta = 90^\circ$), transition ($\theta = 105^\circ$), and Kagome ($\theta = 120^\circ$) nanoribbons with three types of edges: (i) straight [Fig. 81 (a)], (ii) bearded [Fig. 81 (b)], and (iii) asymmetric [Fig. 81 (c)]. In this figure, we show how the lines are numbered along the finite size y direction, the structural termination edges, and the unit cell (red dashed lines) for the three different nanoribbons investigated. The straight edge [Fig. 81 (a)] is characterized by its first and last lines being formed by B and C sites. For the case of the bearded edge [Fig. 81 (b)], we have that its first and last lines are formed by sites of type A. Finally, for the case of the asymmetric edge [Fig. 81 (c)], we have the composition of the two previous edges, *i.e.*, one side of the nanoribbon has a straight edge, and the other side has a bearded edge. In this way, the first line of atoms of the nanoribbon is formed by sublattices of the type B and C, and its last line is

formed by sublattices of the type A.

Analyzing how the lines are numbered in Fig. 81, we notice that for the case of the bearded edge [Fig. 81 (b)], we have $N_A = (N+1)/2$ and $N_B = N_C = (N-1)/2$, where N is the total number of lines defining the ribbon width $W = (N-1)a_0$, and N_A, N_B, and N_C correspond to the number of lines of sites A, B, and C, respectively. As for the case of the straight edge [Fig. 81 (a)], we have $N_A = (N-1)/2$ and $N_B = N_C = (N+1)/2$. Finally, for the case of the asymmetric edge [Fig. 81 (c)], where the first line is composed only of sites of type B and C, and the last line is composed of sites of type A, we have $N_A = N_B = N_C = N/2$. N is always odd in the case of straight or bearded edges. For asymmetric edges, on the other hand, N is necessarily an even number (UCHOA, 2023).

4.2.2 Tight-binding model for Lieb-Kagome nanoribbons without ISO coupling

Due to the periodicity of the ribbon structures along the x direction, which are characterized by the number of lines as shown in Fig. 81, it is convenient to write the operators do general TB Hamiltonian [Eq. (3.2a)], that can describe the charge carrier's dynamics, in the Fourier basis as

$$\hat{s}_i = \frac{1}{\sqrt{N_{cells}}} \sum_{k_x} \sum_{n} e^{ik_x x_i} \hat{s}_{k_x,n}, \tag{4.1a}$$

$$\hat{s}_i^{\dagger} = \frac{1}{\sqrt{N_{cells}}} \sum_{k_x} \sum_{n} e^{-ik_x x_i} \hat{s}_{k_x,n}^{\dagger}, \tag{4.1b}$$

where N_{cells} is the number of unit cells and $s_{k_x,n}(s_{k_x,n}^{\dagger})$ destroys (creates) an electron with momentum $\hbar k_x$ at the site of type $\hat{s} = \{\hat{a}, \hat{b}, \hat{c}\}$ at line n.

Replacing the operators of Eq. (4.1) in Eq. (3.2a), multiplying the resulting expression by the factor $e^{-ik'_x x_i} e^{ik'_x x_i} = 1$, and using the appropriate Kronecker delta function representation, we obtain the following Hamiltonian for generic nanoribbons:

$$\hat{H}_0 = \sum_{k_x} \sum_{n,n'} \tau_{0\,n,n'}^{AB} a_{k_x,n}^{\dagger} b_{k_x,n'} + \sum_{k'_x} \sum_{n',n''} \tau_{0\,n',n''}^{BC} b_{k'_x,n'}^{\dagger} c_{k'_x,n''} + \sum_{k_x} \sum_{n,n''} \tau_{0\,n,n''}^{AC} a_{k_x,n}^{\dagger} c_{k_x,n''} + h.c., \tag{4.2}$$

where $\tau_{0\,n,n'}^{ij}$, with $i,j = (A,B,C)$, are matrix elements defined for each type of nanoribbon termination adopted. Writing $\boldsymbol{k} = (k_x, 0)$, one can find for the three types of edges,

$$\tau_{0\,n',n''}^{BC} = \delta_{n',n''} t_{BC} \left(e^{i\boldsymbol{R}_{BC}\cdot\boldsymbol{k}} + e^{-i\boldsymbol{R}_{BC}\cdot\boldsymbol{k}} \right) + \delta_{n',n''-1} t'_{BC} e^{-i\boldsymbol{R}'_{BC}\cdot\boldsymbol{k}} + \delta_{n',n''+1} t'_{BC} e^{i\boldsymbol{R}'_{BC}\cdot\boldsymbol{k}}. \tag{4.3}$$

For straight [Fig. 81 (a)] and asymmetric [Fig. 81 (c)] nanoribbons, we obtain

$$\tau_{0\,n,n'}^{AB} = \delta_{n,n'}\left(t_{AB}e^{-i\boldsymbol{R}_{BA}\cdot\boldsymbol{k}} + t'_{AB}e^{-i\boldsymbol{R}'_{BA}\cdot\boldsymbol{k}}\right) + \delta_{n,n'-1}\left(t_{AB}e^{i\boldsymbol{R}_{BA}\cdot\boldsymbol{k}} + t'_{AB}e^{i\boldsymbol{R}'_{BA}\cdot\boldsymbol{k}}\right), \tag{4.4a}$$

$$\tau_{0\,n,n''}^{AC} = \delta_{n,n''}\left(t_{AC}e^{i\boldsymbol{R}_{AC}\cdot\boldsymbol{k}} + t'_{AC}e^{-i\boldsymbol{R}'_{AC}\cdot\boldsymbol{k}}\right) + \delta_{n,n''-1}\left(t_{AC}e^{-i\boldsymbol{R}_{AC}\cdot\boldsymbol{k}} + t'_{AC}e^{i\boldsymbol{R}'_{AC}\cdot\boldsymbol{k}}\right), \tag{4.4b}$$

and for bearded [Fig. 81 (b)] nanoribbons, we obtain

$$\tau_{0\,n,n'}^{AB} = \delta_{n,n'}\left(t_{AB}e^{i\boldsymbol{R}_{BA}\cdot\boldsymbol{k}} + t'_{AB}e^{i\boldsymbol{R}'_{BA}\cdot\boldsymbol{k}}\right) + \delta_{n,n'+1}\left(t_{AB}e^{-i\boldsymbol{R}_{BA}\cdot\boldsymbol{k}} + t'_{AB}e^{-i\boldsymbol{R}'_{BA}\cdot\boldsymbol{k}}\right), \tag{4.5a}$$

$$\tau_{0\,n,n''}^{AC} = \delta_{n,n''}\left(t_{AC}e^{-i\boldsymbol{R}_{AC}\cdot\boldsymbol{k}} + t'_{AC}e^{i\boldsymbol{R}'_{AC}\cdot\boldsymbol{k}}\right) + \delta_{n,n''+1}\left(t_{AC}e^{i\boldsymbol{R}_{AC}\cdot\boldsymbol{k}} + t'_{AC}e^{-i\boldsymbol{R}'_{AC}\cdot\boldsymbol{k}}\right). \tag{4.5b}$$

As in Ch. 3, t_{ij} are the hopping parameters that obey Eq. (3.4).

To find the Lieb-Kagome nanoribbon band structure, we apply the standard Heisenberg equation of motion, $i\hbar d\hat{\mathcal{O}}/dt = [\hat{\mathcal{O}}, \hat{H}_0]$, to the operators $\hat{\mathcal{O}} \equiv \{\hat{s}^{\dagger}_{k_x,n}$ and $\hat{s}_{k_x,n}\}$ in line n. Assuming that the time dependence of the modes behaves like $e^{-\frac{iEt}{\hbar}}$, one obtains $E\hat{s}_{k_x,n} = [\hat{s}_{k_x,n}, \hat{H}_0]$ for the three operators $\hat{s} \equiv \{\hat{a}, \hat{b}, \hat{c}\}$, and thus

$$[\hat{a}_{k_x,n}, \hat{H}_0] = \sum_{n'=1}^{N_B} \tau_{0\,n,n'}^{AB}\hat{b}_{k_x,n'} + \sum_{n'=1}^{N_C} \tau_{0\,n,n'}^{AC}\hat{c}_{k_x,n'}, \tag{4.6a}$$

$$[\hat{b}_{k_x,n}, \hat{H}_0] = \sum_{n'=1}^{N_A} \tau_{0\,n,n'}^{BA}\hat{a}_{k_x,n'} + \sum_{n'=1}^{N_C} \tau_{0\,n,n'}^{BC}\hat{c}_{k_x,n'}, \tag{4.6b}$$

$$[\hat{c}_{k_x,n}, \hat{H}_0] = \sum_{n'=1}^{N_B} \tau_{0\,n,n'}^{BC}\hat{b}_{k_x,n'} + \sum_{n'=1}^{N_A} \tau_{0\,n,n'}^{AC}\hat{a}_{k_x,n'}. \tag{4.6c}$$

Combining this set of coupled equations [Eqs. (4.6a), (4.6b), and (4.6c)], one arrives at the following matrix equation

$$\mathscr{T}_0 \begin{pmatrix} \hat{a}_{k_x,n} \\ \hat{b}_{k_x,n} \\ \hat{c}_{k_x,n} \end{pmatrix} = E \begin{pmatrix} \hat{a}_{k_x,n} \\ \hat{b}_{k_x,n} \\ \hat{c}_{k_x,n} \end{pmatrix}, \tag{4.7}$$

where $\mathscr{T}_0$ is the hopping matrix without ISO coupling of order $N_A + N_B + N_C$ that depends on the ribbon configuration, given by

$$\mathscr{T}_0 = \begin{pmatrix} [\tau_0{}^{AA}]_{N_A\times N_A} & [\tau_0{}^{AB}]_{N_A\times N_B} & [\tau_0{}^{AC}]_{N_A\times N_C} \\ [\tau_0{}^{BA}]_{N_B\times N_A} & [\tau_0{}^{BB}]_{N_B\times N_B} & [\tau_0{}^{BC}]_{N_B\times N_C} \\ [\tau_0{}^{CA}]_{N_C\times N_A} & [\tau_0{}^{CB}]_{N_C\times N_B} & [\tau_0{}^{CC}]_{N_C\times N_C} \end{pmatrix}, \tag{4.8}$$

with $\tau_0{}^{AA}$, $\tau_0{}^{BB}$, and $\tau_0{}^{CC}$ standing for the on-site energies of sites A, B, and C, respectively, that are assumed here to be zero. To illustrate an example of a non-null on-site energy case,

one has that Lieb-Kagome nanoribbons subjected to perpendicular or in-plane electric fields are simulated by changing the on-site energies in the corresponding appropriate way. As discussed by Uchoa (2023), according to the number of lines for each Lieb-Kagome nanoribbon, the order of the matrix $\mathscr{T}_0$ is $(3N-1)/2$, $(3N+1)/2$, and $3N/2$ for nanoribbons with bearded, straight, and asymmetric edges, respectively. Therefore, straight-edged nanoribbons have an additional mode compared to bearded-edged nanoribbons of the same size (UCHOA, 2023).

From Eq. (4.9), we obtain

$$[\mathscr{T}_0 - E\mathbb{I}] \begin{pmatrix} \hat{a}_{k_x,n} \\ \hat{b}_{k_x,n} \\ \hat{c}_{k_x,n} \end{pmatrix} = 0, \tag{4.9}$$

such that the condition $\det[\mathscr{T}_0 - E\mathbb{I}] = 0$ provides the energy spectrum of the nanoribbons.

Practically, to obtain the energy levels without ISO coupling, the hopping matrix $\mathscr{T}_0$ is diagonalized by choosing the ribbon features, such as the angle θ, which determines the lattice type, the type of edge, and the total number of lines N associated with the width of the nanoribbon.

4.2.3 Tight-binding model for Lieb-Kagome nanoribbons with ISO coupling

Following an analogous path to the previous section, it is convenient to write the operators of the ISO coupling contribution to the general TB Hamiltonian [Eq. (3.3)], in the Fourier basis as

$$\hat{s}_{i,\sigma} = \frac{1}{\sqrt{N_{cells}}} \sum_{k_x} \sum_{n} e^{ik_x x_i} \hat{s}_{k_x,\sigma,n}, \tag{4.10a}$$

$$\hat{s}^{\dagger}_{i,\sigma} = \frac{1}{\sqrt{N_{cells}}} \sum_{k_x} \sum_{n} e^{-ik_x x_i} \hat{s}^{\dagger}_{k_x,\sigma,n}, \tag{4.10b}$$

where $s_{k_x,\sigma,n}(s^{\dagger}_{k_x,\sigma,n})$ destroys (creates) an electron with spin σ and momentum $\hbar k_x$ at the site of type $\hat{s} = \{\hat{a}, \hat{b}, \hat{c}\}$ at line n.

Replacing the operators of Eq. (4.10) in Eq. (3.3), multiplying the resulting expression by the factor $e^{-ik'_x x_i} e^{ik'_x x_i} = 1$, and using the appropriate Kronecker delta function representation, we obtain the following ISO coupling Hamiltonian for generic nanoribbons:

$$\begin{aligned} \hat{H}_{\mathrm{ISO}} = & \sum_{k_x,\sigma,\sigma'} \sum_{n,n'} \tau_{ISO}{}^{AB}_{n,n'} a^{\dagger}_{k_x,\sigma,n} \sigma_z b_{k_x,\sigma',n'} + \sum_{k'_x,\sigma,\sigma'} \sum_{n',n''} \tau_{ISO}{}^{BC}_{n',n''} \sigma_z b^{\dagger}_{k'_x,\sigma,n'} c_{k'_x,\sigma',n''} \\ & + \sum_{k_x,\sigma,\sigma'} \sum_{n,n''} \tau_{ISO}{}^{AC}_{n,n''} a^{\dagger}_{k_x,\sigma,n} \sigma_z c_{k_x,\sigma',n''} + h.c., \end{aligned} \tag{4.11}$$

where $\tau_{ISO}{}^{ij}_{n,n'}$, with $i,j=(A,B,C)$, are ISO coupling matrix up-spin elements defined for each type of nanoribbon termination adopted. The σ_z is responsible for constructing the complete ISO coupling matrix that contains both up-spin and down-spin elements, as constructed later. Writing $\boldsymbol{k}=(k_x,0)$, one can find for the three types of edges,

$$\tau_{ISO}{}^{BC}_{n',n''}=i\delta_{n',n''}\left(-\lambda_{BC}e^{i\boldsymbol{R}_{BC}\cdot\boldsymbol{k}}-\lambda_{BC}e^{-i\boldsymbol{R}_{BC}\cdot\boldsymbol{k}}\right)+i\delta_{n',n''-1}\lambda'_{BC}e^{-i\boldsymbol{R}'_{BC}\cdot\boldsymbol{k}}+i\delta_{n',n''+1}\lambda'_{BC}e^{i\boldsymbol{R}'_{BC}\cdot\boldsymbol{k}}. \tag{4.12}$$

For straight [Fig. 81 (a)] and asymmetric [Fig. 81 (c)] nanoribbons that

$$\tau_{ISO}{}^{AB}_{n,n'}=i\delta_{n,n'}\left(-\lambda_{AB}e^{-i\boldsymbol{R}_{BA}\cdot\boldsymbol{k}}+\lambda'_{AB}e^{-i\boldsymbol{R}'_{BA}\cdot\boldsymbol{k}}\right)+i\delta_{n,n'-1}\left(-\lambda_{AB}e^{i\boldsymbol{R}_{BA}\cdot\boldsymbol{k}}+\lambda'_{AB}e^{i\boldsymbol{R}'_{BA}\cdot\boldsymbol{k}}\right), \tag{4.13a}$$

$$\tau_{ISO}{}^{AC}_{n,n''}=i\delta_{n,n''}\left(\lambda_{AC}e^{i\boldsymbol{R}_{AC}\cdot\boldsymbol{k}}-\lambda'_{AC}e^{-i\boldsymbol{R}'_{AC}\cdot\boldsymbol{k}}\right)+i\delta_{n,n''-1}\left(\lambda_{AC}e^{-i\boldsymbol{R}_{AC}\cdot\boldsymbol{k}}-\lambda'_{AC}e^{i\boldsymbol{R}'_{AC}\cdot\boldsymbol{k}}\right), \tag{4.13b}$$

and for bearded [Fig. 81 (b)] nanoribbons, one gets

$$\tau_{ISO}{}^{AB}_{n,n'}=i\delta_{n,n'}\left(-\lambda_{AB}e^{i\boldsymbol{R}_{BA}\cdot\boldsymbol{k}}+\lambda'_{AB}e^{i\boldsymbol{R}'_{BA}\cdot\boldsymbol{k}}\right)+i\delta_{n,n'+1}\left(-\lambda_{AB}e^{-i\boldsymbol{R}_{BA}\cdot\boldsymbol{k}}+\lambda'_{AB}e^{-i\boldsymbol{R}'_{BA}\cdot\boldsymbol{k}}\right), \tag{4.14a}$$

$$\tau_{ISO}{}^{AC}_{n,n''}=i\delta_{n,n''}\left(\lambda_{AC}e^{-i\boldsymbol{R}_{AC}\cdot\boldsymbol{k}}-\lambda'_{AC}e^{i\boldsymbol{R}'_{AC}\cdot\boldsymbol{k}}\right)+i\delta_{n,n''+1}\left(\lambda_{AC}e^{i\boldsymbol{R}_{AC}\cdot\boldsymbol{k}}-\lambda'_{AC}e^{-i\boldsymbol{R}'_{AC}\cdot\boldsymbol{k}}\right). \tag{4.14b}$$

As in Ch. 3, the λ_{ij} represent the amplitudes of the ISO coupling, which obey Eq. (3.6).

To find the Lieb-Kagome nanoribbon band structure with ISO coupling, we apply the standard Heisenberg equation of motion, $i\hbar\frac{d\hat{\mathscr{O}}}{dt}=[\hat{\mathscr{O}},\hat{H}]$, to the operators $\hat{\mathscr{O}}\equiv\{\hat{s}^{\dagger}_{k_x,\sigma,n},\hat{s}_{k_x,\sigma,n}\}$ in line n. By Eq. (3.1), $\hat{H}=\hat{H}_0+\hat{H}_{\rm ISO}$, with $\hat{H}_0$ given by Eq. (4.2) and $\hat{H}_{\rm ISO}$ given by Eq. (4.11), in the current context of nanoribbons.

Assuming that the time dependence of the modes behaves like $e^{-\frac{iEt}{\hbar}}$, one obtains $E\hat{s}_{k_x,\sigma,n}=[\hat{s}_{k_x,\sigma,n},\hat{H}]$ for the three operators $\hat{s}\equiv\{\hat{a},\hat{b},\hat{c}\}$, and thus one arrives at the following matrix equation

$$\mathscr{T}\begin{pmatrix}\hat{a}_{k_x,\uparrow,n}\\ \hat{b}_{k_x,\uparrow,n}\\ \hat{c}_{k_x,\uparrow,n}\\ \hat{a}_{k_x,\downarrow,n}\\ \hat{b}_{k_x,\downarrow,n}\\ \hat{c}_{k_x,\downarrow,n}\end{pmatrix}=E\begin{pmatrix}\hat{a}_{k_x,\uparrow,n}\\ \hat{b}_{k_x,\uparrow,n}\\ \hat{c}_{k_x,\uparrow,n}\\ \hat{a}_{k_x,\downarrow,n}\\ \hat{b}_{k_x,\downarrow,n}\\ \hat{c}_{k_x,\downarrow,n}\end{pmatrix}, \tag{4.15}$$

where

$$\mathscr{T}=\mathscr{T}_0\otimes\mathbb{1}_{2\times2}+\mathscr{T}_{\rm ISO}\otimes\sigma_z, \tag{4.16}$$

analogously to Eq. (3.9), such that $\mathscr{T}_{\mathrm{ISO}}$ is the ISO coupling matrix corresponding to the up spin component, of order $N_A + N_B + N_C$, which depends on the ribbon configuration, given by

$$\mathscr{T}_{\mathrm{ISO}} = \begin{pmatrix} [\tau_{ISO}{}^{AA}]_{N_A \times N_A} & [\tau_{ISO}{}^{AB}]_{N_A \times N_B} & [\tau_{ISO}{}^{AC}]_{N_A \times N_C} \\ [\tau_{ISO}{}^{BA}]_{N_B \times N_A} & [\tau_{ISO}{}^{BB}]_{N_B \times N_B} & [\tau_{ISO}{}^{BC}]_{N_B \times N_C} \\ [\tau_{ISO}{}^{CA}]_{N_C \times N_A} & [\tau_{ISO}{}^{CB}]_{N_C \times N_B} & [\tau_{ISO}{}^{CC}]_{N_C \times N_C} \end{pmatrix}, \tag{4.17}$$

with $\tau_{ISO}{}^{AA}$, $\tau_{ISO}{}^{BB}$, and $\tau_{ISO}{}^{CC}$ standing for the ISO coupling between equivalent sites, which are considered null in this thesis.

Finally, to obtain the energy levels of the Lieb-Kagome nanoribbons with ISO coupling, the matrix $\mathscr{T}$ is diagonalized by choosing the ribbon features, such as the angle θ that determines the lattice type, the type of edge, and the total number of lines N associated with the width of the nanoribbon. The matrix $\mathscr{T}$ consists of two uncoupled blocks corresponding to the spin-up and spin-down projections, related by TR symmetry. In Ch. 3, we consider that due to the TR and inversion symmetries, the ISO coupling is unable to lift the spin degeneracy in Lieb-Kagome lattices. In the case of nanoribbons, we have inversion symmetry only in the y direction in straight and bearded nanoribbons, such that we obtain exactly the same energy spectrum for both spin-up and spin-down cases, resulting in bands that are doubly degenerate. However, in the case of asymmetric edge nanoribbons, this symmetry is broken, and we find different spectra depending on whether we consider spin-up or spin-down, with greater differences in the edge states.

4.2.4 Calculation of the density of states

By leveraging the calculated energy levels, one can determine the DOS, which serves as a crucial function in condensed matter physics and materials science. The DOS quantifies the number of available electronic states at each energy level within a specified energy range, playing a pivotal role in understanding various electronic properties of materials, such as electrical conductivity, optical characteristics, and thermal capacity (ASCROFT; MERMIM, 1976; KITTEL, 2005).

To compute the DOS, we employ a method that involves the superposition of individual energy states. Each of these states is broadened using a Gaussian function, transitioning from a discrete to a continuous representation of energy levels. This broadening is imperative for accommodating the inherent uncertainties and variations present in real-world materials, where perfectly discrete energy levels are rarely observed.

The Gaussian function used for broadening is mathematically represented as follows:

$$f(E) = e^{-\frac{(E-E_0)^2}{\gamma^2}}, \tag{4.18}$$

where E represents the energy variable, E_0 denotes the central energy level around which the broadening occurs, and γ is the broadening factor that determines the width of the Gaussian peak (SILVA, 2015).

The parameter γ is of critical importance, as it ensures the Gaussian function effectively smooths the density of states without obscuring the inherent separations between discrete energy levels. A carefully chosen γ value, smaller than the typical energy level separations, guarantees that the broadening does not inappropriately merge distinct states, thereby preserving the physical accuracy of the model (SILVA, 2015).

In this context, we adopt a standard broadening factor γ of $0.05t$, unless otherwise stated. This specific value is selected based on the typical energy scales in the systems under study and provides a balanced approach to broadening. By using $\gamma = 0.05t$, we maintain a consistent and reproducible method for calculating the DOS across Lieb-Kagome lattice nanoribbons. From this point onward, all DOS results presented will utilize this standard broadening factor, ensuring that our analysis remains coherent and comparable throughout the study. Specifically, in the next section, we admit values of $n < 8$ in Eq. (3.4) in comparison with $n = 8$, to investigate the effects of including NNN sites in the energy spectrum of Lieb, transition ($\theta = 105°$) and Kagome nanoribbons within the TB model.

4.3 Effects of next-nearest-neighbors sites

To include increasingly noticeable effects of sites more distant than the NN sites (e.g., the NNN sites) in the energy spectra of Lieb-Kagome nanoribbons, consider increasingly smaller values of $n < 8$, as in Ch. 2 (LIMA *et al.*, 2023). In fact, from Eq. (3.4), it is seen that the value of n controls the magnitude of the hopping parameters. For a given distance between sites, the corresponding hopping value will decrease (increase) as the value of the n-parameter increases (decreases). As discussed by Lima *et al.* (2023), the effects of sites more distant than the NN sites are suppressed for $n \geq 8$ and intensified for $n < 8$. With $n = 8$, we obtain both nearly-flat bands and smooth transitions between the two lattices (JIANG *et al.*, 2019c), thus finding a good approximation for the TB model of NN sites in the specific cases of the Lieb and

Figure 82 – Energy spectra (panels with subscript 1) and DOS (panels with subscript 2) of nanoribbons with: (a-c) asymmetric edges [$N = 30$], (d-f) straight edges [$N = 31$], and (g-i) bearded edges [$N = 31$] for (a,d,g) Lieb, (b,e,h) transition, and (c,f,i) Kagome lattices without ISO coupling, *i.e.*, $\lambda_{\mathrm{ISO}} = 0$ (Eq. (3.6)). The cases presented are: (i) $n = 1$ [black dash-dotted line], (ii) $n = 4$ [dashed red line], and (iii) $n = 8$ [solid blue line].

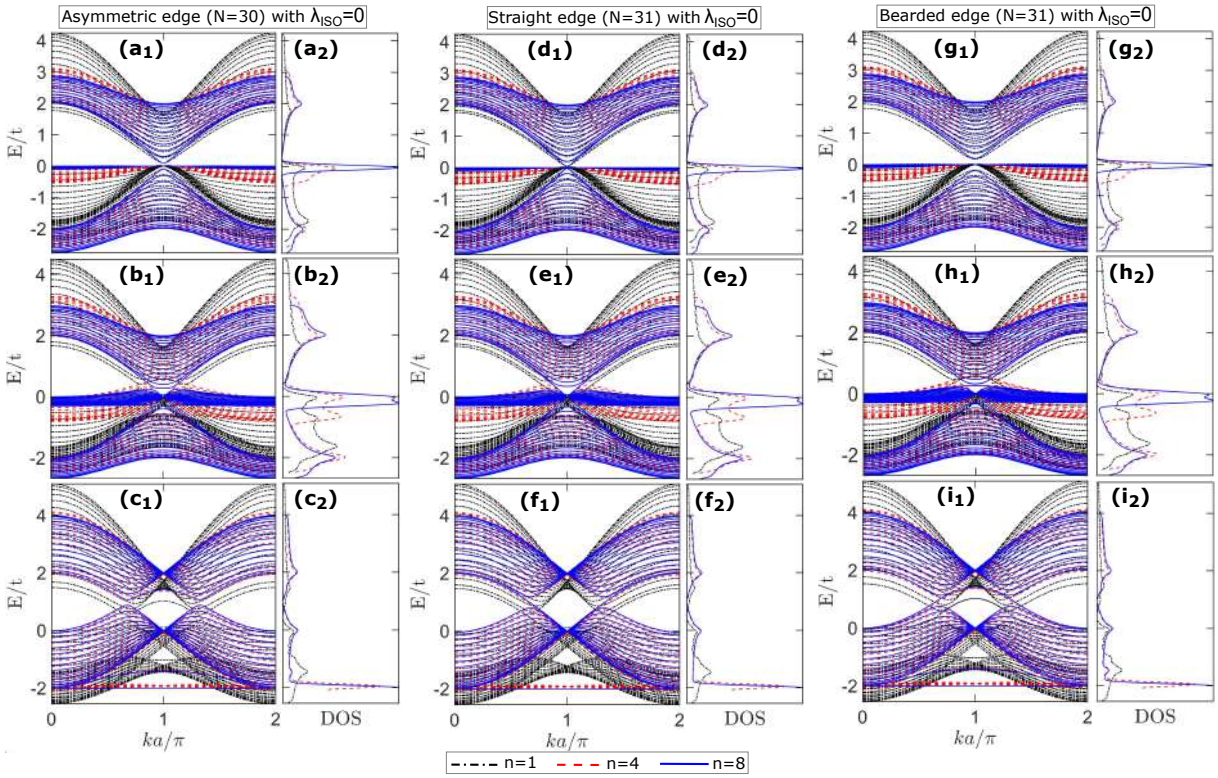

Source: The author.

Kagome nanoribbons (JIANG *et al.*, 2019c; LIMA *et al.*, 2023).

Figure 82 shows the effects of sites further apart than the NN sites, such as the NNN sites, on the energy spectra of Lieb, transition ($\theta = 105^{\circ}$), and Kagome nanoribbons with asymmetric ($N = 30$), straight ($N = 31$), and bearded ($N = 31$) edges, respectively. We note that the inclusion of NNN sites does not close or open an energy gap. The main effect observed is that the modes originating from the flat band of the corresponding infinite lattice spectrum become increasingly spaced as more distant neighbors are included in the model. This is confirmed by the DOS, which initially shows well-localized peaks corresponding to the nearby modes in the NN TB model. As NNN sites and even more distant neighbors are included in the model, these peaks become less localized and consequently cover a wider energy range compared to the peaks of the NN sites model.

Indeed, when considering only NN sites, the flat bands, which are degenerate N_A times, persist in the energy spectrum of Lieb, transition, and kagome nanoribbons for all three edge types. However, the inclusion of NNN-sites breaks this degeneracy in all cases,

transforming the flat bands into nearly-flat bands. These nearly-flat bands remain nearly-flat due to the constraint $n = 8$ in Eq. (3.4). It is important to mention that for $n < 8$, as discussed in Ch. 2, these bands become increasingly dispersive.

Regardless of the value of n, in the Lieb nanoribbon [Fig. 82 (a_2, d_2, g_2)], the DOS panels show a pronounced sharp peak around $E = 0$ associated with the N_A nearly-degenerate states, with its peak width related to the nearly-flat states subband width. Additionally, around $E/t \approx \pm 2$, the DOS of the Lieb nanoribbons exhibits van Hove singularities (peaks) corresponding to energy levels with almost zero group velocity at the corners of the BZ. These peaks are more pronounced in larger Lieb nanoribbons (compare black and blue curves, where the former represents the shortest Lieb nanoribbon). These van Hove singularities have also been reported in other flat-band nanostructured systems, such as Dice lattice nanoribbons (SONI *et al.*, 2020).

The DOS of transition nanoribbons [Fig. 82 (b_2, e_2, h_2)] shows a splitting of the van Hove singularity corresponding to the nearly-flat bands observed in the DOS of the Lieb nanoribbon [Fig. 82 (a_2, d_2, g_2)]. This splitting occurs near the energy $E = 0$ and is observed in transition nanoribbons for all three edge configurations. This effect provides evidence for the interconvertibility process between Lieb and Kagome nanoribbons (UCHOA, 2023).

The DOS of Kagome nanoribbons displays van Hove singularities around $E = -2t$, corresponding to the nearly-flat bands, similar to the DOS of Lieb nanoribbons near $E = 0$. Peaks in the DOS around $E = +2t$ and $E = 0$ arise from degenerate points at $ka = \pi$. Additionally, bearded and asymmetric Kagome nanoribbons exhibit an additional peak in the DOS around $E = -1.5t$, which originates from two (one) states in the bearded (asymmetric) case. These states are considered nearly-flat bands since they are in close proximity to the other nearly-flat bands at $ka = 0$ and $ka = 2\pi$, but deviate from them as k approaches π (UCHOA, 2023).

4.4 Effects of intrinsic spin-orbit coupling

Figure 83 depicts the energy levels of Lieb [Fig. 83 (a,d,g)], transition [Fig. 83 (b,e,h)], and Kagome [Fig. 83 (c,f,i)] asymmetric-edged nanoribbons for the three investigated cases: (a-c) without ISO coupling ($\lambda_{\mathrm{ISO}} = 0$), and (d-i) with ISO coupling ($\lambda_{\mathrm{ISO}} = 0.2t$), where (d-f) $\lambda_{AB} \neq 0$, $\lambda_{BC} \neq 0$, and (g-i) $\lambda_{AB} = \lambda_{BC} = 0$.

The results obtained without ISO coupling reveal the presence of N_A nearly-flat modes localized around the infinite-sheet nearly-flat band, which is at $E = 0$ in the Lieb and transition lattices, and $E = -2t$ in the Kagome lattice. Additionally, there are N_B subbands for

Figure 83 – Energy spectra of nanoribbons with asymmetric edges ($N = 30$) for (a,d,g) Lieb, (b,e,h) transition, and (c,f,i) Kagome lattices. The cases presented are (a-c) $\lambda_{\mathrm{ISO}} = 0$, and (d-i) $\lambda_{\mathrm{ISO}} = 0.2t$, with (d-f) $\lambda_{AB} \neq 0$, $\lambda_{BC} \neq 0$, and (g-i) $\lambda_{AB} = \lambda_{BC} = 0$. The solid black lines represent the states with $\lambda_{\mathrm{ISO}} = 0$, while the states with $\lambda_{\mathrm{ISO}} \neq 0$ are represented by solid blue lines (spin-up) and dashed red lines (spin-down).

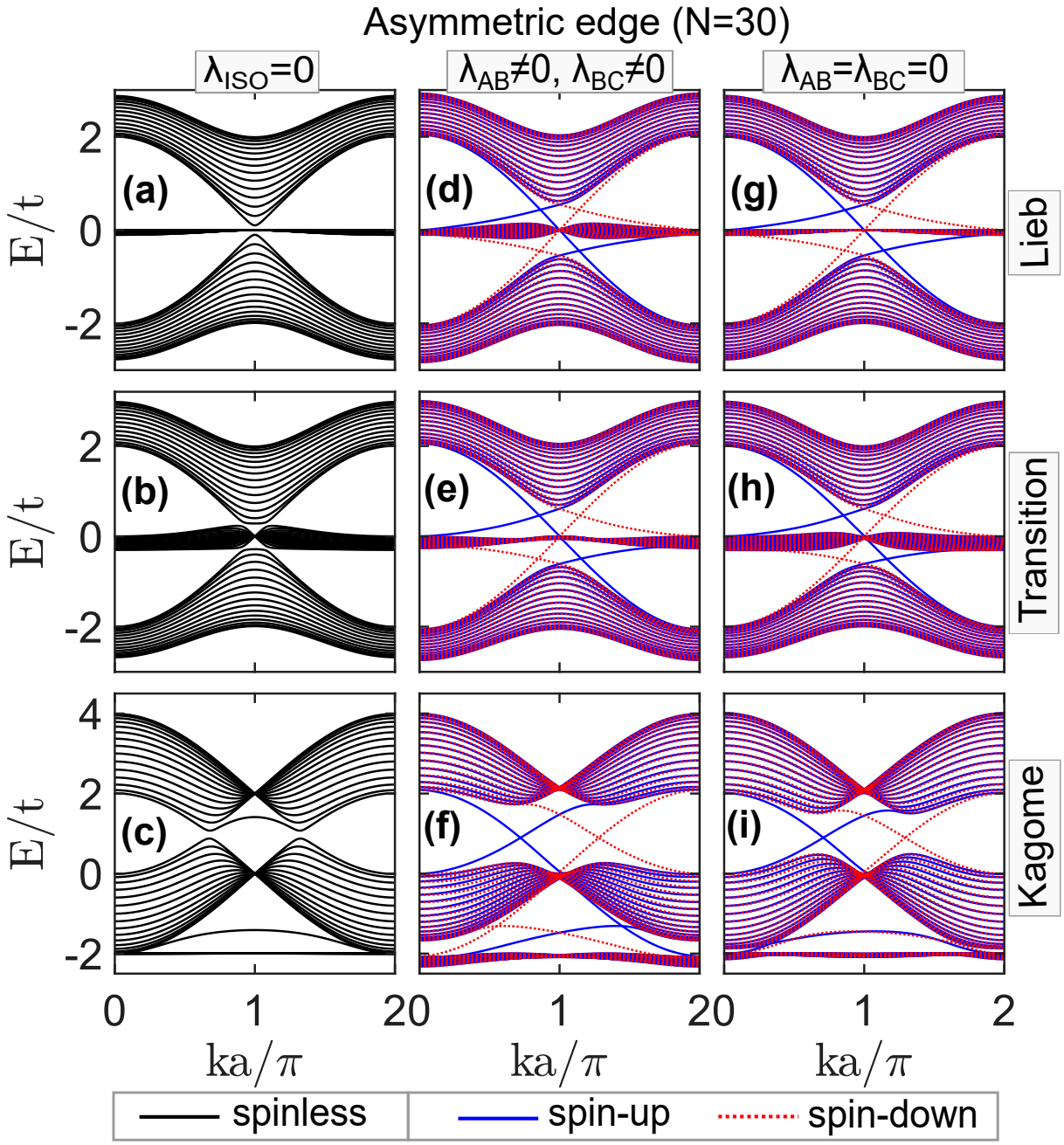

Source: The author.

each of the two dispersive bands, originating from the infinite-sheet lower (E_1) and upper (E_3) bands in the Lieb and transition lattices, and from the middle (E_2) and upper (E_3) bands in the case of Kagome, as indicated in Figs. 48(d), 48(e), and 48(f), respectively, for the Lieb, transition, and Kagome lattices.

The spectrum of transition nanoribbons, shown in Fig. 83 (b), differs from the Lieb

[Fig. 83 (a)] one mainly due the shape of the nearly-flat modes, which are more dispersive than those of Lieb nanoribbons. This behavior is a consequence of the interconvertibility process of the transition nanoribbon, similar to that between Lieb and Kagome infinite lattices. The evolution of the θ parameter from Lieb ($\theta = 90^\circ$) to Kagome ($\theta = 120^\circ$) destroys the nearly-flat bands located in the middle of the spectrum of Lieb nanoribbon and reconstructs them in the lower (upper) part of the energy spectrum of Kagome nanoribbon for positive (negative) hopping parameters [see Fig. 49]. Furthermore, in the case of the asymmetric edge, all states of nearly-flat bands are degenerate in the $ka = \pi$ point.

For the Lieb and transition lattices without ISO coupling [Fig. 83 (a,b)], we observe that due to the confinement effect in the y direction, with an asymmetric nanoribbon cut that does not preserve inversion symmetry in this direction, an energy gap is opened between the dispersive subbands originating from E_1 and the nearly-flat subbands stemming from E_2, and another gap between the subbands of E_2 and E_3. Consequently, the Lieb and transition nanoribbons are semiconductors at $1/3$ and $2/3$ filling. Kagome nanoribbons with asymmetric edges [Fig. 83 (c)] are semiconductors, similar to the equivalent cases in Lieb [Fig. 83 (a)] and transition [Fig. 83 (b)] with that type of edge. However, unlike Lieb and transition, which exhibit two energy gaps between the dispersive bands and the nearly-flat bands, the Kagome nanoribbon presents only one energy gap between the higher-energy dispersive band and the lower-energy upper dispersive band.

Despite this difference, similar to the cases of Lieb and transition, the results obtained for the Kagome nanoribbon [Fig. 83 (c)] reveal the presence of N_A nearly-flat bands. However, in the Kagome case, the nearly-flat bands are located near $E = -2t$ at $ka = 0$ and $ka = 2\pi/a$, rather than at $E = 0$ as in Lieb and transition. Additionally, there are N_B dispersive bands in the middle and upper parts of the energy spectrum, whereas in Lieb and transition, there are N_B dispersive bands in the lower and upper parts of the energy spectrum.

The introduction of ISO coupling opens two energy gaps between the bands E_1 and E_2 (Δ_{12}) and E_2 and E_3 (Δ_{23}) in the spectrum of Lieb-Kagome lattices. A gap is seen between the higher-energy lower dispersive band and the lower-energy nearly-flat band, while another gap appears between the higher-energy nearly-flat band and the lower-energy upper dispersive band. As expected from the bulk-edge correspondence, there are edge states that cross these bulk energy gaps [Fig. 83 (d-i)]. This is the main reason we refer to Lieb-Kagome lattices as topological insulators, as they are insulating in the bulk but exhibit topologically protected edge

Figure 84 – Same as Fig. 83, but now for (a-i) straight and (j-r) bearded edges, both with $N = 31$.

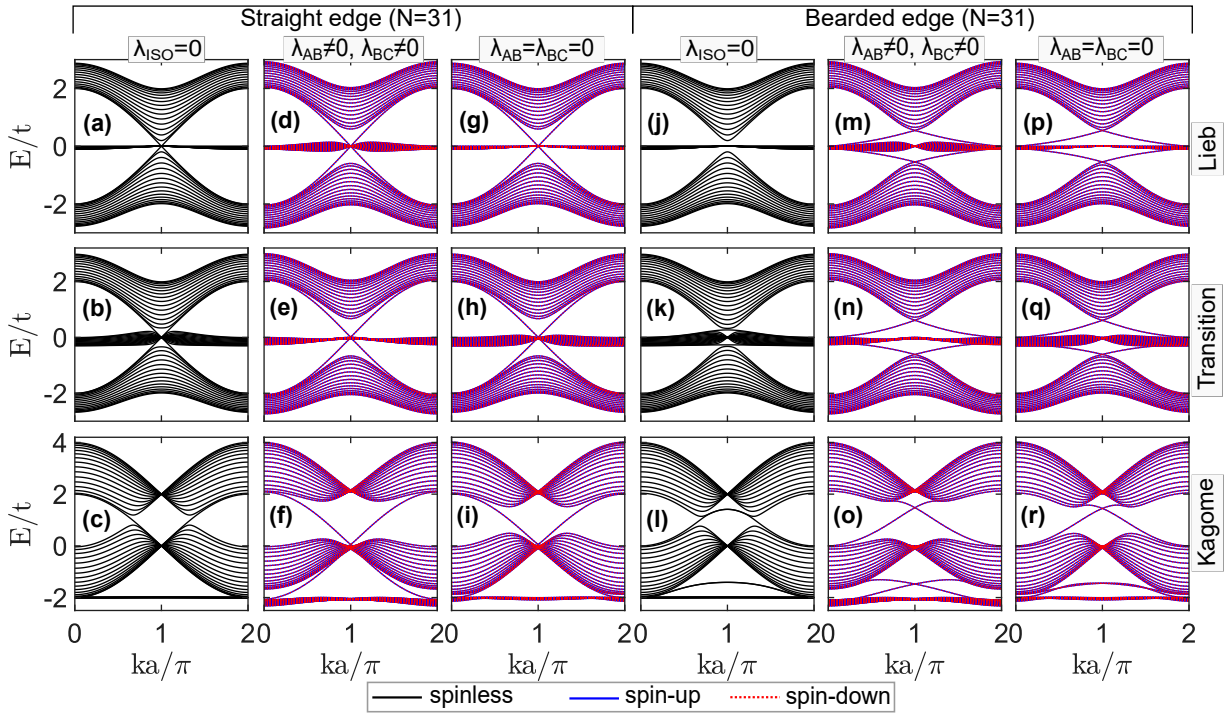

Source: The author.

states.

It is important to note that the chiral spin-up and spin-down states are not doubly degenerate, thus configuring helical states (MANI; BENJAMIN, 2017) due to the inversion symmetry breaking characteristic of the nanoribbon with asymmetric edges [Fig. 81 (c)].

Figure 84 depicts the energy levels of Lieb [Fig. 84 (a,d,g,j,m,p)], transition [Fig. 84 (b,e,h,k,n,q)], and Kagome [Fig. 84 (c,f,i,l,o,r)] nanoribbons with straight [Fig. 84 (a-i)] and bearded [Fig. 84 (j-r)] edges for the three investigated cases: (a-c) without ISO coupling ($\lambda_{\mathrm{ISO}} = 0$), and (d-i) with ISO coupling ($\lambda_{\mathrm{ISO}} = 0.2t$), where (d-f) $\lambda_{AB} \neq 0$, $\lambda_{BC} \neq 0$, and (g-i) $\lambda_{AB} = \lambda_{BC} = 0$.

Notably, without ISO coupling, the Dirac cone observed in the energy spectrum of the infinite-sheet Lieb lattice (JIANG *et al.*, 2019c) is verified only in the case of Lieb ribbons with straight edges [Fig. 84 (a)]. This can be attributed to the fact that the straight-edged nanoribbon is the only one of the three edge terminations that is completely symmetrical and free of dangling bonds, thus preserving the defect-free structural features of the Lieb lattice. Consequently, it exhibits the main energetic aspects of the Lieb lattice in its infinite-sheet spectrum, *i.e.*, the coexistence of a Dirac cone and a nearly-flat band. For Lieb nanoribbons with bearded edges [Fig. 84 (j)], one can notice the appearance of two energy gaps, similar to the case of asymmetric edges: one of these gaps is situated between the higher energy (E_1) of the lower dispersive

subband and the lower energy of the nearly-flat subband, and the other energy gap emerges between the higher energy of the nearly-flat subband and the lower energy of the upper dispersive subband (ZHANG *et al.*, 2016; UCHOA, 2023). Based on the presence or absence of an energy gap in the energy spectrum, one can characterize straight-edged Lieb nanoribbons as metallic, while bearded and asymmetric-edged Lieb nanoribbons can be characterized as semiconductor systems.

For the transition nanoribbon, similar to the Lieb nanoribbons, only the straight edge exhibits the Dirac-like spectrum [Fig. 84 (b)]. The main difference between the bearded [Fig. 84 (k)] and asymmetric edges in the transition spectrum is manifested in the nearly-flat subbands. In the case of the bearded edge, the least energetic and most energetic nearly-flat subbands separate from the other nearly-flat subbands in the vicinity of the $ka = \pi$ point [see Fig. 84 (k)], whereas in the case of the asymmetric edge, as mentioned earlier, all nearly-flat subbands are degenerate at this k point [Fig. 84 (b)]. Moreover, the bearded edge nanoribbon always has an extra nearly-flat mode when compared to the other two configurations, when compared without ISO coupling.

Kagome nanoribbons with straight edges are metallic, lacking an energy gap [Fig. 84 (c)], similar to Lieb [Fig. 84 (a)] and transition [Fig. 84 (b)] nanoribbons with the same edge type. Conversely, Kagome nanoribbons with bearded edges [Fig. 84 (l)] are also metallic, which contrasts with Lieb [Fig. 84 (j)] and transition [Fig. 84 (k)] nanoribbons with bearded edges, as these are semiconductors.

When the ISO coupling is included, the energy spectra of nanoribbons exhibit notable differences based on edge configurations. In contrast to the spectra of asymmetric-edged nanoribbons, Fig. 84 shows doubly degenerate spin-up and spin-down states for nanoribbons with straight or bearded edges, which preserve inversion symmetry. Generally, in nanoribbons with straight edges, the edge states form a V-shape in the positive energy region, while those with bearded edges exhibit a Λ-shape in the same region. The combination of these two types of edge states explains the edge states observed in nanoribbons with asymmetric edges. Indeed, nanoribbons with asymmetric edges feature both straight and bearded edge types, resulting in a mixture of the corresponding edge state characteristics.

In Fig. 85, we compare the energy spectrum region of nanoribbons for Kagome lattice cases, seeking to identify the differences and similarities between the cases with $\lambda_{AB} = \lambda_{BC} = 0$ and $\lambda_{AB} \neq 0$ and $\lambda_{BC} \neq 0$ for the three edge types. The results for the asymmetric edge show that

Figure 85 – Representation of zoomed-in regions of the energy spectra of nanoribbons of the Kagome lattice shown in Figs. 83 and 84 in the lower energy region, comprising the nearly-flat modes, for (a,d,g) asymmetric edges, (b,e,h) bearded edges, and (c,f,i) straight edges. We present the cases with (a-c) $\lambda_{\mathrm{ISO}} = 0$, and (d-i) $\lambda_{\mathrm{ISO}} = 0.2t$, with (d-f) $\lambda_{AB} \neq 0$, $\lambda_{BC} \neq 0$, and (g-i) $\lambda_{AB} = \lambda_{BC} = 0$. The solid black lines represent the states with $\lambda_{\mathrm{ISO}} = 0$, while the states with $\lambda_{\mathrm{ISO}} \neq 0$ are represented by solid blue lines (spin-up) and dashed red lines (spin-down).

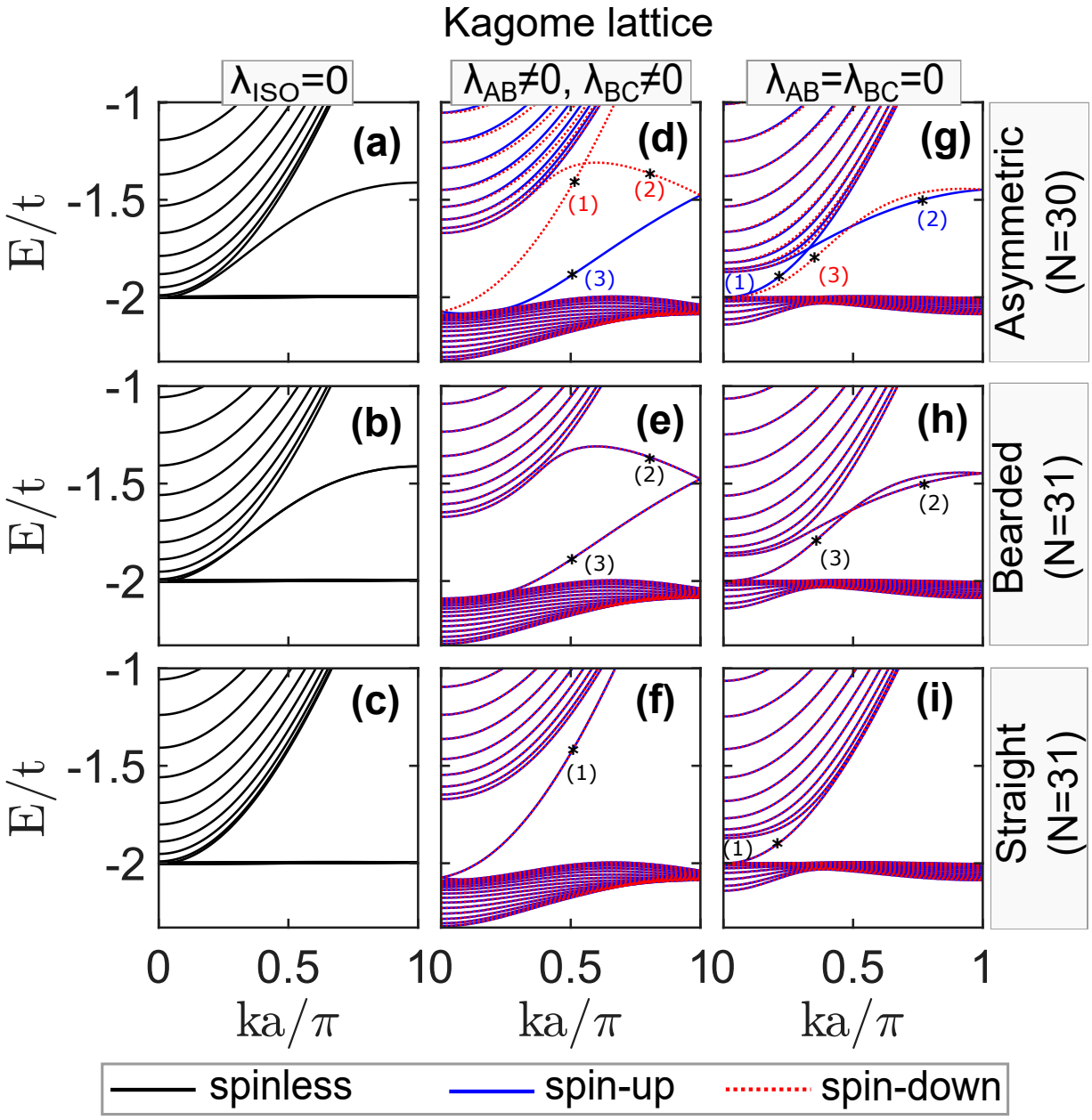

Source: The author.

there is a spin-up and spin-down flip due to the change in the Chern number of the cases analyzed in Figs. 85 (d) and 85 (g). Note that modes (1) and (2), which correspond to spin-down states when $\lambda_{AB} \neq 0$ and $\lambda_{BC} \neq 0$, with $C^{\uparrow} = (1, 0, -1)$, become spin-up states when $\lambda_{AB} = \lambda_{BC} = 0$, as $C^{\uparrow} = (-1, 2, -1)$, as represented in Fig. 51 (e_4 and f_4). Similarly, mode (3) changes from spin-up to spin-down when there is a phase transition of $\Delta C^{\uparrow} = (1, 0, -1) - (-1, 2, -1) = (2, -2, 0)$ at

$\theta = 118.3°$, as discussed in Sec. 3.5.2. This spin-flip behavior occurs again, most evidently, in the strain-driven cases analyzed below. Additionally, the other panels show the states originating from the bearded and straight edges, helping to identify which edge belongs to the state shown in the case of the asymmetric edge. Specifically, we observe that mode (1) in the spectrum of the asymmetric-edged Kagome nanoribbon is located at the lower straight edge, whereas modes (2) and (3) are located at the upper asymmetric edge, as represented in Fig. 81 (c).

In Fig. 86, we present the energy spectra of Lieb, transition, and Kagome nanoribbons with asymmetric edge type for the smallest possible number of lines, $N = 4$, and for an intermediate number, $N = 12$. Similarly, we show the energy spectrum for nanoribbons with straight (see Fig. 87) and bearded (see Fig. 88) edges for the smallest number of lines admitted by these types of edges, *i.e.*, $N = 5$, as well as for an intermediate number, $N = 13$. For all these results, the previous conclusions for the spectra with $N = 30$ (asymmetric edge) and $N = 31$ (straight and bearded edge) remain valid, with one exception. We observe that Kagome nanoribbons with bearded edges [Fig. 88(c)] exhibit a gap between the higher-energy lower nearly-flat subband and the lower-energy dispersive subband only for $N \leq 7$, while they present a null full band gap for $N \geq 9$, as identified for $N = 13$ [Fig. 88(l)]. In this example with $N = 13$, the $1/3$-filled system would classify the bulk as a semimetal, preventing the helical edge states from being observed. In the semimetallic regime, *i.e.*, with partially filled bands, the spin Hall conductivity is not quantized. For $2/3$ filling, regardless of N, there is no gap, which would classify the bulk in a metallic regime, prohibiting any spin Hall conductivity carried by the helical edge states from being experimentally observed, differing from Lieb and transition nanoribbons with bearded edges, which are TI both in $1/3$ filling and $2/3$ filling.

Through these plots, we see more clearly that the inclusion of ISO coupling causes the N_A nearly-flat subbands of the case without ISO coupling to become $2N_A$ nearly-flat subbands, with N_A spin-up and N_A spin-down. Similarly, the N_B dispersive subbands become $2N_B$, with N_B spin-up and N_B spin-down. In the case of straight and bearded edges, as previously mentioned, the energy spectrum is doubly degenerate concerning the spin-up and spin-down modes. However, for asymmetric edges, this does not occur due to the breaking of mirror symmetry in y.

In asymmetric-edged nanoribbons, we observe that edge states form from an anti-crossing between nearly-flat subbands and dispersive subbands [Fig. 86 (d-i)]. As N increases, helical edge states form, which completely cross the bulk gaps generated by the inclusion of ISO coupling, characteristic of Z_2 topological insulators [Fig. 86 (m-r)]. The formation of edge states

Figure 86 – Energy spectra of nanoribbons with asymmetric edges for (a-i) $N = 4$ and (j-r) $N = 12$, showing (a,d,g,j,m,p) Lieb, (b,e,h,k,n,q) transition, and (c,f,i,l,o,r) Kagome lattices. We present the cases with (a-c,j-l) $\lambda_{\mathrm{ISO}} = 0$ and (d-i,m-r) $\lambda_{\mathrm{ISO}} = 0.2t$, with (d-f,m-o) $\lambda_{AB} \neq 0$, $\lambda_{BC} \neq 0$, and (g-i,p-r) $\lambda_{AB} = \lambda_{BC} = 0$. The solid black lines represent the states with $\lambda_{\mathrm{ISO}} = 0$, while the states with $\lambda_{\mathrm{ISO}} \neq 0$ are represented by solid blue lines (spin-up) and dashed red lines (spin-down).

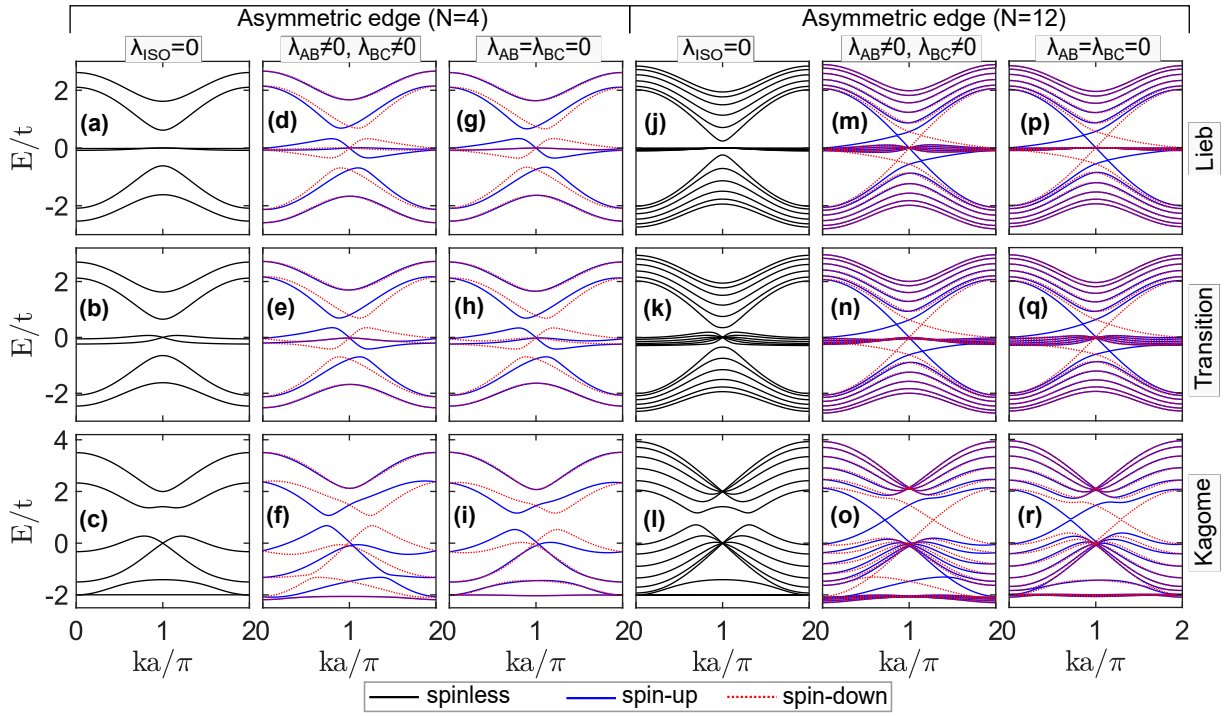

Source: The author.

in bearded-edged Lieb and transition nanoribbons also occurs through anticrossing at the point $k = \pi/a$, as represented in Figs. 88 (d-i, m-r).

Figure 87 – Same as Fig. 86, but for the straight edge with (a-i) $N = 5$ and (j-r) $N = 13$.

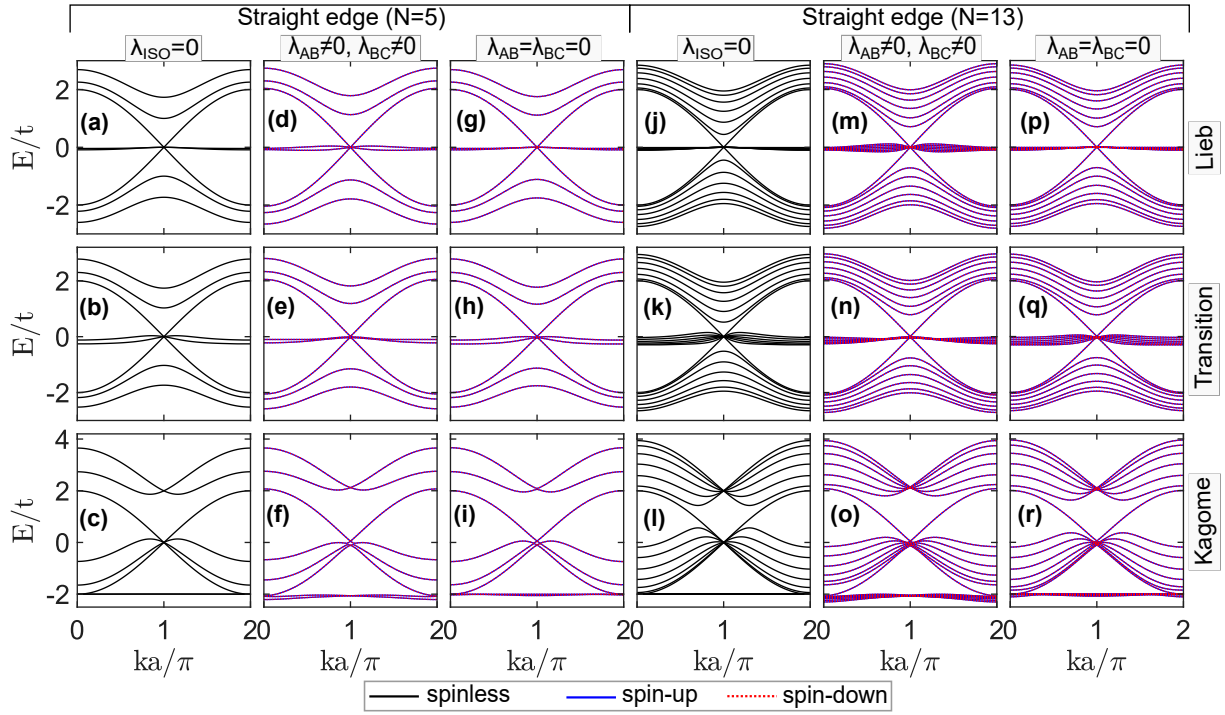

Source: The author.

Figure 88 – Same as Fig. 86, but for the bearded edge with (a-i) $N = 5$ and (j-r) $N = 13$.

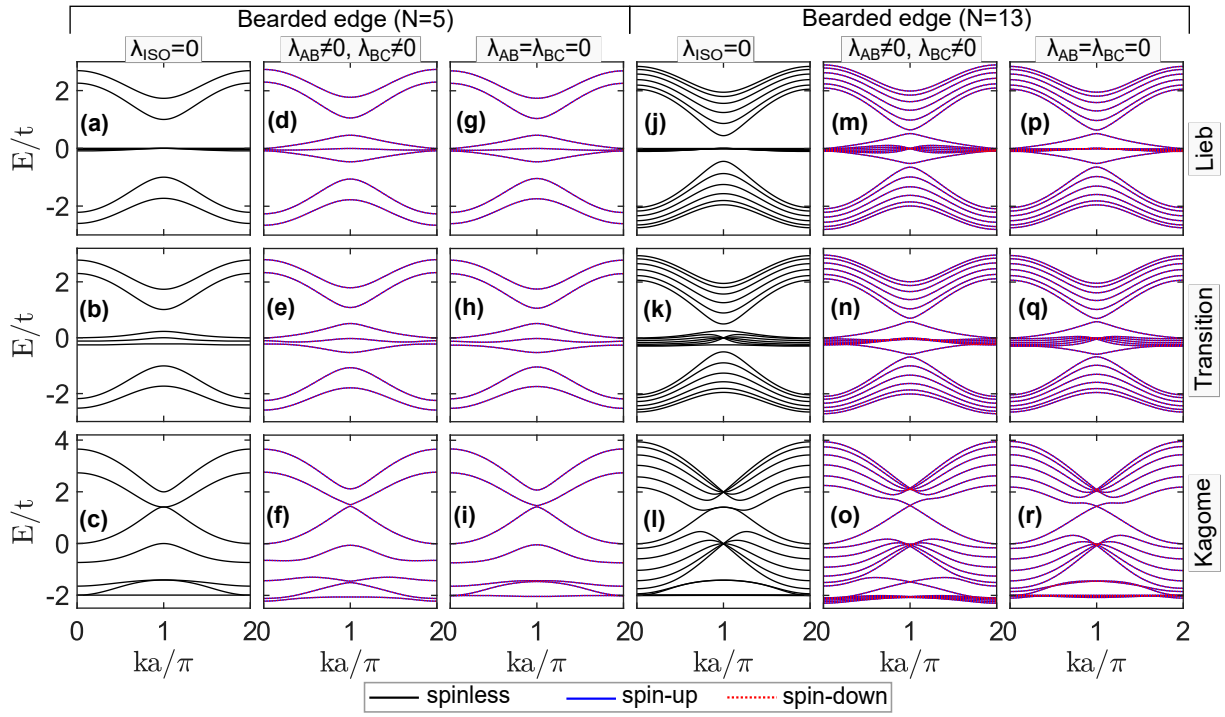

Source: The author.

Figure 89 – Energy spectra of nanoribbons for the cases presented in Fig. 59 (a-c). The solid black lines represent the states with $\lambda_{ISO} = 0$, while the states with $\lambda_{ISO} \neq 0$ are represented by solid blue lines (spin-up) and dashed red lines (spin-down).

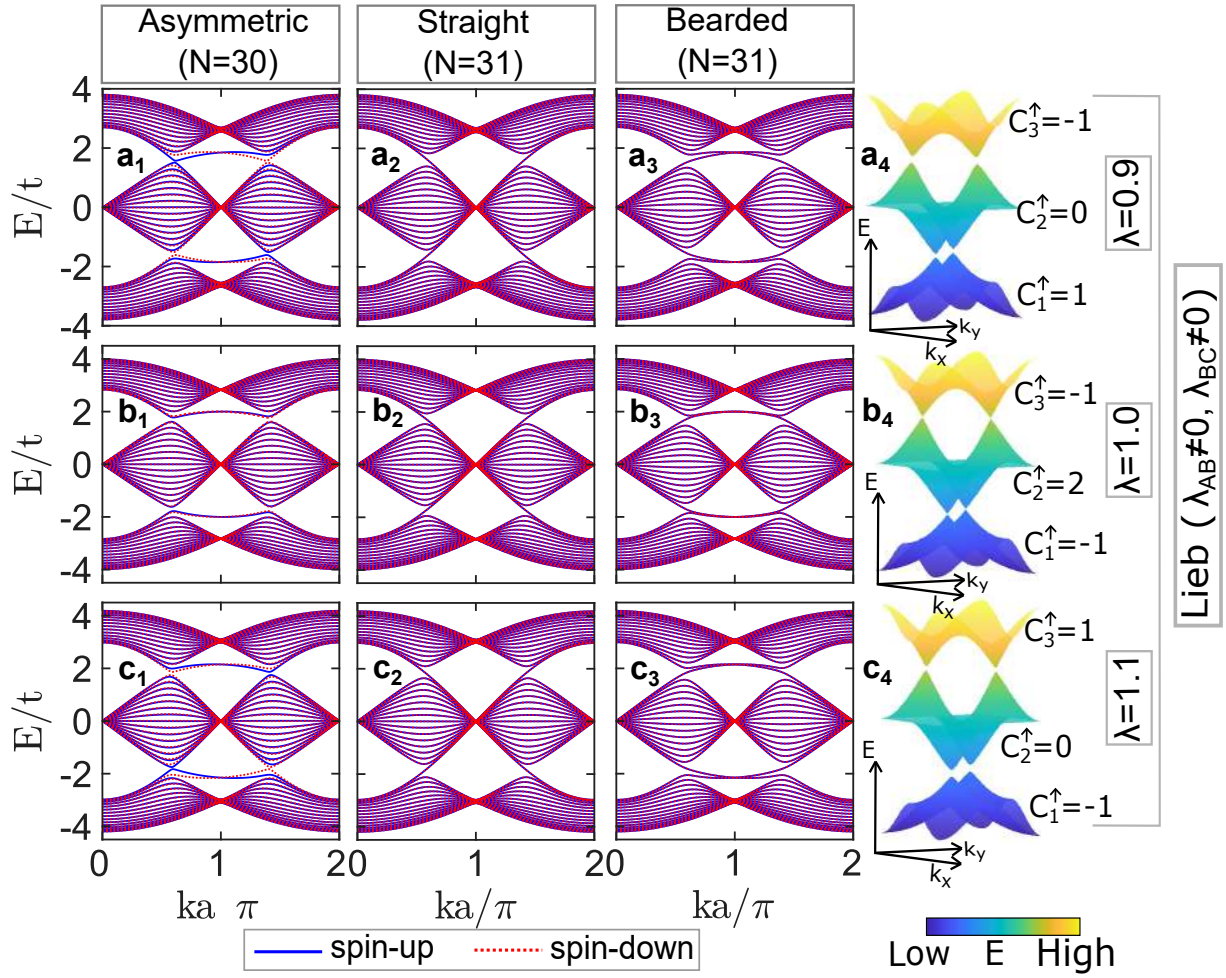

Source: The author.

4.5 Effects of topological phase transitions driven by λ and θ on edge states of Lieb-Kagome nanoribbons

Figs. 89, 90, and 91 present the energy spectrum of the unstrained nanoribbons for the cases where the Berry curvature was shown in Fig. 59 in the previous chapter. We observe that the effects on the nanoribbon spectrum are mainly in the evolution of the edge states of asymmetric-edged nanoribbons (panels of Figs. 89, 90, and 91 with subscript 1), as the spectra obtained for straight (panels of Figs. 89, 90, and 91 with subscript 2) and bearded (panels of Figs. 89, 90, and 91 with subscript 3) edges are similar before and after the TPT.

In the Lieb lattice, the TPT at $\lambda = 0.98$ causes the variation $\Delta C^{\uparrow} = (1,0,-1) - (-1,2,-1) = (2,-2,0)$, while at $\lambda = 1.03$, it causes $\Delta C^{\uparrow} = (-1,2,-1) - (-1,0,1) = (0,2,-2)$, as discussed in Ch. 3. Notably, we observe that the edge states of asymmetric nanoribbons

Figure 90 – Energy spectra of nanoribbons for the cases presented in Fig. 59 (d-e). The solid black lines represent the states with $\lambda_{ISO} = 0$, while the states with $\lambda_{ISO} \neq 0$ are represented by solid blue lines (spin-up) and dashed red lines (spin-down).

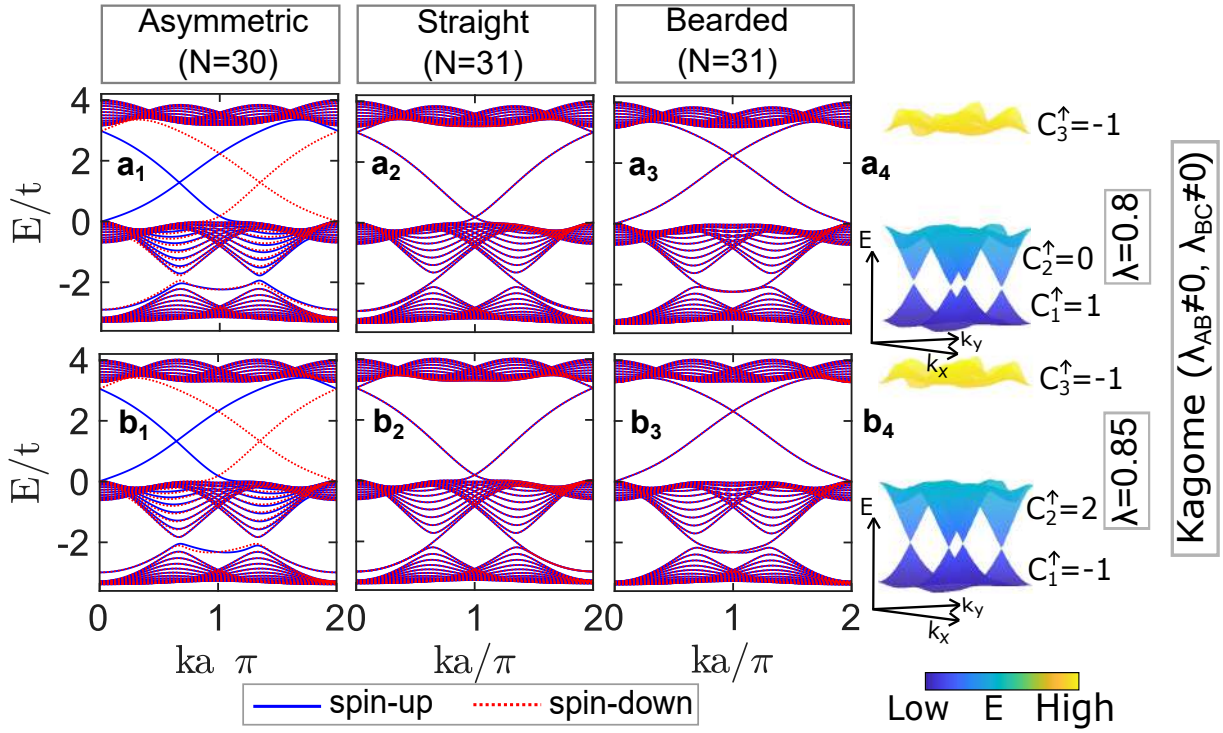

Source: The author.

undergo changes in these two TPTs. In the first transition, by comparing Figs. 89 (a_1,b_1), we see that the spin-up and spin-down edge states, which are clearly non-degenerate in the configuration $C^{\uparrow} = (1,0,-1)$ in Fig. 89 (a_1), tend to become degenerate in the configuration $C^{\uparrow} = (-1,2,-1)$ in Fig. 89 (b_1).

Despite this, we observe that the change in the sign of $C_1^{\uparrow}$ indeed induces a change from spin-up to spin-down and vice versa in the bulk-gap Δ_{12}, which corresponds to the $1/3$-filling in the spectrum of the corresponding infinite lattice. This change is evident in Fig. 89 (c_1), with the configuration $C^{\uparrow} = (-1,0,1)$ when compared to Fig. 89 (a_1). We conclude that the carriers with the same spin move in opposite directions along the same edge of the material in the configurations shown in Fig. 89 (a_1) and (c_1). Whenever there is a change in the sign of the corresponding Chern number, this results in opposite spin currents.

Our findings are also observed in the TPT driven by λ evolution that occurs at $1/3$ filling in the Kagome lattice at the critical point $\lambda = 0.84$, where $\Delta C^{\uparrow} = (1,0,-1) - (-1,2,-1) = (2,-2,0)$ [Fig. 90]. It is important to note that the edge states do not fully cross the Δ_{12} bulk-gap in the spectrum of the asymmetric-edged nanoribbon [Fig. 90 (a_1,b_1)], although they do completely cross this gap in the spectra of the corresponding straight [Fig. 90

Figure 91 – Energy spectra of nanoribbons for the cases presented in Fig. 59 (f-g). The solid black lines represent the states with $\lambda_{\mathrm{ISO}} = 0$, while the states with $\lambda_{\mathrm{ISO}} \neq 0$ are represented by solid blue lines (spin-up) and dashed red lines (spin-down).

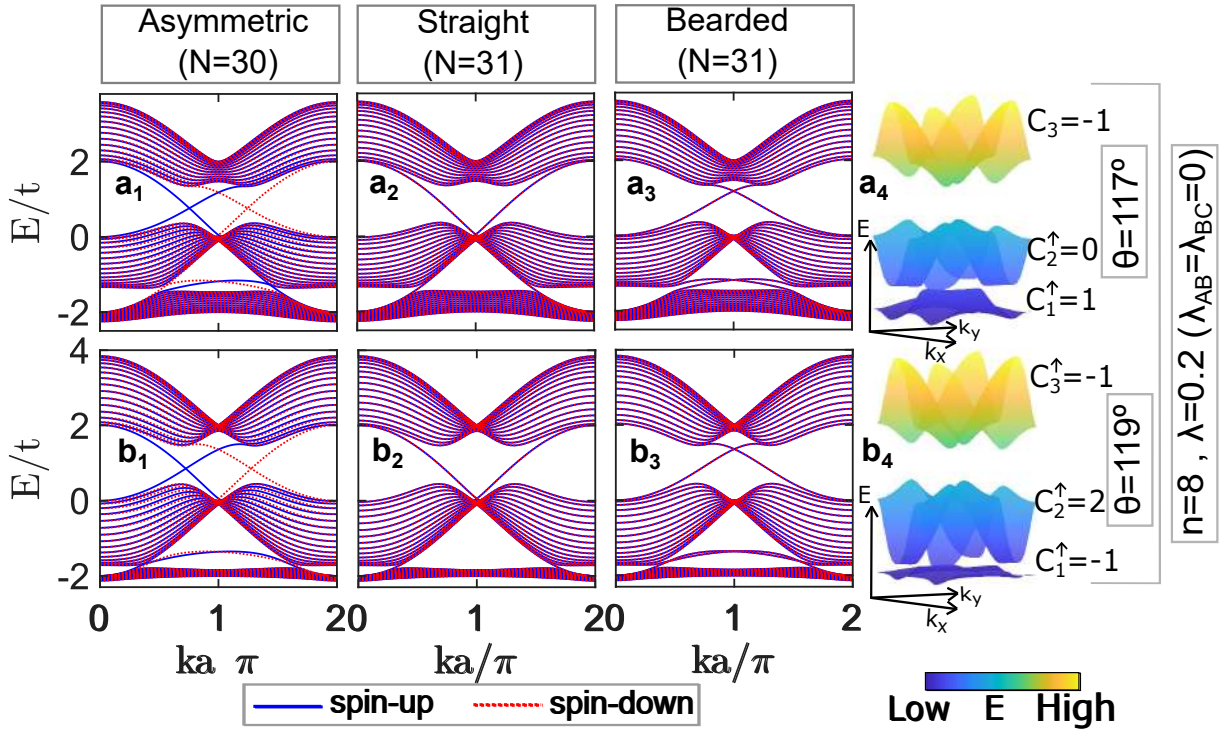

Source: The author.

(a_2,b_2)] and bearded-edged [Fig. 90 (a_3,b_3)] nanoribbons. We argue that, by the bulk-edge correspondence, it is suggested that the gap in the asymmetric-edged nanoribbon is effectively an anticrossing between the states that cross the gap in the spectra of bearded and straight-edged nanoribbons, such as those in Fig. 86 (d-i). This is because the energy subbands of the asymmetric-edged nanoribbon consist of a combination of the edge states from straight and bearded-edged nanoribbons.

In Fig. 91, we highlight two configurations before and after the TPT that occur at $\theta = 118.3^\circ$ during the interconversion process with $\lambda_{AB} = \lambda_{BC} = 0$ [Fig. 57 (d)], where we confirm the findings highlighted in Fig. 85. This comparison focuses on the energy spectrum region of nanoribbons for Kagome lattice cases, seeking to identify the differences and similarities between the cases with $\lambda_{AB} = \lambda_{BC} = 0$ and $\lambda_{AB} \neq 0$ and $\lambda_{BC} \neq 0$ for the three edge types.

The TPT represented by $\Delta C^{\uparrow} = (1,0,-1) - (-1,2,-1) = (2,-2,0)$ at $\theta = 118.3^\circ$ causes a spin flip at $1/3$ filling. Additionally, the other panels show the states originating from the bearded and straight edges, helping to identify which edge belongs to the state shown in the case of the asymmetric edge. In all open gaps, the system behaves as a QSHI, with a spin Hall conductivity of $\sigma_{\mathrm{SH}} = \pm 1$. For $\theta < 118.3^\circ$, the conductivities in the lower (1/3 filling) and upper

Figure 92 – Energy spectra of nanoribbons for the cases presented in Fig. 68 (a-b). The subbands for spin-up (spin-down) charges are represented by solid blue lines (dashed red lines).

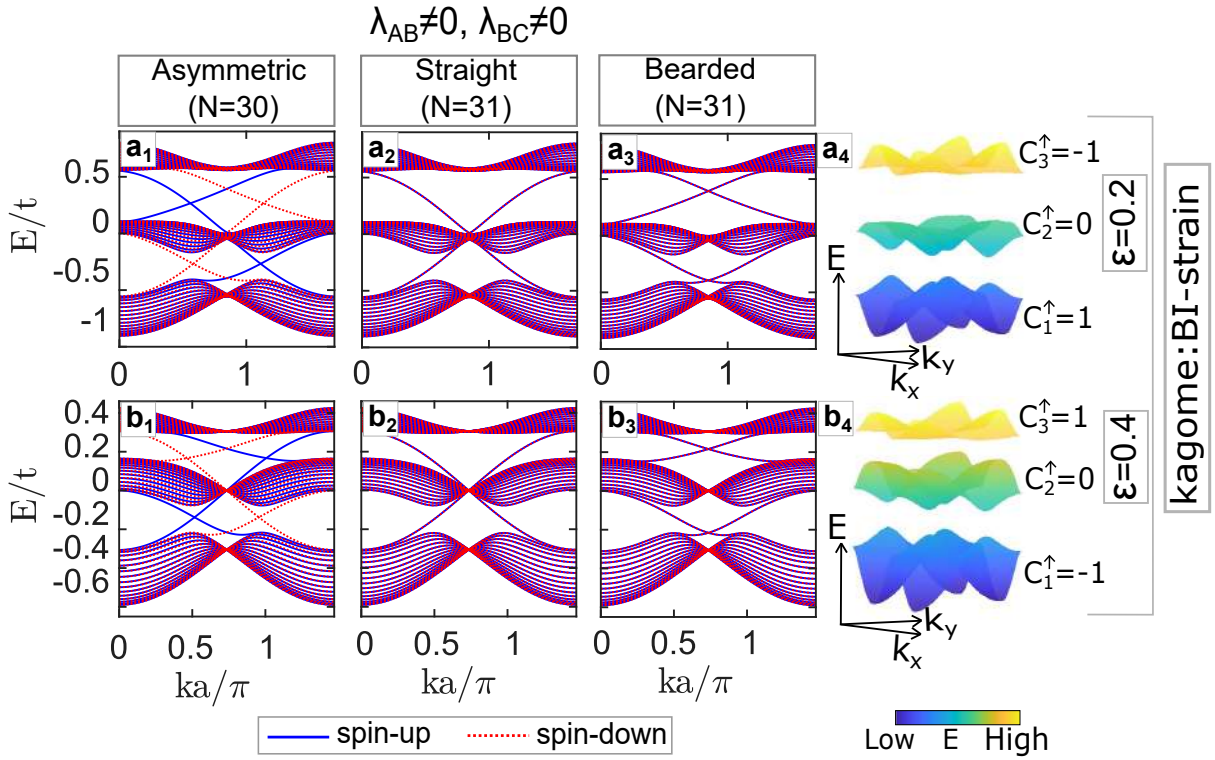

Source: The author.

(2/3 filling) gaps are equal since the middle band has zero Chern number. For $\theta > 118.3°$, the two bands have opposite conductivities (BEUGELING *et al.*, 2012).

4.6 Effects of topological phase transitions driven by strain on edge states of Lieb-Kagome nanoribbons

In Figs. 92, 93, 94, 95, and 96, we present the energy spectrum of the strained nanoribbons before and after the TPT identified in Fig. 64 for the cases with $\lambda_{AB} \neq 0$ and $\lambda_{BC} \neq 0$, whose Berry curvatures were shown in Figs. 68. Similarly, in Figs. 98, 99, 100, and 101, we present the energy spectrum of the strained nanoribbons before and after the TPT identified in Fig. 64 for some cases with $\lambda_{AB} = \lambda_{BC} = 0$, whose Berry curvatures were shown in Figs. 76. These cases are of interest because they present non-equivalent situations that we considered, calculated before and after the TPT, *i.e.*, the closing and opening of the energy gaps and the change of the Chern number calculated for the infinite lattices.

It can be observed that a pair of robust gapless edge states reside within both bulk bandgaps in TI states, where carriers with identical spins travel in opposite directions along the same edge of the material when considering asymmetric-edged nanoribbons. As previously

Figure 93 – Energy spectra of nanoribbons for the cases presented in Fig. 68 (c-e). The subbands for spin-up (spin-down) charges are represented by solid blue lines (dashed red lines).

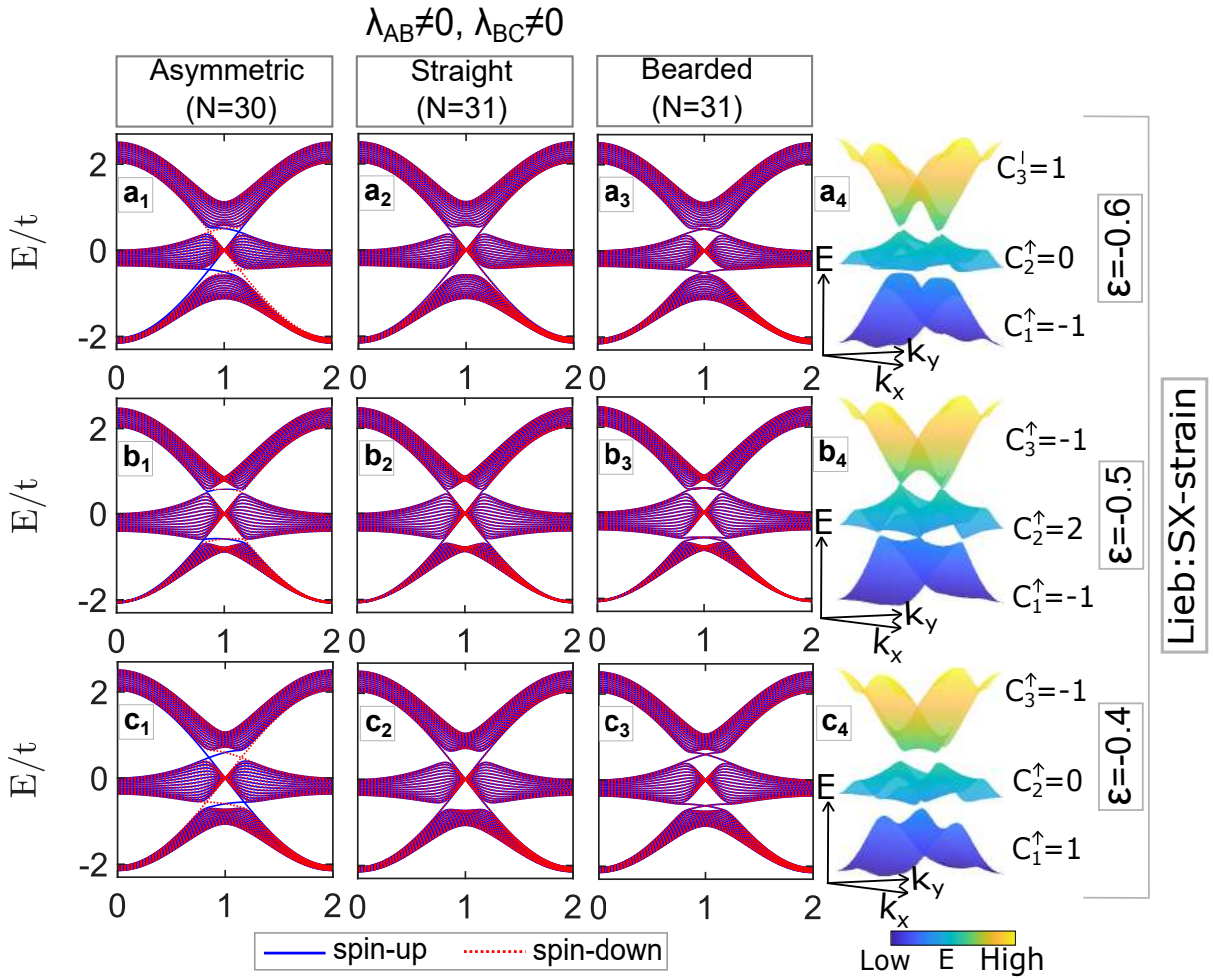

Source: The author.

discussed in Ch. 3, we identify the topological states by calculating both the spin Chern numbers and Berry curvature. By the bulk-edge correspondence, we expect that edge states emerge crossing the bulk gap regions, as definitively observed in the three types of edges. The edge states correspond to energy modes that completely traverse the gap in straight and bearded-edged nanoribbons. In the spectra of asymmetric-edged Lieb-Kagome nanoribbons, this occurs through anticrossing, as can be more clearly observed in Fig. 97, which presents an enlarged view of the energy spectra of asymmetric-edged nanoribbons shown in Figs. 92, 93, 94, 95, and 96, as well as in Fig. 102 for the cases shown in Figs. 98, 99, 100, and 101.

In all cases of TPT evaluated in Figs. 92, 93, 94, 95, and 96, as well as in Figs. 98, 99, 100, and 101, the considerations made in the previous section remain applicable here. Spin-up edge states become spin-down, and vice versa, when comparing before and after the change in the sign of the corresponding Chern number caused by a TPT. This indicates that the number of edge

Figure 94 – Energy spectra of nanoribbons for the cases presented in Fig. 68 (f-h). The subbands for spin-up (spin-down) charges are represented by solid blue lines (dashed red lines).

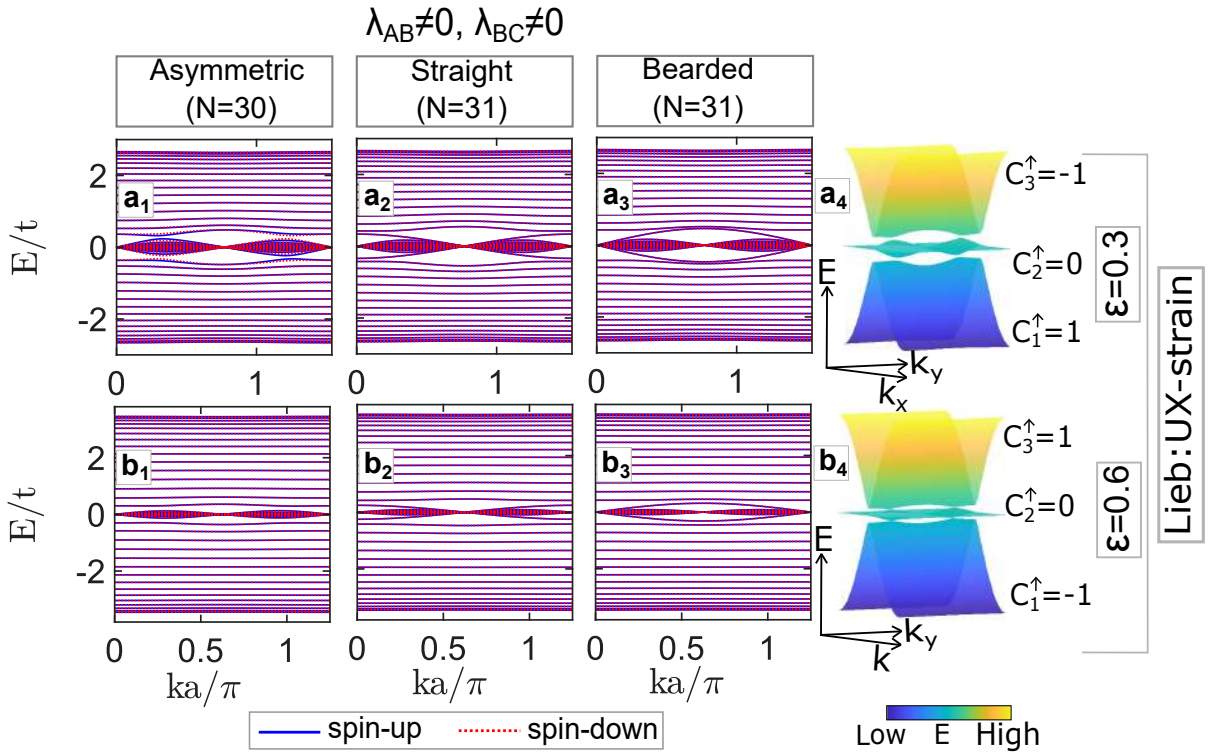

Source: The author.

state pairs is strain invariant and that the strains applied in Lieb-Kagome lattices can generate opposite spin currents, as pictorially exemplified in Fig. 103 for the classifications identified in this thesis: (i) $C^{\uparrow} = (1,0,-1)$ [Fig. 97 (a,e,h,i,k) and Fig. 102 (b,d-i)], (ii) $C^{\uparrow} = (-1,2,-1)$ [Fig. 97 (d,g) and Fig. 102 (a,c)], and (iii) $C^{\uparrow} = (-1,0,1)$ [Fig. 97 (b,c,f,j,l)].

Since the edge states are helical in bearded-edged nanoribbons, the spin-flip indicates that the modes corresponding to charges with spin-up [spin-down] and positive [negative] group velocity in a topological phase classified by $C^{\uparrow} = (1,0,-1)$, such as modes (1) [(2)] represented in Fig. 103 (c) with $E < 0$, due to a TPT that results in the topological phase with $C^{\uparrow} = (-1,2,-1)$, will transform into modes of charges with spin-down [spin-up] and positive [negative] group velocity, as modes (6) [(5)], respectively. Modes with $E > 0$ do not exhibit spin flip because this TPT does not affect the $2/3$ filling, i.e., the gap Δ_{23} does not close during this evaluated TPT. In other words, at $1/3$ filling, the edge states of charges with spin-up and spin-down reverse the direction of the group velocity on the edges of the asymmetric nanoribbon. When there is a TPT at $2/3$ filling, resulting in the phase $C^{\uparrow} = (-1,0,1)$, we observe spin flips in modes with $E > 0$. Some TPTs occur immediately from $\Delta C^{\uparrow} = (1,0,-1) - (-1,0,1) = (2,0,-2)$, in these cases all pairs of edge states exhibit spin flip, regardless of the energy interval.

Figure 95 – Energy spectra of nanoribbons for the cases presented in Fig. 68 (i-j). The subbands for spin-up (spin-down) charges are represented by solid blue lines (dashed red lines).

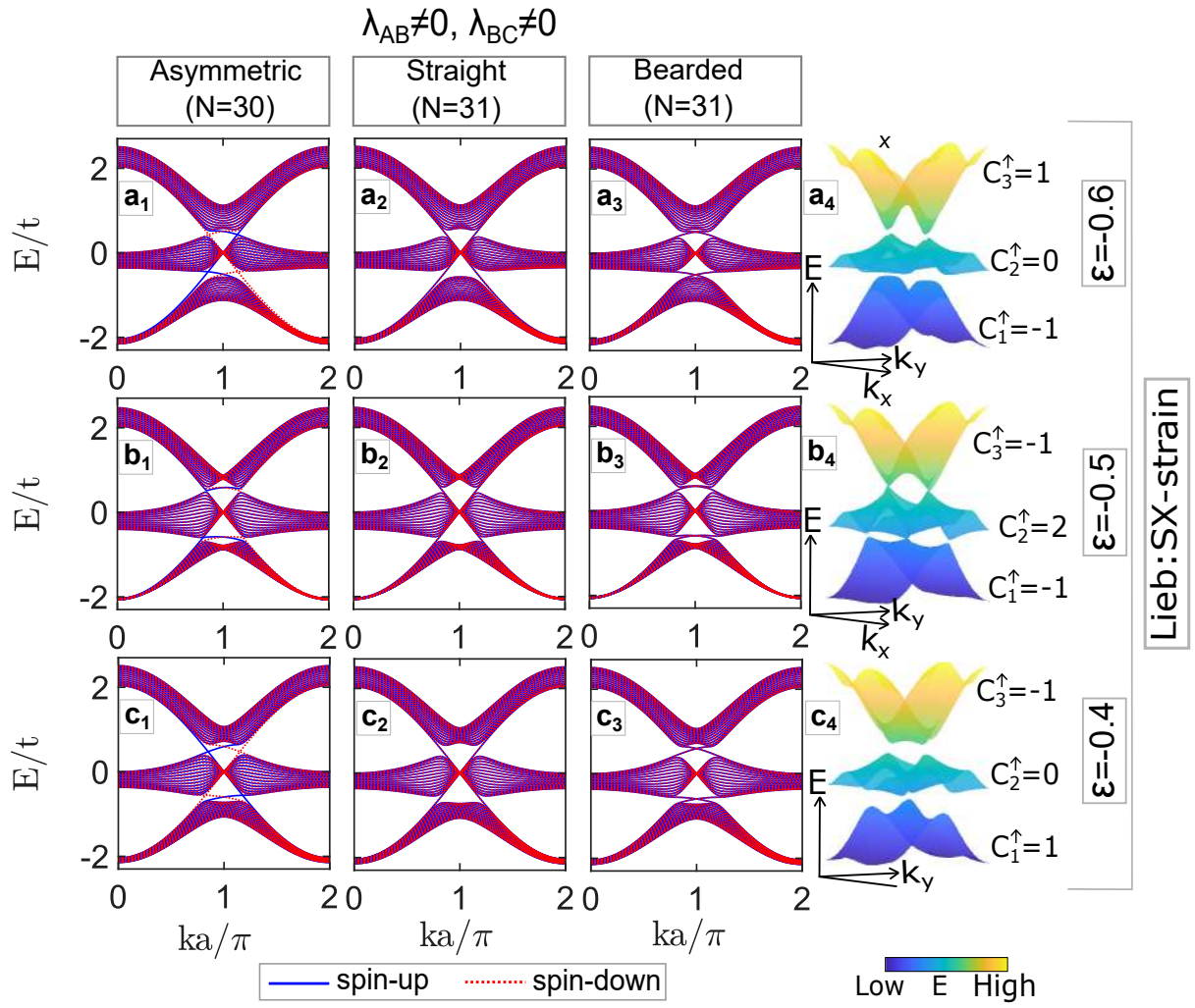

Source: The author.

Figure 96 – Energy spectra of nanoribbons for the cases presented in Fig. 68 (k-l). The subbands for spin-up (spin-down) charges are represented by solid blue lines (dashed red lines).

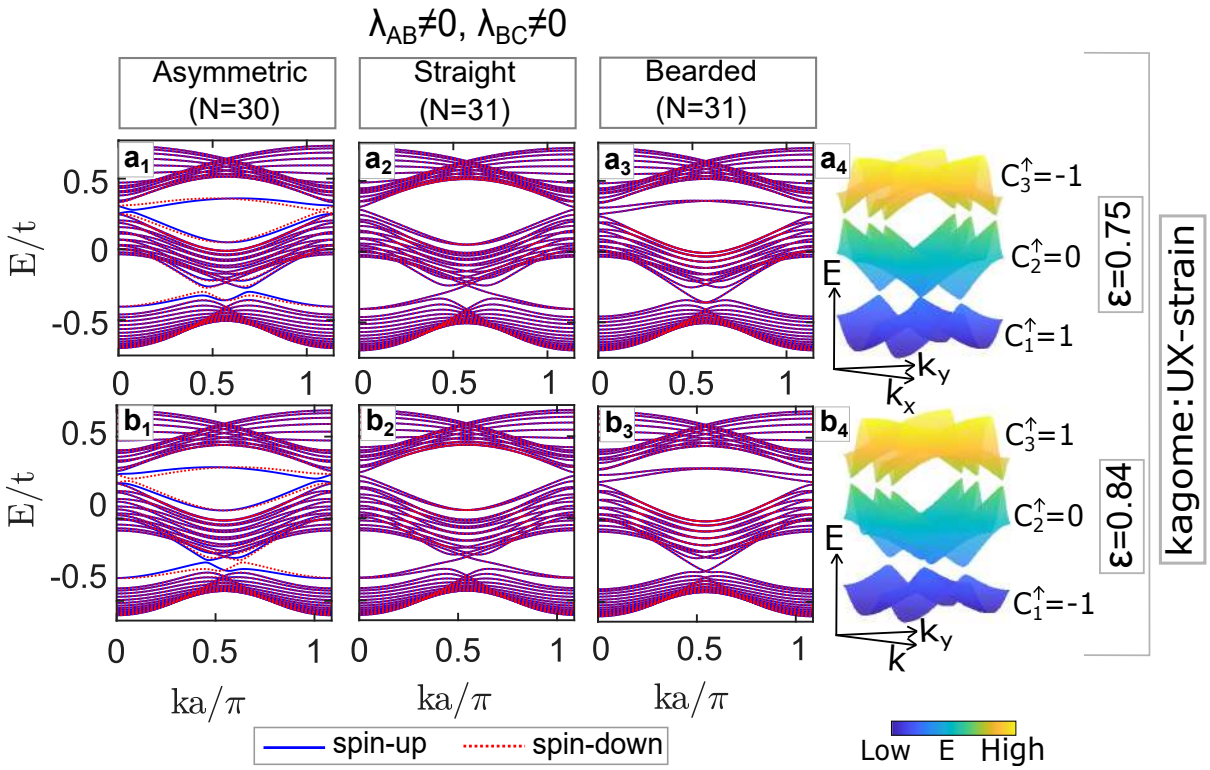

Source: The author.

Figure 97 – Enlarged region of the energy spectra of asymmetric-edged nanoribbons in Figs. 92, 93, 94, 95, and 96, highlighting the evolution of edge states. The subbands for spin-up (spin-down) charges are represented by solid blue lines (dashed red lines).

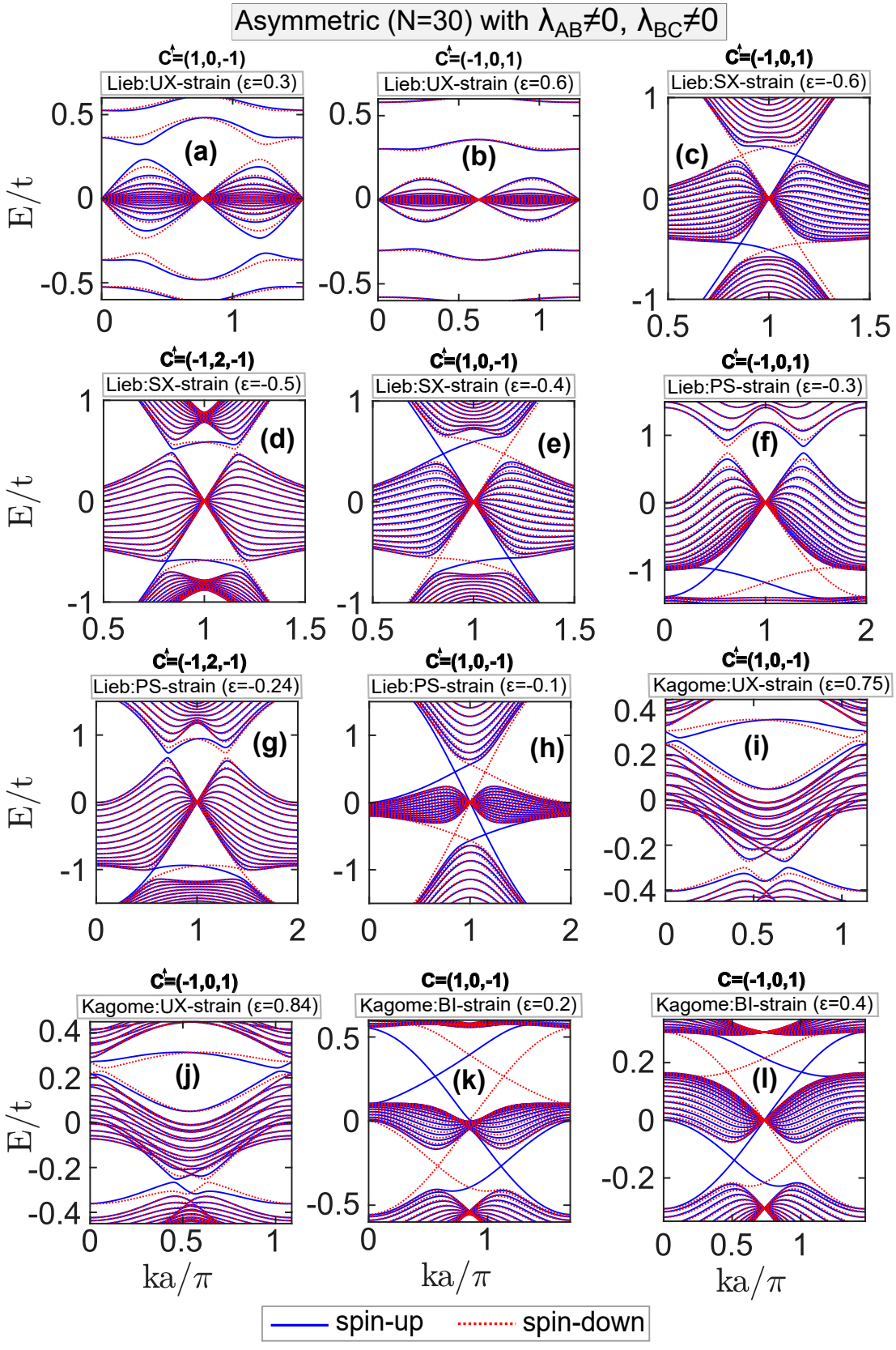

Source: The author.

Figure 98 – Energy spectra of nanoribbons for the cases presented in Fig. 76 (a-d). The subbands for spin-up (spin-down) charges are represented by solid blue lines (dashed red lines). Panels (e-i) with $C^{\uparrow} = (1, 0, -1)$ should be compared with the case of the unstrained Kagome lattice with $C^{\uparrow} = (-1, 2, -1)$ shown in Fig. 83 (i), with an enlarged region in Fig. 85 (g).

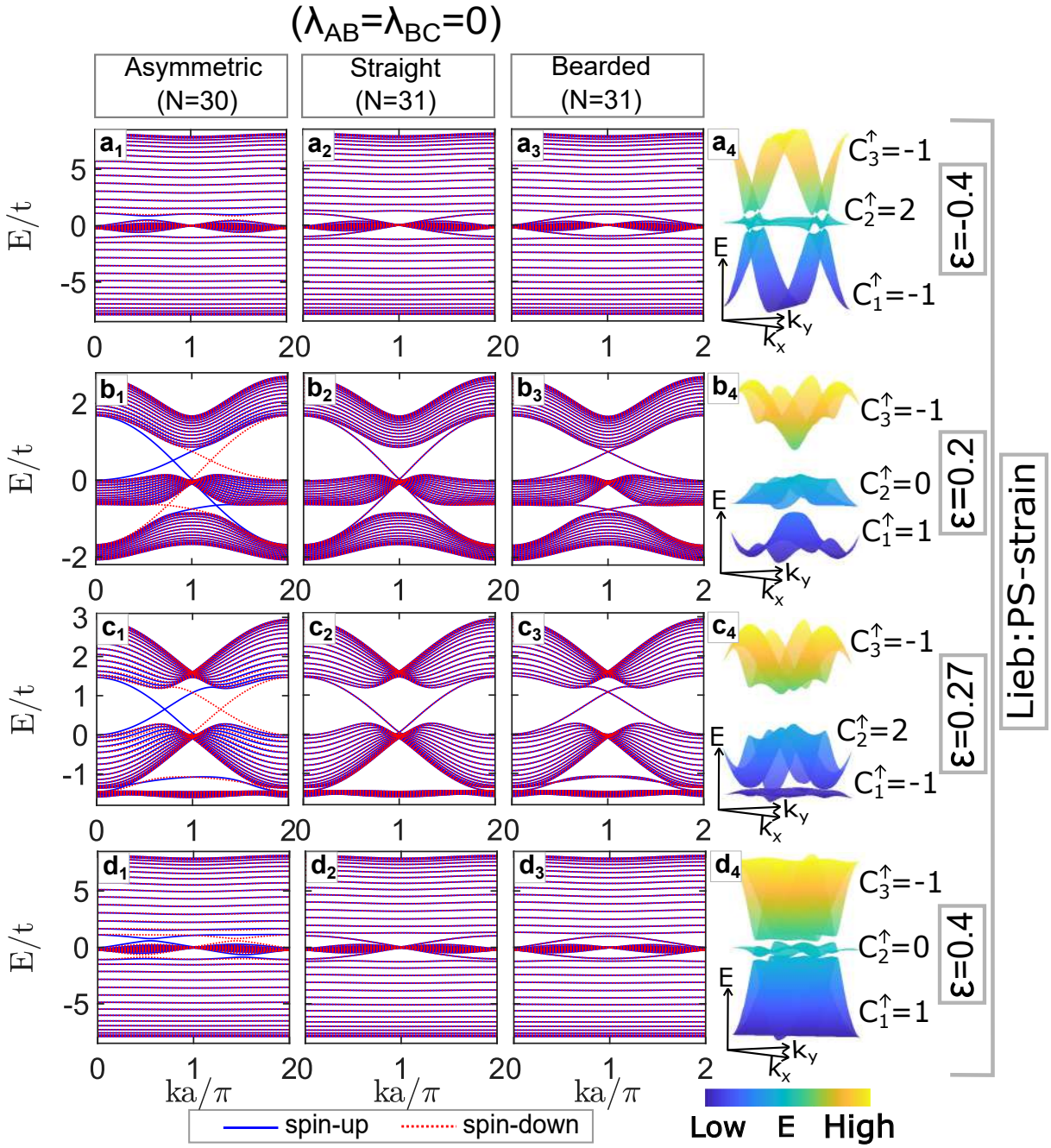

Source: The author.

Figure 99 – Energy spectra of nanoribbons for the cases presented in Fig. 76 (e-f). The subbands for spin-up (spin-down) charges are represented by solid blue lines (dashed red lines). Panels (e-i) with $C^{\uparrow} = (1,0,-1)$ should be compared with the case of the unstrained Kagome lattice with $C^{\uparrow} = (-1,2,-1)$ shown in Fig. 83 (i), with an enlarged region in Fig. 85 (g).

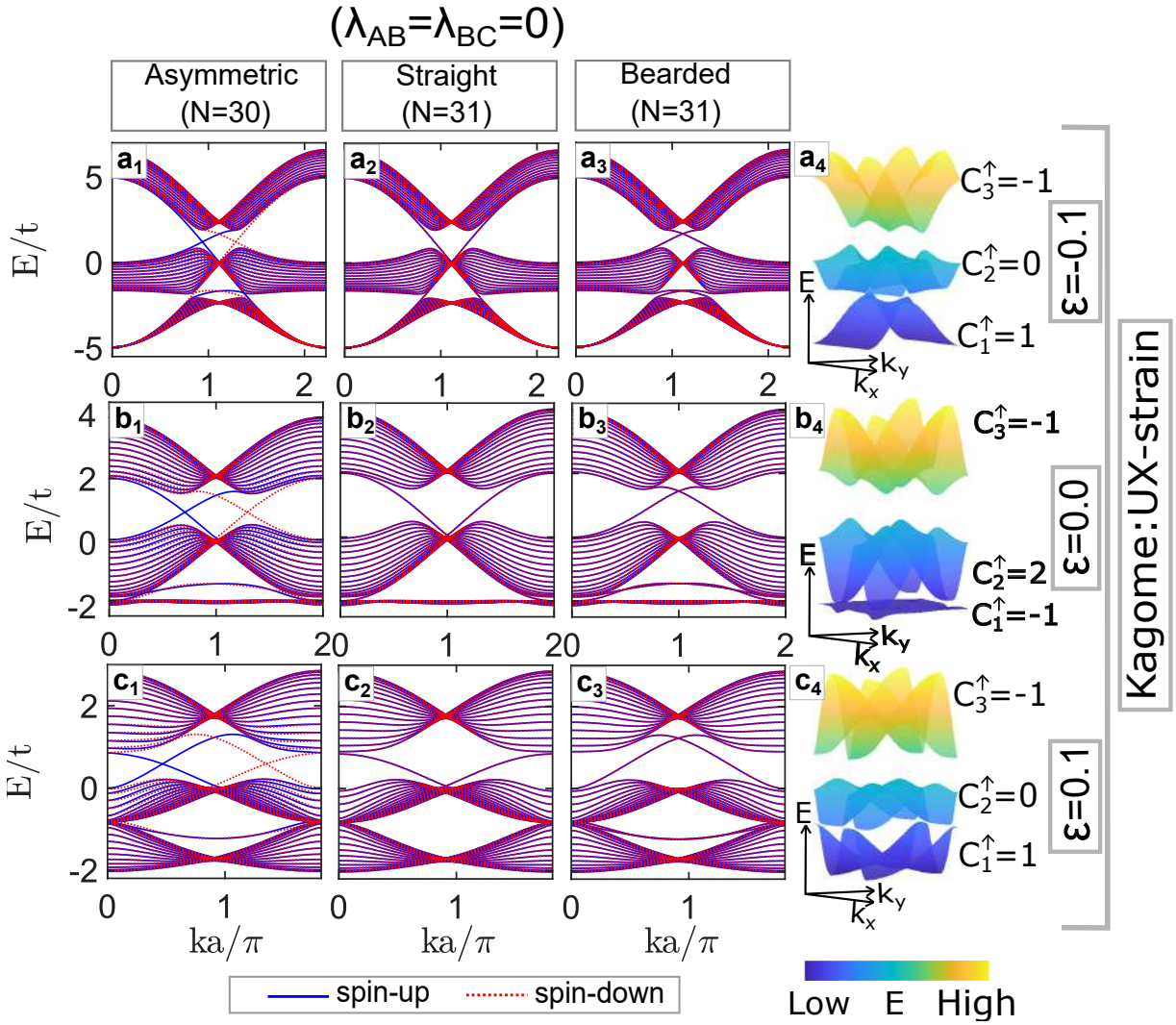

Source: The author.

Figure 100 – Energy spectra of nanoribbons for the cases presented in Fig. 76 (g). The subbands for spin-up (spin-down) charges are represented by solid blue lines (dashed red lines). Panels (e-i) with $C^{\uparrow} = (1,0,-1)$ should be compared with the case of the unstrained Kagome lattice with $C^{\uparrow} = (-1,2,-1)$ shown in Fig. 83 (i), with an enlarged region in Fig. 85 (g).

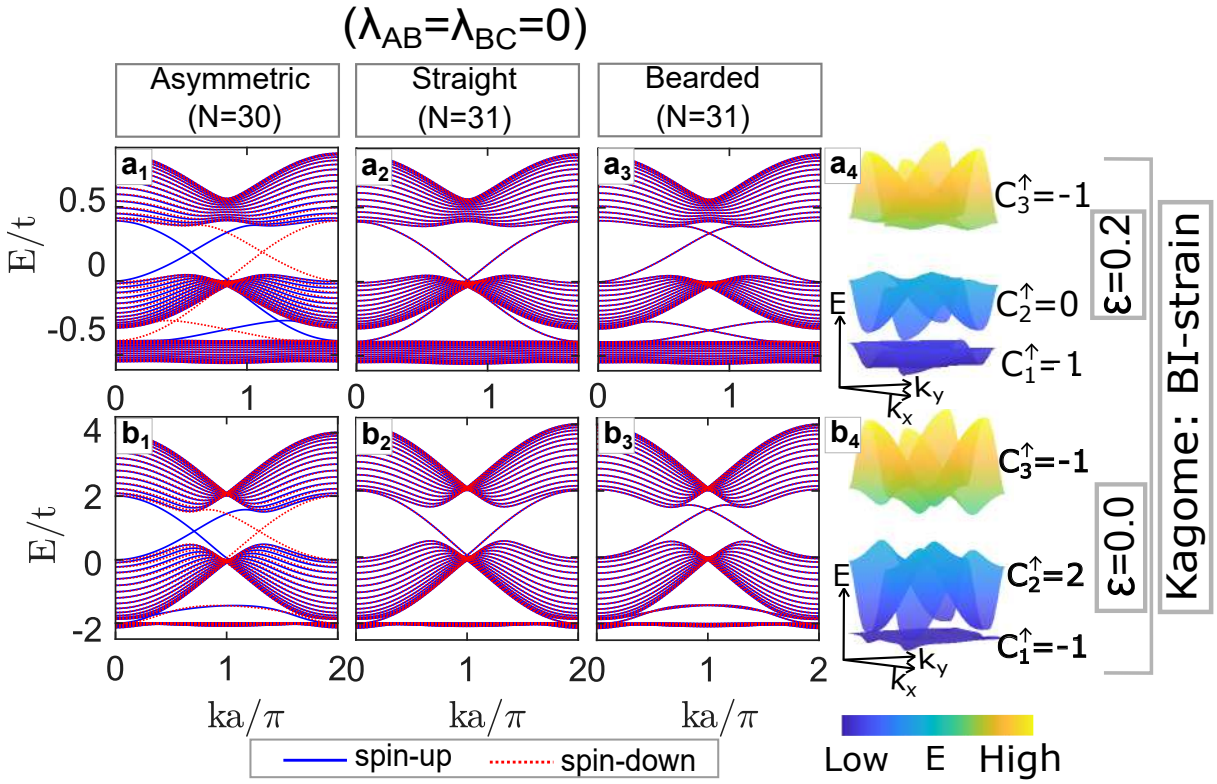

Source: The author.

Figure 101 – Energy spectra of nanoribbons for the cases presented in Fig. 76 (h-i). The subbands for spin-up (spin-down) charges are represented by solid blue lines (dashed red lines). Panels (e-i) with $C^{\uparrow} = (1,0,-1)$ should be compared with the case of the unstrained Kagome lattice with $C^{\uparrow} = (-1,2,-1)$ shown in Fig. 83 (i), with an enlarged region in Fig. 85 (g).

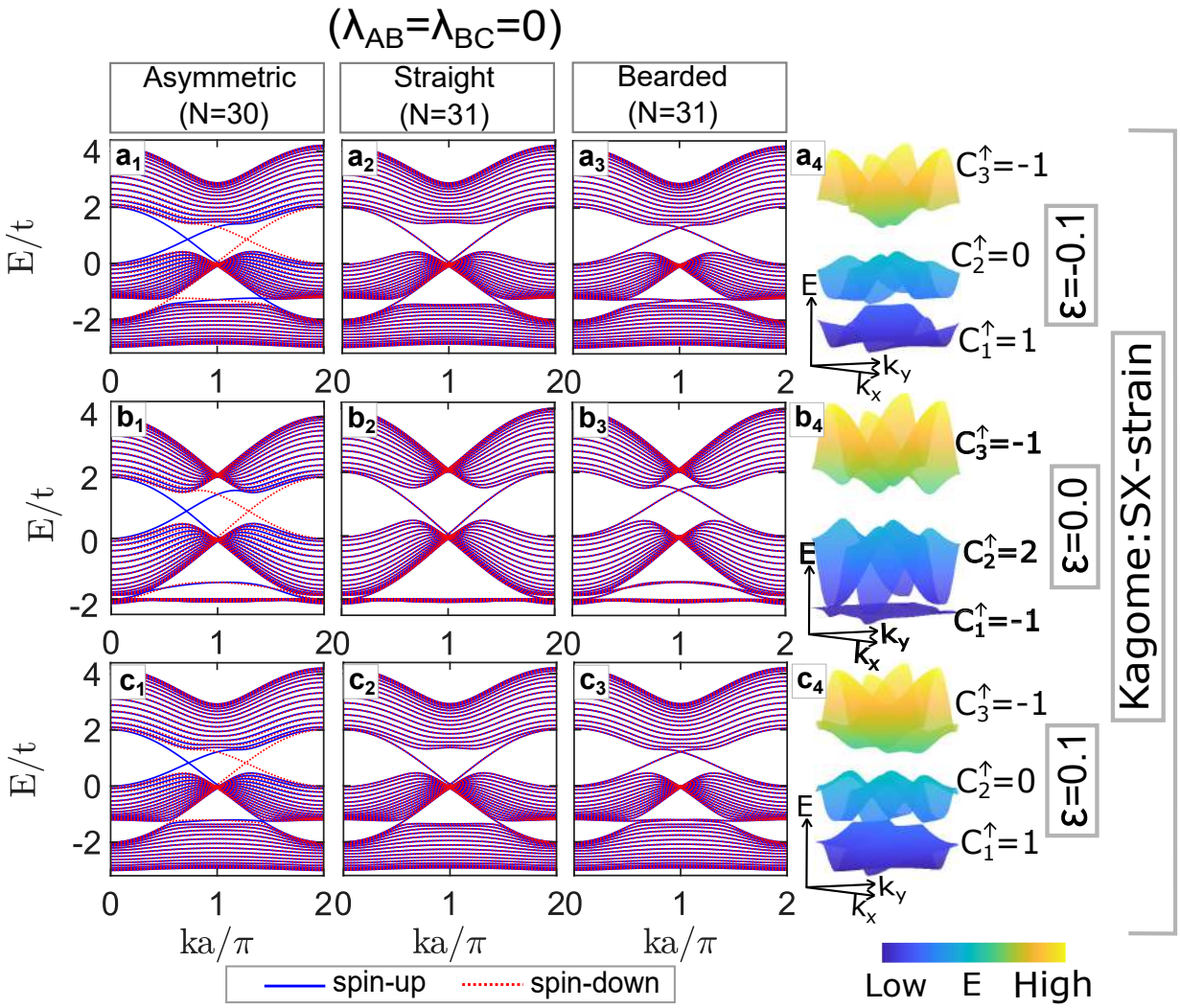

Source: The author.

Figure 102 – Enlarged region of the energy spectra of asymmetric-edged nanoribbons in Figs. 98, 99, 100, and 101, highlighting the evolution of edge states. The subbands for spin-up (spin-down) charges are represented by solid blue lines (dashed red lines).

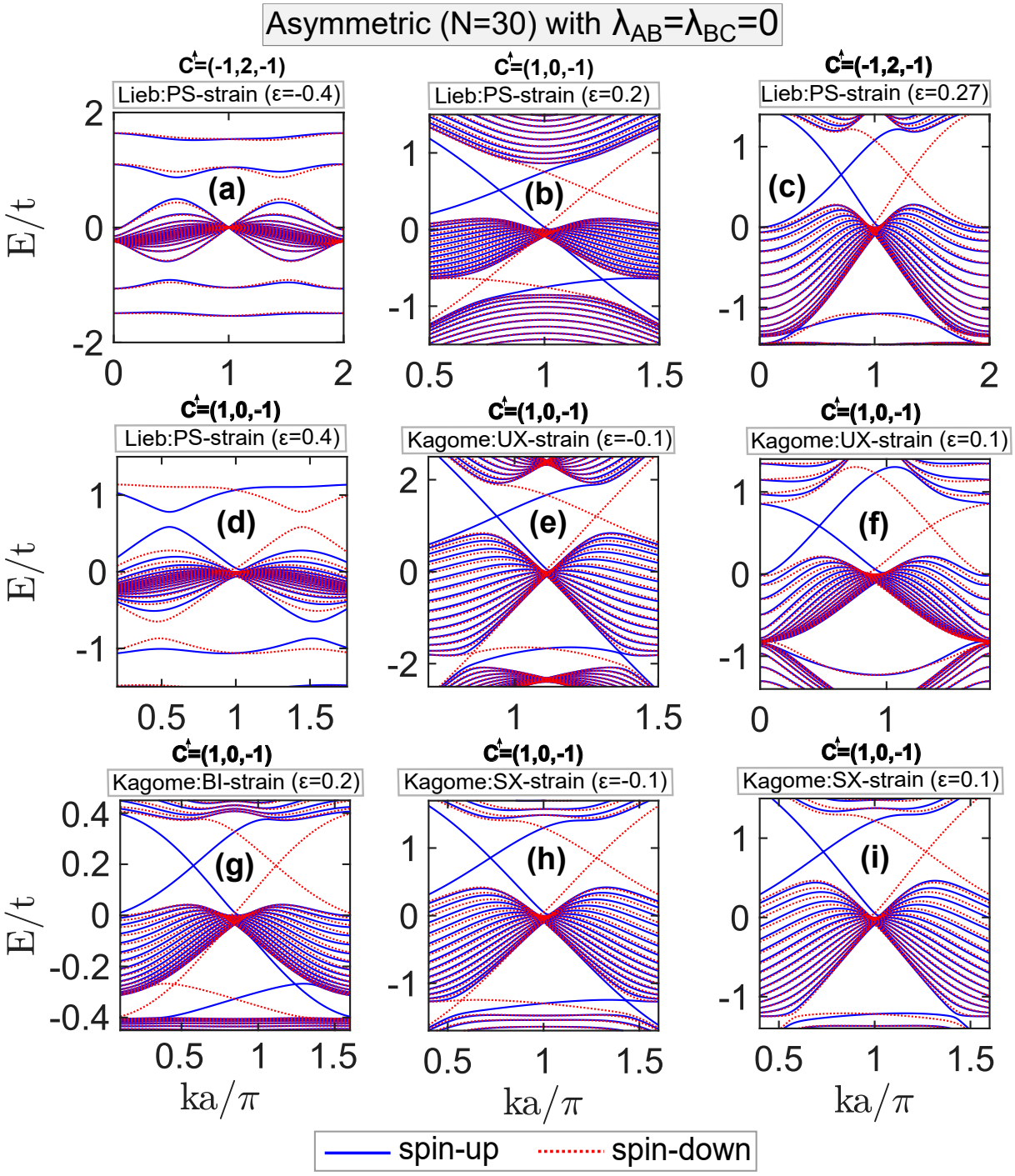

Source: The author.

Figure 103 – (a-b) Representation of the spin-flipping effect driven by strain in Lieb-Kagome nanoribbons with asymmetric edges for (a) $C^{\uparrow} = (1,0,-1)$ with $E > 0$ or $E < 0$ and $C^{\uparrow} = (-1,2,-1)$ with $E > 0$, (b) $C^{\uparrow} = (-1,0,1)$ with $E > 0$ or $E < 0$ and $C^{\uparrow} = (-1,2,-1)$ with $E < 0$. Red (blue) lines indicate the spin-up (spin-down) edge current directions. In (c-e) we highlight the states presented in the case of the SX-strained Lieb lattice shown in Fig. 97 (c-e).

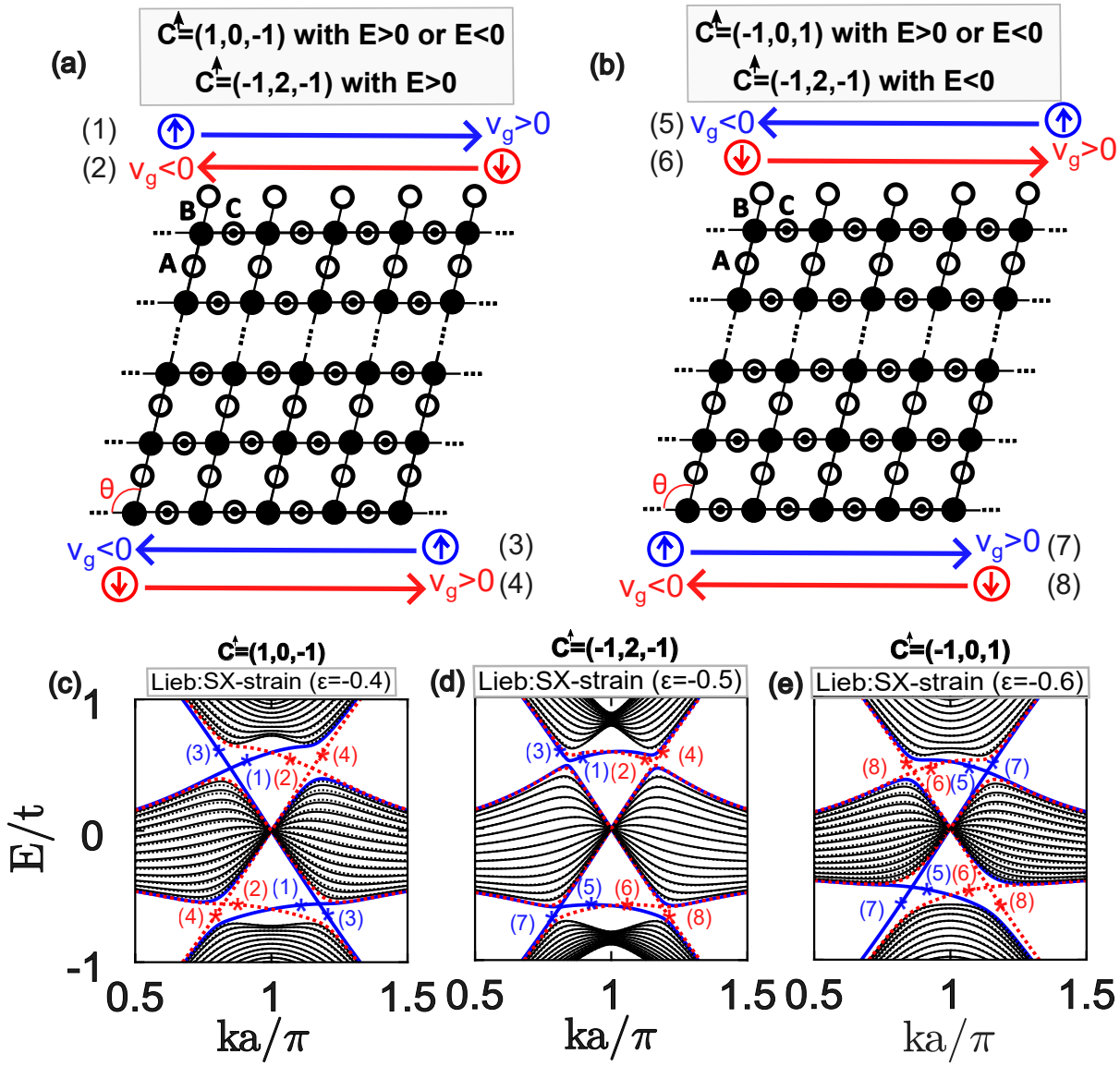

Source: The author.

4.7 Conclusions

Analyzing the finite effects in the energy spectrum of the Lieb, transition, and Kagome lattices, we identified that there are edge states that cross the gaps opened by the spin-orbit interaction between the bulk states in the energy spectrum of nanoribbons constructed from these lattices. In all cases, the Chern numbers of different energy bands for the unstrained Lieb, transition, and Kagome lattices are consistent with the number of quantized edge states.

We noticed that the edge states corresponding to nanoribbons with straight edges have a V-shape in the region of positive energies, while those corresponding to the bearded edges have a Λ-shape in the same region, and that the junction of these two types of edge states approximately results in the edge states of nanoribbons with asymmetric edges, as expected, except in some cases where, instead of crossing the modes, they exhibit anticrossing.

In the TPT processes driven by strain, when the sign of the spin Chern numbers per band changes, curiously, we identified that the spin-up edge states become spin-down, and vice versa. Thus, we found that the strain can cause spin-flip (spin inversion), i.e., the sign of the spin depends on the strain strength in the Lieb, transition, and Kagome lattices. We intend to theoretically investigate some possible devices that benefit from this strain-driven spin-flipping effect since deformations can generate opposite spin currents under strains that cause TPT, such as stretching and compressive strain.

5 FINAL REMARKS AND PERSPECTIVES

In this thesis, we have conducted a systematic study on the effects of various strains on the electronic properties of Lieb-Kagome lattices. After an introduction in Ch. 1, in Ch. 2, we systematically study the effects of strain on Lieb-Kagome lattices without ISO coupling. In Ch. 3, we integrate the ISO coupling into the model to investigate the strain-induced TPT, presenting the effects of these TPT on the evolution of edge states in straight, bearded, and asymmetric-edged nanoribbons in Ch. 4.

Specifically, in Ch. 2, we systematically study the effects of shear and uniaxial strains, applied along different crystallographic directions and also jointly applied, generating the pure shear and biaxial strains, on the electronic properties of Lieb and Kagome lattices. For this, we use the TB method within a general Hamiltonian description by assuming a generic lattice with just one control parameter, which, in turn, allows us to map both Lieb and Kagome lattices, as well as to verify the evolution of their electronic properties. Previous studies investigated the stability of the nearly-flat band and band-touching points due to breathing anisotropy in the Kagome lattice, the site disorder on the Kagome lattice, and the dispersion relations of strained and complex Lieb lattices. In a more general way, our theoretical framework extends these previous studies reported in the literature that treated separately the deformed Lieb or Kagome lattices. Our findings showed some effects analogous to those observed for strained graphene, such as: (i) the presence of anisotropic Fermi velocity, (ii) the approach or separation of the Dirac cones, and (iii) the existence of strain-induced pseudovector potentials for some types of strain. Opposite to graphene, we observed that none of the six types of the investigated strains applied in the Lieb and Kagome lattices are able to open an energy gap in their energy spectra. Instead, in general terms, we identified effects such as the deformation of the nearly-flat bands, division of the triple degenerate Dirac point into two doubly degenerated Dirac points (in the Lieb lattice), as well as the appearance of non-null vector pseudopotential terms in some types of strain.

Additionally, in Ch. 3, we use the TB method within a general Hamiltonian description with ISO coupling, assuming again a strained generic lattice with just one control parameter. Previous studies have investigated TPT in Lieb and Kagome lattices, but did not employ a versatile generic TB model to study transition lattices, and primarily focused on uniaxial or biaxial strains without exploring the full range of strain types that we have incorporated into our model. More generally, our theoretical framework extends these previous studies reported

in the literature that treated separately the deformed Lieb or Kagome lattices, using interconvertibility as a methodological resource to investigate the topological evolution of the Lieb, transition, and Kagome lattices with ISO coupling under uniaxial and shear strains along various crystallographic directions. We find (i) TPT that connect topological insulating phases with different Spin Chern Numbers, where the system behaves as a quantum spin Hall insulator, (ii) a non-topological phase transition into a semimetallic regime at $1/3$ filling, characterized by partially filled bands and non-quantized spin Hall conductivity, while at $2/3$ filling, the system behaves as an insulator, with the spin Hall conductivity carried by the helical edge states becoming experimentally observable, and (iii) transitions to a metallic phase with zero gaps, inhibiting any spin Hall conductivity. Additionally, we interestingly identify TPT due to the process of interconvertibility, and note that the TPT driven by strain do not occur in the case of hypothetical strains, showing that they are primarily driven by changes in the Hamiltonian parameters rather than due to the change in the distances between the lattice sites.

Furthermore, in Ch. 4, we present a theoretical study on the impact of ISO coupling and mechanical strain on the topological properties of nanoribbons constructed from Lieb, Kagome, and transition lattices. Our analysis of the energy spectrum and DOS for nanoribbons with different edge configurations—straight, bearded, and asymmetric—has led to several important findings: (i) The combination of ISO coupling and applied strains along different crystallographic directions can induce TPT, fundamentally altering the dynamics of the edge states and potentially leading to the generation of opposite spin currents. (ii) The edge states in these strained nanoribbons show unique characteristics; straight edges exhibit a V-shaped energy profile, while bearded edges display a Λ-shape in the region of positive energies. Moreover, (iii) our investigations have highlighted how strain-induced modifications in the spin Chern numbers correlate with a switch in the spin orientation of the edge states, leading to intriguing possibilities for spintronic applications.

We believe that such a systematic study pertinent to the effects of different types of strains applied in 2D lattices with the coexistence of nearly-flat and conical bands is very interesting for understanding the defects' effects on the optoelectronic properties of nearly-flat band 2D systems. Moreover, the general theoretical framework presented in this manuscript allows for the investigation of the evolution stages between Lieb and Kagome lattices and the consequences on their physical properties by means of just one control parameter. This research underscores the ability of strain engineering to fine-tune electrical and optical properties, offering

new avenues for controlling band gap tunability and band deformations. Such advancements are pivotal for the future of 2D lattice-based device technologies, marking a significant contribution to both the fundamental understanding and practical applications of these materials in nanoscale electronics and photonics. We propose further theoretical exploration into devices that could exploit this strain-driven spin flipping effect, which holds significant promise for future technologies harnessing topological properties under mechanical strain.

As an immediate perspective already underway, we will investigate the evolution of wave functions across the nanoribbon. This line of inquiry aims to deepen our understanding of the interplay between strain, topology, and electronic properties at the boundaries of these materials, potentially revealing new phenomena relevant to nanoscale device engineering. Additionally, we will promptly extend our systematic study to other materials that exhibit nearly-flat bands in their energy spectra, such as α-τ_3 lattices. Both research perspectives are already in the early stages of development.

BIBLIOGRAPHY

ABLOWITZ, M. J.; COLE, J. T. Topological insulators in longitudinally driven waveguides: Lieb and kagome lattices. **Physical Review A**, American Physical Society, v. 99, p. 033821, Mar 2019.

AGAPITO, L. A.; KIOUSSIS, N.; III, W. A. G.; ONG, N. P. Novel family of chiral-based topological insulators: Elemental tellurium under strain. **Physical Review Letters**, APS, v. 110, n. 17, p. 176401, 2013.

AGARWALA, A.; SHENOY, V. B. Topological insulators in amorphous systems. **Physical Review Letters**, v. 118, n. 23, p. 236402, 2017.

ALEM, N.; ERNI, R.; KISIELOWSKI, C.; ROSSELL, M. D.; GANNETT, W.; ZETTL, A. Atomically thin hexagonal boron nitride probed by ultrahigh-resolution transmission electron microscopy. **Physical Review B**, American Physical Society, v. 80, n. 15, p. 155425, 2009.

ARAÚJO, A. d. L. **Isolantes topológicos protegidos por simetria cristalina**. Tese (Doutorado) – Universidade Federal de Uberlândia, 2018.

ASCROFT, N. W.; MERMIM, N. D. **Solid State Physics**. Philadelphia: Holt-Saunders, 1976.

BALLENTINE, L. E. **Quantum mechanics**: a modern development. [*S. l.*]: World Scientific Publishing Company, 2014.

BANDEIRA, N. S.; COSTA, D. R. da; CHAVES, A.; FARIAS, G. A.; COSTA FILHO, R. N. Gap opening in graphene nanoribbons by application of simple shear strain and in-plane electric field. **Journal of Physics**: Condensed Matter, IOP Publishing, v. 33, n. 6, p. 065503, 2020.

BANDRES, M. A.; RECHTSMAN, M. C.; SZAMEIT, A.; SEGEV, M. Lieb photonic topological insulator. **Conference on Lasers and Electro-Optics**: Laser Science to Photonic Applications, p. 1–2, 2014.

BANSIL, A.; LIN, H.; DAS, T. Colloquium: Topological band theory. **Reviews of Modern Physics**, American Physical Society, v. 88, p. 021004, Jun 2016.

BATTILOMO, R.; SCOPIGNO, N.; ORTIX, C. Berry curvature dipole in strained graphene: a fermi surface warping effect. **Physical Review Letters**, APS, v. 123, n. 19, p. 196403, 2019.

BERCIOUX, S. O. D. Solid-state platforms. **Nature Physics**, Nature Publishing Group, v. 13, 2017.

BERNEVIG, B. A. **Topological insulators and topological superconductors**. [*S. l.*]: Princeton university press, 2013.

BERRY, M. V. Quantal phase factors accompanying adiabatic changes. **Proceedings of the Royal Society of London. A. Mathematical and Physical Sciences**, The Royal Society London, v. 392, n. 1802, p. 45–57, 1984.

BEUGELING, W.; EVERTS, J.; SMITH, C. M. Topological phase transitions driven by next-nearest-neighbor hopping in two-dimensional lattices. **Physical Review B**, APS, v. 86, n. 19, p. 195129, 2012.

BHATTARAI, R.; MINCH, P.; LIANG, Y.; ZHANG, S.; RHONE, T. D. Strain-induced topological phase transition in ferromagnetic janus monolayer $MnSbBiS_2Te_2$. **Physical Chemistry Chemical Physics**, Royal Society of Chemistry, v. 26, n. 13, p. 10111–10119, 2024.

BILITEWSKI, T.; MOESSNER, R. Disordered flat bands on the kagome lattice. **Physical Review B**, American Physical Society, v. 98, p. 235109, Dec 2018.

BINH, T. V.; BO, N. D.; SON, N. H.; TIEN, T. M. Interplay between the spin-orbit coupling and lattice modulation on the lieb lattice. **Journal of Physics**: Conference Series, v. 1274, n. 1, p. 012001, 2019.

BLAKSLEE, O.; PROCTOR, D.; SELDIN, E.; SPENCE, G.; WENG, T. Elastic constants of compression-annealed pyrolytic graphite. **Journal of applied physics**, American Institute of Physics, v. 41, n. 8, p. 3373–3382, 1970.

BLOCK, M. S.; D'EMIDIO, J.; KAUL, R. K. Kagome model for a Z_2 quantum spin liquid. **Physical Review B**, APS, v. 101, n. 2, p. 020402, 2020.

BOCQUILLON, E.; DEACON, R. S.; WIEDENMANN, J.; LEUBNER, P.; KLAPWIJK, T. M.; BRÜNE, C.; ISHIBASHI, K.; BUHMANN, H.; MOLENKAMP, L. W. Gapless andreev bound states in the quantum spin hall insulator hgte. **Nature Nanotechnology**, v. 12, p. 137–143, 2017.

BOLENS, A.; NAGAOSA, N. Topological states on the breathing kagome lattice. **Physical Review B**, APS, v. 99, n. 16, p. 165141, 2019.

BROEKE, J. J. van den; SWART, I.; SMITH, C. M.; VANMAEKELBERGH, D. Effective spin-orbit gaps in the s and p orbital bands of an artificial honeycomb lattice. **Physical Review Materials**, APS, v. 5, n. 11, p. 116001, 2021.

CASTRO NETO, A.; GUINEA, F.; PERES, N. M.; NOVOSELOV, K. S.; GEIM, A. K. The electronic properties of graphene. **Reviews of modern physics**, American Physical Society, v. 81, n. 1, p. 109, 2009.

CHANG, A. M. Chiral luttinger liquids at the fractional quantum hall edge. **Reviews of Modern Physics**, v. 75, p. 1449–1505, 2003.

CHANG, C.-Z.; ZHANG, J.; FENG, X.; SHEN, J.; ZHANG, Z.; GUO, M.; LI, K.; OU, Y.; WEI, P.; WANG, L.-L.; JI, Z.-Q.; FENG, Y.; JI, S.; CHEN, X.; JIA, J.; DAI, X.; FANG, Z.; ZHANG, S.-C.; HE, K.; WANG, Y.; LU, L.; MA, X.-C.; XUE, Q.-K. Experimental observation of the quantum anomalous hall effect in a magnetic topological insulator. **Science**, American Association for the Advancement of Science, v. 340, p. 167–170, 2013.

CHEN, H.; ZHOU, P.; LIU, J.; QIAO, J.; OEZYILMAZ, B.; MARTIN, J. Gate controlled valley polarizer in bilayer graphene. **Nature Communications**, v. 11, p. 1202, 2020.

CHEN, R.; ZHOU, B. Finite size effects on the helical edge states on the lieb lattice. **Chinese Physics B**, IOP Publishing, v. 25, n. 6, p. 067204, 2016.

CHEN, R.; ZHOU, B. Spin chern number and topological phase transition on the lieb lattice with spin–orbit coupling. **Physics Letters A**, Elsevier, v. 381, n. 10, p. 944–948, 2017.

CHRISTIAN, J. W. **The Theory of Transformations in Metals and Alloys**. 3rd. ed. [*S. l.*]: Pergamon, 2002.

COCCO, G.; CADELANO, E.; COLOMBO, L. Gap opening in graphene by shear strain. **Physical Review B**, American Physical Society, v. 81, p. 241412, Jun 2010.

CUI, B.; ZHENG, X.; WANG, J.; LIU, D.; XIE, S.; HUANG, B. Realization of lieb lattice in covalent-organic frameworks with tunable topology and magnetism. **Nature Communications**, v. 11, p. 66, 12 2020.

CUI, M.; HE, Z.; TANG, Y.; QIU, C. Crystal growth and magnetic properties of a kagome compound $Cs_2NaMn_3F_{12}$. **Journal of Crystal Growth**, v. 475, p. 256 – 260, 2017.

DÁVILA, M.; XIAN, L.; CAHANGIROV, S.; RUBIO, A.; LAY, G. L. Germanene: a novel two-dimensional germanium allotrope akin to graphene and silicene. **New Journal of Physics**, IOP Publishing, v. 16, n. 9, p. 095002, 2014.

DEAN, C. R.; YOUNG, A. F.; MERIC, I.; LEE, C.; WANG, L.; SORGENFREI, S.; WATANABE, K.; TANIGUCHI, T.; KIM, P.; SHEPARD, K. L.; HONE, J. Boron nitride substrates for high-quality graphene electronics. **Nature Nanotechnology**, Nature Publishing Group, v. 5, n. 10, p. 722–726, 2010.

DENG, L.; GOOCH, M.; LIU, H.; SALKE, N. P.; BONTKE, T.; SHAO, S.; YOU, J.; SCHULZE, D. J.; KUMAR, R.; YIN, J.-X.; SHI, Y.; HEMLEY, R. J.; FENG, Y.; CHANG, G.; SI, Q.; CHU, C.-W. Effect of fermi surface topology change on the kagome superconductor CeRu2 under pressure. **Materials Today Physics**, Elsevier, v. 40, p. 101322, 2024.

DENG, Y.; YU, Y.; SHI, M. Z.; GUO, Z.; XU, Z.; WANG, J.; CHEN, X. H.; ZHANG, Y. Quantum anomalous hall effect in intrinsic magnetic topological insulator $MnBi_2Te_4$. **Science**, American Association for the Advancement of Science, v. 367, p. 895–900, 2020.

DEPENBROCK, S.; MCCULLOCH, I. P.; SCHOLLWÖCK, U. Nature of the spin-liquid ground state of the $s = 1/2$ heisenberg model on the kagome lattice. **Physical Review Letters**, American Physical Society, v. 109, p. 067201, Aug 2012.

DEY, M.; MAITI, S. K.; KARMAKAR, S. Magnetic field induced metal-insulator transition in a kagome nanoribbon. **Journal of Applied Physics**, American Institute of Physics, v. 110, n. 9, p. 094306, 2011.

DIEBEL, F.; LEYKAM, D.; KROESEN, S.; DENZ, C.; DESYATNIKOV, A. S. Conical diffraction and composite lieb bosons in photonic lattices. **Physical Review Letters**, APS, v. 116, n. 18, p. 183902, 2016.

DOWNIE, L.; ARDASHNIKOVA, E.; TANG, C.; VASILIEV, A.; BERDONOSOV, P.; DOLGIKH, V.; VRIES, M.; LIGHTFOOT, P. Novel s = 1/2 kagome lattice materials: $Cs_2TiCu_3F_{12}$ and $Rb_2TiCu_3F_{12}$. **Crystals**, v. 5, p. 226, 05 2015.

DROST, R.; OJANEN, T.; HARJU, A.; LILJEROTH, P. Topological states in engineered atomic lattices. **Nature Physics**, Nature Publishing Group UK London, v. 13, n. 7, p. 668–671, 2017.

DU, L.; KNEZ, I.; SULLIVAN, G.; DU, R. R. Robust helical edge transport in gated InAs/GaSb bilayers. **Physical Review Letters**, v. 114, p. 096802, 2015.

ESCHRIG, H. **Topology and geometry for physics**. [*S. l.*]: Springer Science & Business Media, 2011. v. 822.

ESSAFI, K.; JAUBERT, L. D. C.; UDAGAWA, M. Flat bands and dirac cones in breathing lattices. **Journal of Physics**: Condensed Matter, IOP Publishing, v. 29, n. 31, p. 315802, jun 2017.

FEI, Z. Y.; PALOMAKI, T.; WU, S.; ZHAO, W.; CAI, X.; SUN, B.; NGUYEN, P.; FINNEY, J.; XU, X.; COBDEN, D. H. Edge conduction in monolayer WTe_2. **Nature Physics**, v. 13, p. 677–682, 2017.

FRADKIN, E. **Field Theories of Condensed Matter Physics**. 2nd. ed. [*S. l.*]: Cambridge University Press, 2013.

FRANKEL, T. **The geometry of physics**: An introduction. [*S. l.*]: Cambridge University Press, 2011.

FRUCHART, M.; CARPENTIER, D. An introduction to topological insulators. **Comptes Rendus Physique**, Elsevier, v. 14, n. 9-10, p. 779–815, 2013.

FU, L.; KANE, C. L. Topological insulators with inversion symmetry. **Physical Review B**, APS, v. 76, n. 4, p. 045302, 2007.

FUKUI, T.; HATSUGAI, Y. Topological aspects of the quantum spin-hall effect in graphene: Z_2 topological order and spin chern number. **Physical Review B**, APS, v. 75, n. 12, p. 121403, 2007.

FUKUI, T.; HATSUGAI, Y.; SUZUKI, H. Chern numbers in discretized brillouin zone: Efficient method of computing (spin) hall conductances. **Journal of the Physical Society of Japan**, The Physical Society of Japan, v. 74, n. 6, p. 1674–1677, 2005.

GAIL, R. D.; FUCHS, J.-N.; GOERBIG, M.; PIÉCHON, F.; MONTAMBAUX, G. Manipulation of dirac points in graphene-like crystals. **Physica B**: Condensed Matter, Elsevier, v. 407, n. 11, p. 1948–1952, 2012.

GARDENIER, T. S.; BROEKE, J. J. V. D.; MOES, J. R.; SWART, I.; DELERUE, C.; SLOT, M. R.; SMITH, C. M.; VANMAEKELBERGH, D. p orbital flat band and dirac cone in the electronic honeycomb lattice. **ACS Nano**, ACS Publications, v. 14, n. 10, p. 13638–13644, 2020.

GOLDENFELD, N. **Lectures on Phase Transitions and the Renormalization Group**. [*S. l.*]: Addison-Wesley, 1992.

GOLDMAN, N.; URBAN, D.; BERCIOUX, D. Topological phases for fermionic cold atoms on the lieb lattice. **Physical Review A**, APS, v. 83, n. 6, p. 063601, 2011.

GOLDMAN, N.; URBAN, D. F.; BERCIOUX, D. Topological phases for fermionic cold atoms on the lieb lattice. **Physical Review A**, v. 83, p. 063601, 2011.

GRAF, G. M.; PORTA, M. Bulk-edge correspondence for two-dimensional topological insulators. **Communications in Mathematical Physics**, Springer, v. 324, p. 851–895, 2013.

GUO, H. M.; FRANZ, M. Topological insulator on the kagome lattice. **Physical Review B**, v. 80, p. 113102, 2009.

GUZMÁN-SILVA, D.; MEJÍA-CORTÉS, C.; BANDRES, M.; RECHTSMAN, M.; WEIMANN, S.; NOLTE, S.; SEGEV, M.; SZAMEIT, A.; VICENCIO, R. Experimental observation of bulk and edge transport in photonic lieb lattices. **New Journal of Physics**, IOP Publishing, v. 16, n. 6, p. 063061, 2014.

HALDANE, F. D. M. Nonlinear field theory of large-spin heisenberg antiferromagnets: Semiclassically quantized solitons of the one-dimensional easy-axis néel state. **Physical Review Letters**, APS, v. 50, n. 15, p. 1153, 1983.

HALDANE, F. D. M. Model for a quantum hall effect without landau levels: Condensed-matter realization of the "parity anomaly". **Physical Review Letters**, APS, v. 61, n. 18, p. 2015, 1988.

HAN, T.-H.; HELTON, J. S.; CHU, S.; NOCERA, D. G.; RODRIGUEZ-RIVERA, J. A.; BROHOLM, C.; LEE, Y. S. Fractionalized excitations in the spin-liquid state of a kagome-lattice antiferromagnet. **Nature**, Nature Publishing Group, v. 492, n. 7429, p. 406–410, 2012.

HART, S.; REN, H.; WAGNER, T.; LEUBNER, P.; MÜHLBAUER, M.; BRÜNE, C.; BUHMANN, H.; MOLENKAMP, L. W.; YACOBY, A. Induced superconductivity in the quantum spin hall edge. **Nature Physics**, v. 10, p. 638–643, 2014.

HASAN, M. Z.; KANE, C. L. Colloquium: Topological insulators. **Reviews of Modern Physics**, American Physical Society, v. 82, p. 3045–3067, Nov 2010.

HATSUGAI, Y. Chern number and edge states in the integer quantum hall effect. **Physical Review Letters**, American Physical Society, v. 71, p. 3697–3700, Nov 1993.

HOR, Y.; RICHARDELLA, A.; ROUSHAN, P.; XIA, Y.; CHECKELSKY, J.; YAZDANI, A.; HASAN, M.; ONG, N. P.; CAVA, R. J. p-type Bi_2Se_3 for topological insulator and low-temperature thermoelectric applications. **Physical Review B**, APS, v. 79, n. 19, p. 195208, 2009.

HOUTEN, H. van; BEENAKKER, C. Quantum point contacts. **Physics Today**, v. 49, p. 22–27, 1996.

HSIEH, D.; XIA, Y.; QIAN, D.; WRAY, L.; MEIER, F.; DIL, H.; OSTERWALDER, J.; PATTHEY, L.; FEDOROV, A.; LIN, H.-H.; BANSIL, A.; GRAUER, D.; HOR, Y.; CAVA, R.; HASAN, M. Z. Observation of time-reversal-protected single-dirac-cone topological-insulator states in Bi_2Te_3 and Sb_2Te_3. **Physical Review Letters**, APS, v. 103, n. 14, p. 146401, 2009.

HUANG, H.; LIU, F. Quantum spin hall effect and spin bott index in a quasicrystal lattice. **Physical Review Letters**, v. 121, n. 12, p. 126401, 2018.

HUANG, H.; LIU, F. Theory of spin bott index for quantum spin hall states in nonperiodic systems. **Physical Review B**, v. 98, n. 12, p. 125130, 2018.

HUANG, H.; LIU, F. Comparison of quantum spin hall states in quasicrystals and crystals. **Physical Review B**, v. 100, n. 8, p. 085119, 2019.

HUANG, K.; FU, H.; WATANABE, K.; TANIGUCHI, T.; ZHU, J. High-temperature quantum valley hall effect with quantized resistance and a topological switch. **Science**, American Association for the Advancement of Science, p. eadj3742, 2024.

HWANG, Y.; RHIM, J.-W.; YANG, B.-J. Flat bands with band crossings enforced by symmetry representation. **Physical Review B**, APS, v. 104, n. 8, p. L081104, 2021.

JIANG, W.; HUANG, H.; LIU, F. A lieb-like lattice in a covalent-organic framework and its stoner ferromagnetism. **Nature Communications**, v. 10, n. 1, 5 2019.

JIANG, W.; KANG, M.; HUANG, H.; XU, H.; LOW, T.; LIU, F. Supplemental material for: topological band evolution between lieb and kagome lattices. **Physical Review B**, American Physical Society, v. 99, p. 125131, Mar 2019.

JIANG, W.; KANG, M.; HUANG, H.; XU, H.; LOW, T.; LIU, F. Topological band evolution between lieb and kagome lattices. **Physical Review B**, American Physical Society, v. 99, p. 125131, Mar 2019.

JIANG, W.; LIU, Z.; MEI, J.-W.; CUI, B.; LIU, F. Dichotomy between frustrated local spins and conjugated electrons in a two-dimensional metal–organic framework. **Nanoscale**, Royal Society of Chemistry, v. 11, n. 3, p. 955–961, 2019.

JIANG, W.; ZHANG, S.; WANG, Z.; LIU, F.; LOW, T. Topological band engineering of lieb lattice in phthalocyanine-based metal–organic frameworks. **Nano Letters**, ACS Publications, v. 20, n. 3, p. 1959–1966, 2020.

JIN, E.; ASADA, M.; XU, Q.; DALAPATI, S.; ADDICOAT, M. A.; BRADY, M. A.; XU, H.; NAKAMURA, T.; HEINE, T.; CHEN, Q.; JIANG, D. Two-dimensional sp_2 carbon–conjugated covalent organic frameworks. **Science**, American Association for the Advancement of Science, v. 357, n. 6352, p. 673–676, 2017.

JU, L.; SHI, Z.; NAIR, N.; LV, Y.; JIN, C.; JR, J. V.; OJEDA-ARISTIZABAL, C.; BECHTEL, H. A.; MARTIN, M. C.; ZETTL, A.; ANALYTIS, J.; WANG, F. Topological valley transport at bilayer graphene domain walls. **Nature**, Nature Publishing Group UK London, v. 520, n. 7549, p. 650–655, 2015.

KANE, C. L. An insulator with a twist. **Nature Physics**, v. 4, p. 348–349, May 2008.

KANE, C. L.; MELE, E. J. Quantum spin hall effect in graphene. **Physical Review Letters**, American Physical Society, v. 95, p. 226801, Nov 2005.

KANE, C. L.; MELE, E. J. Z_2 topological order and the quantum spin hall effect. **Physical Review Letters**, APS, v. 95, n. 14, p. 146802, 2005.

KANÔ, K.; NAYA, S. Antiferromagnetism. the kagomé ising net. **Progress of theoretical physics**, Oxford University Press, v. 10, n. 2, p. 158–172, 1953.

KEIMER, B.; KIVELSON, S. A.; NORMAN, M. R.; UCHIDA, S.; ZAANEN, J. From quantum matter to high-temperature superconductivity in copper oxides. **Nature**, v. 518, p. 179–186, 2015.

KIBIS, O.; KYRIIENKO, O.; SHELYKH, I. Structure of surface electronic states in strained mercury telluride. **New Journal of Physics**, IOP Publishing, v. 21, n. 4, p. 043016, 2019.

KILLI, M.; WEI, T.-C.; AFFLECK, I.; PARAMEKANTI, A. Tunable luttinger liquid physics in biased bilayer graphene. **Physical Review Letters**, v. 104, p. 216406, 2010.

KIM, S.; JO, I.; DILLEN, D.; FERRER, D.; FALLAHAZAD, B.; YAO, Z.; BANERJEE, S.; TUTUC, E. Direct measurement of the fermi energy in graphene using a double-layer heterostructure. **Physical Review Letters**, American Physical Society, v. 108, n. 11, p. 116404, 2012.

KIMURA, T.; TAMURA, H.; SHIRAISHI, K.; TAKAYANAGI, H. Magnetic field effects on the ferromagnetism and transport properties of kagome dot superlattices. **Physica E**: Low-dimensional Systems and Nanostructures, Elsevier, v. 12, n. 1-4, p. 197–199, 2002.

KIRTSCHIG, F.; BRINK, J. van den; ORTIX, C. Surface-state spin textures in strained bulk hgte: Strain-induced topological phase transitions. **Physical Review B**, APS, v. 94, n. 23, p. 235437, 2016.

KITT, A. L.; PEREIRA, V. M.; SWAN, A. K.; GOLDBERG, B. B. Lattice-corrected strain-induced vector potentials in graphene. **Physical Review B**, American Physical Society, v. 85, p. 115432, Mar 2012.

KITT, A. L.; PEREIRA, V. M.; SWAN, A. K.; GOLDBERG, B. B. Erratum: lattice-corrected strain-induced vector potentials in graphene [physical review b 85, 115432 (2012)]. **Physical Review B**, American Physical Society, v. 87, p. 159909, Apr 2013.

KITTEL, C. **Introduction to solid state physics**. 8ª. ed. [*S. l.*]: John Wiley and Sons, 2005.

KLITZING, K. v.; DORDA, G.; PEPPER, M. New method for high-accuracy determination of the fine-structure constant based on quantized hall resistance. **Physical Review Letters**, APS, v. 45, n. 6, p. 494, 1980.

KLITZING, K. von; CHAKRABORTY, T.; KIM, P.; MADHAVAN, V.; DAI, X.; MCIVER, J.; TOKURA, Y.; SAVARY, L.; SMIRNOVA, D.; REY, A. M.; FELSER, C.; GOOTH, J.; QI, X. 40 years of the quantum hall effect. **Nature Reviews Physics**, Nature Publishing Group, v. 2, n. 8, p. 397–401, 2020.

KÖNIG, M.; WIEDMANN, S.; BRÜNE, C.; ROTH, A.; BUHMANN, H.; MOLENKAMP, L. W.; QI, X.-L.; ZHANG, S.-C. Quantum spin hall insulator state in hgte quantum wells. **Science**, v. 318, p. 766–770, 2007.

KONSCHUH, S.; GMITRA, M.; FABIAN, J. Tight-binding theory of the spin-orbit coupling in graphene. **Physical Review B**, APS, v. 82, n. 24, p. 245412, 2010.

KOSTERLITZ, J. M.; THOULESS, D. J. Ordering, metastability and phase transitions in two-dimensional systems. In: **Basic Notions Of Condensed Matter Physics**. [*S. l.*]: CRC Press, 2018. p. 493–515.

LALMI, B.; OUGHADDOU, H.; ENRIQUEZ, H.; KARA, A.; VIZZINI, S.; EALET, B.; AUFRAY, B. Epitaxial growth of a silicene sheet. **Applied Physics Letters**, AIP Publishing, v. 97, n. 22, 2010.

LANG, J.-P.; HANAFI, H.; IMBROCK, J.; DENZ, C. Tilted dirac cones and asymmetric conical diffraction in photonic lieb-kagome lattices. **Physical Review A**, APS, v. 107, n. 2, p. 023509, 2023.

LEE, J.; WATANABE, K.; TANIGUCHI, T.; LEE, H. J. Realisation of topological zero-energy mode in bilayer graphene in zero magnetic field. **Scientific Reports**, v. 7, p. 6466, 2017.

LEYKAM, D.; ANDREANOV, A.; FLACH, S. Artificial flat band systems: from lattice models to experiments. **Advances in Physics**: X, Taylor & Francis, v. 3, n. 1, p. 1473052, 2018.

LI, J.; HE, C.; MENG, L.; XIAO, H.; TANG, C.; WEI, X.; KIM, J.; KIOUSSIS, N.; STOCKS, G. M.; ZHONG, J. Two-dimensional topological insulators with tunable band gaps: Single-layer hgte and hgse. **Scientific Reports**, Nature Publishing Group, v. 5, n. 1, p. 1–9, 2015.

LI, J.; MORPURGO, A.; BÜTTIKER, M.; MARTIN, I. Marginality of bulk-edge correspondence for single-valley hamiltonians. **Physical Review B**, v. 82, p. 245404, 2010.

LI, J.; WANG, K.; MCFAUL, K. J.; ZERN, Z.; REN, Y.; WATANABE, K.; TANIGUCHI, T.; QIAO, Z.; ZHU, J. Gate-controlled topological conducting channels in bilayer graphene. **Nature Nanotechnology**, v. 11, p. 1060–1065, 2016.

LI, J.; ZHANG, R.-X.; YIN, Z.; ZHANG, J.; WATANABE, K.; TANIGUCHI, T.; LIU, C.; ZHU, J. A valley valve and electron beam splitter. **Science**, v. 362, p. 1149–1152, 2018.

LI, L.; YU, Y.; YE, G. J.; GE, Q.; OU, X.; WU, H.; FENG, D.; CHEN, X. H.; ZHANG, Y. Black phosphorus field-effect transistors. **Nature Nanotechnology**, Nature Publishing Group, v. 9, n. 5, p. 372–377, 2014.

LI, L.; YU, Y.; YE, G. J.; GE, Q.; OU, X.; WU, H.; FENG, D.; CHEN, X. H.; ZHANG, Y. Black phosphorus field-effect transistors. **Nature Nanotechnology**, Nature Publishing Group, v. 9, n. 5, p. 372, 2014.

LI, S.; QIU, W. X.; GAO, J. H. Designing artificial two dimensional electron lattice on metal surface: a kagome-like lattice as an example. **Nanoscale**, v. 8, p. 12747–12754, 2016.

LI, T.; JIANG, S.; SHEN, B.; ZHANG, Y.; LI, L.; TAO, Z.; DEVAKUL, T.; WATANABE, K.; TANIGUCHI, T.; FU, L.; SHAN, J.; MAK, K. F. Quantum anomalous hall effect from intertwined moiré bands. **Nature**, Nature Publishing Group, v. 600, p. 641–646, 2021.

LI, T.; WANG, P.; FU, H.; DU, L.; SCHREIBER, K. A.; MU, X.; LIU, X.; SULLIVAN, G.; CSÁTHY, G. A.; LIN, X.; DU, R.-R. Observation of a helical luttinger liquid in InAs/GaSb quantum spin hall edges. **Physical Review Letters**, v. 115, p. 136804, 2015.

LI, W.; QIAN, X.; LI, J. Phase transitions in 2D materials. **Nature Reviews Materials**, Nature Publishing Group UK London, v. 6, n. 9, p. 829–846, 2021.

LI, Y.; JIANG, X.; LIU, Z.; LIU, Z. Strain effects in graphene and graphene nanoribbons: the underlying mechanism. **Nano Research**, v. 3, n. 8, p. 545–556, Aug 2010.

LI, Z.; ZHUANG, J.; WANG, L.; FENG, H.; GAO, Q.; XU, X.; HAO, W.; WANG, X.; ZHANG, C.; WU, K.; DOU, S. X.; CHEN, L.; HU, Z.; DU, Y. Realization of flat band with possible nontrivial topology in electronic kagome lattice. **Science Advances**, American Association for the Advancement of Science, v. 4, n. 11, 2018.

LIARTE, D. B.; STENULL, O.; LUBENSKY, T. Multifunctional twisted kagome lattices: tuning by pruning mechanical metamaterials. **Physical Review E**, APS, v. 101, n. 6, p. 063001, 2020.

LIEB, E. H. Two theorems on the hubbard model. **Physical Review Letters**, v. 62, p. 1201–1204, 1989.

LIM, L.-K.; FUCHS, J.-N.; PIÉCHON, F.; MONTAMBAUX, G. Dirac points emerging from flat bands in lieb-kagome lattices. **Physical Review B**, American Physical Society, v. 101, p. 045131, Jan 2020.

LIMA, F. C. D.; FERREIRA, G. J.; MIWA, R. Topological flat band, dirac fermions and quantum spin hall phase in 2D archimedean lattices. **Physical Chemistry Chemical Physics**, Royal Society of Chemistry, v. 21, n. 40, p. 22344–22350, 2019.

LIMA, F. Crasto de; FERREIRA, G.; MIWA, R. Layertronic control of topological states in multilayer metal-organic frameworks. **The Journal of Chemical Physics**, v. 150, p. 234701, 06 2019.

LIMA, W. P. **Efeitos de strain nos espectros de energias do grafeno e das redes de Lieb e Kagome calculados via aproximação tight-binding**. Dissertação (Mestrado), 2020.

LIMA, W. P.; ARAÚJO, F. R. V.; COSTA, D. R. da; SENA, S. H. R.; PEREIRA, J. Tight-binding model in first and second quantization for band structure calculations. **Brazilian Journal of Physics**, Springer, v. 52, n. 2, p. 1–17, 2022.

LIMA, W. P.; COSTA, D. R. da; SENA, S. H. R.; PEREIRA, J. M. Effects of uniaxial and shear strains on the electronic spectrum of lieb and kagome lattices. **Physical Review B**, American Physical Society, v. 108, p. 125433, Sep 2023.

LIN, Z.; CHOI, J.-H.; ZHANG, Q.; QIN, W.; YI, S.; WANG, P.; LI, L.; WANG, Y.; ZHANG, H.; SUN, Z.; WEI, L.; ZHANG, S.; GUO, T.; LU, Q.; CHO, J.-H.; ZENG, C.; ZHANG, Z. Flatbands and emergent ferromagnetic ordering in Fe_3Sn_2 kagome lattices. **Physical Review Letters**, APS, v. 121, n. 9, p. 096401, 2018.

LIU, E.; SUN, Y.; KUMAR, N.; MUECHLER, L.; SUN, A.; JIAO, L.; YANG, S.-Y.; LIU, D.; LIANG, A.; XU, Q.; KRODER, J.; Süß, V.; BORRMANN, H.; SHEKHAR, C.; WANG, Z.; XI, C.; WANG, W.; SCHNELLE, W.; WIRTH, S.; FELSER, C. Giant anomalous hall effect in a ferromagnetic kagome-lattice semimetal. **Nature Physics**, v. 14, 11 2018.

LIU, G.; ZHU, S.-L.; JIANG, S.; SUN, F.; LIU, W. Simulating and detecting the quantum spin hall effect in the kagome optical lattice. **Physical Review A**, APS, v. 82, n. 5, p. 053605, 2010.

LIU, H.; NEAL, A. T.; ZHU, Z.; LUO, Z.; XU, X.; TOMÁNEK, D.; YE, P. D. Phosphorene: an unexplored 2D semiconductor with a high hole mobility. **ACS Nano**, ACS Publications, v. 8, n. 4, p. 4033–4041, 2014.

LIU, J.; XU YONG E WU, J. e. G. B.-L. e. Z. S. e. D. W. Manipulating topological phase transition by strain. **Acta Crystallographica Section C**: Structural Chemistry, International Union of Crystallography, v. 70, n. 2, p. 118–122, 2014.

LIU, R.; CHEN, W.-C.; WANG, Y.-F.; GONG, C.-D. Topological quantum phase transitions and topological flat bands: On the kagomé lattice. **Journal of Physics**: Condensed Matter, IOP Publishing, v. 24, n. 30, p. 305602, 2012.

LIU, T. Strain-induced pseudomagnetic field and quantum oscillations in kagome crystals. **Physical Review B**, APS, v. 102, n. 4, p. 045151, 2020.

LIU, Z.; WANG, L.; YAO, D.-X. Triply degenerate nodal lines in topological and nontopological metals. **Physical Review B**, APS, v. 103, n. 20, p. 205145, 2021.

LODGE, M. S.; YANG, S. A.; MUKHERJEE, S.; WEBER, B. Atomically thin quantum spin hall insulators. **Advanced Materials**, v. 33, p. e2008029, 2021.

LU, J. L.; LUO, W.; LI, X. Y.; YANG, S. Q.; CAO, J.-X.; GONG, X. G.; XIANG, H.-J. Two dimensional node line semimetals in a honeycomb kagome lattice. **Chinese Physics Letters**, IOP Publishing, v. 34, n. 5, p. 057302, may 2017.

MA, S.-K. **Modern Theory of Critical Phenomena**. [*S. l.*]: W. A. Benjamin, Advanced Book Program, 1976.

MAHONEY, A. C.; COLLESS, J. I.; PEETERS, L.; PAUKA, S. J.; FOX, E. J.; KOU, X.; PAN, L.; WANG, K. L.; GOLDHABER-GORDON, D.; REILLY, D. J. Zero-field edge plasmons in a magnetic topological insulator. **Nature Communications**, v. 8, p. 1836, 2017.

MAK, K. F.; LEE, C.; HONE, J.; SHAN, J.; HEINZ, T. F. Atomically thin MoS_2: a new direct-gap semiconductor. **Physical Review Letters**, American Physical Society, v. 105, n. 13, p. 136805, 2010.

MANI, A.; BENJAMIN, C. Probing helicity and the topological origins of helicity via non-local hanbury-brown and twiss correlations. **Scientific Reports**, Nature Publishing Group UK London, v. 7, n. 1, p. 6954, 2017.

MANIA, E.; CADORE, A. R.; TANIGUCHI, T.; WATANABE, K.; CAMPOS, L. C. Topological valley transport at the curved boundary of a folded bilayer graphene. **Communications Physics**, v. 2, p. 6, 2019.

MARTIN, I.; BLANTER, Y. M.; MORPURGO, A. F. Topological confinement in bilayer graphene. **Physical Review Letters**, v. 100, p. 036804, 2008.

MEKATA, M. Kagome: the story of the basketweave lattice. **Physics Today**, v. 56, 02 2003.

MERMIN, N. D. Crystalline order in two dimensions. **Physical Review**, American Physical Society, v. 176, n. 1, p. 250, 1968.

MIELKE, A. Exact ground states for the hubbard model on the kagome lattice. **Journal of Physics A**: Mathematical and General, IOP Publishing, v. 25, n. 16, p. 4335–4345, aug 1992.

MILIĆEVIĆ, M.; MONTAMBAUX, G.; OZAWA, T.; JAMADI, O.; REAL, B.; SAGNES, I.; LEMAÎTRE, A.; GRATIET, L. L.; HAROURI, A.; BLOCH, J.; AMO, A. Type-III and tilted dirac cones emerging from flat bands in photonic orbital graphene. **Physical Review X**, APS, v. 9, n. 3, p. 031010, 2019.

MITCHELL, N. P.; NASH, L. M.; HEXNER, D.; TURNER, A. M.; IRVINE, W. T. M. Amorphous topological insulators constructed from random point sets. **Nature Physics**, v. 14, n. 4, p. 380–385, 2018.

MIZOGUCHI, T.; UDAGAWA, M. Flat-band engineering in tight-binding models: Beyond the nearest-neighbor hopping. **Physical Review B**, APS, v. 99, n. 23, p. 235118, 2019.

MOJARRO, M.; ULLOA, S. E. Strain-induced topological transitions and tilted dirac cones in kagome lattices. **2D Materials**, IOP Publishing, v. 11, n. 1, p. 011001, 2023.

MONTAMBAUX, G.; LIM, L.-K.; FUCHS, J.-N.; PIÉCHON, F. Winding vector: How to annihilate two dirac points with the same charge. **Physical Review Letters**, American Physical Society, v. 121, p. 256402, Dec 2018.

MONTAMBAUX, G.; PIECHON, F.; FUCHS, J.; GOERBIG, M. Merging of dirac points in a two-dimensional crystal. **Physical Review B**, v. 80, 04 2009.

MONTAMBAUX, G.; PIECHON, F.; FUCHS, J.-N.; GOERBIG, M. A universal hamiltonian for motion and merging of dirac points in a two-dimensional crystal. **European Physical Journal B**, v. 72, p. 509–520, 07 2009.

MOORE, J. E. The birth of topological insulators. **Nature**, v. 464, p. 194–198, Mar 2010.

MUKHERJEE, S.; SPRACKLEN, A.; CHOUDHURY, D.; GOLDMAN, N.; ÖHBERG, P.; ANDERSSON, E.; THOMSON, R. R. Observation of a localized flat-band state in a photonic lieb lattice. **Physical Review Letters**, APS, v. 114, n. 24, p. 245504, 2015.

MUKHERJEE, S.; SPRACKLEN, A.; CHOUDHURY, D.; GOLDMAN, N.; ÖHBERG, P.; ANDERSSON, E.; THOMSON, R. R. Observation of a localized flat-band state in a photonic lieb lattice. **Physical Review Letters**, APS, v. 114, n. 24, p. 245504, 2015.

MURAKAMI, S. Phase transition between the quantum spin hall and insulator phases in 3D: Emergence of a topological gapless phase. **New Journal of Physics**, IOP Publishing, v. 9, n. 9, p. 356, 2007.

MURAKAMI, S.; ISO, S.; AVISHAI, Y.; ONODA, M.; NAGAOSA, N. Tuning phase transition between quantum spin hall and ordinary insulating phases. **Physical Review B**, APS, v. 76, n. 20, p. 205304, 2007.

MUTCH, J.; CHEN, W.-C.; WENT, P.; QIAN, T.; WILSON, I. Z.; ANDREEV, A.; CHEN, C.-C.; CHU, J.-H. Evidence for a strain-tuned topological phase transition in $ZrTe_5$. **Science advances**, American Association for the Advancement of Science, v. 5, n. 8, p. eaav9771, 2019.

NAKAHARA, M. **Geometry, topology and physics**. [*S. l.*]: CRC press, 2018.

NAKAMURA, J.; LIANG, S.; GARDNER, G. C.; MANFRA, M. J. Direct observation of anyonic braiding statistics. **Nature Physics**, v. 16, p. 931–936, 2020.

NAKATSUJI, S.; KIYOHARA, N.; HIGO, T. Large anomalous hall effect in a non-collinear antiferromagnet at room temperature. **Nature**, v. 527, p. 212–215, 2015.

NASCIMENTO, J. S.; COSTA, D. R. da; ZARENIA, M.; CHAVES, A.; PEREIRA, J. M. Magnetic properties of bilayer graphene quantum dots in the presence of uniaxial strain. **Physical Review B**, APS, v. 96, n. 11, p. 115428, 2017.

NAUMIS, G. G.; BARRAZA-LOPEZ, S.; OLIVA-LEYVA, M.; TERRONES, H. Electronic and optical properties of strained graphene and other strained 2D materials a review. **Reports on Progress in Physics**, IOP Publishing, v. 80, n. 9, p. 096501, aug 2017.

NAYAK, C.; SIMON, S. H.; STERN, A.; FREEDMAN, M.; SARMA, S. D. Non-abelian anyons and topological quantum computation. **Reviews of Modern Physics**, v. 80, p. 1083–1159, 2008.

NELSON, D. R.; KOSTERLITZ, J. Universal jump in the superfluid density of two-dimensional superfluids. **Physical Review Letters**, APS, v. 39, n. 19, p. 1201, 1977.

NICHOLSON, C. W.; RUMO, M.; PULKKINEN, A.; KREMER, G.; SALZMANN, B.; MOTTAS, M.-L.; HILDEBRAND, B.; JAOUEN, T.; KIM, T. K.; MUKHERJEE, S.; MA, K.; MUNTWILER, M.; ROHR, F. O. von; CACHO, C.; MONNEY, C. Uniaxial strain-induced phase transition in the 2D topological semimetal $IrTe_2$. **Communications Materials**, Nature Publishing Group UK London, v. 2, n. 1, p. 25, 2021.

NITA, M.; OSTAHIE, B.; ALDEA, A. Spectral and transport properties of the two-dimensional lieb lattice. **Physical Review B**, v. 87, p. 125428, Mar 2013.

NOVOSELOV, K. Nobel lecture graphene: Materials in the flatland. **Reviews of Modern Physics**, American Physical Society, v. 83, n. 3, p. 837, 2011.

NOVOSELOV, K. S.; GEIM, A. K.; MOROZOV, S. V.; JIAN, D.; ZHANG, Y.; DUBONOS, S. V.; GRIGORIEVA, I. V.; FIRSOV, A. A. Electric field effect in atomically thin carbon films. **Science**, v. 306, p. 666–669, 2004.

OHGUSHI, K.; MURAKAMI, S.; NAGAOSA, N. Spin anisotropy and quantum hall effect in the kagomé lattice: chiral spin state based on a ferromagnet. **Physical Review B**, American Physical Society, v. 62, p. R6065–R6068, Sep 2000.

OLIVA-LEYVA, M.; NAUMIS, G. G. Understanding electron behavior in strained graphene as a reciprocal space distortion. **Physical Review B**, APS, v. 88, n. 8, p. 085430, 2013.

OLIVA-LEYVA, M.; NAUMIS, G. G. Generalizing the fermi velocity of strained graphene from uniform to nonuniform strain. **Physics Letters A**, v. 379, n. 40, p. 2645 – 2651, 2015.

OLIVA-LEYVA, M.; WANG, C. Low-energy theory for strained graphene: an approach up to second-order in the strain tensor. **Journal of Physics**: Condensed Matter, IOP Publishing, v. 29, n. 16, p. 165301, mar 2017.

ONO, T.; MORITA, K.; YANO, M.; TANAKA, H.; FUJII, K.; UEKUSA, H.; NARUMI, Y.; KINDO, K. Magnetic susceptibilities in a family of $S = 1/2$ kagome antiferromagnets. **Physical Review B**, American Physical Society, v. 79, p. 174407, May 2009.

ONSAGER, L. Crystal statistics. i. a two-dimensional model with an order-disorder transition. **Physical Review**, APS, v. 65, n. 3-4, p. 117, 1944.

OWERRE, S. A. Strain-induced topological magnon phase transitions: applications to kagome-lattice ferromagnets. **Journal of Physics**: Condensed Matter, IOP Publishing, v. 30, n. 24, p. 245803, may 2018.

PAL, K.; WAGHMARE, U. V. Strain induced Z_2 topological insulating state of β-As_2Te_3. **Applied Physics Letters**, AIP Publishing LLC, v. 105, n. 6, p. 062105, 2014.

PANCHARATNAM, S. Generalized theory of interference and its applications. In: SPRINGER. **Proceedings of the Indian Academy of Sciences-Section A**. [*S. l.*], 1956. v. 44, n. 6, p. 398–417.

PEREIRA, J. M.; PEETERS, F.; CHAVES, A.; FARIAS, G. Klein tunneling in single and multiple barriers in graphene. **Semiconductor science and technology**, IOP Publishing, v. 25, n. 3, p. 033002, 2010.

PEREIRA, V. M.; CASTRO NETO, A. H.; PERES, N. M. R. Tight-binding approach to uniaxial strain in graphene. **Physical Review B**, American Physical Society, v. 80, p. 045401, Jul 2009.

PESIN, D.; BALENTS, L. Mott physics and band topology in materials with strong spin–orbit interaction. **Nature Physics**, Nature Publishing Group, v. 6, n. 5, p. 376–381, 2010.

PETRESCU, A.; HOUCK, A. A.; HUR, K. L. Anomalous hall effects of light and chiral edge modes on the kagomé lattice. **Physical Review A**, American Physical Society, v. 86, p. 053804, Nov 2012.

QI, X.-L.; HUGHES, T. L.; ZHANG, S.-C. Topological field theory of time-reversal invariant insulators. **Physical Review B**, APS, v. 78, n. 19, p. 195424, 2008.

QI, X.-L.; ZHANG, S.-C. Topological insulators and superconductors. **Reviews of Modern Physics**, American Physical Society, v. 83, p. 1057–1110, Oct 2011.

QIAN, X.; FU, L.; LI, J. Topological crystalline insulator nanomembrane with strain-tunable band gap. **Nano Research**, Springer, v. 8, n. 3, p. 967–979, 2015.

QIAN, X.; LIU, J.; FU, L.; LI, J. Solid state theory. quantum spin hall effect in two-dimensional transition metal dichalcogenides. **Science**, v. 346, p. 1344–1347, 2014.

QIAO, Z.; JUNG, J.; NIU, Q.; MACDONALD, A. H. Electronic highways in bilayer graphene. **Nano Letters**, v. 11, p. 3453–3459, 2011.

QIAO, Z.; YANG, S. A.; FENG, W.; TSE, W.-K.; DING, J.; YAO, Y.; WANG, J.; NIU, Q. Quantum anomalous hall effect in graphene from rashba and exchange effects. **Physical Review B**, APS, v. 82, n. 16, p. 161414, 2010.

QU, L.-H.; ZHANG, J.-M.; XU, K.-W.; JI, V. Armchair graphene nanoribbons under shear strain. **Physica E**: Low-dimensional Systems and Nanostructures, v. 60, p. 156–159, 2014.

RADISAVLJEVIC, B.; RADENOVIC, A.; BRIVIO, J.; GIACOMETTI, V.; KIS, A. Single-layer MoS_2 transistors. **Nature Nanotechnology**, Nature Publishing Group, v. 6, n. 3, p. 147–150, 2011.

RAMIRES, A.; LADO, J. L. Electrically tunable gauge fields in tiny-angle twisted bilayer graphene. **Physical Review Letters**, APS, v. 121, n. 14, p. 146801, 2018.

RECHTSMAN, M. C.; ZEUNER, J. M.; PLOTNIK, Y.; LUMER, Y.; PODOLSKY, D.; DREISOW, F.; NOLTE, S.; SEGEV, M.; SZAMEIT, A. Photonic floquet topological insulators. **Nature**, Nature Publishing Group UK London, v. 496, n. 7444, p. 196–200, 2013.

REICH, S.; MAULTZSCH, J.; THOMSEN, C.; ORDEJON, P. Tight-binding description of graphene. **Physical Review B**, APS, v. 66, n. 3, p. 035412, 2002.

REICHARDT, S.; JURKUTAT, M.; GUEHNE, R.; KOHLRAUTZ, J.; ERB, A.; HAASE, J. Bulk charge ordering in the CuO_2 plane of the cuprate superconductor $YBa_2Cu_3O_{6.9}$ by high-pressure NMR. **Condensed Matter**, v. 3, p. 23, 07 2018.

REIS, F.; LI, G.; DUDY, L.; BAUERNFEIND, M.; GLASS, S.; HANKE, W.; THOMALE, R.; SCHAFER, J.; CLAESSEN, R. Bismuthene on a SiC substrate: A candidate for a high-temperature quantum spin hall material. **Science**, v. 357, n. 6348, p. 287–290, 2017.

REN, Y.; QIAO, Z.; NIU, Q. Topological phases in two-dimensional materials: a review. **Reports on Progress in Physics**, IOP Publishing, v. 79, n. 6, p. 066501, 2016.

RHODES, D.; CHAE, S. H.; RIBEIRO-PALAU, R.; HONE, J. Disorder in van der waals heterostructures of 2D materials. **Nature Materials**, v. 18, p. 541–549, 2019.

SACHDEV, S. **Quantum Phase Transitions**. 2nd. ed. [*S. l.*]: Cambridge University Press, 2011.

SAITO, R.; DRESSELHAUS, G.; DRESSELHAUS, M. S. **Physical Properties of Carbon Nanotubes**. London: Imperial College Press, 1998.

SAKURAI, J. Modern quantum mechanics (revised edition) addison-wesley. **Reading**, v. 41, p. 221–223, 1994.

SARMA, S. D.; PINCZUK, A. **Perspectives in quantum hall effects**: Novel quantum liquids in low-dimensional semiconductor structures. [*S. l.*]: John Wiley & Sons, 2008.

SCHULZ, S. A.; UPHAM, J.; O'FAOLAIN, L.; BOYD, R. W. Photonic crystal slow light waveguides in a kagome lattice. **Optics Letters**, OSA, v. 42, n. 16, p. 3243–3246, Aug 2017.

SENA, S. H. R.; PEREIRA JÚNIOR, J. M.; FARIAS, G. A.; PEETERS, F. M.; COSTA FILHO, R. N. The electronic properties of graphene and graphene ribbons under simple shear strain. **Journal of Physics**: Condensed Matter, IOP Publishing, v. 24, n. 37, p. 375301, aug 2012.

SERLIN, M.; TSCHIRHART, C. L.; POLSHYN, H.; ZHANG, Y.; ZHU, J.; WATANABE, K.; TANIGUCHI, T.; BALENTS, L.; YOUNG, A. F. Intrinsic quantized anomalous hall effect in a moiré heterostructure. **Science**, American Association for the Advancement of Science, v. 367, p. 900–903, 2020.

SHEN, R.; SHAO, L. B.; WANG, B.; XING, D. Y. Single dirac cone with a flat band touching on line-centered-square optical lattices. **Physical Review B**, v. 81, p. 041410(R), 2010.

SHENG, D.; WENG, Z.; SHENG, L.; HALDANE, F. Quantum spin-hall effect and topologically invariant chern numbers. **Physical Review Letters**, APS, v. 97, n. 3, p. 036808, 2006.

SI, C.; SUN, Z.; LIU, F. Strain engineering of graphene a review. **Nanoscale**, The Royal Society of Chemistry, v. 8, p. 3207–3217, 2016.

SILVA, E. Z. da. Energy and density of states calculations for various materials. **Journal of Computational Materials Science**, Elsevier, v. 98, p. 192–198, 2015.

SIMON, S. H. **The Oxford**: Solid state basics. New York: Oxford University Press, 2013.

SLOT, M.; KEMPKES, S.; KNOL, E.; WEERDENBURG, W. V.; BROEKE, J. V. D.; WEGNER, D.; VANMAEKELBERGH, D.; KHAJETOORIANS, A.; SMITH, C. M.; SWART, I. p-band engineering in artificial electronic lattices. **Physical Review X**, APS, v. 9, n. 1, p. 011009, 2019.

SLOT, M. R.; GARDENIER, T. S.; JACOBSE, P. H.; MIERT, G. C. V.; KEMPKES, S. N.; ZEVENHUIZEN, S. J.; SMITH, C. M.; VANMAEKELBERGH, D.; SWART, I. Experimental realization and characterization of an electronic lieb lattice. **Nature physics**, Nature Publishing Group UK London, v. 13, n. 7, p. 672–676, 2017.

SONI, R.; KAUSHAL, N.; OKAMOTO, S.; DAGOTTO, E. Flat bands and ferrimagnetic order in electronically correlated dice-lattice ribbons. **Physical Review B**, APS, v. 102, n. 4, p. 045105, 2020.

SWAIN, N.; KARMAKAR, M. Strain-induced superconductor-insulator transition on a lieb lattice. **Physical Review Research**, APS, v. 2, n. 2, p. 023136, 2020.

TAIE, S.; OZAWA, H.; ICHINOSE, T.; NISHIO, T.; NAKAJIMA, S.; TAKAHASHI, Y. Coherent driving and freezing of bosonic matter wave in an optical lieb lattice. **Science Advances**, American Association for the Advancement of Science, v. 1, n. 10, p. e1500854, 2015.

TANG, E.; MEI, J.-W.; WEN, X.-G. High-temperature fractional quantum hall states. **Physical Review Letters**, American Physical Society, v. 106, p. 236802, Jun 2011.

TAO, L.; CINQUANTA, E.; CHIAPPE, D.; GRAZIANETTI, C.; FANCIULLI, M.; DUBEY, M.; MOLLE, A.; AKINWANDE, D. Silicene field-effect transistors operating at room temperature. **Nature nanotechnology**, Nature Publishing Group UK London, v. 10, n. 3, p. 227–231, 2015.

TESHOME, T.; DATTA, A. Topological phase transition in Sb_2Mg_3 assisted by strain. **ACS omega**, ACS Publications, v. 4, n. 5, p. 8701–8706, 2019.

THIEL, C.; VOSS, J.; MARTIN, R. J.; NEFF, P. Shear, pure and simple. **International Journal of Non-Linear Mechanics**, Elsevier, v. 112, p. 57–72, 2019.

THOULESS, D. J.; KOHMOTO, M.; NIGHTINGALE, M. P.; NIJS, M. den. Quantized hall conductance in a two-dimensional periodic potential. **Physical Review Letters**, APS, v. 49, n. 6, p. 405, 1982.

TITVINIDZE, I.; LEGENDRE, J.; GROTHUS, M.; IRSIGLER, B.; HUR, K. L.; HOFSTETTER, W. Spin-orbit coupling in the kagome lattice with flux and time-reversal symmetry. **Physical Review B**, APS, v. 103, n. 19, p. 195105, 2021.

UCHOA, E. d. S. **Estados eletrônicos de nanofitas de redes de Lieb, transição e Kagome**. Dissertação (Mestrado), 2023.

UOWNOW. **2D Electronic Kagome Lattice**. 2019. Disponível em: <https://www.youtube.com/watch?v=TPP2ieJ2Q4A>. Acesso em: 04 maio 2024.

VANDERBILT, D. **Berry Phases in Electronic Structure Theory**: Electric polarization, orbital magnetization and topological insulators. [*S. l.*]: Cambridge University Press, 2018.

VICENCIO, R. A.; CANTILLANO, C.; MORALES-INOSTROZA, L.; REAL, B.; MEJÍA-CORTÉS, C.; WEIMANN, S.; SZAMEIT, A.; MOLINA, M. I. Observation of localized states in lieb photonic lattices. **Physical Review Letters**, American Physical Society, v. 114, p. 245503, Jun 2015.

WAN, X.; TURNER, A. M.; VISHWANATH, A.; SAVRASOV, S. Y. Topological semimetal and fermi-arc surface states in the electronic structure of pyrochlore iridates. **Physical Review B**, APS, v. 83, n. 20, p. 205101, 2011.

WANG, D.; CHEN, L.; LIU, H.; SHI, C.; WANG, X.; CUI, G.; ZHANG, P.; CHEN, Y. Strain induced band inversion and topological phase transition in methyl-decorated stanene film. **Scientific reports**, Nature Publishing Group, v. 7, n. 1, p. 1–8, 2017.

WANG, Q.; LEI, H.; QI, Y.; FELSER, C. Topological quantum materials with kagome lattice. **Accounts of Materials Research**, ACS Publications, 2024.

WANG, Q. H.; KALANTAR-ZADEH, K.; KIS, A.; COLEMAN, J. N.; STRANO, M. S. Electronics and optoelectronics of two-dimensional transition metal dichalcogenides. **Nature Nanotechnology**, Nature Publishing Group, v. 7, n. 11, p. 699–712, 2012.

WANG, R.; QIAO, Q.; WANG, B.; DING, X.-H.; ZHANG, Y.-F. The topological quantum phase transitions in lieb lattice driven by the rashba soc and exchange field. **The European Physical Journal B**, Springer, v. 89, p. 1–6, 2016.

WEEKS, C.; FRANZ, M. Topological insulators on the lieb and perovskite lattices. **Physical Review B**, v. 82, p. 085310, 2010.

WEN, X.-G. Colloquium: Zoo of quantum-topological phases of matter. **Reviews of Modern Physics**, APS, v. 89, n. 4, p. 041004, 2017.

WIEDER, B. J.; ZHANG, F.; KANE, C. L. Critical behavior of four-terminal conductance of bilayer graphene domain walls. **Physical Review B**, v. 92, p. 085425, 2015.

WILCZEK, F.; SHAPERE, A. **Geometric phases in physics**. [*S. l.*]: World Scientific, 1989. v. 5.

WRAY, L. A.; XU, S.-Y.; XIA, Y.; HSIEH, D.; FEDOROV, A. V.; HOR, Y. S.; CAVA, R. J.; BANSIL, A.; LIN, H.; HASAN, M. Z. A topological insulator surface under strong coulomb, magnetic and disorder perturbations. **Nature Physics**, Nature Publishing Group, v. 7, n. 1, p. 32–37, 2011.

WU, L.; BRAHLEK, M.; AGUILAR, R. V.; STIER, A.; MORRIS, C.; LUBASHEVSKY, Y.; BILBRO, L.; BANSAL, N.; OH, S.; ARMITAGE, N. A sudden collapse in the transport lifetime across the topological phase transition in $(Bi_{1-x}\ In_x)_2Se_3$. **Nature Physics**, Nature Publishing Group UK London, v. 9, n. 7, p. 410–414, 2013.

WU, S.; FATEMI, V.; GIBSON, Q. D.; WATANABE, K.; TANIGUCHI, T.; CAVA, R. J.; JARILLO-HERRERO, P. Observation of the quantum spin hall effect up to 100 kelvin in a monolayer crystal. **Science**, v. 359, p. 76–79, 2018.

WU, W.; SUN, S.; TANG, C. S.; WU, J.; MA, Y.; ZHANG, L.; CAI, C.; ZHONG, J.; MILOSEVIC, M.; WEE, A.; YIN, X. Realization of a two-dimensional lieb lattice in a metal-inorganic framework with flat bands and topological edge states. **arXiv preprint arXiv:2404.18430**, 2024.

XIA, F.; WANG, H.; XIAO, D.; DUBEY, M.; RAMASUBRAMANIAM, A. Two-dimensional material nanophotonics. **Nature Photonics**, v. 8, 10 2014.

XIA, S.; HU, Y.; SONG, D.; ZONG, Y.; TANG, L.; CHEN, Z. Demonstration of flat-band image transmission in optically induced lieb photonic lattices. **Optics Letters**, Optica Publishing Group, v. 41, n. 7, p. 1435–1438, 2016.

XIA, Y.; QIAN, D.; HSIEH, D.; WRAY, L.; PAL, A.; LIN, H.; BANSIL, A.; GRAUER, D.; HOR, Y. S.; CAVA, R. J.; HASAN, M. Z. Observation of a large-gap topological-insulator class with a single dirac cone on the surface. **Nature Physics**, Nature Publishing Group, v. 5, n. 6, p. 398–402, 2009.

XING, S.; ZHAO, T.; ZHOU, J.; SUN, Z. Strain-modulated phase transition in 2D V_3F_8 kagome lattice with topological flat band. **The Journal of Physical Chemistry C**, ACS Publications, 2024.

XU, S.-Y.; XIA, Y.; WRAY, L. A.; JIA, S.; MEIER, F.; DIL, J. H.; OSTERWALDER, J.; SLOMSKI, B.; BANSIL, A.; LIN, H.; CAVA, R. J.; HASAN, M. Z. Topological phase transition and texture inversion in a tunable topological insulator. **Science**, American Association for the Advancement of Science, v. 332, n. 6029, p. 560–564, 2011.

XUE, J.; SANCHEZ-YAMAGISHI, J.; BULMASH, D.; JACQUOD, P.; DESHPANDE, A.; WATANABE, K.; TANIGUCHI, T.; JARILLO-HERRERO, P.; LEROY, B. J. Scanning tunnelling microscopy and spectroscopy of ultra-flat graphene on hexagonal boron nitride. **Nature materials**, Nature Publishing Group, v. 10, n. 4, p. 282–285, 2011.

YANG, Y.; XU, Z.; SHENG, L.; WANG, B.; XING, D.; SHENG, D. Time-reversal-symmetry-broken quantum spin hall effect. **Physical Review Letters**, APS, v. 107, n. 6, p. 066602, 2011.

YAZYEV, O. An upside-down magnet. **Nature Physics**, v. 15, 02 2019.

YE, L.; KANG, M.; LIU, J.; CUBE, F.; WICKER, C.; SUZUKI, T.; JOZWIAK, C.; BOSTWICK, A.; ROTENBERG, E.; BELL, D.; FU, L.; COMIN, R.; CHECKELSKY, J. Massive dirac fermions in a ferromagnetic kagome metal. **Nature**, v. 555, 03 2018.

YIN, J.; ZHANG, S.; CHANG, G.; WANG, Q.; TSIRKIN, S.; GUGUCHIA, Z.; LIAN, B.; ZHOU, H.; JIANG, K.; BELOPOLSKI, I.; SHUMIYA, N.; MULTER, D.; LITSKEVICH, M.; COCHRAN, T.; LIN, H.; WANG, Z.; NEUPERT, T.; JIA, S.; LEI, H.; HASAN, M. Z. Negative flat band magnetism in a spin–orbit-coupled correlated kagome magnet. **Nature Physics**, v. 15, 05 2019.

YIN, J.-X.; LIAN, B.; HASAN, M. Z. Topological kagome magnets and superconductors. **Nature**, Nature Publishing Group UK London, v. 612, n. 7941, p. 647–657, 2022.

ZARENIA, M.; PEREIRA, J. M.; FARIAS, G. A.; PEETERS, F. M. Chiral states in bilayer graphene: Magnetic field dependence and gap opening. **Physical Review B**, v. 84, p. 125451, 2011.

ZHANG, F.; MACDONALD, A. H.; MELE, E. J. Valley chern numbers and boundary modes in gapped bilayer graphene. **Proceedings of the National Academy of Sciences of the United States of America**, v. 110, p. 10546–10551, 2013.

ZHANG, L.; TONG, P. Staggered potential and magnetic field tunable electronic switch in a kagome nanoribbon junction. **Journal of Physics**: Condensed Matter, IOP Publishing, v. 31, n. 30, p. 305302, 2019.

ZHANG, R.-X.; LIU, C.-X. Fingerprints of a bosonic symmetry-protected topological state in a quantum point contact. **Physical Review Letters**, v. 118, p. 216803, 2017.

ZHANG, W.; OHTA, H.; OKUBO, S.; FUJISAWA, M.; SAKURAI, T.; OKAMOTO, Y.; YOSHIDA, H.; HIROI, Z. High-field esr measurements of s= 1/2 kagome lattice antiferromagnet $BaCu_3V_2O_8(OH)_2$. **Journal of the Physical Society of Japan**, The Physical Society of Japan, v. 79, n. 2, p. 023708, 2010.

ZHANG, Y.; LIU, X.; BELIC, M. R.; ZHONG, W.; LI, C.; CHEN, H.; ZHANG, Y. Dispersion relations of strained and complex lieb lattices based on the tight-binding method. **Romanian Reports in Physics**, v. 68, n. 230, p. 28, 2016.

ZHANG, Y.; SUN YAN E YAN, B. Berry curvature dipole in weyl semimetal materials: an ab initio study. **Physical Review B**, APS, v. 97, n. 4, p. 041101, 2018.

ZHAO, X.; WANG, Z.; CHEN, J.; WANG, B. Topological properties and optical conductivities tuned by spin-orbit coupling and strain in kagome lattices. **Results in Physics**, Elsevier, v. 35, p. 105360, 2022.

ZHONG, H.; WANG, R.; YE, F.; ZHANG, J.; ZHANG, L.; ZHANG, Y.; BELIć, M.; ZHANG, Y. Topological insulator properties of photonic kagome helical waveguide arrays. **Results in Physics**, v. 12, 12 2018.

ZHOU, M.; MING, W.; LIU, Z.; WANG, Z.; LI, P.; LIU, F. Epitaxial growth of large-gap quantum spin hall insulator on semiconductor surface. **Proceedings of the National Academy of Sciences of the United States of America**, v. 111, n. 40, p. 14378–14381, 2014.

ZONG, Y.; XIA, S.; TANG, L.; SONG, D.; HU, Y.; PEI, Y.; SU, J.; LI, Y.; CHEN, Z. Observation of localized flat-band states in kagome photonic lattices. **Optics Express**, v. 24, p. 8877, 04 2016.

APPENDIX A – DEFINITIONS OF THE THEORY OF BERRY

In this appendix, we concisely present the definitions of the main concepts of the theory of Berry in the context of topological insulators, namely, Berry phase, Berry potential, Berry curvature, and Chern number. For a detailed discussion, see Bernevig (2013) and/or Vanderbilt (2018).

A1. Berry phase

The geometric (PANCHARATNAM, 1956) or Berry phase (BERRY, 1984) is a quantity that describes how a global phase accumulates as some complex vector is carried around a closed loop in a complex vector space (WILCZEK; SHAPERE, 1989; FRANKEL, 2011; NAKAHARA, 2018; ESCHRIG, 2011). Is usually applied to the adiabatic dynamics of finite quantum systems, where the vector in question is Bloch wavevector, and the path lies in the space of wavevectors $\boldsymbol{k}$ within the BZ.

In the continuum formulation, we can take the path to be parametrized by a real variable λ such that $|u_\lambda\rangle$ traverses the path as λ evolves from 0 to 1, with $|u_{\lambda=0}\rangle \equiv |u_{\lambda=1}\rangle$ (see Fig. 104(a)). We assume here that $|u_\lambda\rangle$ is a smooth and differentiable function of λ. Thus, the continuum expression for the Berry phase is (BERRY, 1984; WILCZEK; SHAPERE, 1989)

$$\phi = \oint \langle u_\lambda | i\partial_\lambda u_\lambda \rangle \, d\lambda. \tag{A.1}$$

A2. Berry potential

The integrand on the right-hand side of Eq. (A.1) is known as the Berry connection or Berry potential

$$A(\lambda) = \langle u_\lambda | i\partial_\lambda u_\lambda \rangle . \tag{A.2}$$

in terms of which the Berry phase is

$$\phi = \oint A(\lambda) d\lambda. \tag{A.3}$$

The Berry connection is not gauge-invariant for a gauge transformation of form

$$|\tilde{u}_\lambda\rangle = e^{-i\beta(\lambda)} |u_\lambda\rangle , \tag{A.4}$$

but the Berry phase is gauge-invariant modulo 2π, or in other words, gauge-invariant when regarded as a phase angle. Although the quantum probabilities is proportional to the norm

Figure 104 – (a) Evolution of a state vector $|u_\lambda\rangle$ in continuum limit, in which the parameter runs over $\lambda \in [0,1]$ with $|u_{\lambda=0}\rangle = |u_{\lambda=1}\rangle$. (b) Region S of a two-dimensional $\lambda = (\lambda_x, \lambda_y)$ parameter space, bounded by loop P.

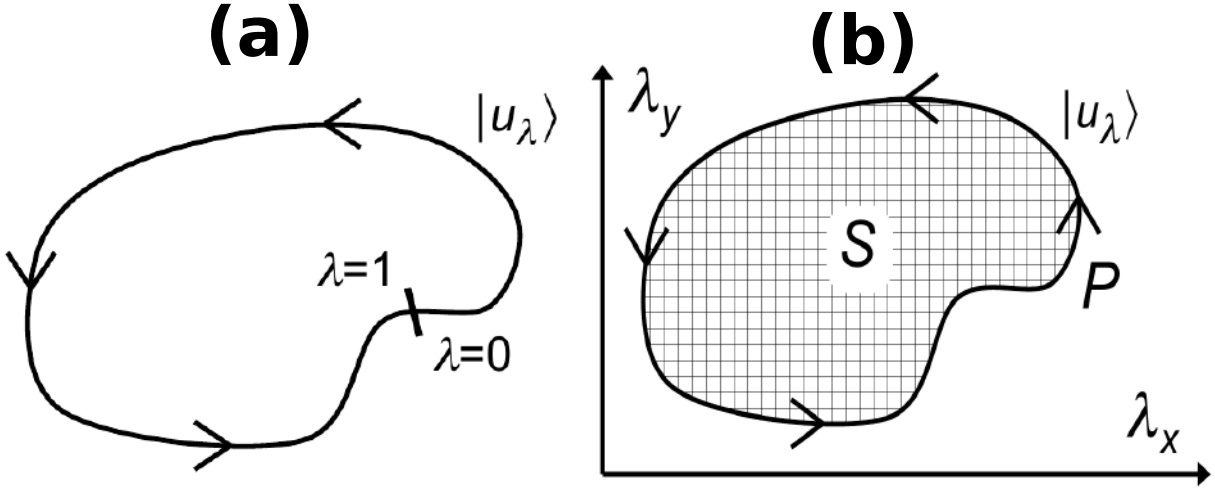

Source: Adapted from (a) Vanderbilt (2018, p. 84) and (b) Vanderbilt (2018, p. 215).

squared of an amplitude, the phases can lead to interference phenomena that are physically important. For example, if duplicate copies of a system are prepared, subjected to parallel transport along different paths in parameter space, and then recombined, the resulting phase difference can lead to physical and measurable interference effects (VANDERBILT, 2018).

A3. Berry curvature

Consider a two-dimensional parameter space such as that illustrated in Fig. 104(b), so that we have vectors $|u_{\boldsymbol{\lambda}}\rangle$ as a function of $\boldsymbol{\lambda} = (\lambda_x, \lambda_y)$. Then the definition of the Berry connection in Eq. (A.2) naturally generalizes to that of a λ-dependent 2D vector $\boldsymbol{A} = (A_x, A_y)$ via

$$A_\mu = \langle u_{\boldsymbol{\lambda}} | i\partial_\mu u_{\boldsymbol{\lambda}} \rangle \,. \tag{A.5}$$

where $\partial_\mu = \partial/\partial\lambda_\mu$ ($\mu = x, y$), and the Berry phase expression of Eq. (A.3) can be written as a line integral around the loop P, i.e.,

$$\phi = \oint_P \boldsymbol{A} \cdot d\boldsymbol{\lambda}. \tag{A.6}$$

Then the Berry curvature $\Omega(\boldsymbol{\lambda})$ is defined as the Berry phase per unit area in (λ_x, λ_y) space. In a continuum framework, it becomes just the curl of the Berry connection, such that we can use Stokes' theorem to relate the "Berry flux" Φ_S through surface patch S to the Berry phase around the boundary P,

$$\Phi_S = \int_S \boldsymbol{\Omega}(\boldsymbol{\lambda}) \cdot d\boldsymbol{S} = \oint_P \boldsymbol{A} \cdot d\boldsymbol{\lambda} = \phi_P. \tag{A.7}$$

where P traces the boundary of region S in the positive sense of circulation. That is, the Berry flux through the surface is equal to the Berry phase around its boundary. It is worth mentioning that the Berry curvature is gauge-invariant.

There is a close analogy connecting the real-space electromagnetic vector potential $\mathbf{A(r)}$ and its curl, the magnetic field B(r), with the parameter-space Berry connection $\boldsymbol{A(\lambda)}$ and its curl $\boldsymbol{\Omega(\lambda)}$. In both cases, the "potential" $\boldsymbol{A}$ is gauge-dependent, while the "field" $\boldsymbol{B}$ or $\boldsymbol{\Omega}$ is not, essentially because the gauge freedom is removed when the curl is taken (VANDERBILT, 2018).

A4. Chern theorem

A consequence of the previous definitions is Chern's theorem which states: The Berry flux Φ_S computed on any closed 2D manifold is quantized to be 2π times an integer, i.e.,

$$\int_S \boldsymbol{\Omega}(\boldsymbol{\lambda}) \cdot d\boldsymbol{S} = 2\pi C, \tag{A.8}$$

for some integer C known as the Chern number or Chern index of the surface, and can regarded as a "topological index" or "topological invariant" attached to the manifold of states $|u_{\boldsymbol{\lambda}}\rangle$ defined over the surface S. It is worth mentioning that the Chern index depends not on the geometry of the surface, but on the manifold of states $|u_{\boldsymbol{\lambda}}\rangle$ defined over it.

APPENDIX B – PUBLICATION RELATED TO THIS THESIS

– LIMA, W. P.; ARAÚJO, F. R. V.; COSTA, D. R. da; SENA, S. H. R.; PEREIRA JR., J. Milton **Tight-binding model in first and second quantization for band structure calculations**. Brazilian Journal of Physics, v. 52, n. 2, p. 42, 2022.

– LIMA, W. P.; COSTA, D. R. da; SENA, S. H. R.; PEREIRA JR., J. Milton. **Effects of uniaxial and shear strains on the electronic spectrum of Lieb and kagome lattices**. Physical Review B, v. 108, n. 125433, 26 set. 2023.